Plasma Deposition and Modification of Electrical Barrier Coatings

REBEKAH CATHERINE FRASER

Plasma Deposition and Modification of Electrical Barrier Coatings

Rebekah Catherine Fraser

Ph.D. Thesis

Department of Chemistry

University of Durham

2018

Declaration

The work described in this thesis was carried out in the Department of Chemistry at Durham University between October 2013 and September 2016. It is the original work of the author except where otherwise acknowledged and has not been previously submitted for a degree in this or any other University. Polymer deposition, plasma fluorination and XPS analysis, Chapter 4, Section 4.4.3, were performed by Isaias Castañeda-Montes, 2018.

Statement of Copyright

Acknowledgements

I would like to thank the members of Lab 98, past and present. In particular, special thanks go to Matthew Wilson, Hannah Blacknell, Andrea Carletto, Isaias Castañeda-Montes, and James Wigzell for providing so much support and help, both in and out of the lab.

Also, I would like to express my deepest gratitude and sincerest thanks to Professor Badyal, for his guidance throughout my time in Lab 98.

Thanks also go to P2i Ltd., in particular Neil Poulter, Elina Siokou, and Delwyn Evans, for all the support they gave during and after my PhD.

Special thanks go to my family, friends, and Stuart, for their tireless patience and continued support.

List of Publications Arising from this Thesis

1. Plasmachemical Double Click Thiol–ene Reactions for Wet Electrical Barrier" Fraser, R. C.; Carletto, A.; Wilson, M.; Badyal, J. P. S. *ACS Appl. Mater. Interfaces* **2016**, *8*, 21832–21838.

2. Electrical Barrier Coating, GB Filing Patent No 1610481.2, GB Filing Date 14th June 2016

Collaborative Publications

1. Von Spreckelsen, R. M.; Harris, M. T.; Wigzell, J. M.; Fraser, R. C.; Carletto, A.; Mosquin, D. P. K.; Justice, D.; Badyal, J. P. S. Bioinspired Breathable Architecture for Water Harvesting. *Sci. Rep*. **2015**, 5, 1–6.

2. Recyclable Palladium Catalyst Cloths for Carbon-Carbon Coupling Reactions. Wilson, M.; Kore, R.; Fraser, R. C.; Beaumont, S. K.; Srivastava, R.; Badyal, J. P. S. *Colloids Surf., A* **2017**, *520*, 788–795.

3. Palladium–Poly(Ionic Liquid) Membranes for Permselective Sonochemical Flow Catalysis. Wilson, M.; Kore, R.; Ritchie, A. W.; Fraser, R. C.; Beaumont, S. K.; Srivastava, R.; Badyal, J. P. S. *Colloids Surf., A* **2018**, *545*, 78–85.

Abstract

Protective coatings for electronics are of great importance due to the increase in use of smartphones and other personal devices across the world. The exposure of the circuits and components of these devices to water can cause irreparable damage through corrosion, resulting in complete failure of the device. Due to the high costs of personal electronics and their widespread use, it is important to provide as much protection as possible from water ingress and the subsequent damage that can occur. Chapter 1 of this thesis detailed this problem and the consequent importance of protective coatings, as well as the theory behind electrical barrier coatings. The experimental methods used throughout this thesis for the preparation and analysis of barrier coatings are described in Chapter 2.

Chapter 3 described in detail the process of preparing a barrier coating which provided complete protection from water damage to a circuit board. This process applied the theory of thiol-ene click chemistry in a new way; a polyisoprene layer was deposited on the circuit board, which was then coated with plasma deposited allyl mercaptan. This worked to form a barrier coating in a two-fold manner. The allyl mercaptan reacted both with the unsaturated polyisoprene layer, to create a strong linkage between the two layers and with the vinyl groups in the allyl mercaptan itself, to form a highly crosslinked top-layer. This coating functioned as a highly effective wet electrical barrier layer on the circuit board, giving compete protection from corrosion, even at high applied voltages.

Chapter 4 described the formation of an extremely superhydrophobic coating, which as well as functioning as a wet electrical barrier coating had an extremely high water contact angle and low contact angle hysteresis. This coating was prepared by the deposition of a polyisoprene layer which was then functionalised by plasma fluorination of the coating surface. This could be done to the same level of fluorination at relatively low plasma powers and durations, resulting in a highly superhydrophobic coating, which also imparted a degree of oleophobicity. When immersed in water an air layer remained trapped between the coating and the surrounding water, due to the high water contact angle. This functionalised coating, when deposited on glass also allowed the sample to be floated on the surface of the water, and when deposited on a circuit board pre-

coated with a thin plasma deposited base layer acted as a wet electrical barrier coating protecting the circuit board from corrosion. Gas pulsing was used to deposit a tetramethylsilane and oxygen base layer, which although was a poor electrical barrier on its own, significantly improved the overall barrier performance of the fluorinated polyisoprene coating.

Chapter 5 described the use of plasmachemical thiol-acrylate coatings applied as wet electrical barrier coatings. Based off the findings of Chapter 3, it was posited that the dual deposition of allyl mercaptan with an acrylate could also be used to form a highly crosslinked layer imparting water protection to circuit boards. Although a composite coating was formed from this dual deposition method, no improvement was seen over the plasmachemical thiol-ene coating, with both the single and composite layers on a polyisoprene base layer exceeding the detection limit for the measurement system.

Chapter 6 summarised the conclusions arising from thesis, highlighting the areas where significant improvements in the wet electrical barrier performance were found, particularly with respect to the novel approaches and new chemistries used. Also included is a brief description of other potential barrier coating testing techniques which could be used to more completely validate the coatings.

Table of Contents

List of Figures

List of Tables

Chapter 1 : Introduction

1.1. The Necessity of Barrier Coatings

Accidental damage is the leading cause of smartphone failure,[1,2] with liquid damage making up almost 50% of all inadvertent smartphone breakages.[3–5] In the United Kingdom, this adds up to over £2 billion spent on phone repair and replacement each year.[2] Aside from the costs of repair and replacement of electronic devices, there are other factors which should be taken into account when looking at the problem of electronic damage. The displays, speakers and circuitry of smartphones, tablets and other touchscreen electronics contain the rare earth metals (with the exception of promethium),[6–8] and obtaining these elements is often fraught with hazards. Apart from the inherent dangers associated with any mining process, rare earth element mining has been shown to result in heavy and persistent contamination of surrounding crop-land, leading to bioaccumulation and chronic toxicity.[9–14] Recycling of these elements from electronic applications currently stands at approximately 1% due to the difficulty of elemental separation, the high turnover rate of personal electronics, and the lack of awareness and infrastructure to allow an efficient recycling process.[7,8] Unfortunately, there are often no direct replacements for these metals which are cheap, easily accessible, and serve the same purpose,[15] so it stands to reason that reducing the consumption of the devices which require these rare earth elements would be economically and environmentally sound.

Personal electronics, such as smartphones, tablets and wearable devices are often exposed to conditions that can be damaging, such as rain, sea spray, sweat, or accidental submersion. Water ingress into the electronic system of these devices can cause corrosion and short-circuiting when the liquid forms a conductive medium between two points in a circuit. Although sometimes if there has only been a small amount of liquid permeation, this can be allowed to evaporate and there will be no long-term impairment, the damage can often be immediate and permanent. For example, spilling pure deionised water on an electronic device is unlikely to cause any major problems if it is allowed to fully dry,

but allowing impure or salt water to come into contact with the device can cause significant damage due to the higher conductivity of the solution.

As handheld devices become more and more complex the need for protection becomes much greater. As the size of the device is reduced, or the number of internal components increases, the circuits and electrical mechanisms have to reside much closer together, and even slight liquid damage to one can spread to the others in a short space of time. Larger and less complex circuit boards do not experience this problem to the same level, as damage to one area, whilst far from ideal, can theoretically be isolated to a single circuit, preserving the rest of the electrical components. Of course, this difference is much less important for full submersion of the electronics where both types are likely to be severely and irreversibly damaged, but it does show that protection against minor splashing and condensation (which can occur incredibly easily from rain, sea spray and day to day proximity to water splashed and moisture) could make the difference between damage and loss of functionality, and preservation of the electronic device.

1.2. Background of Barrier Coatings

A barrier coating can be applied to a surface in order to increase its efficiency and longevity, without greatly affecting the bulk properties or the look and feel of the material.[16,17] Barrier coatings have also been generally used to enhance the properties of the substrate,[18] such as imparting water repellency or thermal protection. There are three main types of barrier coating in use for protective purposes: gas barriers, water barriers, and electrical barriers. Water and gas barriers are widely used, particularly in the food packaging and electronics industries to protect from atmospheric oxygen and water permeation. Electrical barriers can be used as insulation layers for internal connections to prevent cross talk, short circuiting and tunnelling within circuits. Barriers which have a combination of these properties are of vital importance in the electronics industry acting as high resistance protective barriers.

The resistance of ion motion through a coating to the substrate when immersed in water is thought to determine the extent of the protection the coating

provides.[19] For electronic applications, this degree of protection is ranked using the ingress protection (IP) scale, e.g. a rating of IPx2 can protect against light water splashes, and IPx7 can protect against immersion of less than 1 m depth for 30 min. A high resistance means that there is little ion motion through the coating, only a small amount of ion transport occur, and a low resistance indicates that the ion motion is too extensive for the layer to be considered an effective electrical barrier.[19] The ideal situation when the substrate is immersed in water under an applied voltage would subsequently be no current flow, and an effectively open circuit, see Chapter 2, Section 2.2.

Factors such as the chemical composition and thickness of the coating, the conformation and size of the permeant, and the pressure and temperature of the surroundings all have an effect on the permeability of the coating. The resistivity of a film or surface, i.e. its resistance to current flow in relation to the area of the surface is an important property when designing and manufacturing barrier layers for electronic items.[20] The resistance of a barrier layer can greatly affect the design and process parameters of thin film electronics, so it must be carefully measured and quantified before large scale manufacture.[21] In addition, it is known that as the thickness of the polymer is reduced below a certain point (approximately 1 μm) the dielectric strength increases, resulting in an increased conductivity.[22] Polymeric materials are widely used as electronic component coatings since they offer a great advantage as electrical insulator layers due to their dielectric isolation, electrical insulation and low permeation properties.[23,24] The insulating properties possessed by many polymers arise from the large band gap, and as such they show a very low conductivity in relation to the strength of the applied electric field.

1.3. Types of Barrier Coating

There are different types of barrier coating depending on the protection requirements, such as oxygen barriers for food packaging and thermal barriers for temperature sensitive substrates. Specific barrier effects can be achieved though tailoring of the coating type and the preparation method used.

1.3.1. Multilayered

A common problem associated with thin film deposition is the formation of defects. The types of defects which affect the permeation of a gas or vapour through the film can be classified into three general categories:[25]

1. Small defects (<3 Å): the permeant, typically a gas, must be able to diffuse through the film. If a film solely contains these types of defects the permeation is usually low, which is desirable.
2. Medium defects (3–10 Å): the permeant must be able to diffuse through very narrow channels and defects. This usually gives a moderate permeation level.
3. Large defects (>10 Å): moisture vapour can easily pass through the film, giving a high permeation and a poor overall barrier performance. These defects are typically three to four times larger than a permeant molecule and so provides little resistance to permeation.[26]

These defects can be cracks, pores, fissures, pinholes or pores, and can be formed during the deposition process e.g. “island” formation, or caused by contamination on the substrate prior to the coating process, or damage to the coating after deposition, such as abrasions or scratches.[19] To diminish the effects of these defects, multilayered barrier coatings can be applied. Multilayering refers to the process of building up of several layers of thin films to form a thicker coating with multiple interfaces.[27] Any coating made up of several thin layers is much less likely to have continuous defects or pin-holes than one single layer of a comparable thickness, which is beneficial in barrier coatings, Figure 1-1.[28–30] Even if each deposited layer has several defects, the likelihood of them sufficiently aligning to allow a continuous path is very low, and decreases as the number of layers increases. In such a system, any permeant has to either follow a tortuous path to reach the substrate, increasing the length of time the coating is performing as a barrier, or will simply be blocked in its entirety.

As a result, multilayered films can be used as extremely effective barrier layers, and have been reported to achieve low water transmission rates (WVTRs).[31] WVTRs as low as 1 $x10^{-5}$–1 $x10^{-6}$ g m^{-2} day^{-1} have been achieved,

which is the required level for a coating to be deemed a good moisture barrier.[31] Commonly, sequentially deposited organic and inorganic layers can be applied as a barrier coating to give the benefits of both layer types, such as the combination of the resistance of a polymer layer with the hardness of a silicon based layer.[32,33] The layering can be repeated several times, to build up a laminate structure of many alternating layers of complementary materials, or layers with specific functions.[34–42]

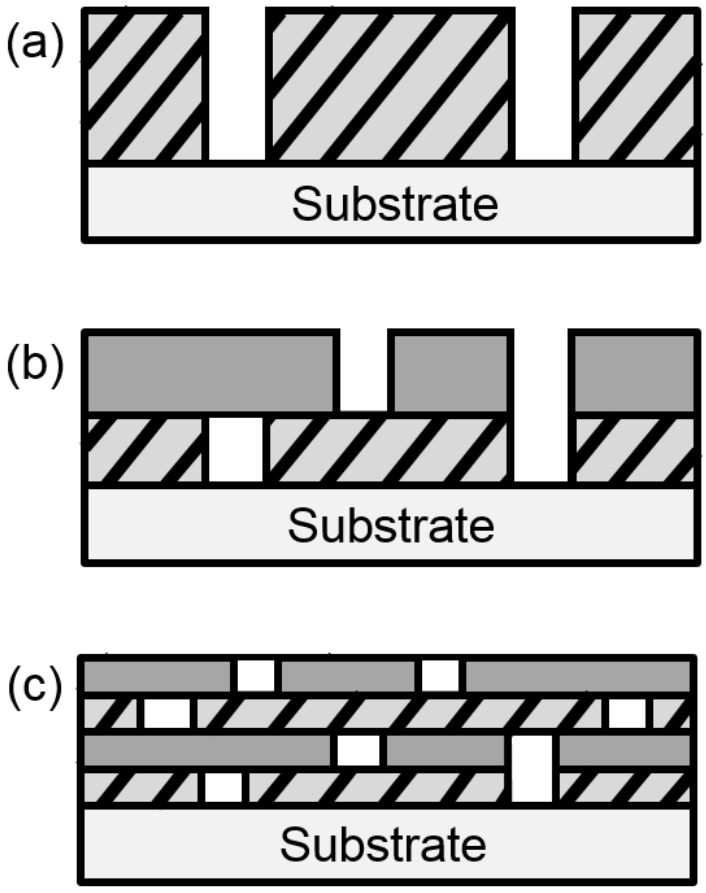

Figure 1-1: Schematic of multilayering showing: (a) a single layer coating with defects through which permeant molecules can pass; (b) two layers, adding up to the same total thickness with some defects blocked; and (c) multiple thin layers, adding up the same total thickness, with all the continuous defects blocked.

1.3.2. Crosslinking and Annealing

As mentioned previously, Section 1.2, polymer layers have often been used as barrier coatings. Crosslinking and annealing have been reported to improve the

barrier properties of the coatings, for example, if a layer is annealed before measurement of the WVTR, the permeation can be reduced by approximately 85% overall when compared against the water uptake of a non-annealed coating.[34,43] This vast improvement in the quality of the barrier is due to the rearrangement which occurs when the annealing process takes the organic layer above its glass transition temperature (T_g). Raising the organic polymeric film above the T_g allows the entire layer structure to reorganize, reducing the overall roughness of the surface and increasing the density and alignment of the molecules within the coating.[34]

Crosslinking can also cause an increase in strength, elasticity, and adhesion of the polymer to the substrate, which can be extremely desirable when designing a barrier coating. As a result of these structural changes, crosslinked coatings have been extensively used to improve barrier properties of polymer layers, or enhance other properties, such as hardness. When compared to non-crosslinked layers, polymer layers with some degree of crosslinking tend to perform better as barrier coatings, Appendix 1, because as the increase in density reduces the size of pores, the water solubility of the coating is decreased. Therefore strong three-dimensional networks can be formed, reducing permeation of small molecules.[42,44–48]

Crosslinking agents or UV-curing can also be used to strengthen coatings, Section 1.5, and the processes can be tailored to which method is most appropriate for the desired application.[42,44,49] For example, substrates which are UV sensitive could be thermally cured or benefit from the incorporation of a crosslinking agent.

1.3.3. Water Repellency

A water repellent coating is one that does not allow any water that comes into contact with the coating surface to spread or to be absorbed into the coating, resulting in the water beading up and rolling off the surface. The water repellency, or conversely, wettability, is mainly governed by the surface structure and the nature of the chemical groups at the interface between the surface and the

water.[50–52] Water repellent coatings have historically been used to protect automobiles,[53] wood,[54] glass,[55] and clothing.[56,57]

Due to the high electronegativity of the fluorine atom, fluorinated polymers are highly hydrophobic,[58] and thus offer protection against water permeation. This hydrophobicity decreases the WVTR and the incorporation of water molecules into the structure. The size, large free volume and polarity of halogen atoms attached to the coating surface reduces the permeability of oxygen and water molecules through the coating by effectively blocking the permeation path.[59] The halogen atoms replace the hydrogen atoms in the polymer, either in their entirety or solely on the surface, which leads to an increase in the barrier properties, and better water repellency.[60–63] Fluorinated polymers are also relatively inert and thermally stable in comparison to other polymers which can be susceptible to photocatalysis, making the fluorinated films excellent candidates for electronic barrier coatings.[64]

Fluorination can be used to enhance the protective properties further, as fluorinated polymers have a lower dielectric constant and higher resistance compared to their non-fluorinated counterparts. The larger free volume they possess and the lower polarisability is thought to be the cause of this effect.[65,66] Using a halogenated rather than a non-halogenated monomer to form a polymer layer gives a lower permeability to water, as has been seen by the decreased permeation of steam through halogenated polycarbonates and polyolefins.[67–69] This is a particularly useful property when considering how much water can be absorbed by a polymer film under immersion, because when the volume of water incorporated into the polymer structure increases the ion conductivity increases also.[70] Surface superhydrophobicity can be employed to provide protection from water ingress by utilisation of the Cassie-Baxter effect, which is the formation of a trapped air layer between a roughened surface and the surrounding water, which can result in water contact angles ranging from 150–160°.[71–92]

1.4. Plasma Deposition of Barrier Layers

Plasma processes can be used to deposit barrier coatings on a variety of substrates, due to the conformal nature of the coating process.[17] Despite the

benefits of multilayer coatings, Section 1.3.1, single layered barriers are often desired for the ease and speed of development and large scale processing. Dielectric films produced by plasma processes tend to give very good single layer results as barrier films when compared to other single layered barriers.[29] This is because films produced by plasma deposition tend to be denser than conventionally produced films, which gives a better performance as a water barrier due to restricted permeation.[93] The use of plasma processes for the deposition of barrier coatings allows the formation of glassy, amorphous protective layers on the substrate, unlike many other cold, low energy methods, e.g. sputtering, which will typically will form columnar and particulate structures. Coatings produced by the latter techniques are often porous coatings with many defects and pin-holes.[94]

The majority of plasma deposited barrier layer research has been focused on silicon based films. Aluminium and silicon based layers, particularly silicon oxides and nitrides, are very common forms of barrier coatings currently in use for substrate protection,[95–106] as these show excellent barrier properties against water and oxygen permeation. The plasma fluorination of these layers reduces the hydrogen content and enhances the barrier properties further, whilst leaving the layer transparent, tough and with good adhesion to the substrate.[96,97,107,108] Additionally, fluorine containing layers can be deposited by plasma enhanced chemical vapour deposition (PECVD) to form “Teflon-like” coatings, which are promising candidates for use as barriers to water vapour transmission, due to the high fluorine content, Section 1.3.3.[109] Increasing the oxygen content of the films by co-depositing the plasma polymer with H_2O_2 can also decrease the permeability of hydrogen gas through barrier layers.[110] Other commonly used barrier layers are amorphous carbon based films,[111–113] and fluoropolymers.[114–116]

To further improve barrier performance, several thin films can be plasma deposited sequentially on top of each other, to create a laminate system. Due to the lack of continuous defects, Section 1.3.1, these tend to offer greater protection than a single layer coating of comparable thickness.[35,36] As a further enhancement to oxygen and water permeation, the layering of organic and inorganic layers can be applied as a nanolaminate system. For example, a ceramic layer (composed of SnO_2, In_2O_3, ITO, Al_2O_3, or SiO_2) can be deposited between two plasma deposited

polymer layers (usually plasma polymerised acrylic, methacrylic, propylene layers etc.) to give a composite coating with complementary features.[35,117–123]

1.5. Thiol–Ene Reactions

Vulcanisation has long been used as a method of increasing the durability, resilience, hardness and strength of rubbers in general, and in particular, polybutadiene.[124,125] Vulcanisation can be thought to occur first by the formation of an accelerating agent, usually a sulphur radical, and secondly by the crosslinking process, wherein sulphide and carbon bridges are formed, giving rise to a strong three dimensional crosslinked network, Figure 1-2.[126,127]

Many reaction mechanisms of thiol groups with unsaturated polymers rely on photo- or thermal-initiation as a means of creating the necessary sulphur radicals, and as such, a photosensitive initiator can be included. In the first step, the activated sulphur reacts preferentially with allylic carbon, and the sulphur radical formed, known here as the thiyl radical, also reacts with allylic carbon, leading to disulphide crosslinks. The preference of allylic carbon chains is shown by the lack of success in vulcanisation of hydrogenated polymers e.g. polyisobutylene, showing that double bonds are a required reactant for this process.[128]

The propagation of this mechanism shows the radical residing on the polymer backbone, and the formation of the polymer network occurring as two radical polymer structures combine and terminate the reaction. Alternatively, the polymer network can be formed when two chains are linked via a disulphide bridge.

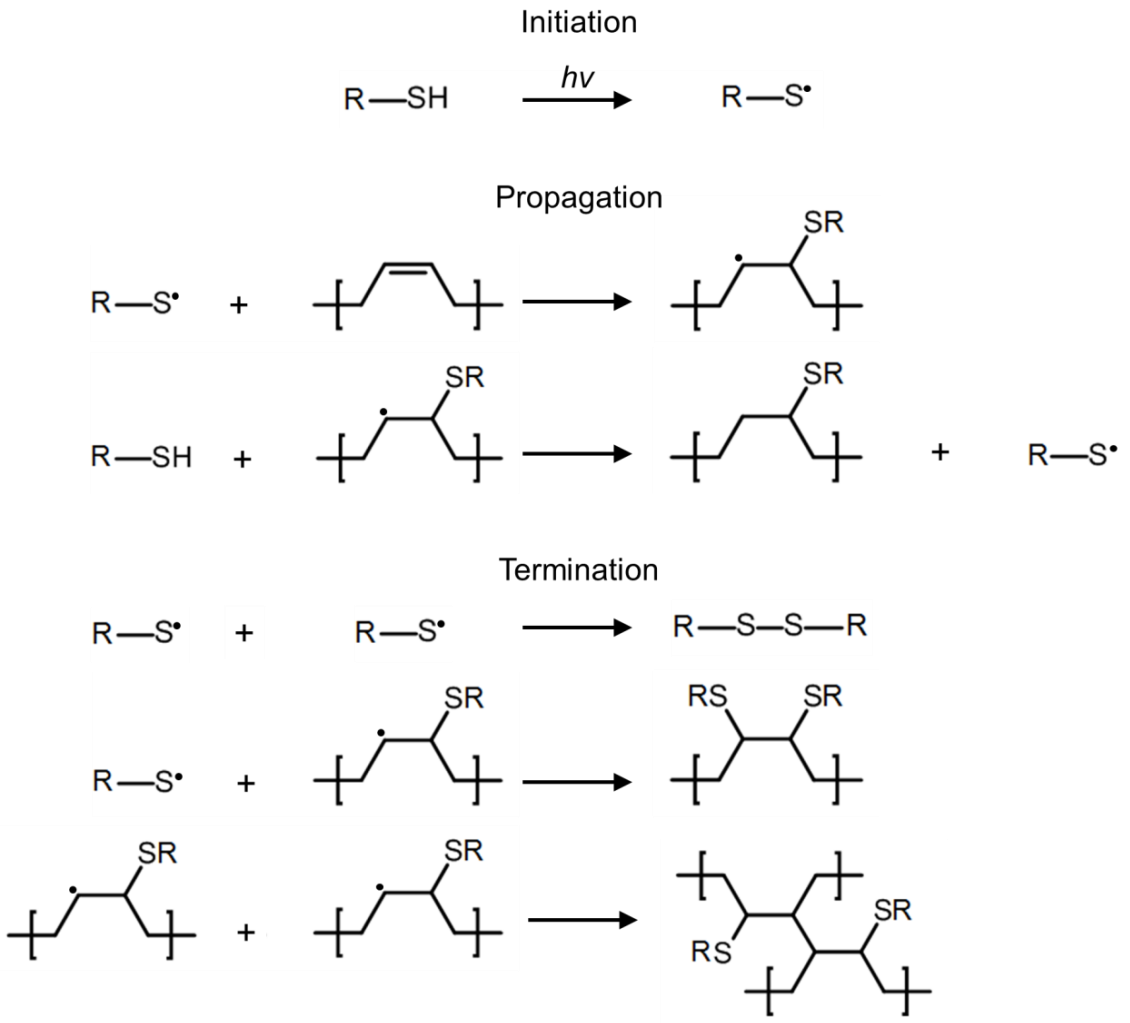

Figure 1-2: Schematic representation of the sulphur mediated crosslinking of polymer chains, showing the initiation through UV generation of the thiyl radical, the propagation of the reaction, with the radical sitting on the polymer back bone and the regeneration of the thiyl radical, followed by the termination of the reaction, wherein a sulphonated polymer is formed and two polymer chains are linked by sulphur or a carbon bond.[127]

The process has been expanded in recent years, and is now encompassed by the term “thiol–ene chemistry,” or “click thiol–ene chemistry,” which refers to the radical addition of thiols across carbon-carbon double bonds Figure 1-3.[129] Click chemistry refers to any mechanism wherein the reactants can be switched for other reactants with the same critical functional groups, e.g. regardless of the specific precursor, as long as there is a source of available double bonds a thiol radical can perform thiol–ene reactions.[130] As such, the process can be applied to various polymers with unsaturated groups, e.g. acrylates, natural rubbers and triple bond containing monomers. Accordingly, natural rubber (polyisoprene) which

has many double bonds, reacts well with thiols to form bonds between the polymer chains, giving a loss of unsaturation and the formation of a three-dimensional network.[131]

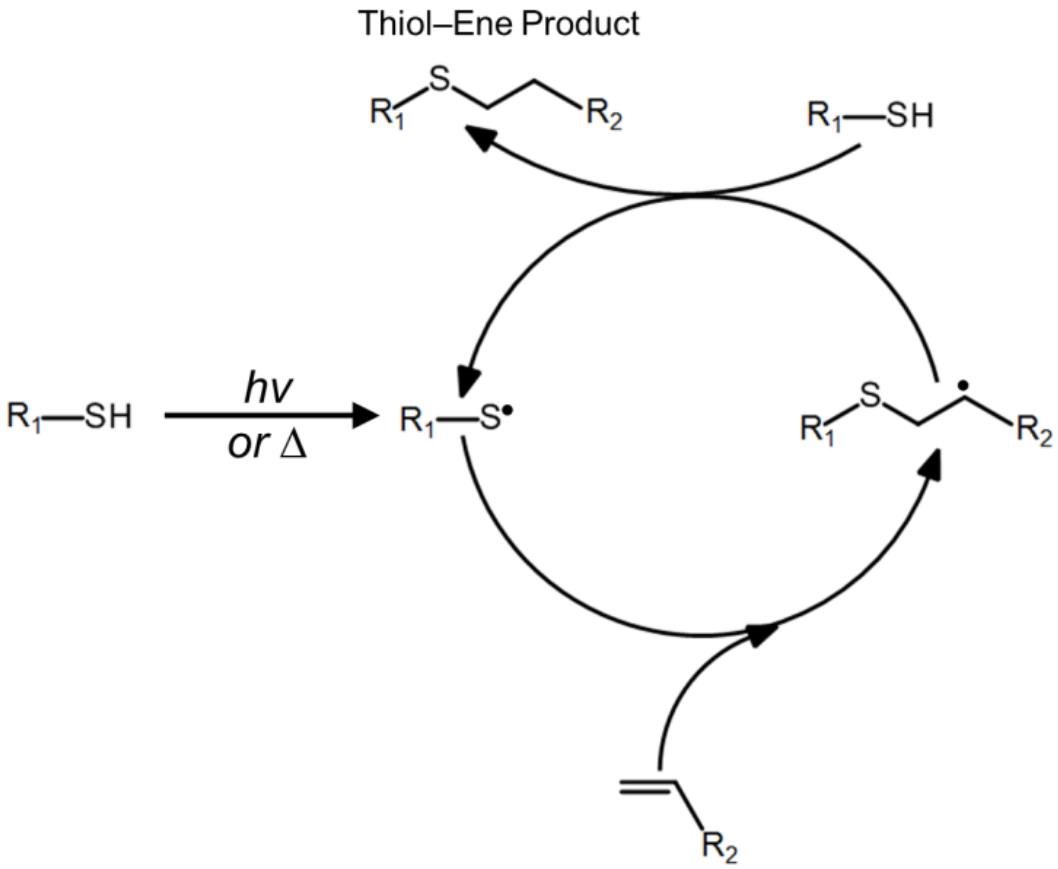

Figure 1-3: A schematic representation of the thiol–ene cycle, showing the activation of the sulphur radical progressing by initiation by light or heat, followed by exposure to a terminal double bond. This allows the radical to reside on the polymer back bone where it can then abstract the hydrogen of another thiol molecule, resulting in the thiol–ene end product and regeneration of the thiyl radical.[129]

A proposed mechanism of thiol–ene modification of polybutadiene is by intermolecular cyclisation of the polybutadiene.[132] This mechanism also relies upon the generation of sulphur radicals, although it is specific to 1,2-polybutadiene, and larger thiol precursors are most often used. Allyl mercaptan and other mercaptan analogues have been commonly used in the vulcanisation of polybutadiene and other unsaturated polymers in solution, using UV light for photoinitiation of the mercaptan to generate the sulphur radicals, or simply milling the rubber with the accelerator.[133–135] Mercaptans are known for their use as

vulcanisation accelerators,[136] so as long as the sulphur radical can be generated, the vulcanisation reaction should proceed by the above mechanisms. Additionally, unsaturated mercaptans are able to self-polymerise, following a step-wise addition reaction.[137] The double bond present in allyl mercaptan can react with the sulphur moiety of another allyl mercaptan molecule, giving rise to two different outcomes: a branched or unbranched chain, Figure 1-4.[138]

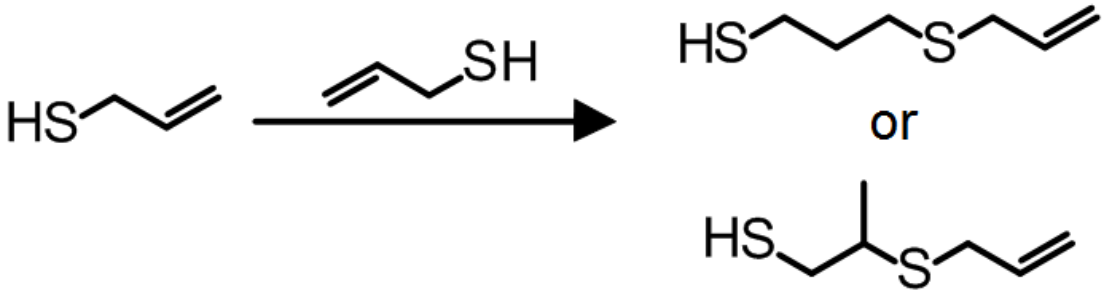

Figure 1-4: Allyl mercaptan self-reaction mechanism.

1.6. Conclusions

Barrier coatings are a critically important consideration in the electronic devices sector, as well as many other industries, such as food and beverage packaging, clothing, and construction. Improvements in barrier coatings, i.e. making them thinner, more durable, and higher performing, are of great benefit, as this reduces waste and cost by protecting the item, or giving it a longer shelf life, Section 1.1.

Polymeric coatings and composite multilayer systems have long been used as barrier layers, designed to enhance the barrier properties by creating multiple interfaces, and thus reducing permeation, Section 1.3.1. The application of complementary layers can impart specific properties tailored to the item to be protected. Additionally, crosslinking can be used to enhance the strength and adhesion of barrier coatings, increasing the density and reducing the permeation of small molecules at the same time, Section 1.3.2. Water repellency has also been commonly used, wherein a hydrophobic or superhydrophobic layer gives the protected surface as little contact with water as possible. This reduced water contact, and consequently reduced water permeation, which can be imparted by the halogenation of a base layer, gives protection to the substrate by preventing

corrosion or degradation caused by water ingress, Section 1.3.3. The combination of two or more of these protection methods can give a greater barrier performance than for simply the unmodified coating, using a simple methodology, Appendix 1.

Electrical barriers exploiting these methods can easily be prepared using plasma deposition and modification. A simple spin or spray coated polymer layer can be enhanced by the deposition of a plasma polymer layer on top, or vice versa, to create a multilayer system. Similarly, a base layer can be modified or functionalised by exposure to a plasma, to impart the desired surface properties, such as roughness and water repellency. Plasma deposition and modification are conformal processes allowing non-flat surfaces and 3D structures, such as circuit boards, to be coated without leaving untreated areas; any area of the surface exposed to the surrounding environment will be treated. Additionally, these processes can be carried out at low temperatures and powers, and use only a minimal amount of reagent, which is of great benefit for large-scale processes and industries looking to reduce costs.

1.7. Scope of Thesis

The results presented herein utilise the principles outlined in this section to develop barrier coatings for electronics. These barrier coatings were deposited on micro-circuit boards and tested via immersion in tap water under an applied voltage in order to replicate a “real world” scenario of an electronic item submerged in water.

Chapter 3 describes an electrical barrier coating comprising two layers. Thiol–ene reactions were intrinsic to the functionality of this coating, causing strong linkages between the thiol containing top layer and the unsaturated base layer, as well as the top layer itself undergoing thiol–ene crosslinking. This resulted in a highly effective, novel wet electrical barrier coating, which was able to impart protection to a circuit board when immersed in water. Thiol–ene reactions and their potential for use in plasma deposited electrical barrier coatings were further investigated in Chapter 5, where thiol and acrylate containing precursors were deposited simultaneously. Proof of concept for a crosslinked coating with high wet

electrical barrier performance was demonstrated, with further work being required to expand upon these findings.

Chapter 4 describes how superhydrophobicity was put into effect to develop a barrier coating which when immersed in water formed a protective air layer between the surface and the surrounding water. The superhydrophobicity resulted from a two-fold plasma process of roughening and functionalisation of an unsaturated polymer layer. This coating worked in conjunction with a plasma deposited base layer, giving superior wet electrical barrier performance when immersed in water under an applied voltage.

The coatings described herein are comparable in quality to the state-of-the-art plasma deposited barrier coatings. Fluoropolymer coatings deposited by RF plasma have a resistivity of 1.44×10^{4} Ω nm^{-1}.[139] This is exceeded by both the plasmachemical thiol–ene coating, Chapter 3, and the superhydrophobic polyisoprene coating, Chapter 4, presented here. These coatings also exceed the resistivity of 8.81×10^{-4} Ω nm^{-1}, obtained by a multilayered organosilicon coating deposited by low pressure PECVD.[140] These comparisons are not perfect, due to the nature of the electrical barrier test methods. The tests vary to a degree, although they are similar in nature: interdigitated electrodes which are non-conductive unless immersed in a conductive medium, where the role of the barrier coating is to prevent corrosion of the electrodes. Although this is not a direct comparison, it gives an idea of where the coatings described in this thesis lie in relation to the commercially available barrier coatings. Other measurement techniques, such as dielectric strength or surface resistivity are commonly used to evaluate electrical barrier coatings, but no significant comparison can be made with the coatings presented herein. For example, hydrophobic ceramic and organometallic coatings deposited by atmospheric plasma processes have been reported to have dielectric strengths of almost 30 kV mm^{-1} and surface resistivities of up to 7 kΩ $\square^{-1}$.[141,142] Because of this difficulty in regards to comparison further investigation into the barrier coatings described in the following chapters should include benchmarking electrical measurements such as surface resistivity, volume resistivity, and dielectric strength.

The coatings described in this thesis are presented with regards to their functionality as wet electrical barrier coatings with discussion of the potential applications of such barrier coatings. The further work required to fully substantiate the proof of concept claims is also evaluated, and as well as other potential test methods which could be used to determine the protective limits of the barrier coatings.

1.8. References

1 SquareTrade Ltd., SquareTrade Research. 26% of Iphones Fail Over 2 Years, a Decrease From 2009 (accessed 13/09/16).

2 SquareTrade Ltd., SquareTrade Protection Plans. Revealed: Britain's £5 Billion Mobile Problem (accessed 13/09/16).

3 Insure My Smartphone, Insurance Survey. http://www.insuremysmartphone.co.uk/news/smartphone-insurance-survey (accessed 13/09/16).

4 The Street Inc. Your Smartphone's Biggest Hazard is You. https://www.thestreet.com/story/11674110/1/your-smartphones-biggest-hazard-is-you.html (accessed 13/09/16).

5 El Mundo Tech LLC. T-Mobile/Kelton Research: Smartphone Safety. http://www.elmundotech.com/2012/07/13/t-mobilekelton-research-smartphone-safety/ (accessed 13/09/16).

6 Techradar Ltd. Our Smartphone Addiction is Costing the Earth. http://www.techradar.com/news/phone-and-communications/mobile-phones/our-smartphone-addiction-is-costing-the-earth-1299378 (accessed 13/09/16).

7 Chancerel, P.; Marwede, M.; Nissen, N. F.; Lang, K.-D. Estimating the Quantities of Critical Metals Embedded in ICT and Consumer Equipment. *Resour. Conserv. Recy.* **2015**, *156*, 239–258.

8 Chancerel, P.; Rotter, V. S.; Uebershaar, M.; Marwede, M.; Nissen, N. F.; Lang, K.-D. Data Availability and the Need for Research to Localize, Quantify and Recycle Critical Metals in Information Technology, Telecommunication and Consumer Equipment. *Waste Manage. Res.* **2013**, *31*, 3–16.

9 D'Aquino, L.; Morgana, M.; Carboni, M. A.; Staiano, M.; Antisari, M. V.; Re, M.; Lorito, M.; Vinale, F.; Abadi, K. M.; Woo, S. L. Effect of Some Rare Earth Elements on the Growth and Lanthanide Accumulation in Different Trichoderma Strains. *Soil Biol. Biochem.* **2009**, *41*, 2406–2413.

10 Šmuc, N. R.; Dolenec, T.; Serafimovski, T.; Dolenec, M.; Vrhovnik, P. Geochemical Characteristics of Rare Earth Elements (REEs) in the Paddy Soil and Rice (Oryza Sativa L.) System of Kočani Field, Republic of Macedonia. *Geoderma* **2012**, *183*, 1–11.

11 Li, X.; Chen, Z.; Chen, Z.; Zhang, Y. A Human Health Risk Assessment of Rare Earth Elements in Soil and Vegetables from a Mining Area in Fugian Province, Southeast China. *Chemosphere* **2013**, *93*, 2406–2413.

12 Ichihashi, H.; Morita, H.; Tatsukawa, R. Rare Earth Elements (REEs) in Naturally Grown Plants in Relation to Their Variation in Soils. *Environ. Pollut.* **1992**, *76*, 157–162.

13 Zhang, H.; Feng, J.; Zhu, W.; Liu, C.; Xu, S.; Shao, P.; Wu, D.; Yang, W.; Gu, J. Chronic Toxicity of Rare-Earth Elements on Human Beings. *Biol. Trace Elem. Res.* **2000**, *73*, 1–17.

14 Marzec-Wróblewska, U.; Kamiński, P.; Łakota, P.; Ludwikowski, G.; Szymański, M.; Wasilow, K.; Stuczyński, T.; Buciński, A.; Jerzak, L. Determination of Rare Earth Elements in Human Sperm and Association with Semen Quality. *Arch. Environ. Contam. Toxicol*. **2015**, *69*, 191–201.

15 Graedel, T. E.; Harper, E. M.; Nassar, N. T.; Reck, B. K. On the Materials Basis of Modern Society. *Proc. Natl. Acad. Sci. U.S. A.* **2015**, *112*, 6295–6300.

16 Coulson, S. R.; Evans, D. R. Nano-coating Protection of Medical Devices. Lecture Notes of the Institute of Computer Sciences, *Social Informatics and Telecommunications Engineering* **2010**, *55*, 245–251.

17 Mukhopadhyay, S. M.; Joshi, P.; Datta, S.; Macdaniel, J. Plasma Assisted Coating of Porus Solids. *Appl. Surf. Sci.* **2002**, *201*, 219–226.

18 Sangaj, M. S.; Malshe, V. C. Permeability of Polymers in Protective Organic Coatings – A Review. *Prog. Org. Coat.* **2004**, *50*, 28–39.

19 Taylor, S. R. Assessing the Moisture Barrier Properties of Polymeric Coatings Using Electrical and Electrochemical Methods. *Transac. Elec. Insul.* **1989**, *24*, 787–806.

20 Aono, M.; Nitta, S. High Resistivity and Low Dielectric Constant Amorphous Carbon Nitride Films: Application to Low-k Materials for ULSI. *Diamond Relat. Mater.* **2002**, *11*, 1219–1222.

21 Klauk, H.; Schmid, G.; Radlik, W.; Weber, W.; Zhou, L.; Sheraw, C. D.; Nichols, J. A.; Jackson, T. N. Contact Resistance in Organic Thin Films Transistors. *Solid State Electron.* **2003**, *47*, 297–301.

22 Bashara, N. M.; Doty, C. T. Electrical Conduction in Very Thin Polybutadiene Films Formed in a Glow Discharge. *J. Appl. Phys.* **1964**, *35*, 3498–3507.

23 Kao, K. C. In the Proceedings of the 6th International Conference on Properties and Applications of Dielectric Materials, *Electrical Conduction and Breakdown in Insulating Polymers*, Xi'an, China, June 21–June 26; 2000.

24 Goosey, M. T. Permeability Effects in Electrical and Electronic Component Coatings. In *Polymer Permeability;* Comyn, J., Ed.; Elsevier Applied Science Publishers: Essex, 1985; Page 331.

25 Saitoh, K; Kumar, R. S.; Chua, S.; Masuda, A.; Matsumura, H. Estimation of Moisture Barrier Ability of Thin Film SiNx Single Layer on Polymer Substrates Prepared by a Cat-CVD Method. *Thin Solid Films* **2008**, *516,* 607–610.

26 Roberts, A. P.; Henry, B. M.; Sutton, A. P.; Grovenor, C. R. M.; Briggs, G. A. D.; Miyamoto, T.; Kano, M.; Tsukahara, Y.; Yanaka, M. Gas Permeation in Silicon-Oxide/Polymer (SiO_x/PET) Barrier Films: Role of the Oxide Lattice, Nano-Defects and Macro-Defects. *J. Membr. Sci*. **2002**, *208*, 75–88.

27 Batey, J.; Boland, J.; Parsons, G. N. Pulsed Gas Plasma-Enhanced Chemical Vapour Deposition of Silicon. *Patent* EP0526779, February 10, 1993.

28 Yoshida, S.; Okawara, C.; Ozeki, K. Process for Producing Multi-Layered Gas Barrier Film. *Patent* EP2397574, December 21, 2011.

29 Lewis, J. S.; Weaver, M. S. Thin-Film Permeation-Barrier Technology for Flexible Organic Light Emitting Devices. *IEEE J. Sel. Top. Quant.* **2004**, *10*, 45–57.

30 Charton, C.; Schiller, N.; Fahland, M.; Holländer, A.; Wedel, A.; Noller, K. Development of High Barrier Films on Flexible Polymer Substrates. *Thin Solid Films* **2006**, *502*, 99–103.

31 Graff, G. L.; Williford, R. E.; Burrows, P. E. Mechanisms of Vapour Permeation Through Multilayer Barrier Films: Lag Time Versus Equilibrium Permeation. *J. Appl. Phys.* **2004**, *96*, 1840.

32 Priolo, M. A.; Gamboa, D.; Holder, K. M.; Grunlan, J. C. Super Gas Barrier of Transparent Polymer-Clay Multilayer Ultrathin Films. *Nano Lett*. **2010**, *10*, 4970–4974.

33 Yang, Y.-C. Bolling, L.; Priolo, M. A.; Grunlan, J. C. Super Gas Barrier and Selectivity of Graphene Oxide-Polymer Multilayer Thin Films. *Adv. Mater*. **2013**, *25*, 503–508.

34 Kim, Y.; Kim, N.; Kim, H.; Graham, S. In Electronic Components and Technology Conference, *The Development of Thin Film Barriers for Encapsulating Organic Electronics*, Lake Buena Vista, Florida, May 21–June 3; 2011.

35 Affinito, J. D. Environmental Barrier for Organic Light Emitting Device and Method of Making. *Patent* US6268695, July 31, 2001.

36 Harvey, T. B.; Shi, S. Q.; So, F. Passivated Organic Device Having Altering Layers of Polymer and Dielectric. *Patent* US5757126, May 26, 1998.

37 Langereis, E.; Creatore, M.; Heil, S. B.; Van de Sanden, M. C.; Kessels, W. M. Plasma-Assisted Atomic Layer Deposition of Al_2O_3 Moisture Permeation Barriers on Polymers. *Appl. Phys. Lett.* **2006**, *89*, 081915.

38 Carcia, P. F.; McLean, R. S.; Reilly, M. H.; Groner, M. D.; George, S. M. Ca Test of Al_2O_3 Gas Diffusion Barriers by Atomic Layer Deposition on Polymers. *Appl. Phys. Lett.* **2006**, *89*, 031915.

39 Carcia, P. F.; McLean, R. S.; Groner, M. D.; Dameron, A. A.; George, S. M. Gas Diffusion Ultrabarriers on Polymer Substrates Using Al_2O_3 Atomic Layer Deposition and SiN Plasma-Enhanced Chemical Vapour Deposition. *J. Appl. Phys.* **2009**, *106*, 023533.

40 Granstrom, J.; Villet, M.; Chaterjee, T.; Gerbec, J. A.; Jerkunica, E.; Roy, A. Multilayer Barrier Films Comprising Nitrogen Spacers Between Free-Standing Barrier Layers. *Appl. Phys. Lett*. **2009**, *95*, 093306–093307.

41 Dameron, A. A.; Davidson, S. D.; Burton, B. B.; Carcia, P. F.; McLean, R. S.; George, S. M. Gas Diffusion Barriers on Polymers Using Multilayers Fabricated by Al_2O_3 and Rapid SiO_2 Atomic Layer Deposition. *J. Phys. Chem. C* **2008**, *112*, 4573–4580.

42 Lange, J.; Stenroos, E.; Johansson, M.; Malmström, E. Barrier Coatings for Flexible Packaging Based on Hyperbranched Chains. *Polymer* **2001**, *42*, 7403–7410.

43 Heya, A.; Niki, T.; Takano, M.; Yonezawa, Y.; Minamikawa, T.; Munoi, S.; Minami, S.; Ikari, T.; Izumi, A.; Masuda, A. Moisture-Resistive Properties of SiNx Films Prepared by Catalytic Chemical Vapour Deposition Below 100 °C for Flexible Organic Light-Emitting Diode Displays. *Jpn. J. Appl. Phys*. **2005**, *44*, 1923-1927.

44 Vreugdenhil, A. J.; Gelling, V. J.; Woods, M. E.; Schmelz, J. R.; Enderson, B. P. The Role of Crosslinkers in Epoxy-Amine Crosslinked Silicon Sol-Gel Barrier Protection Coatings. *Thin Solid Films* **2008**, *517*, 538–543.

45 Haas, K.-H.; Amberg-Schwab, S.; Rose, K.; Schottner, G. Functionalized Coatings Based on Inorganic-Organic Polymers (ORMOCERs) and Their Combination with Vapour Deposited Inorganic Thin Films. *Surf. Coat. Technol*. **1999**, *111*, 72–79.

46 Thomas, N. L. The Barrier Properties of Paint Coatings. *Prog. Org. Coat*. **1991**, *19*, 101–121.

47 Delucchi, M.; Turri, S.; Barbucci, A.; Bassi, M.; Novelli, S.; Cerisola, G. Fluoropolyether Coatings: Relationships of Electrochemical Impedance Spectroscopy Measurements, Barrier Properties, and Polymer Structure. *J. Polym. Sci., Part B: Polym. Phys.* **2001**, *40*, 52–64.

48 Delor-Jestin, F.; Tomer, N. S.; Singh, R. P.; Lacoste, J. Durability of Crosslinked Polydimethylsyloxanes: The Case of Composite Insulators. *Sci. Technol. Adv. Mater*. **2008**, *9*, 024406-024412.

49 Trochimczuk, A. W.; Kabay, A. N.; Arda, M.; Streat, M. Satbilization of Solvent Impregnated Resins (SIRs) by Coating with Water Soluble Polymers and Chemical Crosslinking. *React. Funct. Polym*. **2004**, *59*, 1–7.

50 Holloway, P. J. Surface Factors Affecting the Wetting of Leaves. *Pest Manag. Sci*. **1970**, *1*, 156–163.

51 Teshima, K.; Sugimura, H.; Inoue, Y.; Takai, O.; Takano, A. Transparent Ultra Water-Repellent Poly(ethylene terephthalate) Substrates Fabricated by Oxygen Plasma Treatment and Subsequent Hydrophobic Coating. *Appl. Surf. Sci*. **2005**, *244*, 619–622.

52 Öner, D.; McCarthy, T. J. Ultrahydrophobic Surfaces. Effect of Topography Length Scales on Wettability. *Langmuir* **2000**, *16*, 7777–7782.

53 Nanoprotect Ltd., Nano for Car. http://www.nanoprotect.co.uk/nano-for-car.html (accessed 28/10/16).

54 Wolman Gmbh, RainCoat Clear Water Repellent (Water Base) http://www.rustoleum.com/en/product-catalog/consumer-brands/wolman /raincoat-clear-water-repellent-water-base (accessed 28/10/16).

55 Aculon Inc., Perfomance Surface Solutions. http://www.aculon.com/hydrophobic-coatings.php (accessed 28/10/16).

56 Water Will Never be the Same: Experience Hydrobead and What it Means to be Absolutely Water-Proof. http://www.hydrobead.com/ (accessed 28/10/2016).

57 P2i, Applications. https://www.p2i.com/applications/military/ (accessed 28/10/16).

58 Woodward, I.; Schofield, W. C. E.; Roucoules, V.; Badyal, J. P. S. Super-hydrophobic Surfaces Produced by Plasma Fluorination of Polybutadiene Films. *Langmuir* **2003**, *19*, 3432-3438.

59 Singh, B. High Barrier Solutions for Plastic Containers Using Fluorination Process. *The Economic Times Polymers* **2008**, *19-24* (Accessed 01/07/14).

60 Irwin, C. Blow Moulding. In *The Wiley Encyclopedia of Packaging Technology*. Yam, K. T., Ed.; John Wiley and Sons. 2009.

61 Borcia, G.; Brown, N. M. D. Hydrophobic Coatings on Selected Polymers in an Atmospheric Pressure Dielectric Barrier Discharge. *J. Phys. D.: Appl. Phys.* **2007**, *40*, 1927-1936.

62 Tatsuono, T.; Wakimoto, M.; Kashiwada, S. Water Repellent Coating. *Patent* US561388A, April 1, 1997.

63 Alessandrini, G.; Aglietto, M.; Castelvetro, V.; Ciardelli, F.; Peruzzi, R.; Toniolo, L. Comparative Evaluation of Fluorinated and Unfluorinated Acrylic Copolymers as Water-Repellent Coating Materials for Stone. *J. Appl. Polym. Sci.* **2000**, *6*, 962–977.

64 Biloiu, C.; Biloiu, I. A.; Ohta, A.; Sakai, Y.; Suda, Y. Amorphous Fluorocarbon Polymer (a-C:F) Films Obtained by Plasma Enhanced Chemical Vapour Deposition of Perfluoro-octane (F_8C_{18}) Vapour 1: Deposition, Morphology, Structural and Chemical Properties. *J. Vac. Sci. Technol. A.* **2004**, *22*, 13-19.

65 Hill, R. S.; Maria van den Hoek, W. G.; Havemann, R. H. Method of Fabricating Low Dielectric Constant Dielectric Films. *Patent* US6753250, June 22, 2004.

66 Blythe, T.; Bloor, D. Electrical Properties of Polymers. 2nd Ed. Cambridge University Press; Cambridge: 2005, 24.

67 Bergman, B. R. Barrier Layer for Inflatable Articles. *Patent* US0186540, July 25, 2013.

68 Mark, V. Polycarbonate Compositions Having Improved Barrier Properties. *Patent* US4304899, March 25, 1980.

69 D'Angelo, P. F. Treating Hydrocarbon Polymer with Fluorine and Bromine Source. *Patent* US4142032, February 27, 1979.

70 Higikigawa, M.; Miyoshi, S.; Sugihara, T.; Jina, A. A Thin Film Resistance Humidity Sensor. *Sensor. Actuator.* **1983**, *4*, 307-315.

71 Reick, F. G. Substrate Coated with Superhydrophobic Layers. *Patent* US3931428A, January 6, 1976.

72 Cassie, A. D. B.; Baxter, S. Wettability of Porous Surfaces. *T. Faraday Soc.* **1944**, *40*, 546–551.

73 Tokunaga, J.; Kumada, M.; Sugiyama, Y.; Watanabe, N.; Chong, Y. B.; Matsubara, N. Method of Forming Air Film on Submerged Surface of Submerged Part-Carrying Structure, and Film Structure on Submerged Surface. *Patent* WO1994007740A1, April 14, 1994.

74 Hsieh, T.-C.; Wu, F.-L.; Chen, W.-Y. Superhydrophobicity and Superoleophobicity from Hierarchical Silica Sphere Stacking Layers. *Mater. Chem. Phys*. **2010**, *121*, 14–21.

75 Lee, Y.; Park, S.-H.; Kim, K.-B.; Lee, J.-K. Fabrication of Hierarchical Structures on a Polymer Surface to Mimic Natural Superhydrophobic Surfaces. *Adv. Mater.* **2007**, *19*, 2330–2335.

76 Fan, Y.; He, Y.; Luo, P.; Chen, X.; Liu, B. A Facile Electrodeposition Process to Fabricate Corrosion-Resistant Superhydrophobic Surface on Carbon Steel. *Appl. Surf. Sci.* **2016**, *368*, 435–442.

77 Brassard, J. D.; Sarkar, D. K.; Perron, J.; Audibert-Hayet, A.; Melot, D. Nano-Micro Structured Superhydrophobic Zinc Coating on Steel for Prevention of Corrosion and Ice Adhesion. *J. Colloid Interface Sci.* **2014**, *297*, 109–115.

78 Wagner, P.; Fürster, R.; Barthlott, W.; Neinhuis, C. Quantitative Assessment to the Structural Basis of Water Repellency in Natural and Technical Surfaces. *J. Exp. Bot*. **2003**, *54*, 1295–1313.

79 Barthlott, W.; Neinhuis, C. Purity of the Sacred Lotus, or Escape from Contamination in Biological Surfaces. *Planta* **1997**, *202*, 1–8.

80 Wang, M.-F.; Raghunathan, N.; Ziaie, B. A Nonlithographic Top-Down Electrochemical Approach for Creating Hierarchical (Micro-Nano) Superhydrophobic Silicon Surfaces. *Langmuir* **2007**, *23*, 2300–2303.

81 Vakarelski, I. U.; Patankar, N. A.; Marston, J. O.; Chan, D. Y. C.; Thoroddsen, S. T. Stabilization of Leidenfrost Vapour Layer by Textured Superhydrophobic Surfaces. *Nature* **2012**, *489*, 274–277.

82 McCulloch, C. R.; Gill, R. C. Submersible Object Having Drag Reduction and Method. *Patent* US3973510A, August 10, 1976.

83 Tulis, A. J. Flowability Techniques in the Processing of Powdered Explosives, Propellants, and Pyrotechnics. *J. Hazard Mater.* **1980**, *4*, 3–10.

84 Tully, P. R. Water-Repellent Coating Compositions and Method for their Preparation. *Patent* US4102703A, July 25, 1978.

85 Shirtcliffe, N. J.; McHale, G.; Newton, M. I.; Perry, C. C.; Pyatt, F. P. Plastron Properties of a Superhydrophobic Surface. *Appl. Phys. Lett*. **2006**, *89*, 104106.

86 Lin, Y.; Shen, Y.; Liu, A.; Zhu, Y.; Liu, S.; Jiang, H. Bio-Inspiredly Fabricating the Hierarchical 3D Porous Structure Superhydrophobic Surfaces for Corrosion Protection. *Mater. Design* **2016**, *103*, 300–307.

87 Ding, C. D.; Liu, Y.; Wang, M. D.; Wang, T.; Fu, J. J. Self-Healing Superhydrophobic Coating Based on Mechanised Silica Nanoparticles for Reliable Protection of Magnesium Alloys. *J. Mater. Chem. A* **2016**, *4*, 8041–8052.

88 Weng, C.-J.; Chang, C.-H.; Peng, C.-W.; Chen, S.-W.; Yeh, J.-M.; Hsu, C.-L.; Wei, Y. Advanced Anticorrosive Coatings Prepared from the Mimicked Xanthosoma Sagittifolium-Leaf-Like Electroactive Epoxy with Synergistic Effects of Superhydrophobicity and Redox Catalytic Capability. *Chem. Mater.* **2011**, *23*, 2075–2083.

89 Chang, K.-C.; Lu, H.-I.; Peng, C.-W.; Lai, M.-C.; Hsu, S.-C.; Hsu, M.-H.; Tsai, Y.-K.; Chang, C.-H.; Hung, W.-I.; Wei, Y.; Yeh, J.-M. Nanocasting Technique to Prepare Lotus-Leaf-Like Superhydrophobic Electroactive Polyimide as Advanced Anticorrosive Coatings. *ACS Appl. Mater. Interfaces* **2013**, *5*, 1460–1467.

90 Peng, C.-W.; Chang, K.-C.; Weng, C.-J.; Lai, M.-C.; Hsu, C.-H.; Hsu, S.-C.; Li, S.-Y.; Wei, Y.; Yeh, J.-M. UV-Curable Nanocasting Technique to Prepare Bio-Mimetic Super-Hydrophobic Non-Fluorinated Polymeric Surfaces for Advanced Anticorrosive Coatings. *Polym. Chem.* **2013**, *4,* 926–932.

91 Chang, K. C.; Chuang, T. L.; Ji, W. F.; Chang, C. H.; Peng, Y. Y.; Shih, H.; Hsu, C. L.; Yeh, J. M.; Tang, W. C.; Su, Y. C. UV-Curable Nanocasting Technique to Prepare Bioinspired Superhydrophobic Organic-Inorganic Composite Anticorrosion Coatings. *Express Polym. Lett*. **2015**, *9*, 143–153.

92 Yeh, J.-M.; Chang, K.-C.; Hsu, C.-H.; Ji, W.-F.; Hsu, M.-H.; Lu, H.-I.; Lai, M.-C.; Liu, P.-J.; Chuang, T.-L.; Wei, L.; Liu, W.-R.; Hsiao, Y.-R. Anticorrosive Layer Having a Biomimetic Leaf Surface Nano-Microstructure and Application Thereof. *Patent* US20160032111 A1, February 4, 2016.

93 Sadhir, R. K.; Saunders, H. E. Protective Thin Film Coatings by Plasma Polymerisation. *Microelectron. Int.* **1986**, *9*, 28–32.

94 Visco, S. J.; Chu, M.-Y. Protective Coating for Negative Electrodes. *Patent* US6125094, February 15, 2000.

95 Izu, M.; Dotter, B.; Ovshinsky, S. R. High Performance Clear Coat TM Barrier Film, *Soc. Vac. Coaters*, Proc. Annu. Tech. Conf. **1993**, *36*, 333.

96 Dobuzinsky, D. M.; Matsuda, T.; Nguyen, S. V.; Ryan, J. G.; Shapiro, M. PECVD Method of Depositing Fluorine Doped Oxide Using a Fluorine Precursor Containing a Glass-Forming Element. *Patent* US5563105, October 8, 1996.

97 Martinu, L.; Zabeida, O.; Klemberg-Sapieha, J. E. Plasma-Enhanced Chemical Vapour Deposition of Functional Coatings, in *Handbook of Deposition Technologies for Films and Coatings, Third Edition.* Martin, P. M.; Ed.; Elsevier, Inc: Oxford, 2010, 9.

98 Lane, A. P.; Webb, D. A.; Frederick, G. R. Deposition of Silicon-Containing Films Using Organosilicon Compounds and Nitrogen Trifluoride. *Patent* US4894352, January 16, 1990.

99 Loboda, J. M.; Michael, K. W. Silicon Carbide Metal Diffusion Barrier Layer. *Patent* US5818071, October 6, 1998.

100 Batey, J.; Boland, J. J.; Parsons, G. N. Pulsed Gas Plasma-Enhanced Chemical Vapour Deposition of Silicon. *Patent* US5242530, September 7, 1993.

101 Cheung, D.; Yau, W. F.; Mandal, R. P.; Jeng, S. P.; Liu, K. W.; Lu, Y. C.; Barnes, M.; Willecke, R. B.; Moghadam, F.; Ishikawa, T.; Poon, T. W. Plasma

Processes for Depositing Low Dielectric Constant Films. *Patent* US6303523, October 16, 2001.

102 Cheung, D.; Jeng, S. P.; Liu, K.; Yau, W. F.; Yu, Y. C. Low Power Method of Depositing a Low k Dielectric with Organo Silane. *Patent* US6072227, June 6, 2000.

103 Bedjaoui, M.; Delepierre, G.; Poulet, S. Method for Assembling and Encapsulating Lithium Microbatteries and Microbatteries Produced Thereby. *Patent* WO2014006296, January 9, 2014.

104 Nath, P. Apparatus for Plasma Assisted Evaporation of Thin Films and Corresponding Method of Deposition. *Patent* US4514437, April 30, 1985.

105 Cathay, D. A. Jr.; Lee, J. K.; Tjadin, K. High Resistance Resistors for Limiting Cathode Current in Field Emission Displays. *Patent* US5712534, January 27, 1998.

106 Hauser, V. E. Jr.; Sinha, A. K. Method of Coating Semiconductor Substrates. *Patent* US4142004, February 27, 1979.

107 Hudgens, S. J.; Johncock, A. G.; Ovshinsky, S. R. Nath, P. Plasma Deposited Coatings and Low Temperature Method of Making Same. *Patent* US4737379, April 12, 1988.

108 Gutmann, R. J.; Chow, T. P.; Lakshminarayanan, S.; Price, D. T.; Steigerwald, J. M.; You, L.; Murarka, S. P. Integration of Multilevel Copper Interconnects with Oxide and Polymer Interlevel Dielectrics. *Thin Solid Films* **1995**, *270*, 472–479.

109 Favia, P.; d'Agostino, R. Plasma Treatments and Plasma Deposition of Polymers for Biomedical Applications. *Surf. Coat. Technol.* **1998**, *98*, 1102–1106.

110 Crawley, R. L.; Evans, J. L. The Deposition of Oxygen Containing Plasma Polymers for use as Permeation Barrier Coatings. *J. Vac. Sci. Technol.* **1991**, *9*, 824.

111 Bubenzer, A.; Dischler, B.; Brandt, G.; Koidl, P. RF-Plasma Deposited Amorphous Hydrogenated Hard Carbon Thin Films: Preparation, Properties and Applications. *J. Appl. Phys.* **1983**, *54*, 4590–4595.

112 Biederman, H.; Slavinska, D. Plasma Polymer Films and Their Future Prospects. *Surf. Coat. Technol.* **2000**, *125*, 371–376.

113 Cho, S.-J.; Bae, I.-S.; Boo, J.-H.; Park, Y. S.; Hong, B. Study on the Plasma-Polymer Thin Films Deposited by Using PECVD and Application Tests for Low-κ Insulator. *J. Korean Phys. Soc.* **2008**, *53*, 1634–1637.

114 Uhlig, M.; Bertz, A.; Werner, T.; Gressner, T. In *Polymer and Adhesives in Microelectronics and Photonics.* Plasma Deposited CF Polymer Films as Ultra Low κ Intermetal Dielectric, Film Properties and Application. Potsdam, Germany, 21-24 October, 2001.

115 Uhlig, M.; Bertz, A.; Rennau, M.; Schulz, S. E.; Werner, T.; Gessner, T. Electrical and Adhesion Properties of Plasma-Polymerised Ultra-Low k Dielectric Films with High Thermal Stability. *Microelectron. Eng.* **2000**, *50*, 7–14.

116 Uhlig, M.; Bertz, A.; Gessner, T. Integration of Plasma Deposited Fluorocarbon Polymer Low κ Material in a Copper/ Low κ Damascene Architecture. *Technische Universitat, Chemnitz*: Centre for Microtechnologies.

117 Fenn, J. B.; Gibbard, H. F.; Lagos, B. C.; Treger, J.; Wei, G. Light Transparent Multilayer Moisture Barrier for Electrochemical Celltester and Cell Employing Same. *Patent* US5681666, October 28, 1997.

118 Leu, J.; Syu, S. H.; Tu, H. E.; Wang, C. Electroluminescent Device Including Moisture Barrier Layer. *Patent* US20140077691, March 20, 2014.

119 Sheats, J. R.; Hueschen, M. R.; Roitman, D. B.; Seaward, K. L.; Briggs, G. A. D. Transparent, Flexible Permeability Barrier for Organic Electroluminescent Devices. *Patent* US6146225, July 30, 1998.

120 Graff, G. L.; Gross, M. E.; Affinito, J. D.; Shi, M. K.; Hall, M. G.; Mast, E. S.; Waltey, R.; Rutherford, N.; Burrows, P. E.; Martin, P. M. Environmental Barrier Material for Organic Light Emitting Device and Method of Making. *Patent* US6570325, May 27, 2003.

121 Graham, S. Jr.; Kippelen, B.; Kim, N.; Domereq, B. Environmental Barrier Coating for Organic Semiconductor Devices and Methods Thereof. *Patent* US20100132762, June 3, 2010.

122 Liaw, J. J.; Yang, C. Y. Two Step Barrier Process. *Patent* US6177338, January 23, 2001.

123 Dung, N. T.; Teu, N.; Zhihong, Z. Method to Plasma Deposit onto an Organic Polymer Dielectric Film. *Patent* WO2004070793, August 19, 2004.

124 Stingley, N. H. Highly Resilient Polybutadiene Ball. *Patent* US3241834A. March 22, 1966.

125 Hiraoka, H.; Kitaoh, K.; Maruoka, K.; Yamada, M. One-Piece Solid Golf Ball. *Patent* 4974852A. December 4, 1990.

126 Posadas, P.; Fernandez, A.; Brasero, J.; Valentin, J. L.; Marcos, A.; Rodriguez, A.; Gonzalez, L. Vulcanisation of Polybutadiene Rubber with Dipentamethylene Thiuram Tetrasulphide. *J. Appl. Poly. Sci*. **2007**, *106*, 3481–3487.

127 Lenko, D.; Schlogl, S.; Temel, A.; Schaller, R.; Hlzner, A.; Kern, W. Dual Crosslinking of Carboxylated Nitrile Butadiene Rubber Latex Employing the Thiol-ene Photoreaction, *J. Appl. Poly. Sci*. **2013**, *129*, 2735–2743.

128 Armstrong, R. T.; Little, J. R.; Doak, K. W. In *Division of Rubber Chemistry, Am. Chem. Soc*. Chemistry of Sulphur-Olefin Reactions: Application to Vulcanization. New York, 1944.

129 Kade, M. J.; Burke, D. J.; Hawker, C. J. The Power of Thiol-Ene Chemistry. *J. Poly. Sci. A.* **2010**, *48*, 743–750.

130 Hoyle, C. E.; Bowman, C. N. Thiol–Ene Click Chemistry. *Angew. Chem. Int. Ed*. **2010**, *49*, 1540–1573.

131 Kato, H.; Nakatsubo, F.; Abe, K.; Yano, H. Crosslinking via Sulphur Vulcanisation of Natural Rubber and Cellulose Nanofibers Incorporating Unsaturated Fatty Acids. *RSC Adv.* **2015**, *5*, 29814.

132 Brummelhuis, N. T.; Diehl, C.; Schlaad, H. Thiol-Ene Modification of 1,2-Polybutadiene Using UV Light or Sunlight. *Macromolecules* **2008**, *41*, 9946-9947.

133 Jones, P. C.; Mathes, R. A. Vulcanisation of Rubber or the Rubbery Co-Polymer of Butadiene and Styrene. *Patent* US2424175A, July 15, 1947.

134 Jones, P. C.; Mathes, R. A. Vulcanisation of Rubber. *Patent* US30763539A, August 22, 1944.

135 Baum, A. A. Vulcanization of Chloroprene Polymers. *Patent* US2544746A, March 13, 1951.

136 Watt, G. W. Vulcanization of Rubber. *Patent* US2189720A, February 6, 1940.

137 Jacobine, A. F. Thiol–Ene Photopolymers. In *Radiation Curing in Polymer Science and Technology*. J. P. Fouassier, Rabek, J. F. Eds.; Elsevier Science: Essex; 1993, Vol. 3; pp 247–248.

138 Oswald, A. A.; Griesbaum, K. Radical Additions of Thiols to Diolefins and Acetylenes. In *The Chemistry of Organic Sulphur Compounds*. Kharasch, N.; Meyers, C. Y. Eds.; Pergamon Press: Oxford; 1966, Vol. 2; p 243.

139 Coulson, S. R.; Evans, D.; Siokou, A.; Telford, C. Coatings *Patent* US20180171171A1, June 21, 2018.

140 Aresta, G.; Hennighan, G.; Brooks, A. S. H.; Singh, S. V. Coated Electrical Assembly. *Patent* US20170094810A1, March 30, 2017.

141 Gadow, R.; Friedrich, C.; Killinger, A.; Floristán, M. Development of Atmospheric Plasma Sprayed Dielectric Ceramic Coatings for High

Efficiency Tubular Ozone Generators. *J. Water Resource Prot.* **2010**, *2*, 799–808.

142 Mikhael, M. G.; Yializis, A.; Ellwanger, R. E. Barrier Coatings Produced by Atmospheric Glow Discharge. *Patent* WO2004019381A2, May 13, 2004.

Chapter 2 : Experimental Techniques

2.1. Introduction

Throughout this thesis a range of coatings were deposited on small circuit boards, in order to determine their barrier properties. Several analysis techniques were used in order to determine the best wet electrical barrier coating and to establish the qualities possessed by the coating. This chapter summarises those techniques.

2.2. Electrical Barrier

Resistivity, ρ, is a physical property of a material, defined as the ability of the material to oppose the flow of charge, with units of ohm-meter, Ω m (although Ω cm and Ω nm are most commonly used when referring to barrier coatings).[1] Resistivity can be calculated using Equation 2-1:

$$\boldsymbol{\rho = \frac{RA}{l}} \qquad \textbf{Equation 2-1}$$

where R is the resistance (Ω), A is the area (m^2) and l is length (m), Figure 2-1.[1–3]

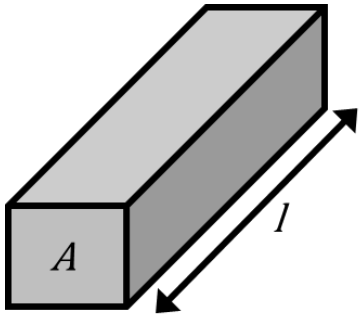

Figure 2-1: Schematic of a section of resistive material, with the dimensions required for the calculation of the volume resistivity.

Typically, the resistivity of polymers is given as volume resistivity, which is the ohmic resistance of a cube of material. Electrical grade polymers typically have a volume resistivity of around 10^{15} Ω cm,[4] although can be as high as 10^{18} Ω cm

for some highly resistive polymers, at room temperature.[5] Surface resistivity, ρ_s, which is also often given in relation to polymeric materials, is the resistance of the surface between two electrodes forming opposite sides of a square, Equation 2-2,

$$\boldsymbol{\rho_s = \frac{RP}{D}} \qquad \textbf{Equation 2-2}$$

where R is the resistance, P is the perimeter of the electrode area, and D is the distance between the electrodes. The size of the square is inconsequential, and the surface resistivity is given in ohms per square, Ω/square or Ω/□.[1] Typical surface resistance values for polymers are 10^7–10^{10} Ω/□.[4]

The surface resistivity is very similar in calculation to sheet resistance, R_s,[6] a specific type of resistivity often quoted when referring to polymer barriers. This can also be calculated from the resistivity, rearranging Equation 2-1 to give Equation 2-3,

$$\boldsymbol{R = \frac{\rho}{t}\frac{l}{W}} \qquad \textbf{Equation 2-3}$$

where the area can be split into the width, W, length, l, and thickness, t, of the polymer, Figure 2-2.

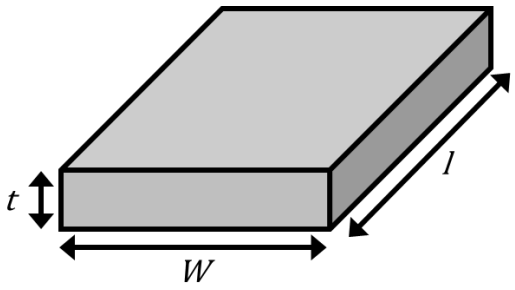

Figure 2-2: Schematic of a section of resistive polymer film, with the dimensions required for the calculation of the resistivity.

Taking the resistivity over thickness gives a value termed the polymer sheet resistance, Equation 2-4.

$$\boldsymbol{R_s = \frac{\rho}{t}} \qquad \textbf{Equation 2-4}$$

As the units of resistivity are Ω m, when divided by the thickness to get sheet resistance, the units become Ω m m^{-1}, or simply Ω. However, to differentiate this

from the bulk resistance it is standard practice to quote it in ohms per square, rather than just ohms, as per the surface resistivity. Often these terms are used interchangeably, but if necessary, sheet resistance can be considered to be a two-dimensional concept, when applied to ultra-thin films. This requires the assumption that the current moves across the plane of the film, and not through the bulk.

There are a variety of techniques which have been used to measure the electrical properties of potential electrical barrier layers. Typically, to measure the current through a film, electrodes are placed on either side of the film, or circular electrodes can be applied to the surface as a set of equivalent contacts, whilst the substrate is taken as the other contact.[7] When measuring the volume resistivity, any surface current leakage must be ignored. To this end, a guard electrode is used to collect this leakage current.[7,8] For films of a defined size and shape, the "four-point probe" method is used; the current source is connected to the outer probes, and the inner probes measure the voltage. Films which are irregularly shaped can be measured using the "Van der Pauw" method, and two sets of current–voltage measurements are taken, Figure 2-3.[7]

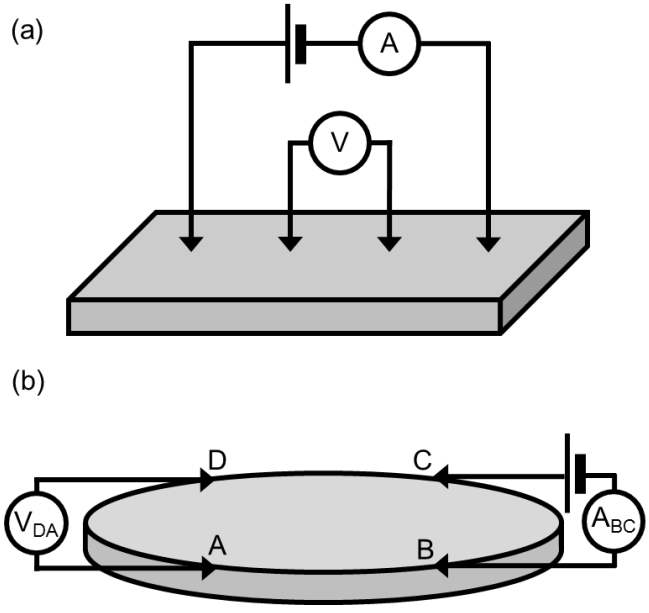

Figure 2-3: Resistivity measurement methods of polymer films: (a) the four-point probe method used to measure sheet resistance of films of a predetermined size; and (b) the Van der Pauw method used to measure the resistivity of non-standard shaped films.

The volume resistivity, surface resistivity and sheet resistance can be significantly reduced by water absorption, which means that a potential water

barrier coating for electronics should not be based on resistivity factors alone. Whilst the volume resistivity can take an extended period of time to decrease on exposure to moisture, the surface resistivity and sheet resistance can drop instantaneously. Additionally, ionic impurities on the surface can also drastically decrease the surface resistance when they become conductive in the presence of water.[4]

As such, these measurements give the electrical parameters of an immaculate coating in its initial state, but give no bearing on the coating's performance when subject to potentially damaging conditions, such as immersion in water. It is under such conditions that the effectiveness of a coating on an electronic device must be tested to show proof of concept. To this end, a separate measurement system is used to evaluate the electrical barrier coatings when immersed in water, whilst the device is in operation. The water used herein is tap water (Northumbrian Water), but any conductive liquid medium could be used with this method e.g. salt water, chlorinated water, etc. Circuit boards were designed comprising two interdigitiated electrodes, with no points of contact between them, resulting in them being initially non-conductive.[9] When an uncoated board is immersed in water, under an applied voltage, current can flow from one electrode to the other through the water, and with enough corrosion, dendrite formation can occur. However, with the application of a barrier coating to the electrodes, this current flow can be avoided, Figure 2-4. A barrier coating which can block the ingress of electrolytes and ions prevents current flow between the two non-connected electrodes.

Considering this, the immersion of a circuit board in tap water under an applied voltage can be used to evaluate electrical barrier performance. A poor wet electrical barrier will show instantaneous current flow, as well as an increase in current flow over time to the point where the current is equal to that of an immersed uncoated circuit board. A moderate barrier coating might initially show no current flow, but the coating can breakdown over time, and current will begin to flow through the circuit, and a good barrier coating will not break down and will appear as an open circuit over the defined testing period.

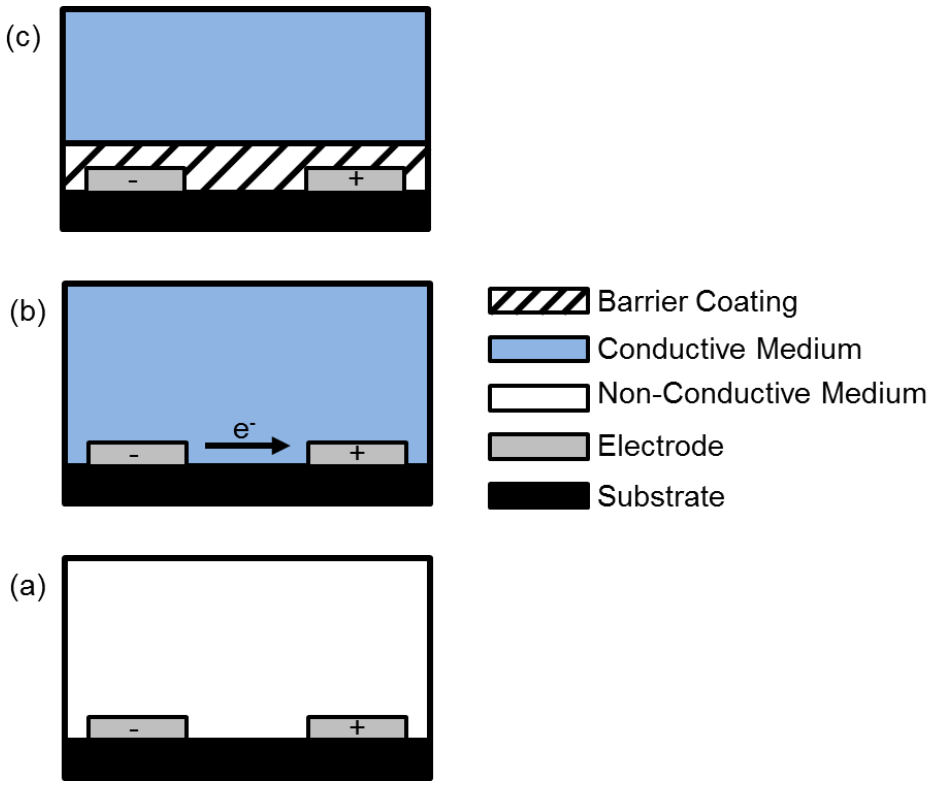

Figure 2-4: Schematic of the wet electrical barrier testing method: (a) there is no current flow between the electrodes in a non-conductive medium, e.g. air; (b) current flow between the electrodes when the circuit board is immersed in a conductive medium, e.g. water; and (c) there is no current flow between the electrodes when the circuit board is immersed in a conductive medium e.g. water, when the electrodes are protected by a barrier coating.

2.3. Plasma

Plasma, one of the fundamental states of matter along with solids, liquids and gases, comprises electrons, ions, metastables and neutral species.[10,11] Classically, plasma is referred to as an electrically conductive ionised gas or vapour due to the presence of free moving electrons, which in itself is electrically neutral. In more modern definitions, plasma is known as a gas comprising electrons, ions, photons, and atoms and molecules in low or high excited states.[12] The energy distribution within a plasma is proportional to the temperature of the plasma, Figure 2-5, as plasmas with a lower energy distribution of the electrons and ions will tend to have a lower temperature, and plasmas with a higher energy distribution will tend to have a higher temperature.[11]

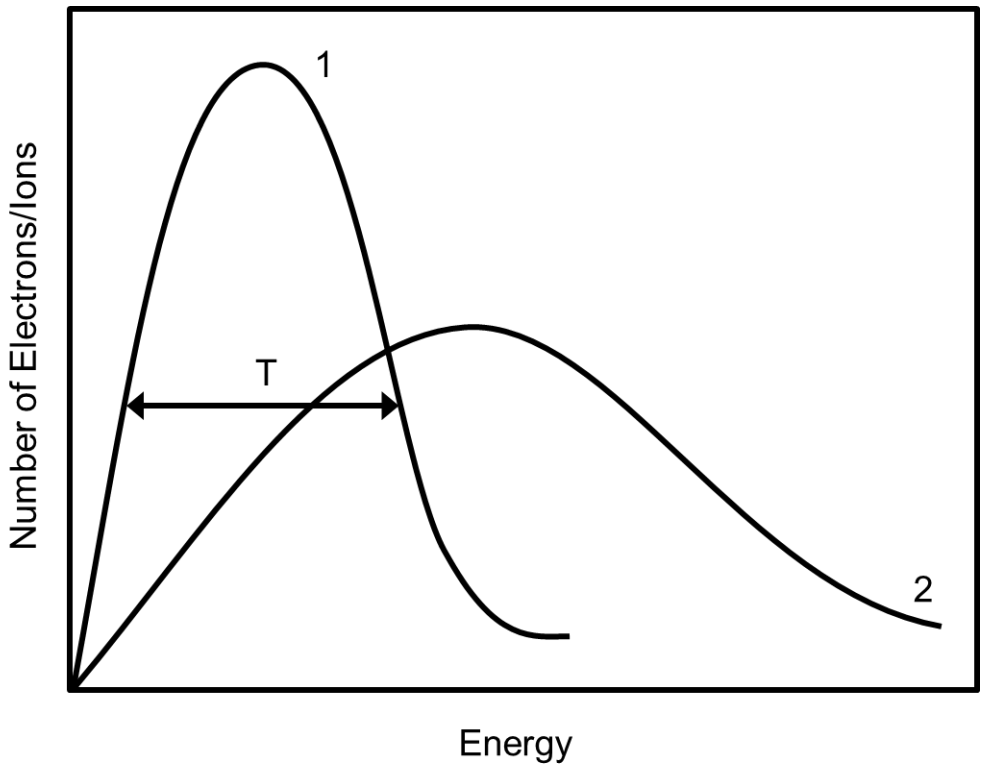

Figure 2-5: Energy distribution of electrons or ions in a plasma, where the temperature is proportional to the energy distribution within the plasma. Line 1 represents a lower energy distribution with a lower temperature than line 2.[10]

A plasma discharge can be generated by the application of an electric field to a gas or vapour within a chamber causing acceleration of the electrons, and subsequent elastic and inelastic collisions, resulting in ionisation and excitation. This causes secondary electron acceleration leading to a plasma cascade, or a Townsend avalanche.

2.3.1. Equilibrium and Non-Equilibrium Plasmas

There are three general types of plasma, depending on the physical properties of the plasma and the method of ionisation. When the energy of the neutral species in a plasma is equal to that of the electrons, the plasma is thermodynamically stable and is termed an equilibrium plasma. Plasmas of this type can be split into two subtypes; they can be in complete thermodynamic equilibrium where all of the constituent parts are at the same temperature, such as stars, or the temperature

of all the plasma species are equal with the exception of the radiation, such as plasma jets or electric arcs.[13] These are termed “thermal” or “hot” plasmas.

Non-equilibrium plasmas are not thermodynamically stable, as the energy of the electrons is much higher than the energy of the neutral species and ions. These plasmas are often classified as “non-thermal” or “cold” plasmas” and can be operated at ambient temperatures.[13] Glow discharges, which are produced in low pressure gases or vapours by stimulation with an electric field are non-equilibrium plasmas.

Beyond these broad plasma categories there are more specific types of plasma generation which can be used for deposition, modification, or etching.

2.3.1.1. Radio Frequency Plasma

In radio frequency (RF) plasmas the energy is supplied to the discharge by either capacitive or inductive coupling and have been known as “electrodeless discharges” as the electrodes need not be in contact with the plasma. The plasma is produced by matching the output impedance of the RF generator, typically 13.56 MHz, to that of the matching unit, coils and chamber contents, with the aid of a matching network consisting of capacitors and inductors, Section 2.3.4. The Standing Wave Ratio (SWR) of the system is minimised in this process, optimising the forward power of the plasma. RF plasmas are relatively homogeneous and can be performed at low pressures.[13]

2.3.1.2. Microwave Plasma

Microwave plasmas operate at a higher frequency (2.45 GHz) and at higher pressures than RF plasmas. The greatest glow intensity of a microwave plasma is at the coupling microwave capacity, which diminishes outside the cavity as the wavelength is much lower than that of RF radiation.[14] Overall, microwave plasmas have greater ion and electron density than plasmas generated by RF, and they have a large amount of high energy electrons.[15] Microwave plasmas have

commonly been used in industrial applications, such as semiconductor processing and surface treatments.

2.3.1.3. DC Glow Discharge

A DC glow discharge is produced for a gas at low pressure by applying a DC voltage between two electrodes. The electrons are accelerated between the cathode and the anode due to the applied electric field, colliding with ions and neutrals causing energy transfer. The electrodes are inserted into the gas which means they are in contact with the plasma during operation. This can be problematic in certain circumstances, such as in the deposition of a dielectric film, as the electrodes can quickly become covered with an insulating layer, and subsequently the plasma will be extinguished.

2.3.1.4. Atmospheric Plasma

Plasmas generated at atmospheric pressures require higher applied voltages to stimulate the breakdown of the gas or vapour. Arcing can occur in these conditions, which is the desired outcome in some situations, e.g. plasma torches. Methods can be employed to lower the temperature of the plasma and avoid arcing, such as the “point and plane” or pointed electrodes used in corona discharges, or the insulated plates in dielectric barrier discharges.[16] A disadvantage of atmospheric plasmas is the lack of uniformity in the plasma, however as they do not require a low pressure chamber atmospheric plasmas can be used in production and assembly lines with little modification.

2.3.2. Plasma Surface Modification

The chemical and morphological properties of a surface can be modified by exposure to a plasma. Commonly, the adhesion, wettability, and refractive index are altered, depending on the type and conditions of the plasma.[17–23] Surface

modification by plasma typically uses non-polymerising gases, such as tetrafluoromethane (CF_4), helium (He) and argon (Ar), causing physical ablation and free-radical formation due to ion sputtering, neutral species collision, and the emission of ultra-violet (UV) radiation. Fragments which have been removed from the surface can be reincorporated into the surface or redeposited as a crosslinked layer. As well as chemical modification, physical etching can also occur. Surface reactions are induced by the plasma, transforming the solid surface material, e.g. silicon or silicon dioxides, into volatile products, such as silicon halides.[24] These volatile products can then desorb from the surface into the gas phase. Etching can be used in conjunction with masks or composite surfaces to give patterned surfaces and specific etched designs.

Accordingly, surfaces which are normally unreactive can be treated through plasma reactions to give surface modification. For example, the treatment of polypropylene with an oxygen plasma results in the incorporation of oxygen containing functional groups on the surface.[22] This type of plasma treatment increases the wettability and adhesion of the polypropylene surface. Alternatively, when CF_4 is subjected to a RF electromagnetic field, Figure 2-6, electron acceleration occurs, resulting in bond cleavage and ionisation of the CF_4 molecule. This results in fluorination of a polymer surface placed in the plasma chamber, e.g. polybutadiene, and an increase in the hydrophobicitiy of the surface, Section 2.8.[25]

CF_4 plasma treatment has been used as a source of F and C atoms, CF_x ($1 \leq x \leq 3$) radicals, and ions for surface treatment. These produce two competitive processes, etching and surface functionalisation. For short treatment times etching of the surface of the substrate or chamber is the dominant process.[26,27] The etching process is produced by charged particles which cause the electron impact that results in dissociation, excitation in the gas phase and ion bombardment of the surface, and fluorine atoms which react with the surface to give volatile products.[28,29]

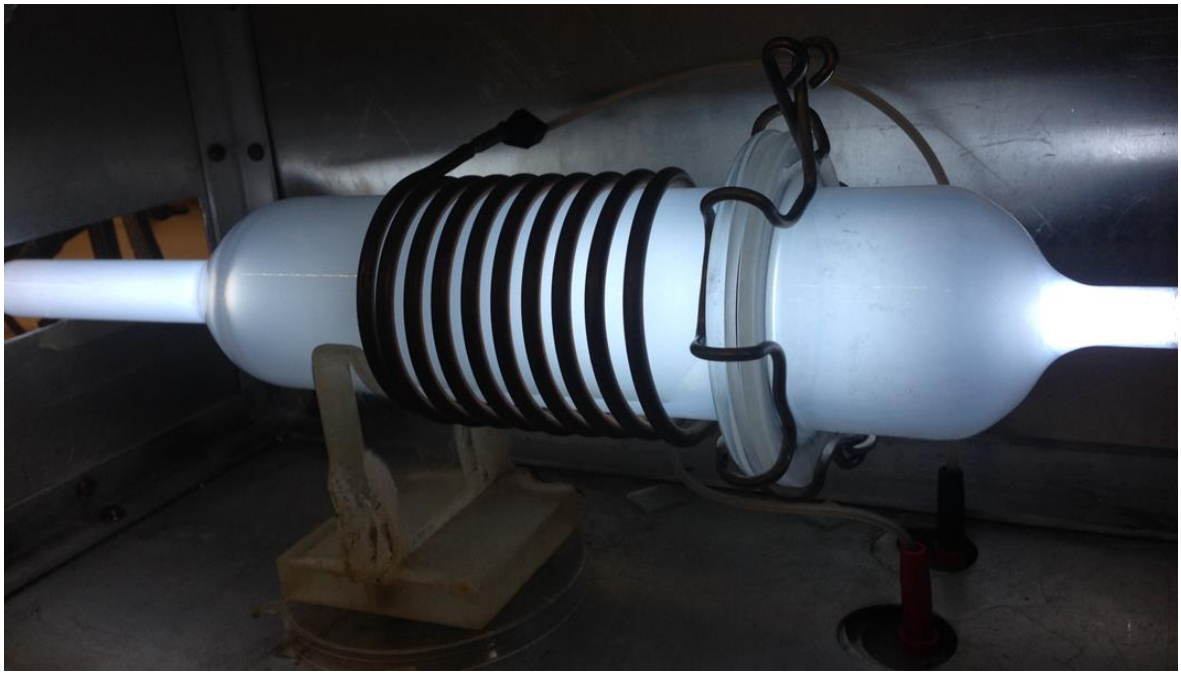

Figure 2-6: Plasma chamber during a CF_4 plasma discharge.

Etching and surface fluorination processes depend on the plasma parameters and chamber conditions, such as the gas flow rate, plasma energy, and the substrate position in relation to the plasma density throughout the chamber. For example, in a capacitively coupled plasma system, in the early stages of CF_4 plasma treatment the etching rate (11.5 nm min^{-1}) is higher than the fluorination rate (3.2 nm min^{-1}). However, later in the CF_4 plasma treatment, the etching rate slows (2.8 nm min^{-1}), becoming less dominant than fluorination. This is because the bond strength increases after substitutions of chemical bonds on the surface (e.g., C-H, C=C, C–O, C–C) by stronger C–F bonds.[30] Additionally, the etching rate decreases in the regions of lower plasma density due to the absence of electrons and low density of ions so that the ion bombardment on the substrate surface is less significant.[29] Therefore, depending on the plasma conditions such as power, substrate position, and treatment time, surface roughness and chemical modification of the polymer surface can be controlled, to give varying degrees of surface fluorination.

2.3.3. Plasma Polymerisation

Plasma polymerisation differs from conventional polymerisation, in that conventional polymerisation is a molecular process, and plasma polymerisation is based upon both atomic and molecular processes. There are two main characteristics of plasma polymerisation:

1. Unlike conventional polymers, plasma polymers deposited via a continuous process contain no obvious repeating units.
2. The monomer used in the polymerisation does not necessarily require a functional group, such as a vinyl bond, although this can be beneficial.

Plasma polymer deposition requires the activation of monomer vapour, to form the monomer radical species required to deposit the plasma polymer, Scheme 2-1.

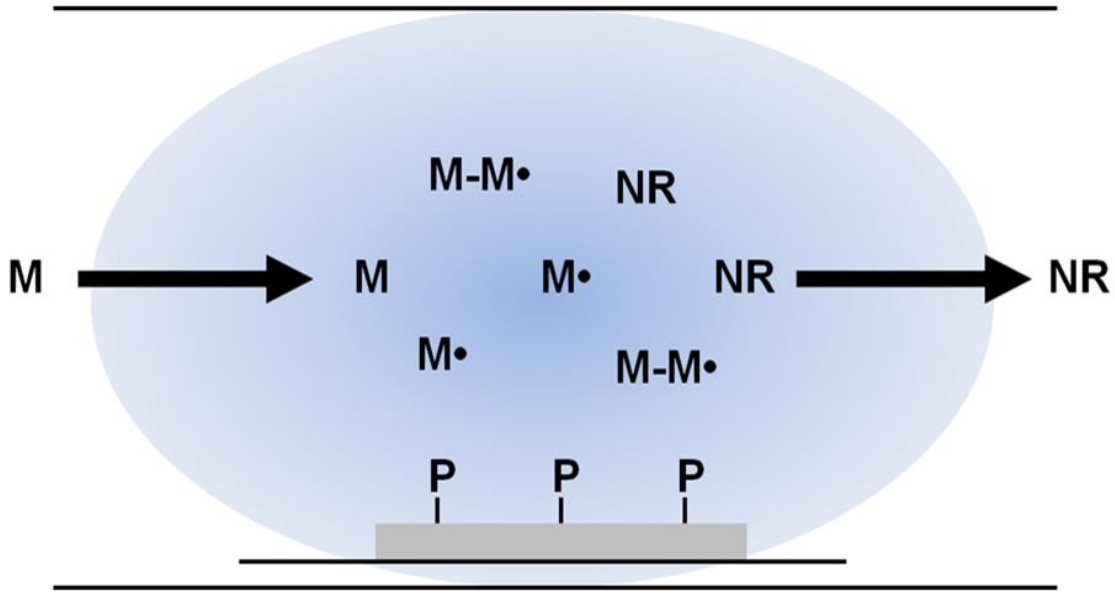

Scheme 2-1: Schematic representation of a plasma reaction. M: Monomer, M•: Reactive monomer species, M-M•: Polymerised reactive species, P: Polymer on the surface, NR: non-reactive species.

Plasma polymer deposition is typically performed in two ways: continuous wave (CW) and pulsed plasma deposition. These result in drastically different plasma polymer films. CW has been thought to occur via plasma-induced polymerisation and plasma-state polymerisation.[12] Plasma-induced

polymerisation generally requires polymerisable functional groups which are excited by the electrons or radicals in the electrical discharge to then form the plasma polymer.[31] The fragmentation of the precursor monomer generating the radicals, ions, and electrons which cause reformation into larger species is known as plasma-state polymerisation. Due to these processes, which require constant excitation of the electrons and radicals by the electric field, the final polymer film does not retain the structural integrity of the precursor monomer, Scheme 2-2.

If required, the structural integrity of the precursor can be retained by using pulsed plasma polymerisation, allowing the functional groups to remain intact, Scheme 2-2, making it much more like conventional polymerisation. A lower amount of fragmentation is achieved by only activating the electric field for a very short time, usually in the realm of μs–ms, and this is followed by an off-time of ms duration. Using this method of plasma deposition, conventional polymerisation reactions can occur during the off-time of the plasma.

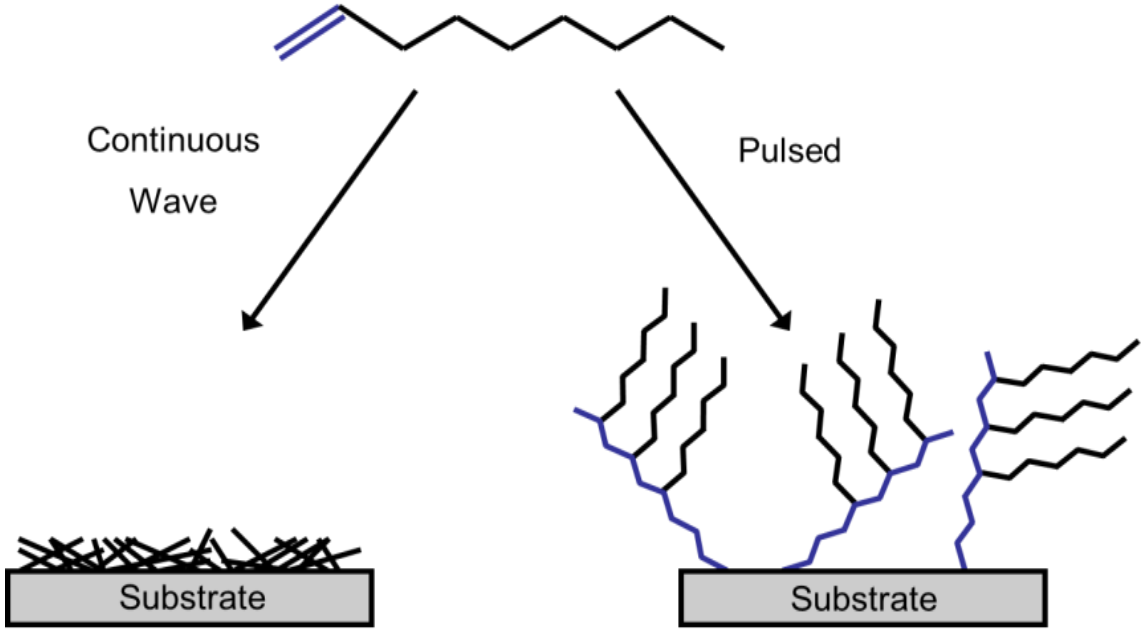

Scheme 2-2: Schematic of differences in plasma polymer films generated by continuous wave versus pulsed plasma.

Like conventional polymerisation, plasma polymerisation occurs in the following steps:

1. Initiation.
2. Propagation.
3. Termination.

The free radicals required for the initiation are produced in the plasma by the collision of electrons and ions with the monomer molecules, or by ion impact of the monomers adsorbed on the surface. The formation of plasma polymer chains for propagation takes place both on the surfaces and in the gas phase. The free radicals on the surface interact with monomer also on the surface or in the gas phase, whilst polymerisation in the gas phase occurs between the radical species and other radicals, monomers, or monomer fragments. Finally, termination occurs both in the gas phase and on the surface, similarly to propagation but ending with either the final product or a closed chain. These neutral final species can be re-initiated, by collision with electrons or the impact of excited molecules.

2.3.4. Reactor Apparatus and Plasma Deposition

The chamber used herein for RF plasma processing was connected to a pumping system, to take the chamber down to the base pressure and keep it under vacuum. A cold trap was placed between the chamber and the pump to remove any reactive species from the gas flow before they reached the pump and to avoid oil backstreaming, in lieu of other clearing mechanisms which could otherwise be employed. A needle valve was used to regulate the precursor flow rate, and a pressure gauge was installed next to the chamber to monitor the pressure.

The plasma treatments were carried out in a cylindrical glass reactor (5 cm diameter, 470 cm^3 volume) connected to a two stage rotary pump (model E2M2, Edwards Vacuum Ltd.) via a liquid nitrogen cold trap, Figure 2-7, (base pressure of 4×10^{-3} mbar and an air leak rate better than 1×10^{-9} mol s^{-1}).[32] An L-C matching unit was used to minimize the SWR of the power transmitted from a 13.56 MHz RF generator to a copper coil (4 mm diameter, 10 turns, spanning 8 cm) externally

wound around the glass chamber.[33] A signal generator (model TG503, Thurlby Thandar Instruments Ltd.) was used to trigger the RF power supply for the case of pulsed plasma deposition. Prior to each plasma treatment, the chamber was scrubbed with detergent, rinsed with propan-2-ol (+99.5 wt%, Fisher Scientific Ltd.), and further cleaned using a 50 W air plasma for at least 30 min. For the dual deposition processes a double feed rig head was used, allowing two monomer tubes to be connected to the apparatus at the same time.

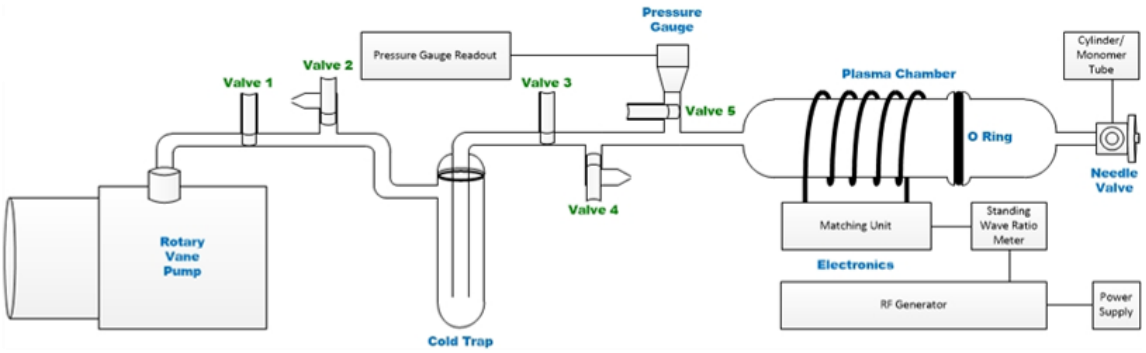

Figure 2-7: Schematic of the plasma apparatus.

The precursors were degassed prior to use by 5 freeze-pump-thaw cycles. 0.2 mbar of precursor vapour was then introduced into the chamber via a fine control needle valve (model LV10K, Edwards Vacuum Ltd.) at a flow rate of 1.7×10^{-7} mol s^{-1}, and the reactor was purged with precursor for 5 min, followed by ignition of the electrical discharge. Film deposition or surface modification was allowed to proceed for a predetermined period, and then the power supply was switched off whilst maintaining precursor flow through the reactor for a further 5 min in order to quench any reactive surface sites before evacuation to base pressure.

The samples for plasma coating were positioned on a glass plate which was inserted into the centre of the plasma chamber, under the coil. The micro-circuit board samples (A–D) were positioned on the centre of the glass plate, and as thickness measurements could not be taken on the micro-circuit boards a piece of silicon (Si) wafer was placed on either side, allowing a thickness range to be obtained across the samples, Figure 2-8.

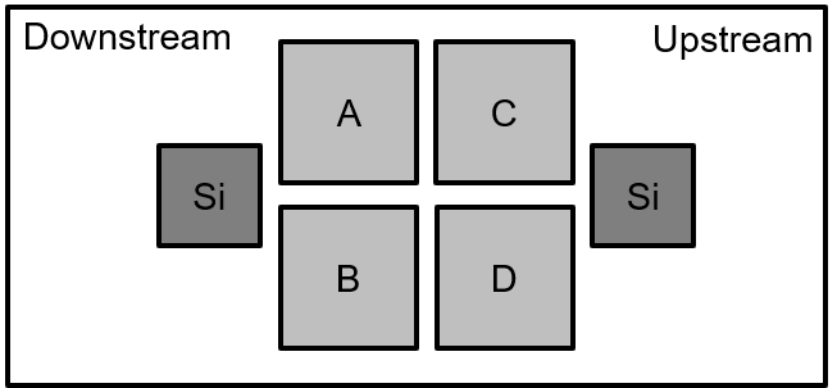

Figure 2-8: Sample layout within the plasma chamber.

The plasma was not completely uniform within the chamber. The density of the plasma was most intense in the glow region directly under the coils, and was less intense downstream towards the pump. This led to a slight unavoidable variance in the thickness of the deposited coatings. This can also lead to variations in the degree of plasma fluorination and etching of the samples, Chapter 4, Section 4.4.2. This was the primary reason for using small samples, as larger samples would have a greater degree of variation in plasma coating thickness or functionalisation. Small samples could be placed close together to mitigate this as much as possible. Another way to lessen the effects of plasma density variations would be to use a larger chamber, which would increase the volume of the region of highest plasma density, allowing more samples to sit in the same region.

2.4. Spin Coating of Polymers

The substrates were fixed onto a glass plate using double sided adhesive tape (product code 1445293, Henkel Ltd.), which in turn was attached to the chuck of a spincoater (model No PRS14E, Cammax Precima Ltd.). Following the coating of the respective polymer layers, the samples were left to dry in a vacuum oven at 60 °C for 60 min in order to remove any trapped solvent. Then the back faces of the substrates were carefully cleaned using a cotton bud and acetone, in order to remove any remaining traces of double-sided adhesive tape which had held the board in place during spin coating. Care was taken to ensure that no acetone came into contact with the coating surface. Prior to further testing, the coatings were visually inspected for the absence of defects.

2.5. Micro-Circuit Board Fabrication

Single sided copper clad micro-circuit boards were prepared using a photoresist board (manufacturer part code 141300, Kelan Circuits Ltd., comprising epoxy woven glass laminate base (National Electrical Manufacturers Association grade FR4 and British Standard BS4584) coated with a 35 μm copper foil and a photoresist top layer (Photoposit SP24, Dow Chemical Company)). A negative image mask (designed using Easy-PC 2000 (version 19) software, Number One Systems Ltd.) was printed onto 100 μm thickness transparent polymer sheets (product code 0224010460, Ryman UK Ltd.) using black ink (product number PGI-520BK, Canon Inc.) and an inkjet printer (model IP3600, Canon Inc.). This negative image mask was then placed on top of the photoresist board, and exposed to UV irradiation (368 nm, 15 W, 2 min exposure, model LV204, Mega Electronics Inc.), Figure 2-9. The UV degraded photoresist regions were dissolved off by immersion into a developer solution for 30 s (1.5% w/v NaOH and 1.5% w/v KOH in water, product code AZ303, GSPK Circuits Ltd.) revealing underlying copper, which was then etched away by dipping into 50% w/v ferric chloride solution for 5 min (ferric chloride pellets (product code 3205022, Mega Electronics Inc.) mixed with 40–50 °C tap water (Northumbrian Water), contained in a bubble etch tank, (model PA104, Mega Electronics Inc.)). Next, the photoresist board was rinsed under tap water to wash away any remaining ferric chloride solution. Finally, the unexposed protective photoresist regions were removed by gently rinsing the surface in acetone (+99.8 wt%, Fisher Scientific Ltd.), followed by soaking in propan-2-ol (+99.5 wt%, Fisher Scientific Ltd.) for 20 min. The circuit boards were designed and prepared by Kelvin Appleby, of the departmental electronics workshop.

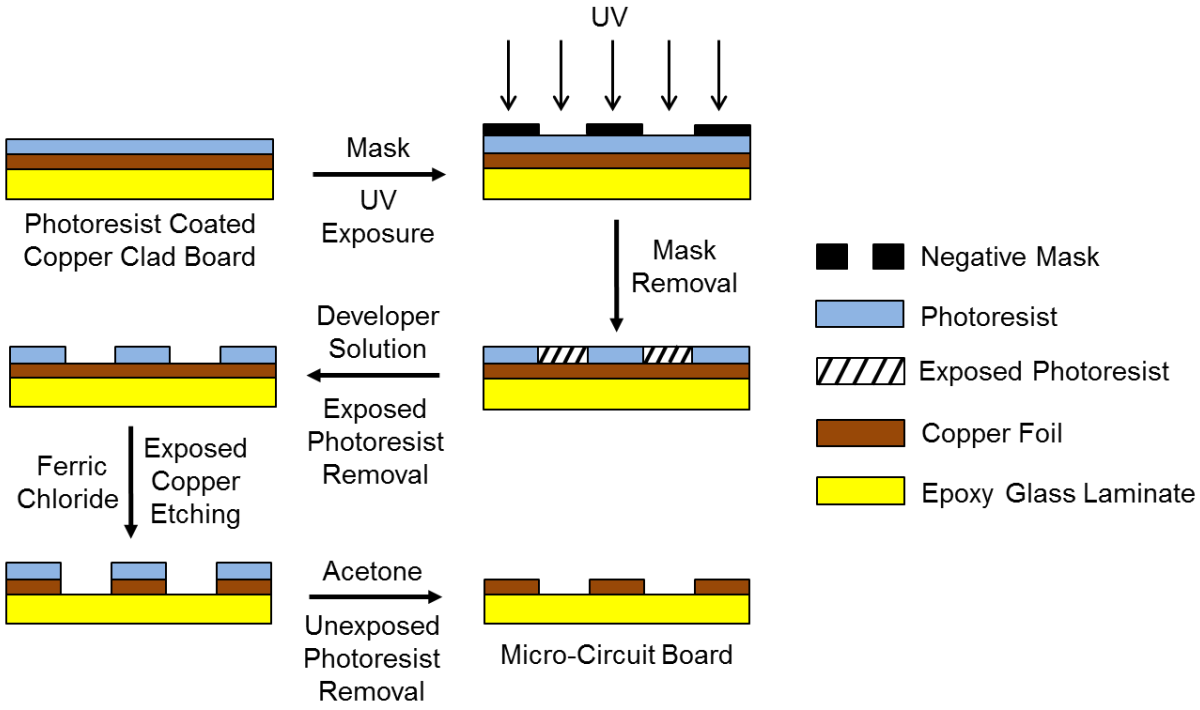

Figure 2-9: Copper track micro-circuit board fabrication.

The fabricated micro-circuit board layout consisted of two copper contact pads connected to respective copper tracks (separated by 0.8 mm) on top of the epoxy glass laminate substrate, Figure 2-10. A small strip of single-sided adhesive tape (product code 1443170, Henkel Ltd.) was applied to the contact pads prior to film deposition in order to mask them (i.e. to keep them clean for subsequent electrical test connection).

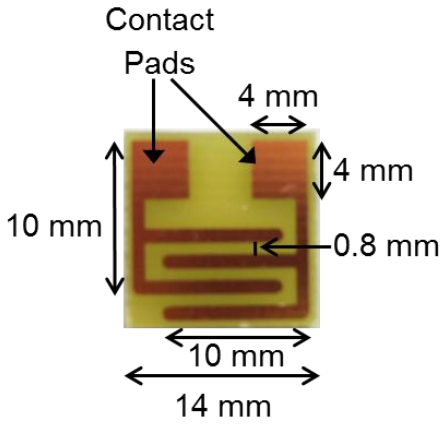

Figure 2-10: Test micro-circuit board copper tracks separated by a 0.8 mm gap.

2.6. Wet Electrical Barrier Measurement

The immersion in water of coated micro-circuit boards whilst measuring electrical resistance is a realistic test for evaluating electrical barrier performance.[34] Tap water (156 µS cm^{-1} conductivity, Northumbrian Water), representing a “real world” scenario for water damage to consumer electronics, was allowed to equilibrate to room temperature (20 °C) prior to usage. A multimeter (with a lower detection limit of 10 nA, Keithley 2000, Tektronix UK Ltd.) was used to measure the current flow for each coated micro-circuit board connected to a variable voltage supply (Model PS-6010, Instek Ltd.), Figure 2-11. The voltage applied across the circuit was checked using a handheld multimeter (model 72-770, Tenma Ltd.). Standard wires and connectors were employed (Flexiplast 2V, stranded wire, 0.75 mm^2 cross sectional area, 129 strands, 0.07 mm diameter, negligible internal resistance, Multi-Contact UK Ltd.).

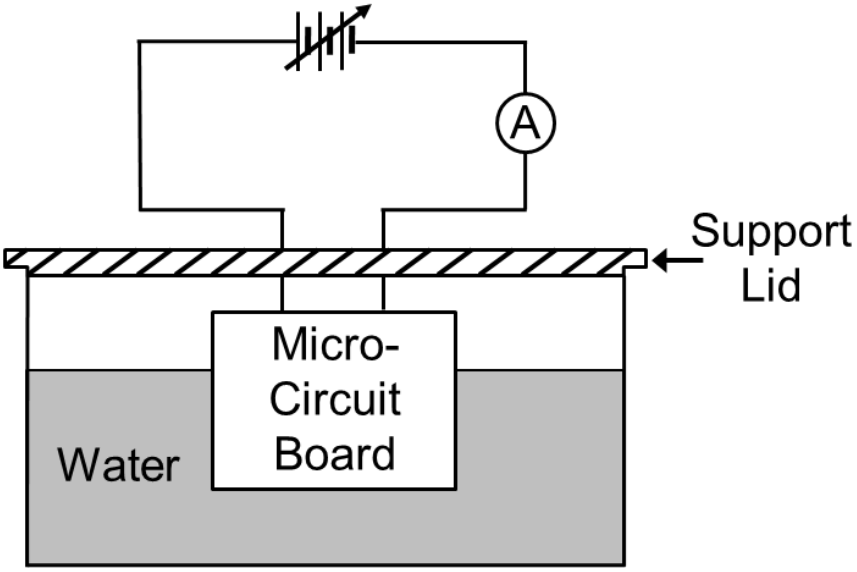

Figure 2-11: Circuit diagram for wet electrical barrier testing.

Two small crocodile clips were carefully cleaned with acetone in order to remove any contaminants, and then fed through two holes in a support lid used to hold the micro-circuit board in place. This was lowered into a 50 mL glass jar filled with 32.5 mL of equilibrated tap water.

A fixed voltage was then applied across the 0.8 mm gap between the micro-circuit board copper tracks whilst immersed in water (e.g. 8 V corresponds to an

electric field of 10 V mm^{-1}). Current measurements were taken every 30 s over a 13 min immersion period.[35] At this stage, the final electrical resistance was calculated using Ohm's law. This resistance value was then divided by the total coating thickness (plasma polymer and polymer base layer combined) in order to yield the electrical barrier performance (units Ω nm^{-1}).

2.7. Thickness Measurements

Spectroscopic reflectometry is a non-destructed measurement method that can be used to determine specific optical constants and the thickness of films deposited on flat, reflective substrates. As the deposited film and the substrate have different refractive indices, n, it will have two interfaces: one with the substrate and one with the surrounding environment (i.e. air), Figure 2-12. When a beam of light (usually 350–1000 nm) is incident on the sample surface some is reflected from the top of the film, some is transmitted and some is absorbed. Of the light transmitted through the film, some is reflected back from the interface between the film and the substrate. Constructive or destructive interference can occur between the light reflected from the two interfaces depending on the difference in the optical path length, which in turn depends upon the wavelength of the light, the thickness of the film, and the optical constants of the film and substrate.[36]

The overall intensity of the reflected light is reliant upon the amount of constructive and destructive interference as well as how much light is absorbed by the film, which is determined by the extinction coefficient, k, and the thickness and roughness of the film. The interference pattern is measured by recording this intensity across the wavelength range and can be fitted using a Cauchy material model using a modified Levenberg Marquardt algorithm to yield the optical constants and film thickness.[37]

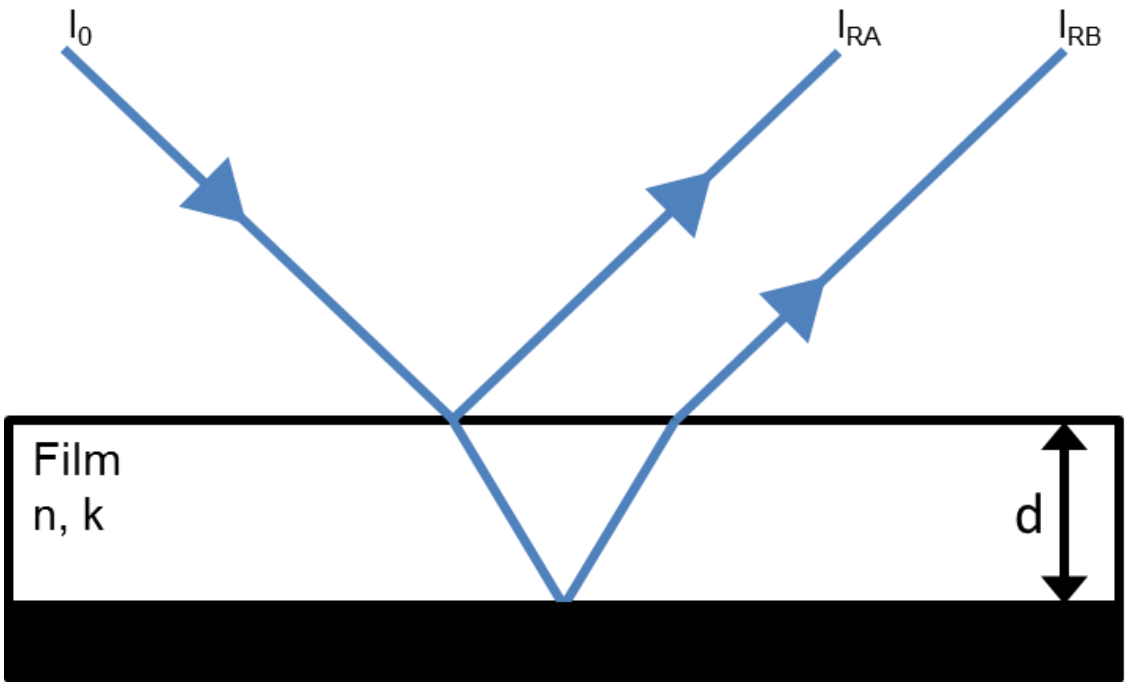

Figure 2-12: The incident monochromatic light (I_0) reflected by the top of the film, (I_{RA}), and the substrate (I_{RB}) causes constructive and destructive interference, from which a reflectance spectrum can be obtained.

If the refractive index of the film is unknown it can be determined by the speed at which light can pass through it, relative to the speed of light in a vacuum, Equation 2-5,[38]

$$n = \frac{c}{v} \qquad \textbf{Equation 2-5}$$

where n is the refractive index of the medium, c is the speed of light in a vacuum, and v is the speed of light in the medium.

In this thesis, thickness measurements were taken using this method. In further work it would be beneficial to confirm the thickness of the samples by SEM or any other separate method. This would serve to qualify the results obtained by this method as well as validating the method itself. The coated micro-circuit boards lacked sufficient reflectivity for thickness measurements, and therefore silicon wafer pieces were used instead and placed alongside the circuit boards during the plasma depositions and modifications. The thickness of the coating on the silicon samples was measured and used to gauge the coating thickness on the circuit boards, although it should be taken into consideration that there may be minor

differences in the actual thickness due to differences in the roughness and wettability of the substrate.

2.8. Water Contact Angle Analysis

When a droplet of water is in contact with a surface the most favourable shape for the droplet to take will depend on the chemistry and the topography of the surface, as well as the parameters of the liquid (surface tension, viscosity, etc.). Consequently, the contact angle between the liquid and the surface can be a very useful analysis technique when characterising a surface. Liquids can interact favourably or unfavourably with a sample surface, typically taking a shape that minimises their surface area, to allow a greater number of interactions with the neighbouring liquid molecules. This droplet shape and the resulting contact angle are determined by the balance of the liquid–solid–vapour surface tensions at the phase boundaries, Young's equation,[39] Equation 2-6,

$$\cos\theta = \frac{\gamma_{SV} - \gamma_{SL}}{\gamma_{LV}} \qquad \textbf{Equation 2-6}$$

where θ is the droplet contact angle, and γ_{sv}, γ_{sl}, γ_{lv}, are the solid–vapour, solid–liquid, and liquid–vapour surface tensions respectively, Figure 2-13.

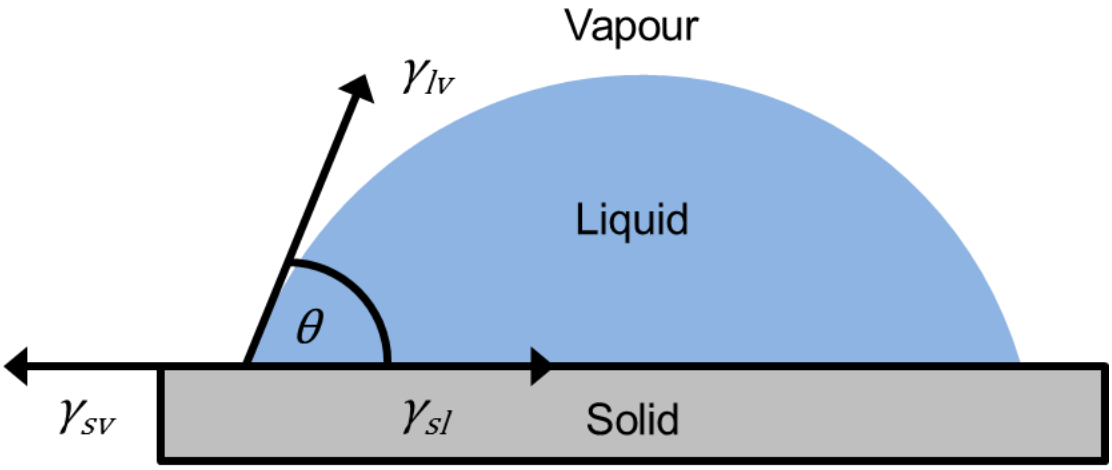

Figure 2-13: Balance of the surface tensions which result in the liquid contact angle.

To measure the contact angle of a surface, a pre-determined volume (e.g. 1 µL) of the desired liquid (e.g. ultra-high purity water) is deposited on the surface

via a syringe. The droplet should be allowed to equilibrate to account for possible spreading. An image of the droplet on the surface is then captured using a backlit microscope optical system or a high-resolution camera, and then a measurement of the angle, θ, between the droplet and the surface can be taken. Both sides of the droplet should be measured, and an average taken.

If the liquid and solid interact favourably, the liquid can spread, resulting in a low contact angle. If water has a low contact angle, the surface is deemed hydrophilic. This term is used for surfaces with water contact angles of less than 90°. This effect can be caused by the surface having groups which can interact favourably with the water droplet, e.g. polar groups.[40] If the surface interactions with the water droplets are unfavourable, a high contact angle is obtained, meaning the surface is hydrophobic. This tends to occur with when the sample has non-polar surface groups.

When a droplet is in contact with a roughened surface there are two scenarios which can occur, Figure 2-14. Firstly, if the droplet penetrates the surface structure, the Wenzel state is achieved,[41] but if the droplet sits on top of the surface features, trapping pockets of air in the spaces, the droplet is in the Cassie-Baxter state.[42]

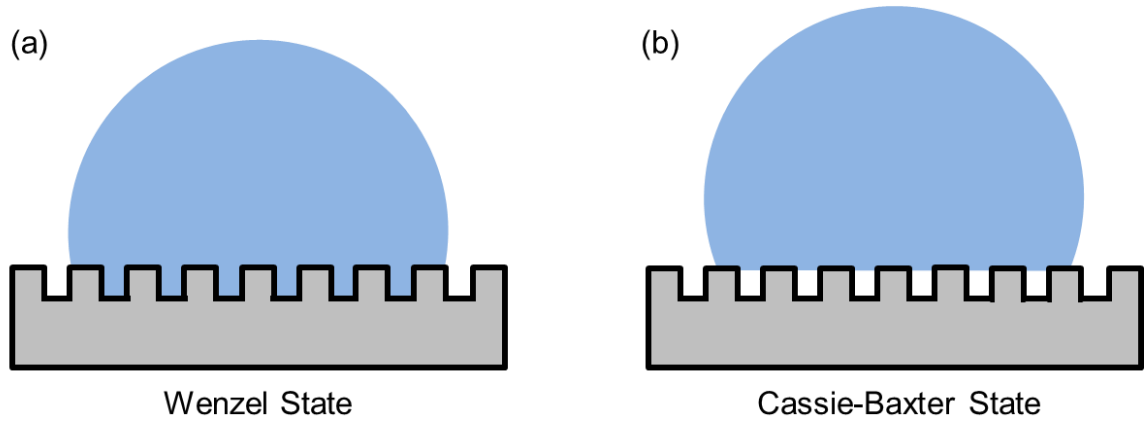

Figure 2-14: A droplet on a rough surface showing: (a) the Wenzel state; and (b) the Cassie-Baxter state.

Young's equation, Equation 2-6, can be modified to fit the Wenzel and Cassie-Baxter states, Equation 2-7 and Equation 2-8 respectively. To apply Young's equation to the Wenzel state, it can be modified to give Equation 2-7,

$$\cos\theta^* = r\,\frac{\gamma_{SV}-\gamma_{SL}}{\gamma_{LV}} \qquad \textbf{Equation 2-7}$$

where θ^* is the apparent contact angle and r is the roughness ratio (the surface area to the projected surface area). The Cassie-Baxter modification requires an additional factor, to give Equation 2-8,

$$\cos\theta^* = r_f\, f\cos\theta + f - 1 \qquad \textbf{Equation 2-8}$$

where r_f is the roughness ratio of the wet surface area, and f is the fraction of solid surface area which is wet by the liquid. As such, surface roughness increases the hydrophilicity of an already hydrophilic surface and increases the hydrophobicity of an already hydrophobic surface.

For a surface to be classed as superhydrophobic, it must have both a high contact angle and a low hysteresis. If a droplet is sitting on a tilted surface, it must overcome an energy barrier to begin moving. The contact angle of the leading edge of the droplet moving down the gradient is termed the advancing contact angle, and the trailing edge is termed the receding contact angle. The advancing and receding edges of the droplet can have different activation energies giving a difference in the contact angles.[43,44] This is known as contact angle hysteresis, Figure 2-15. The hysteresis value is the difference between the advancing (θ_a) and receding (θ_r) contact angles; if θ_a is high and θ_r is low, the contact angle hysteresis is high, and if there is only a small difference between θ_a and θ_r, the contact angle hysteresis is low.

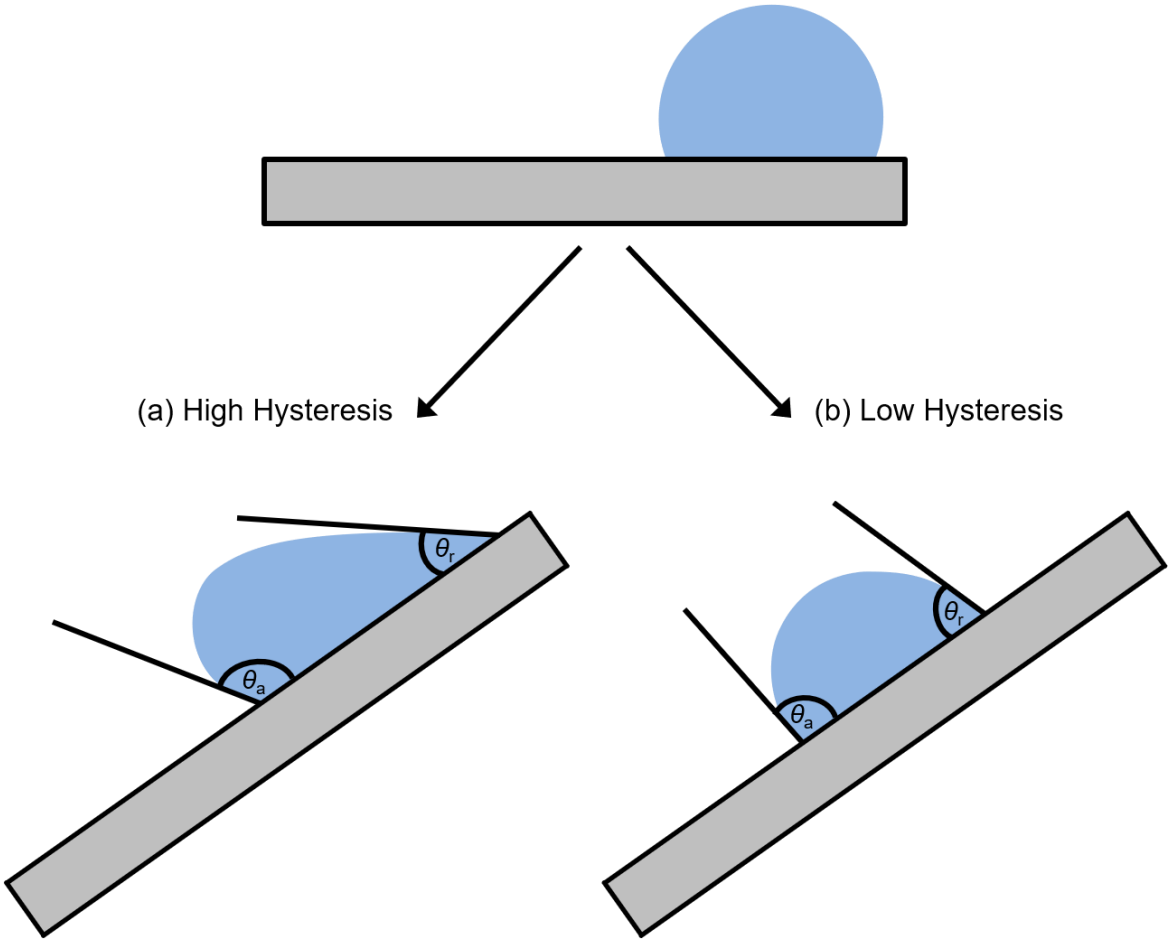

Figure 2-15: High and low hysteresis shown when the surface is tilted: (a) the surface has high hysteresis, θ_a is significantly greater than θ_r; and (b) the surface has low hysteresis there is little difference between θ_a and θ_r.

2.9. Infrared Spectroscopy

An infrared (IR) spectrum is obtained as a result of the absorption of electromagnetic radiation at specific frequencies which are associated with the vibration of bonds within a molecule. The primary requirement of absorption of IR radiation resulting in IR activity is that there must be a net change in the dipole moment of the molecule.[45] This results in absorbances at specific wavelengths, giving a specific "fingerprint" of the molecule. The vibrational modes of molecules occur at the characteristic frequencies dependent on the specific covalent bonds which are excited.[46] The wavelength of light that is absorbed is dependent of the amount of energy required to cause the bond to vibrate, which is related to the

spring constant and the reduced mass of the bond. Strong bonds and small masses of the atoms result in higher frequency absorbances.[47] The frequency of the bond vibration, the mass of the atoms, and bond strength are related by Equation 2-9,

$$\boldsymbol{\nu = \frac{1}{2\pi c}\sqrt{\frac{f}{\mu}}} \qquad \textbf{Equation 2-9}$$

where ν is the frequency, f is the force constant, and μ is the reduced mass. The reduced mass corresponds to the relationship between the masses (m_1 and m_2) of the atoms of the bond in question, Equation 2-10.[46]

$$\boldsymbol{\mu = \frac{m_1 m_2}{m_1 + m_2}} \qquad \textbf{Equation 2-10}$$

The normal modes of vibration for a molecule can be predicted by the number of atoms in said molecule. A molecule comprising *N* atoms will have 3*N* degrees of freedom. In a non-linear molecule, three of these are rotational and three are translational degrees of freedom and remaining degrees of freedom are the fundamental vibrations. In a linear molecule two are rotational and three are translational, leaving the remainder as vibrational degrees of freedom. As such, linear molecules have 3*N*-5 vibrational degrees of freedom, and non-linear molecules have 3*N*-6 vibrational degrees of freedom.[45] As per the selection rules, IR activity arises from the fundamental vibrations that result in a net change in the dipole moment. The most common types of molecular vibrations are stretching (symmetric or asymmetric) and bending of the molecule (in plane or out of plane), with wagging, rocking and scissoring subtypes.[48]

Fourier transform infrared spectroscopy (FTIR) involves the analysis of the absorbance of light. A broadband source is passed through an interferometer comprised of a series of fixed and movable mirrors. In the interferometer the light passes through a beam splitter, which sends the light in two directions at right angles. One beam goes to a stationary mirror and then returns to the beam splitter and the other goes to a moving mirror. The motion of the mirror makes the total path length variable versus that taken by the stationary mirror beam. When the two meet again at the beam splitter, they recombine, but the difference in path lengths creates constructive and destructive interference pattern known as an

interferogram. The various wavelengths of light are blocked or transmitted, due to the constructive and destructive interference of the beams between the mirrors. The movable mirror can be adjusted to tailor the transmitted wavelength. This wavelength is then passed through the sample, and the transmitted raw data results in the IR spectrum, Figure 2-16.[49] The spectrum comprises the light absorption/transmittance at each wavelength measured (typically within the 4000–200 cm^{-1} region). The intensity is generally reported in terms of percent transmittance, i.e. the amount of light that passes through the sample.

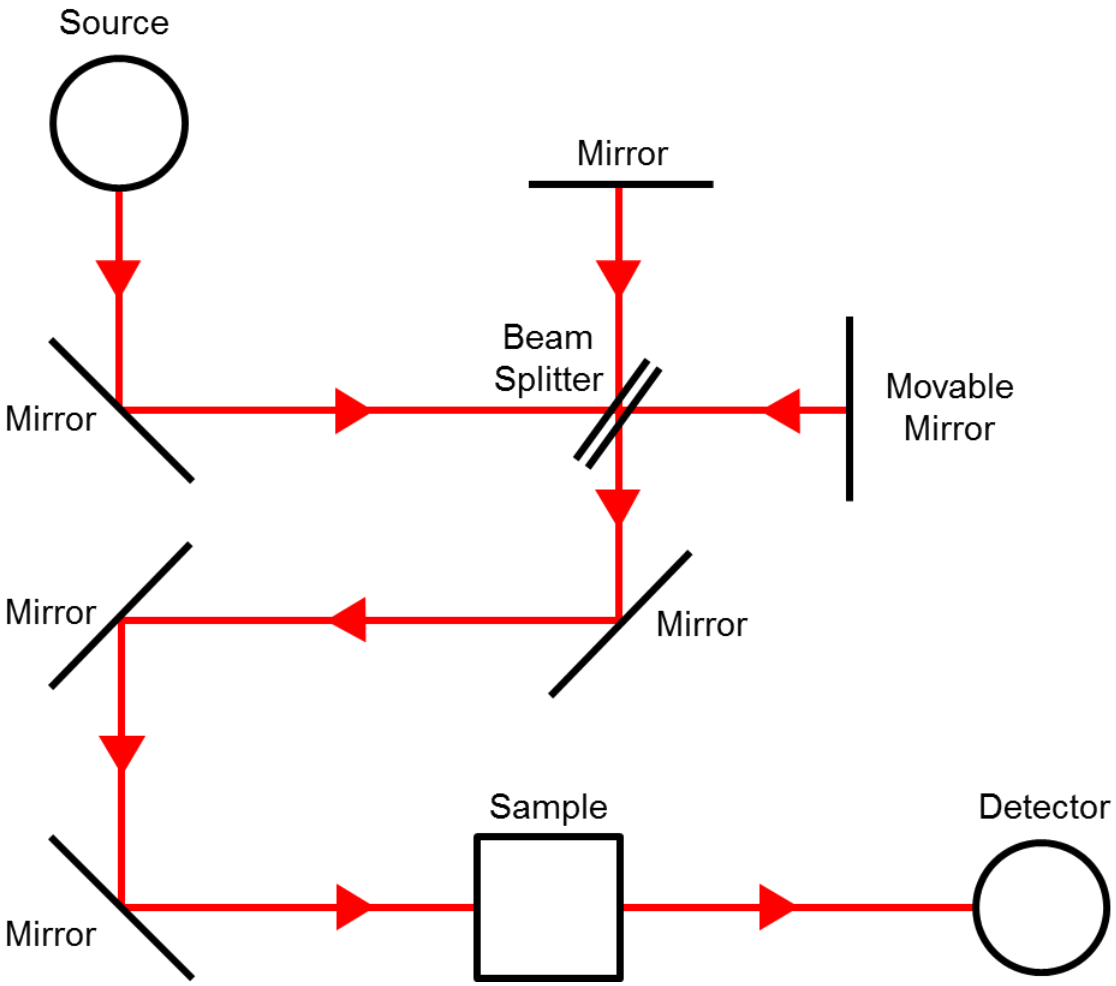

Figure 2-16: Schematic representation of the IR beam path.

The beam which reaches the detector then undergoes Fourier transformation which relates the intensity of the detected beam, $I(\delta)$, to the power at a specific wavenumber, $\bar{\upsilon}$, and is given by $B(\bar{\upsilon})$, Equation 2-11 and Equation 2-12.

$$\boldsymbol{I(\delta) = \int_0^{+\infty} B(\bar{\upsilon}) \cos(2\pi\bar{\upsilon}\delta)\, d\bar{\upsilon}} \qquad \textbf{Equation 2-11}$$

$$\boldsymbol{B}(\bar{\upsilon}) = \int_{\mathbf{0}}^{+\infty} \boldsymbol{I}(\boldsymbol{\delta}) \cos(2\boldsymbol{\pi}\bar{\upsilon}\boldsymbol{\delta})\, \boldsymbol{d\delta} \qquad \textbf{Equation 2-12}$$

Equation 2-11 gives the variation in power density as a function of the pathlength difference, resulting in an interference pattern, and Equation 2-12 shows the variation in intensity as a function of the wavenumber.[49]

Solid samples are typically analysed in one of two ways. Reflection absorption infrared spectroscopy (RAIRS), bounces the light beam off the sample, towards the detector. Very thin films can be analysed using this method, as the beam passes through the sample, exciting the bonds, resulting in the molecular vibrations generating the IR spectrum.

Attenuated total reflectance (ATR) is generally used for thick films and liquid samples. This method involves passing the beam through a diamond crystal, to undergo total internal reflection at the crystal-sample interface. When experiencing internal reflectance, an evanescent wave penetrates into the sample, exciting the bonds at their characteristic frequencies, resulting in the infrared spectrum.

There are two types of detectors which are commonly used in FTIR systems. The deuterated triglycine sulphate (DTGS) detector is a pyroelectric sensor which is a type of thermal detector. This is reliant upon pyroelectricity, which is the ability of certain materials to generate a temporary voltage when they are heated or cooled. The change in temperature modifies the positions of the atoms slightly within the crystal structure, such that the polarization of the material changes. This polarization change gives rise to a voltage across the crystal, which in turn is used to generate the spectrum. The response time and sensitivity of pyroelectric detectors is fairly low in comparison to photoconductive detectors. The mercury cadmium telluride (MCT) detector is a photovoltaic detector. The material is a semiconductor with a narrow band gap, allowing incident IR photons to cause electronic excitations, which generates the spectrum. The thermal noise of these detectors can be high, but is easily cut by cooling the detector, usually with a liquid nitrogen cold trap. Once the thermal noise is reduced, the overall sensitivity of the detector is greatly improved.

2.10. Optical Emission Spectroscopy

Optical emission spectroscopy (OES) is a common diagnostic tool in many light emitting processes, such as flames, arcs, sparks, or plasmas. OES allows identification of the chemical composition of these emission processes by analysis of the spectral lines of the emitted light.[50,51] The main advantage to using this diagnostic method for plasma identification is that it can provide information on the chemical species within the glow discharge, but is non-intrusive, and does not affect the plasma in any way.[51] The intensity of the emitted light is proportional to the quantity of each element; higher peaks suggest a higher proportion of a specific element. Whilst useful for species identification in a continuous plasma, OES is less useful when trying to observe pulsed plasmas, as the power is generally on for such a short time that there is very little emission of light.

The optical emission to be analysed can be produced by electron impact excitation, Equation 2-13, or dissociation, Equation 2-14, or by ion impact, Equation 2-15.

$$\boldsymbol{A + e^- \rightarrow A^* + e^-} \qquad \textbf{Equation 2-13}$$

$$\boldsymbol{AB + e^- \rightarrow A^* + B + e^-} \qquad \textbf{Equation 2-14}$$

$$\boldsymbol{A^+ + X \rightarrow A^*(+M)} \qquad \textbf{Equation 2-15}$$

These processes create the excited species, A*, which can emit a photon to allow it to return back to the ground state, or an excited state at a lower energy level, A**, Equation 2-16.

$$\boldsymbol{A^* \rightarrow A^{**} + hv} \qquad \textbf{Equation 2-16}$$

The transition from the first excited state, W_1, to the ground state, W_0, generally results in the most intensely emitted radiation of the plasma. These levels are quantised for each compound or element, so every transition gives a characteristic spectral line of a defined frequency, ν, and wavelength, λ, Equations 2-17 and 2-18.

$$\boldsymbol{\nu_{1,0} = \frac{W_1 - W_0}{h}} \qquad \textbf{Equation 2-17}$$

$$\lambda_{1,0} = \frac{hc}{W_1 - W_0}$$ **Equation 2-18**

where c is the speed of light.

Typically, an OES comprises a monochromator, to pick up and disperse the light from the plasma, and a photodetector to measure this light, Figure 2-17. Plasma light emissions span a very wide range of frequencies, from the infrared region to the X-ray region, whilst OES is primarily used in the 200–900 nm range, which is the most useful in terms of element identification in most common plasmas.

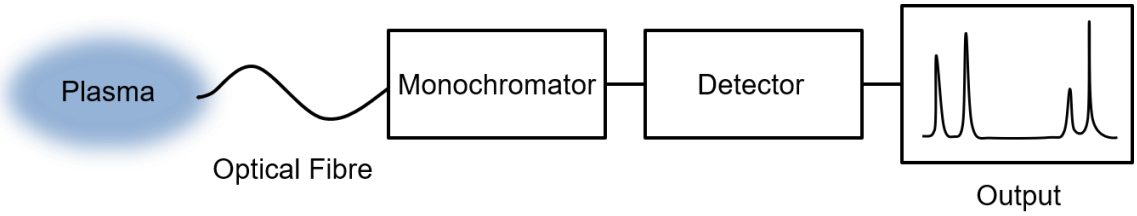

Figure 2-17: Schematic representation of the plasma-OES system**.**

2.11. Atomic Force Microscopy

Atomic force microscopy (AFM) is used to determine the surface topography and morphology of a sample. The surface of the sample is scanned with a very sharp tip attached to a cantilever. The tip responds to the topography of the sample surface, and deflects a laser beam, which is focused on the end of the cantilever. A photodiode monitors the deflection of the laser beam, and links into a feedback loop to control the sample stage Figure 2-18.[52–55] There are three main modes of operation of the AFM, which are selected based on the type of sample surface to be analysed.

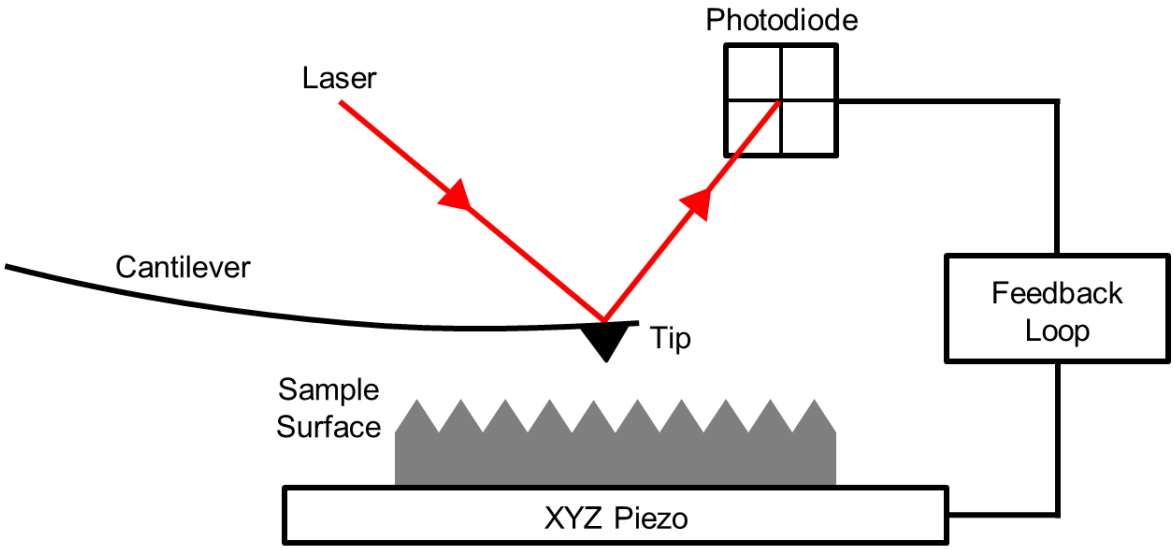

Figure 2-18: Schematic showing the AFM system.[56]

2.11.1. Contact Mode

Bringing the tip into such close proximity to the sample surface that the repulsive forces between the tip and the surface are dominant is a scanning type known as contact mode. During the scan the tip–surface height can be adjusted to maintain a constant force, by sustaining a constant laser deflection. Changes in Z height of the sample piezo are accumulated to form a topographic surface picture.[52] If the Z height is not altered in accordance with the tip–surface height there is a risk of the tip colliding with artefacts or defects on the sample surface, causing damage to the tip. However, even when the height is continually adjusted throughout the scan, soft samples can still be damaged relatively easily due to frictional forces between the tip and sample.

2.11.2. Non-Contact Mode

Oscillating the cantilever close to its resonant frequency slightly above the surface of the sample (approximately 10 nm) is known as non-contact mode. As the tip and sample surface come closer together, the long-range forces between the tip and the surface reduce the resonant frequency of the cantilever. The tip frequency

is maintained at a constant value by the feedback loop adjusting the tip–sample distance. The weak interactions which dominate this scanning method result in the images acquired often having much more noise than other scanning methods.[52] Additionally, hydrodynamic damping can occur if there is any adsorbed liquid on the sample surface. However, the fact that there is no direct contact between the tip and the surface allows soft samples to be scanned without risking damage to the surface.

2.11.3. Tapping Mode

Tapping Mode involves vibrating a tip at the end of a cantilever and bringing the tip into intermittent contact with the sample surface. When the tip interacts with a surface feature its amplitude decreases from its previous amplitude of oscillation. The AFM senses this decrease and the tip is raised away from the sample in order to re-attain the previous amplitude of oscillation. In this way the tip can be rastered across the sample to generate topographical images. Because the interaction of the tip with the sample surface is sensitive to the sample's mechanical properties such as viscoelasticity, an understanding of these qualities can also be gained through tapping mode.[57] Damping and driving forces also have an impact on the motion of the cantilever, not solely the spring tension. The damping force is proportional to the negative of the velocity. Additionally, the reactionary force of the surface must be taken into account.

Tapping mode has a number of advantages over other microscopic techniques, such as low lateral shear forces and the ability to image soft, fragile samples with no risk of damage to the surface, and for this reason tapping mode is very useful for imaging biological and polymer samples.[57,58]

2.12. Scanning Electron Microscopy

The surface morphology of a sample can also be investigated using scanning electron microscopy (SEM). SEM is used to obtain images of a surface by

scanning a sample with a beam of electrons. The secondary electron emission signal caused by the interaction of the electron beam with the sample surface is one of the most commonly used SEM measurement techniques. This interaction of the electron beam with the surface causes ionisation of the atoms within the sample, and any weakly bound electrons can then be emitted and subsequently picked up by the detectors.[59] Secondary electrons have a low energy and are generally emitted from only the first few nanometres of the surface, allowing topographical information to be gathered.[60] Thus, secondary electron detection can be accurately used to obtain a detailed picture of the surface morphology with a good resolution. The secondary electrons are attracted towards an electrically biased grid, then further accelerated towards a scintillator (a material that can fluoresce when struck by charged particles), causing cathodoluminescence. This is conducted to a photomultiplier and the amplified output is displayed as an energy distribution. The brightness of the signal is dependent on the number of secondary electrons reaching the detector.[59] The secondary electrons escape from the activated area where the beam meets the sample. When the beam is perpendicular to the sample a relatively small number of electrons can escape, but when the angle of incidence increases the interaction area also increases, resulting in more secondary electrons being emitted. As a result, edges, peaks and surface roughness appear brighter than flat surfaces, and three-dimensional image is formed.

If an electron escapes the surface with an energy of over 50 eV it is known as a backscattered electron.[59] These are typically associated with the electrons from the electron beam striking a nucleus within the sample and bouncing back towards the source. This is typically observed for 10–50% of electrons from the beam and occurs more often for elements with a higher atomic number, due to the greater positive charge on the nucleus. As such, whilst backscattered electrons can be used to obtain a topographical image of the surface, they can also provide compositional information, e.g. a backscattering yield of ~6% suggests the presence of mostly light elements, whereas a ~50% backscattering yield suggests there are more heavy elements present.[59]

SEM electron beams should ideally have a high current, small spot size, and small dispersion of energy. The beam is focussed using a magnetic field, as it

gives a smaller aberration than an electrostatic field, so a series of magnetic fields are used to alter the electron beam diameter, varying the focal length, Figure 2-19.

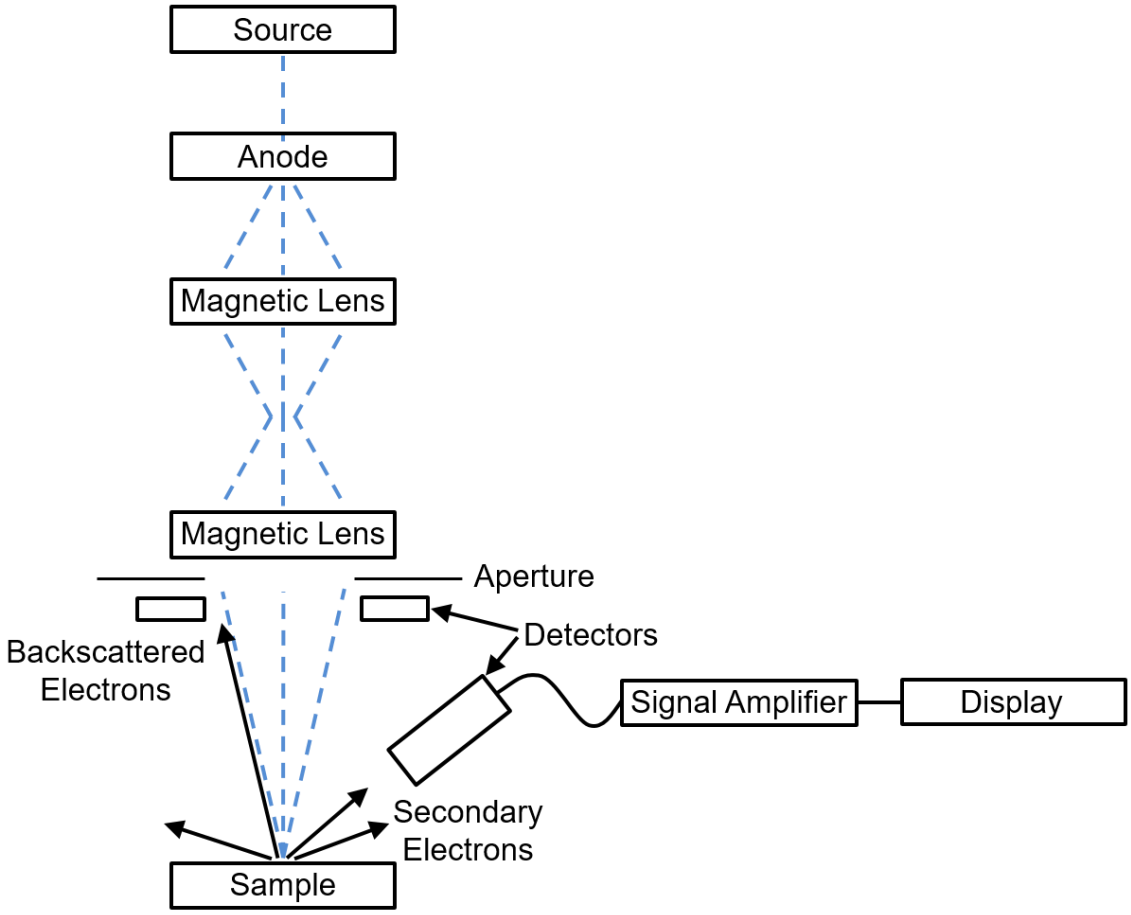

Figure 2-19: Schematic showing the SEM system.

After the electron beam passes through the anode plate of the source it begins to disperse, so a magnetic condenser lens is used to converge the beam. A second condenser lens is then used to add an extra level of regulation over the beam width. Adjustment of these two lenses allows control of the focal length of the beam, so it can be focussed accurately on the sample surface. When the beam reaches the surface, electrons are bounced back (backscattering) towards detectors positioned near the aperture, or weakly held electrons are excited and allowed to escape (secondary electrons). Secondary electron detectors utilise an electron amplifier to enhance the signal.[58] The amplifier accelerates the beam into a cathode to produce more secondary electrons. As the beam can only generate information about the specific spot it is focused upon, it must be repeatedly

scanned across the sample surface. The magnitude of the detected signal is used to build a line by line image of the surface.

2.12.1. Energy Dispersive X-Ray Spectroscopy

Energy dispersive X-ray spectroscopy (EDX or EDS) is a microanalysis technique often used alongside SEM. During the SEM process, Section 2.12, X-rays are emitted from the sample under bombardment by the incident electron beam. The X-rays are then picked up by the EDX detector, and converted to an output signal, the energy of which corresponds to a particular element. The result of this is that the elemental composition of a sample can be characterised using this technique.

The process which causes the X-ray emission is similar to that of the electron emission in SEM. When the electron beam strikes the sample, electrons are ejected. The vacancies left by these lost electrons are then filled by electrons falling from higher energy levels. The energy difference of this transition results in the emission of an X-ray, Figure 2-20.[61,62]

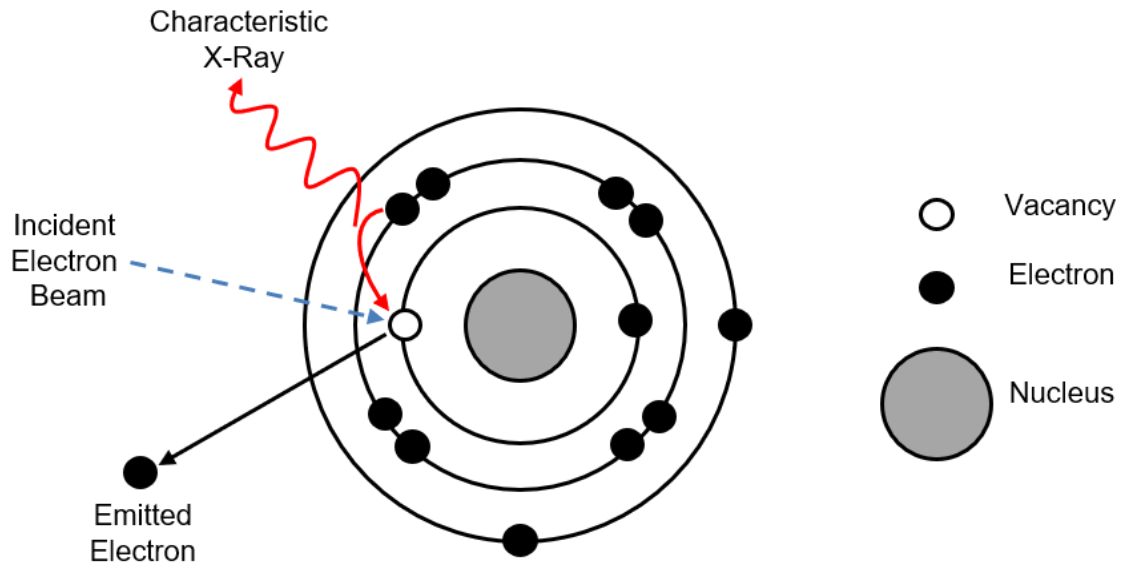

Figure 2-20: X-ray emission for EDX.

The energy of this X-ray is characteristic of the difference in energy between the two electron shells, and is unique to each specific element. The detector (typically a silicon drift or Si(Li) detector) measures the abundance of each

particular energy relative to the amount of emitted X-rays.[63] The crystal contained within the EDS detector absorbs the energy of the incident X-rays, and subsequent ionisation produces free electrons in the crystal resulting in an electrical bias. This electrical signal is then converted to a spectrum. The information gathered here can then be used determine the relative concentrations of each element in the sample, with an output showing an energy peak corresponding to a specific element. As a result, EDX can be used as both a qualitative and quantitative measurement system, giving information on both the type of element present, as well as the overall proportion of each element.

When focusing the electron beam on a sample, it can be useful to look at the surface, to gain information about the chemical composition of the topmost layer. If the sample is tilted the beam can be focused on the edge, Figure 2-21, to determine the composition of the bulk of the sample. If the sample is made up of more than one chemically distinct layer, EDX can be used to examine the interface, showing the boundary between the chemical regions, and the proportion of specific elements within each region. EDX can also be used to look for contaminants within a sample, which can give information about potential failure modes of a coating.

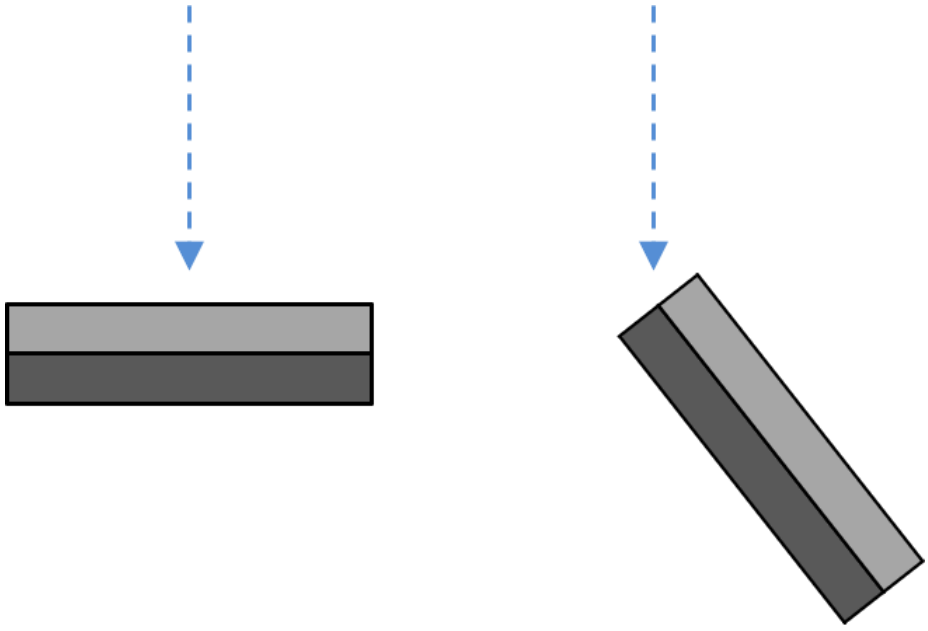

Figure 2-21: EDX sample orientation.

2.13. X-Ray Photoelectron Spectroscopy

X-ray photoelectron spectroscopy (XPS) is a surface analysis technique which is used to determine the chemical composition of a sample. X-ray irradiation is used to stimulate the photoemission of core or valence level electrons from the sample surface (approximately the top 5 nm),[64] by the photoelectric effect, Figure 2-22.[65,66] As the core electrons are relatively insensitive to the surrounding chemical environment so they can retain signature the signature binding energy of the atom. The electrons which participate in chemical bonding result in a “valence band”.

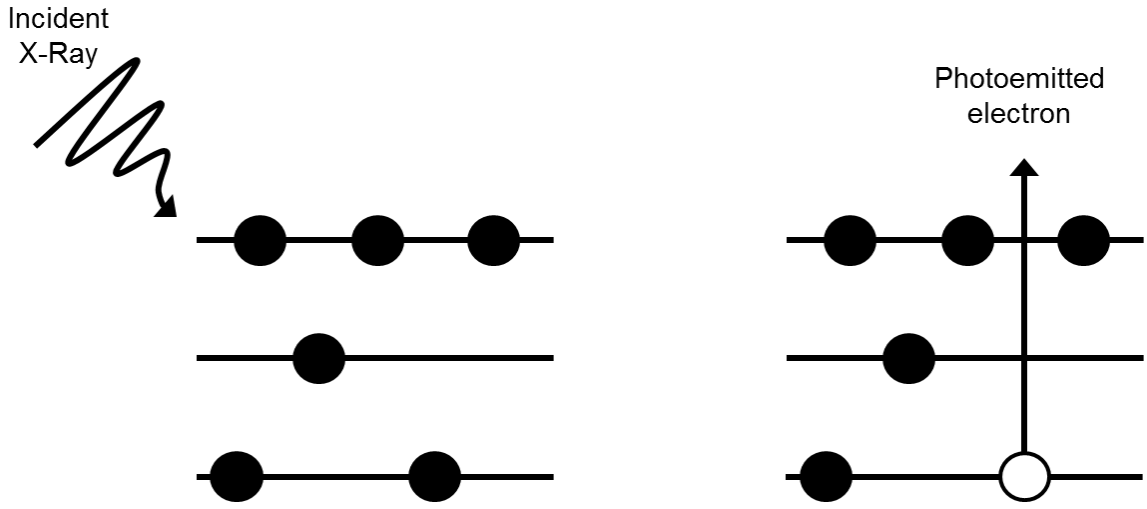

Figure 2-22: Schematic representation of XPS photoemission.

The binding energy of the emitted electron can be calculated from the measured kinetic energy, Equation 2-19,[65–67]

$$\boldsymbol{E_k = h\nu - E_b - \emptyset} \qquad \textbf{Equation 2-19}$$

where E_k is the kinetic energy of the emitted electron, E_b is the binding energy, $h\nu$ is the excitation energy, and Ø is the work function. The binding energy can be viewed as the difference in energy between the final and initial states of the atom after emission of the electron. Due to the wide variety of potential final states of the ions from each atom type, there is a broad range of kinetic energies of the emitted electrons.[66] Additionally, variances in binding energy can arise from spin-orbit splitting: core levels with an orbital angular momentum quantum numbers of greater than 1 (p, d, f orbitals) are split into doublets upon ionisation, and the higher

angular momentum states have lower binding energy, due to the higher kinetic energy.[69] For p levels the splitting ratio is 1:2, for d levels is it 2:3, and for f levels it is 3:4.[66]

The chemical environment around each core electron affects the binding energy, so individual binding energy peaks within a broad envelope can be used to identify the nature of the surrounding environment.[68] The binding energy of the emitted photoelectrons is characteristic to both the element in question and its surrounding environment, so the peaks in the XPS spectrum consist of binding envelopes which can contain multiple peaks characteristic of the different binding environments within the sample. Atoms with a higher nuclear charge have a higher binding energy of the core electrons. The binding energy of the core levels of an atom will depend on the surrounding environment and the chemical species it is bonded to. A shift in the binding energies of the core levels can result from charge transfer giving atoms partial positive or negative charge.[69] Chemical shifts in binding energies are due to differences in the polarizability and chemical potential of the compounds.[66] This is because of changes in the attraction between the core electrons and the nucleus of the atom, and is reliant on the surrounding environment. For example, atoms in higher oxidation states result in peaks at higher binding energies than the same atom in a lower oxidation state. Because of this effect, XPS can be used to identify the chemical states of various material surfaces.[66]

X-Ray photons are generated by the impaction of thermionic electrons on the electrodes, usually magnesium or aluminium (Mg Kα: 1253.6 eV and Al Kα 1486.6 eV respectively).[66] These have the energy required to eject surface electrons from a sample, yet have a limited penetrating power for samples on the order of 1–10 μm. Under ultra-high vacuum (UHV) conditions, the ejected electrons are then captured by a concentric hemispherical analyser, which allows only electrons of a particular kinetic energy to pass through to reach the detector, Figure 2-23.[66,70] The concentric hemispherical analyser consists of two electrically isolated hemispheres, with a potential difference between them. The resulting electrostatic field separates the electrons by only allowing those of a particular kinetic energy (the pass energy) through to the detector. Electrons with too low energy will strike the inner positive hemisphere and be neutralised, and electrons with too high

energy will strike the outer hemisphere and be neutralised. As such, a retard plate should be used to obtain a full spectrum: applying a negative voltage to a retard plate can slow the electrons until they have the exact “pass energy” to allow them to pass through the analyser, allowing scanning of the electron kinetic energies.[69,70] The intensity of the peaks obtained depends on multiple factors, such as the concentration of the atoms, the probability of photoemission, the inelastic mean free path of the photoemitted electron, etc.

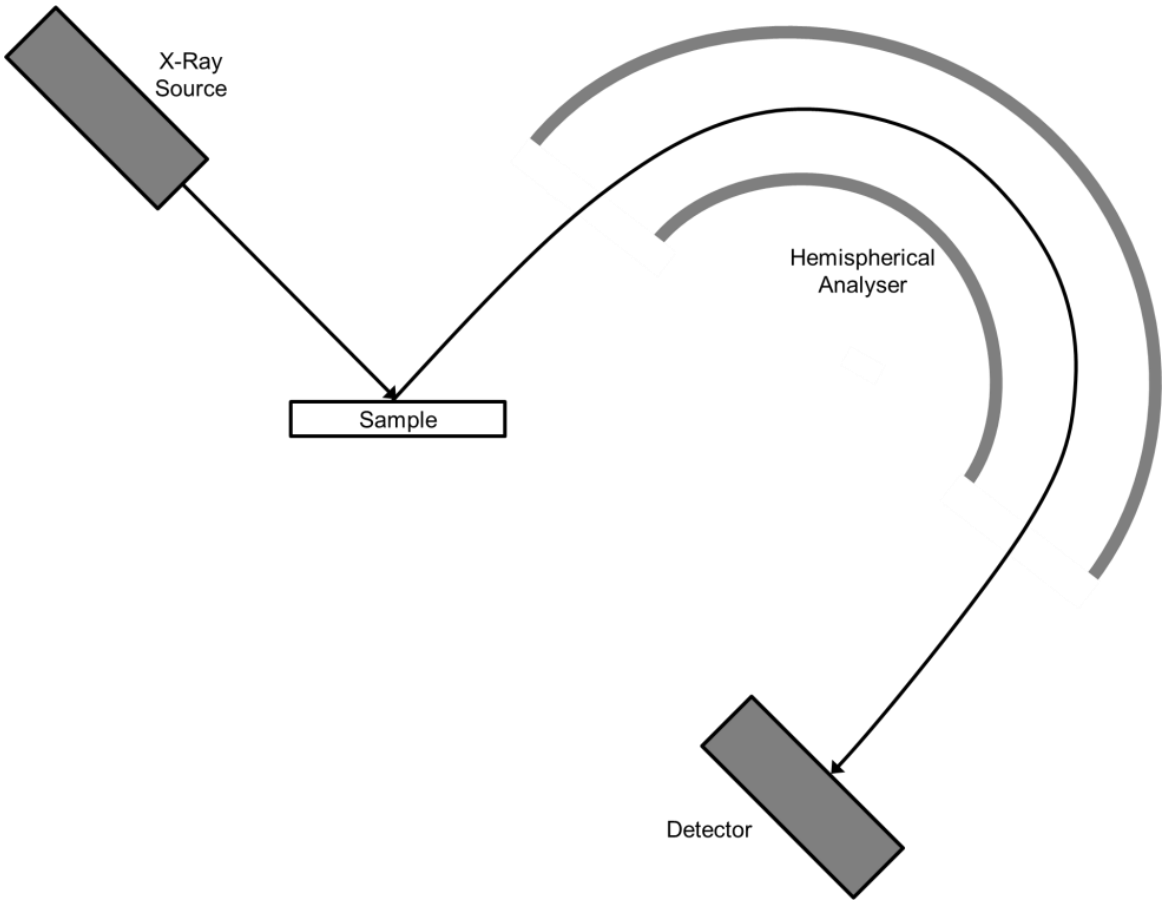

Figure 2-23: Schematic representation of XPS equipment. The incident X-Rays cause photoemission of the electrons, which are accelerated towards the hemispherical analyser. The electrons with the correct energy pass through the hemispherical analyser to reach the detector.

When running XPS without a monochromated X-Ray source, satellite peaks are found on the spectrum.[68,71] These satellite peaks occur at a displacement and intensity specific to the X-Ray anode and machine, and certain anodes, like Mg

Kα anodes, have a relatively small satellite resonance.[66] When the X-Rays interact with the sample surface, inelastic back scattering of electrons from the surface can arise. When the binding energy of the electrons is higher, more back scattering occurs, giving a higher background spectrum. This results in a stepped background on the acquired spectrum. As a range of binding energies are acquired for each sample, a variation in the signal intensity is obtained for each binding energy value. Analysis of the data requires the fitting of a curve to the data, and the area under this curve can be used to determine the proportion of each chemical environment. Consequently, an accurate measure of the chemical composition of a surface can be determined.[72] Most commonly, Gaussian or Lorentzian functions are used to fit peaks to the data curves, and the area of each peak gives the relative amount of each chemical environment present in the sample. The peak intensity is related to the cross section of the ionisation process, and this requires correction with sensitivity factors so that the peak areas can be used to obtain quantitative information about the surface composition.[66]

2.14. References

1 Goosey, T. M. *Electronics Applications of Polymers II.* Volume 10; Rapra Review Reports: Shrewsbury, 2000.

2 Hammond, S. B. Electrical Engineering. Terman, F. E.; Harman, W. W.; Heffner, H.; Truxal, J. G. Eds.; McGraw-Hill Book Company: New York, 1961, 19–22.

3 Definitions. *Handbook of Chemistry and Physics*, 63rd ed.; CRC Press: Boca Raton, 1982, F-110.

4 Hurditch, R. Plastics for Printed Wiring Substrates. In *Plastics for Electronics*; Goosey, T. M., Ed.; Elsevier: Barking, 1985, 287–289.

5 Goosey, T. M. Introduction to Plastics and Their Important Properties for Electronic Applications. In *Plastics for Electronics*; Goosey, M. T., Ed.; Elsevier: Barking, 1985, 10–12.

6 Petty, M. C. *Molecular Electronics from Principles to Practice.* Wiley: West Sussex, 2007, p 69.

7 Ohring, M. *The Materials Science of Thin Films*. Academic Press: San Diego, 1992, 451–455.

8 Greenfield, E. W. Application of Guard Electrodes in Dielectric Measurements. *Rev. Sci. Instrum.* **1942**, *13*, 489–492.

9 Gupta, V.; Diwan, A.; Evans, D.; Telford, C.; Linford, M. R. Self-Termination in the Gas-Phase Layer-by-Layer Growth of an Aza Silane and Water on Planar Silicon and Nylon Substrates. *J. Vac. Sci. Technol. B* **2014**, *32*, 061803–061812.

10 Eliezer, S.; Eliezer, Y. *The Fourth State of Matter: An Introduction to Plasma Science*, 2nd ed.; IOP Publishing: London, 2001.

11 Langmuir, I. The Interaction of Electron and Positive Ion Space Changes in Cathode Sheaths. *Phys. Rev*. **1929**, *33*, 954–989.

12 Yasuda, H. Plasma Polymerisation. Academic Press: Orlando, 1985.

13 Coulson, S. R. (2000) *Liquid Repellent Surfaces,* Durham Theses, Durham University.

14 Grill, A. Cold Plasma in Material Fabrication. IEEE Press: Piscataway, N.J., 1993.

15 Wertheimer, M. R.; Moisan, M. Processing of Electronic Materials by Microwave Plasma. *Pure Appl. Chem*. **1994**, *66*, 1343–1352.

16 Schütze, A.; Jeong, J. Y.; Babayan, S. E.; Park, J.; Selwyn, G. S.; Hicks, R. F. The Atmospheric-Pressure Plasma Jet: A Review and Comparison to Other Plasma Sources. *IEEE T. Plasma Sci*. **1998**, *26*, 1685–1694.

17 Sheu, G. S. Shyu, S. S. Surface Modification of Kevlar 149 Fibers by Gas Plasma Treatment. Part II. Improved Interfacial Adhesion to Epoxy Resin. *J. Adhes. Sci. Technol*. **1994**, *8*, 1027–1042.

18 Gerenser, L. J. X-Ray Photoemission Study of Plasma Modified Polyethylene Surfaces. *J. Adhes. Sci. Technol.* **1987**, *1,* 303–318.

19 Dynes, P. J.; Kaelble, D. H. Plasma Polymerisation on Metals. *J. Macromol. Sci. A Chem*. **1976**, *10*, 535–557.

20 Egitto, F. D.; Matienzo, L. J.; Blackwell, K. G.; Knoll, A. R. Oxygen Plasma Modification of Polyimide Webs: Effect of Ion Bombardment on Metal Adhesion. *J. Adhes. Sci. Technol.* **1994**, *8*, 411–433.

21 Coburn, J. W. Surface Processing with Partially Ionized Plasmas. *IEEE T. Plasma Sci.* **1991**, *19*, 1048–1062.

22 Hansen, R. H.; Pascale, J. V.; De Benedictis, T.; Rentzepis, P. M. Effect of Atomic Oxygen on Polymers. *J. Polym. Sci., Part A: Polym. Chem*. **1965**, *3*, 2205–2214.

23 Tobin, J. A.; Denton, D. D. Effects of Deposition Parameters on the Refractive Index in Plasma Polymerized Methyl Methacrylate Thin Films. *Appl. Phys. Lett.* **1992**, *60*, 2595–2597.

24 Mogab, C. J.; Adams, A. C.; Flamm, D. L. Plasma Etching of Si and SiO2 – The Effect of Oxygen Additions of CF_4 Plasmas. *J. Appl. Phys.* **1978**, *49*, 3796–3803.

25 Woodward, I.; Schofield, W. C. E.; Roucoules, V.; Badyal, J. P. S. Superhydrophobic Surfaces Produced by Plasma Fluorination of Polybutadiene Films. *Langmuir* **2003**, *19*, 3432–3438.

26 Christophorou, L. G.; Olthoff, J. K. Electron Interactions with CF_4, C_2F_6, and C_3F_8. *Fundamental Electron Interactions with Plasma Processing Gases*; Physics of Atoms and Molecules; Springer US: New York, 2004; pp 135–137.

27 Plumb, I. C.; Ryan, K. R. A Model of the Chemical Processes Occurring in CF_4/O_2 Discharges Used in Plasma Etching. *Plasma Chem. Plasma P.* **1986***, 6*, 205–230.

28 Manca, M.; Cortese, B.; Viola, I.; Arico, A. S.; Cingolani, R.; Gigli, G. Influence of Chemistry and Topology on Superhydrophobic CF_4-Plasma-Treated Poly(Dimethylsiloxane) (PDMS). *Langmuir* **2008**, *24*, 1833–1843.

29 D' Agostino R. Plasma Deposition, Treatment, and Etching of Polymers. Academic Press, Inc.: San Diego CA, 1990.

30 Wang, C.; Lai, P.-C.; Syu, S. H.; Leu, J. Effects of CF_4 Plasma Treatment on the Moisture Uptake, Diffusion, of Poly(Ethylene Terephthalate) Flexible Films. *Surf. Coat. Technol.* **2011**, *206*, 318–324.

31 Bradley, A.; Czuha, M.; Jr. Analytical Methods for Surface Grafts. *Anal. Chem*. **1975**, *47*, 1838–1840.

32 Ehrlich, C. D.; Basford, J. A. Recommended Practices for the Calibration and use of Leaks. *J. Vac. Sci. Technol. A* **1992**, *10*, 1–17.

33 Hynes, A. M.; Shenton, M. J.; Badyal, J. P. S. Pulsed Plasma Polymerization of Perfluorocyclohexane. *Macromolecules* **1996**, *29*, 4220–4225.

34 International Standard. Degrees of Protection Provided by Enclosures. IEC 60529; Edition 2.1, Section 14.2.7–14.2.8.

35 Gupta, V.; Diwan, A.; Evans, D.; Telford, C.; Linford, M. R. Self-Termination in the Gas-Phase Layer-by-Layer Growth of an Aza Silane and Water on Planar Silicon and Nylon Substrates. *J. Vac. Sci. Technol. B* **2014**, *32*, 061803-1–061803-9.

36 Lovering, D. NKD-6000 Technical Manual; Aquila Instruments: Cambridge, U.K., 1999.

37 Tabet, M. F.; McGahan, W. A.; Use of Artificial Neural Networks to Predict Thickness and Optical Constants of Thin Films from Reflectance Data. *Thin Solid Films* **2000**, *370*, 122–127.

38 Atkins, P. W. *Physical Chemistry*, 4th ed.; Oxford University Press: Oxford, 1990, 651–652.

39 Young, T. An Essay on the Cohesion of Fluids. *Phil. Trans. R. Soc. Lond.* **1805**, *95*, 65–87.

40 Drelich, J.; Chibowski, E.; Meng, D. D.; Terpolowski, K. Hydrophilic and Superhydrophilic Surfaces and Materials. *Soft Matter* **2011**, *7*, 9804–9828.

41 Wenzel, R. N. Resistance of Solid Surfaces to Wetting by Water. *Ind. Eng. Chem.* **1936**, *28*, 988–994.

42 Cassie, A. D. B.; Baxter, S. Wettability of Porous Surfaces. *T. Faraday Soc.* **1944**, *40*, 546–551.

43 Extrand, C. W. Model for Contact Angles and Hysteresis on Rough and Ultraphobic Surfaces. *Langmuir* **2002**, *18*, 7991–7999.

44 Extrand, C. W. Contact Angles and Hysteresis on Surfaces with Chemically Heterogeneous Islands. *Langmuir* **2003**, *19*, 3793–3796.

45 Coates, J. Interpretation of Infrared Spectra, A Practical Approach. In *Encyclopaedia of Analytical Chemistry*; Meyers, R. A. Ed.; John Wiley & Sons: Chichester, 200.

46 Clayden, J.; Greeves, N.; Warren, S.; Wothers, P. *Organic Chemistry*; Oxford University Press: Oxford, 2001; 65–68.

47 Lin-Vien, D.; Colthup, N. B.; Fateley, W. G.; Grasselli, J. G. *The Handbook of Infrared and Raman Characteristic Frequencies of Organic Molecules*, Academic Press Inc.: San Diego, 1991

48 Sherman Hsu, C.-P. Infrared Spectroscopy. *Handbook of Instrumental Techniques for Analytical Chemistry*. Ed: Settle, F. A.: Prentice Hall, Upper Saddle River, **1997.**

49 Stuart, B. H. Infrared Spectroscopy: Fundamentals and Applications. Ando, D. J. Ed.; *Analytical Techniques in the Sciences Series.* John Wiley & Sons: Chichester, 2004, 18–22.

50 Duguet, T.; Fournée, V.; Dubois, J.; Belmonte, T. Study by Optical Emission Spectroscopy of a Physical Vapour Deposition Process for the Synthesis of Complex AlCuFe(B) coatings. *Surf. Coat. Technol*. **2010**, *205*, 9–14.

51 Devia, D. M.; Rodriguez-Restrepo, L. V.; Restrepo-Parra, E. Methods Employed in Optical Emission Spectroscopy Analysis: A Review. *Ing. Cienc*. **2015**, *11*, 239–267.

52 Rugar, D.; Hansma, P. Atomic Force Microscopy. *Phys. Today* **1990**, *43*, 23–30.

53 Marti, O.; Drake, B.; Hansma, P. K. Atomic Force Microscopy of Liquid-Covered Surfaces: Atomic Resolution Images. *Appl. Phys. Lett*. **1987**, *51*, 484–486.

54 Martin, Y.; Williams, C. C.; Wickramasinghe, H. K. Atomic Force Microscope-Force Mapping and Profiling on a Sub 100-Å Scale. *J. Appl. Phys.* **1987**, *61*, 4723–4729.

55 Marti, O.; Drake, B.; Hansma, P. K. Atomic Force Microscopy of Liquid-Covered Surfaces: Atomic Resolution Images. *Appl. Phys. Lett*. **1987**, *51*, 484–486.

56 Weisenhorn, A. L.; Hansma, P. K.; Albrecht, T. R.; Quate, C. F. Forces in Atomic Force Microscopy in Air and Water. *Appl. Phys. Lett.* **1989**, *54*, 2651–2653.

57 Mate, C. M.; Lorenz, M. R.; Novotny, V. J. Atomic Force Microscopy of Polymeric Liquid Films. *J. Chem. Phys.* **1989**, *90*, 7550–7555.

58 Khulbe, K. C.; Kruczek, B.; Chowdhury, G.; Gagné, S.; Matsuura, T. Surface Morphology of Homogeneous and Asymmetric Membranes Made from Poly(phenylene oxide) by Tapping Mode Atomic Force Microscope. *J. Appl. Poly. Sci.* **1996**, *59*, 1151–1158.

59 Zhou, W.; Apkarian, R. P.; Wang, Z. L.; Joy, D. Fundamentals of Scanning Electron Microscopy. In *Scanning Microscopy for Nanotechnology*; Zhou, W.; Wang, Z. L., Eds.; Springer: New York, 2007; pp 1 – 40.

60 Seiler, H. Secondary Electron Emission in Scanning Electron Microscopy. *J. Appl. Phys.* **1983**, *54*, 1–18.

61 Shindo, D.; Oikawa, T. Energy Dispersive X-Ray Spectroscopy. In *Analytical Electron Microscopy for Materials Science*. Shindo, D.; Oikawa, T. Eds.; Springer-Verlag: Tokyo, 2002, 81–82.

62 Ngo, P. D. Energy Dispersive Spectroscopy. *In Failure Analysis of Integrated Circuits*. Wagner, L. C. Ed.; Kluwer Academic Publishers: Boston, 1999, 205–207.

63 Ii, S. Nanoscale Chemical Analysis in Various Interfaces with Energy Dispersive X-Ray Spectroscopy and Transmission Electron Microscopy. In *X-Ray Spectroscopy*. Sharma, S. K. Ed.; InTech: Rijeka, 2012, 265–268.

64 Seah, M. P.; Dench, W. A. Quantitative Electron Spectroscopy of Surfaces: A Standard Data Base for Electron Inelastic Mean Free Paths in Solids. *Surf. Interface Anal.* **1972**, *1*, 2–11.

65 Briggs, D. XPS: Basic Principles, Spectral Features and Quantitative Analysis. In *Surface Analysis by Auger and X-Ray Photoelectron Spectroscopy*. Briggs, D.; Grant, J. T. Eds.; IM Publications: Chichester, 2003, 31–56.

66 Moulder, J. F.; Stickle, W. F.; Sobol, P. E.; Bomben, K. D. *Handbook of X-ray Photoelectron Spectroscopy*; Chastain, J., Ed.; Perkin-Elmer Corporation: Eden Prairie, 1992; pp 11–28.

67 Seah, M. P.; Briggs, D. A Perspective on the Analysis of Surfaces and Interfaces. In *Practical Surface Analysis: Volume 1 – Auger and X-Ray Photoelectron Spectroscopy,* 2nd ed. Briggs, D.; Seah, M. P. Eds.; John Wiley and Sons: Chichester, 1990, 7–9.

68 Beamson, G.; Briggs, D. *High Resolution XPS of Organic Polymers – The Scienta ESCA300 Database*, John Wiley & Sons: Chichester, 1992; pp 258–259.

69 Attard, G.; Barnes, C. Surfaces. Oxford University Press: Oxford, 1998, 38–41.

70 Rivière, J. C. Instrumentation. In *Practical Surface Analysis: Volume 1 – Auger and X-Ray Photoelectron Spectroscopy,* 2nd ed. Briggs, D.; Seah, M. P. Eds.; John Wiley and Sons: Chichester, 1990, 19–83.

71 Drummond, I. W. XPS: Instrumentation and Performance. In *Surface Analysis by Auger and X-Ray Photoelectron Spectroscopy*. Briggs, D.; Grant, J. T. Eds.; IM Publications: Chichester, 2003, 122–124.

72 Tougaard, S. Quantification of Nano-structures by Electron Spectroscopy. In *Surface Analysis by Auger and X-Ray Photoelectron Spectroscopy*. Briggs, D.; Grant, J. T. Eds.; IM Publications: Chichester, 2003, 295–296.

Chapter 3 : Plasmachemical Double Click Thiol–Ene Electrical Barrier Coating

3.1. Abstract

Plasmachemical click thiol-ene chemistry is demonstrated for the reaction of thiol containing molecules with surface alkene bonds. This reaction mechanism is shown to be two-fold for allyl mercaptan, an alkene and thiol bond containing precursor, leading to self-crosslinked nanolayer deposition in tandem with interfacial crosslinking to the surface alkene bonds of a polyisoprene base layer. A synergistic multilayer structure is attained which displays high wet electrical barrier performance during immersion in water.

3.2. Introduction

The continual drive towards smaller portable electronics with greater functionality (e.g. smartphones and wearable devices) is leading to more stringent demands for device performance (e.g. operation during immersion in water or protection against accidental spillage).[1] Hence, there exists a strong demand for high electrical barrier coatings which block water ingress in order to prevent device failure through corrosion, degradation, or electrical short circuiting.[2] Polymeric layers are at the forefront of such protective coatings due to their high electrical insulation and low permeation properties.[3,4] Examples include polystyrene,[5] parylene,[6] urethane modified polybutadiene,[7] polymer composites,[8] amorphous hydrocarbon films,[9,10] plasma deposited polysilicon coatings,[11] and plasma polymers.[12] Further enhancement of electrical barrier properties can be achieved through crosslinking,[13,14] or multilayering, Section 1.3. In the case of the latter, the layering of ultra-thin films helps to block pin-hole defects.[15–18] Therefore, in

principle, a combination of crosslinking and multilayering should lead to further improvement in electrical barrier performance.[19] However, existing fabrication processes suffer from having extended time frames, involving multiple lengthy steps as well as requiring elevated temperatures.

In this thesis, the attributes of combining interfacial crosslinking with multilayering is accomplished through the utilisation of plasmachemical thiol-ene click reactions leading to high wet electrical barrier performance.[20] A structure-behaviour relationship study has shown that an alkene-thiol precursor (allyl mercaptan) undergoes the formation of a thiol-ene self-crosslinked nanolayer in tandem with interfacial crosslinking to an alkene bond containing polymer base layer (polyisoprene), Scheme 3-1.

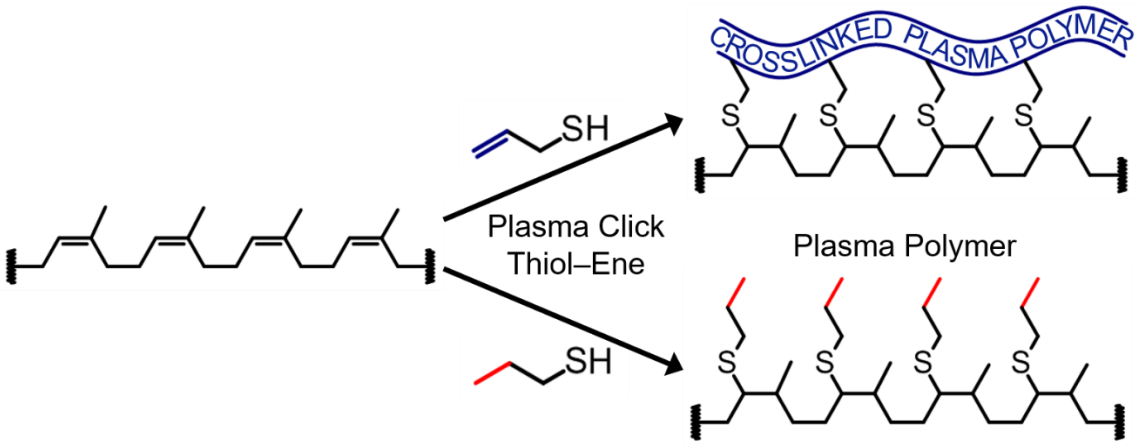

Scheme 3-1: Interfacial thiol-ene crosslinked barrier formation between polyisoprene base layer and 1-propanethiol versus allyl mercaptan plasma polymers. The latter undergoes additional thiol-ene crosslinking between adjacent precursor molecule thiol and alkene groups.[21,22]

3.3. Experimental

3.3.1. Polymer Spin Coating

Spin coating of the polymers was performed as per Section 2.4. A 5% w/v polybutadiene solution was prepared by dissolving 2.5 g polybutadiene (PBD, Mw ~200,000, Sigma-Aldrich Co.) in toluene (99.99 wt%, Fisher Scientific Ltd.) in a 50 mL volumetric flask. The solution was agitated for 3 days (sample shaker Vibrax-

VXR Model No. VX 2, IKA-Werke GmbH) to ensure the polybutadiene had completely dissolved. The polybutadiene solution was spin coated at 3000 rpm onto the prepared micro-circuit boards.

A 10% w/v polyisoprene solution was prepared by dissolving 2 g polyisoprene (PIP, Mw ~40,000, Sigma-Aldrich Co.) in toluene to make up to 20 mL total volume. The solution was agitated for 2 days to ensure the polyisoprene had completely dissolved. The polyisoprene solution was spin coated at 3000 rpm onto the prepared micro-circuit boards.

A 10% w/v polystyrene solution was prepared by dissolving 1 g polystyrene (PS, Mw ~280,000, Sigma-Aldrich Co.) in toluene in a 10 mL volumetric flask. The solution was agitated for 2 days on the sample shaker to ensure the polystyrene was completely dissolved. The polystyrene solution was spin coated onto the prepared micro-circuit boards at 2000 rpm.

3.3.2. Plasmachemical Deposition

Plasma depositions were carried out as per Section 2.3. The precursors used for plasma deposition were 1H,1H,2H,2H-perfluorooctyl acrylate (PFAC-6, +95 wt% purity, Fluorochem Ltd.), glycidyl methacrylate (GMA, +97 wt% purity, Sigma-Aldrich Co.), tetramethylsilane (TMS, +99.9 wt% purity, Alfa Aesar Co. Ltd.), 1-propanethiol (+99 wt% purity, Sigma-Aldrich Co.), and allyl mercaptan (2-propene-1-thiol, +80 wt% purity, Tokyo Chemical Industry Ltd.). Control plasma surface modification using hydrogen sulphide (+99.5% purity, Aldrich Chemical Co.) was also carried out. For each case, polymer base layer coated micro-circuit boards were placed into the centre of the plasma reactor followed by evacuation to system base pressure.

3.3.3. Film Thickness

Film thickness measurements were carried out on coated silicon wafer pieces (1 cm^2, 5–20 Ω cm^{-1} resistivity, Silicon Valley Microelectronics Inc.) using a

spectrophotometer (model nkd-6000, Aquila Instruments Ltd.). The obtained transmittance-reflectance curves (350–1000 nm wavelength range and parallel (P) polarised light source at a 30° incident angle) were fitted to a Cauchy model for dielectric materials,[23] using a modified Levenberg-Marquardt method (version 2.2 software, Pro-Optix, Aquila Instruments Ltd.).[24] The thickness values quoted herein were measured in this way, and prior to taking these coatings towards scale up and industrialisation the thicknesses should be confirmed using other methods, such as microscopy or SEM.

3.3.4. X-Ray Photoelectron Spectroscopy

X-ray photoelectron spectroscopy (XPS) analysis of the plasma deposited 1-propanethiol and allyl mercaptan layers was carried out using a VG ESCALAB II electron spectrometer equipped with a non-monochromated Mg Kα X-ray source (1253.6 eV) and a concentric hemispherical analyser. Photoemitted electrons were collected at a take-off angle of 20° from the substrate normal, with electron detection in the constant analyser energy mode (CAE, pass energy = 20 eV and 50 eV for high resolution and survey scans respectively). Instrument sensitivity (multiplication) factors were experimentally determined to be C(1s):S(2p):O(1s) equals 1.00:0.57:0.35 by using a polysulphone standard (0.005 in film, Westlake Plastics Company Inc.).[25,26] All binding energies were referenced to the C(1s) hydrocarbon peak at 285.0 eV.[25] A background was subtracted from each core level spectrum which was then fitted using fixed full width half maximum (FWHM) Gaussian peaks.[27]

3.3.5. Infrared Spectroscopy

Fourier transform infrared (FTIR) spectroscopic analysis of the 1-propanethiol and allyl mercaptan precursors was performed using a FTIR spectrometer (Spectrum Two, PerkinElmer Inc.) fitted with a transmission cell and a deuterated triglycine sulphate (DTGS) detector. Spectra were acquired across the 450–4000 cm^{-1} range and averaged over 16 scans at a resolution of 4 cm^{-1}. A droplet of precursor

was dispensed between two KBr plates and spectra taken. Reflection-absorption infrared spectroscopy (RAIRS) analysis of plasma deposited layers onto silicon wafers (Silicon Valley Microelectronics, Inc.) was carried out using a liquid nitrogen cooled mercury cadmium telluride (MCT) detector (Spectrum One, PerkinElmer Inc.) and a variable angle accessory (Specac Ltd.) fitted with mirrors aligned at an angle of 66° to the sample normal. The spectra were averaged over 285 scans at a resolution of 4 cm^{-1}.

3.3.6. Energy Dispersive X-ray Spectroscopy

Energy dispersive X-ray spectroscopy (EDX or EDS) images were acquired on a scanning electron microscope (TM3030Plus, Hitachi High-Technologies Corp.) operating in secondary electron detection mode at an accelerating voltage of 15 kV. The microscope was equipped with an energy dispersive X-ray spectrometer (TM3030 series, Hitachi High-Technologies Corp.), to obtain EDX images for element identification, using the associated software (Quantax 70, Bruker Corp.).

3.4. Results and Discussion

3.4.1. Plasma Deposited Top Layer

Diffusion of aqueous ions through a barrier layer towards an underlying electronic circuit governs the overall level of device protection, and therefore electrical resistance measurements taken during water immersion are a strong indicator of a coating's wet electrical barrier performance.[28,29] A structure-behaviour relationship study screened precursors containing a range of different functional groups for plasma deposition onto a polybutadiene base layer: 1H,1H,2H,2H-perfluorooctyl acrylate, glycidyl methacrylate, tetramethylsilane, 1-propanethiol, and allyl mercaptan, Figure 3-1. A general trend was found showing an improvement in wet electrical barrier with increasing plasma polymer layer thickness; for instance, in the case of both glycidyl methacrylate and

tetramethylsilane precursors, an absence of current flow was reached for thicknesses exceeding 1.4 µm. The thinnest plasma deposited layers displaying high electrical barrier were obtained for the allyl mercaptan precursor; whilst in contrast, structurally related 1-propanethiol (which contains no carbon-carbon double bond) was found to be poor at comparable thicknesses, Figure 3-1 and Figure 3-2. It is evident that the plasma deposited allyl mercaptan layer does not follow the general trend observed for the other precursors screened (the latter show increased layer thickness leads to a gradual improvement in wet electrical barrier). Due to the resistance exceeding the detection limit of the apparatus it cannot be unequivocally stated where exactly the allyl mercaptan lies on the graph, only that at similar thicknesses the other coatings do not show the same resistance. H_2S plasma modification of polybutadiene was employed as a control to verify that surface sulphonation alone is insufficient to attain good wet electrical barrier performance. The high wet electrical barrier measured for allyl mercaptan plasma polymer coating exceeds the performance found for existing coatings, such as 1H,1H,2H,2H-perfluorooctyl acrylate plasma polymer, Figure 3-1.[30]

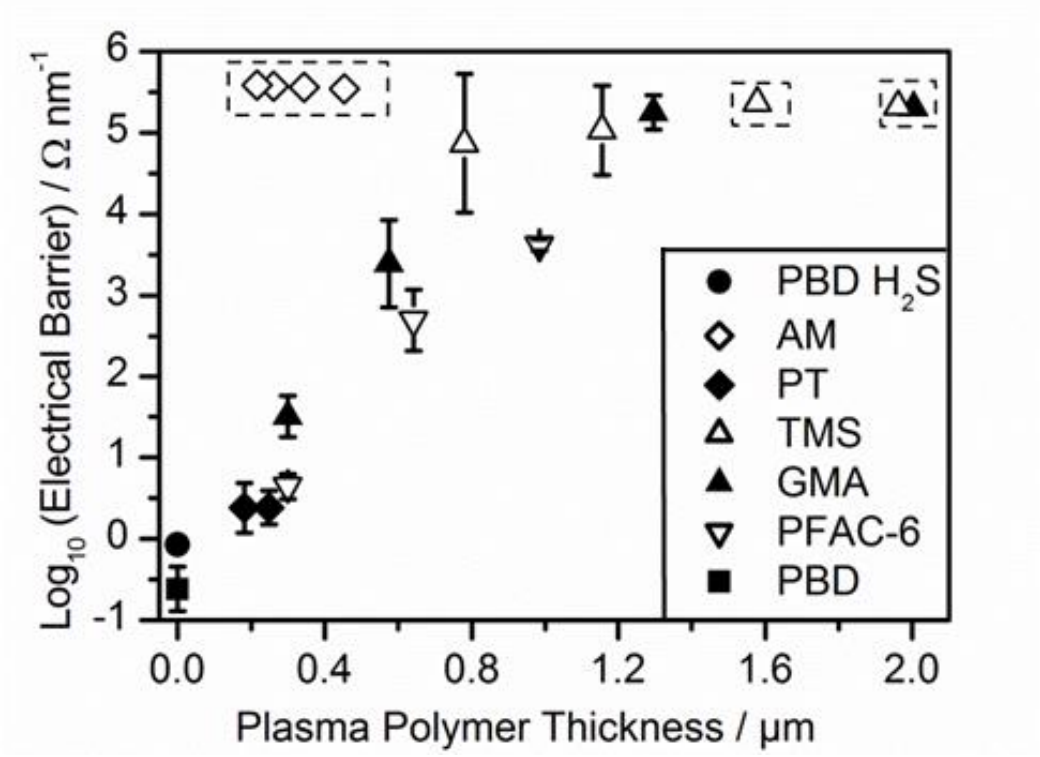

Figure 3-1: Wet electrical barrier after 13 min immersion in water under an applied electric field of 10 V mm^{-1}, for a range of plasma polymers deposited onto spin coated polybutadiene base layer (thickness 1870 ± 40 nm): 1H,1H,2H,2H-perfluorooctyl acrylate (PFAC-6, pulsed duty cycle t_{on} = 20 µs, t_{off} = 20 ms, and P_{on} = 40 W, 0.2 mbar); glycidyl methacrylate (GMA, continuous wave 5 W, 0.2 mbar); tetramethylsilane (TMS, continuous wave 3 W, 0.2 mbar); 1-propanethiol (PT, continuous wave 2 W, 0.2 mbar); and allyl mercaptan (AM, continuous wave 2 W, 0.2 mbar) precursors. Polybutadiene base layer (PBD) and following H_2S plasma exposure (PBD hydrogen sulphide, continuous wave 2 W, 0.2 mbar) are included as controls. Samples marked within dashed boxes reached the instrument detection limit of 8 x 10^8 Ω.

Wet electrical barrier values for the samples which did not remain at the instrument detection limit, namely 1H,1H,2H,2H-perfluorooctyl acrylate, glycidyl methacrylate, tetramethylsilane, and 1-propanethiol, tended to show a significant increase in current flow from the beginning of water immersion (t = 0 min) until the end of the immersion test, Table 3-1. The samples plasma coated with tetramethylsilane initially showed a good electrical barrier, but degraded over the immersion time, whereas the samples coated with 1-propanethiol showed a relatively high current flow initially. The 1H,1H,2H,2H-perfluorooctyl acrylate, glycidyl methacrylate, and tetramethylsilane coated samples, when deposited at

relatively high thicknesses, degraded over time under immersion despite initially showing no current flow.

Table 3-1: Wet electrical barrier measurements under an applied electric field of 10 V mm^{-1}, for a range of plasma polymers deposited onto a spin coated polybutadiene base layer (thickness 1870 ± 40 nm): 1H,1H,2H,2H-perfluorooctyl acrylate (pulsed duty cycle t_{on} = 20 µs, t_{off} = 20 ms, and P_{on} = 40 W, 0.2 mbar); glycidyl methacrylate (continuous wave 5 W, 0.2 mbar); tetramethylsilane (continuous wave 3 W, 0.2 mbar); and 1-propanethiol (continuous wave 2 W, 0.2 mbar). *Reached the instrument detection limit of 8 x 10^8 Ω.

Precursor	**Plasma Polymer Thickness / nm**	**Log Electrical Barrier / Ω nm^{-1}**	
		t = 0 min	**t = 13 min**
1H,1H,2H,2H-perfluorooctyl acrylate	299 ± 45	2.69 ± 1.44	0.64 ± 0.16
	642 ± 71	4.54 ± 0.64	2.69 ± 0.37
	984 ± 76	*	3.62 ± 0.07
Glycidyl methacrylate	299 ± 12	2.74 ± 0.06	1.51 ± 0.26
	574 ± 2	4.69 ± 0.31	3.39 ± 0.54
	1338 ± 59	*	5.25 ± 0.21
Tetramethylsilane	780 ± 38	*	4.87 ± 0.85
	1171 ± 20	*	5.03 ± 0.55
1-Propanethiol	182 ± 11	2.72 ± 0.14	0.38 ± 0.31
	248 ± 33	2.89 ± 0.18	0.38 ± 0.21

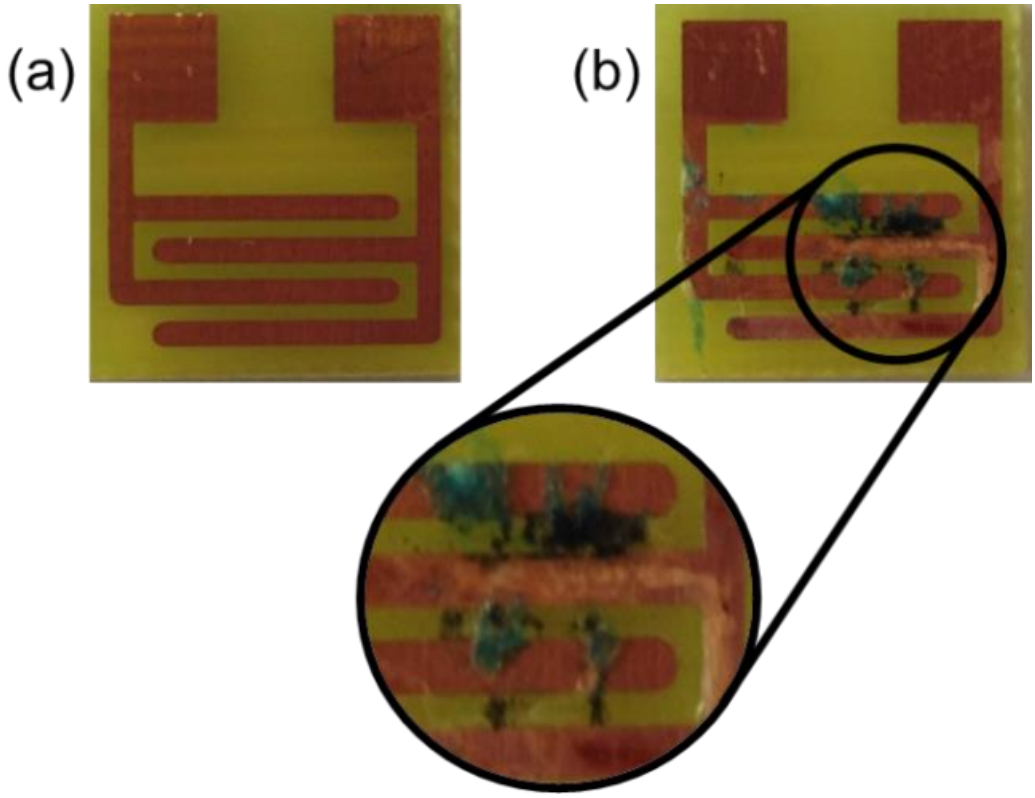

Figure 3-2: Micro-circuit board photographs taken after wet electrical barrier testing (10 V mm^{-1} electric field applied for 13 min): (a) allyl mercaptan plasma polymer on polyisoprene base layer; and (b) 1-propanethiol plasma polymer on polyisoprene base layer. The plasma polymer thickness was 555 ± 23 nm, and the polyisoprene base layer thickness was 1350 ± 40 nm. Similar results were obtained when a polybutadiene base layer was used instead of polyisoprene.

No correlation was found between wet electrical barrier and static water contact angle values, Figure 3-1 and Table 3-2. The most hydrophobic plasma deposited coating (1H,1H,2H,2H-perfluorooctyl acrylate) showed a relatively poor wet electrical barrier performance, whilst the best performing coating (allyl mercaptan) had a comparatively low water contact angle.

Table 3-2: Sessile water drop contact angle measurements of the plasma deposited precursors and the polybutadiene and H_2S plasma treated polybutadiene control samples.

Coating	Deposition Method	Water Contact Angle / °
Polybutadiene	Spin coating	105 ± 1
1H,1H,2H,2H-perfluorooctyl acrylate	Pulsed plasma	129 ± 1
Glycidyl methacrylate	Continuous wave plasma	72 ± 1
Tetramethylsilane	Continuous wave plasma	104 ± 1
1-Propanethiol	Continuous wave plasma	85 ± 1
Allyl mercaptan	Continuous wave plasma	83 ± 1
Polybutadiene / H_2S	Spin coating / continuous wave plasma	96 ± 1

For both 1-propanethiol and allyl mercaptan plasma polymers, XPS analysis detected the presence of elemental carbon, sulphur, and a small amount of oxygen, Figure 3-3 and Table 3-3. The low level of oxygen can be attributed to some aerial surface oxidation during sample transfer from the plasma deposition chamber.[31,32] The C(1s) spectra were consistent with hydrocarbon (285.0 eV) and carbon-sulphur (286.9 eV) environments, Figure 3-3.[25] No significant difference in the measured sulphur concentration was found between the 1-propanethiol and allyl mercaptan plasma polymer layers. The S($2p_{3/2}$) and S($2p_{1/2}$) component peak binding energies are consistent with C–S–C[26,26] or C–S–H (thiol) environments,[33–35] and do not correspond to oxidised sulphur (S($2p_{3/2}$) binding energy range 166–168 eV).[25,33]

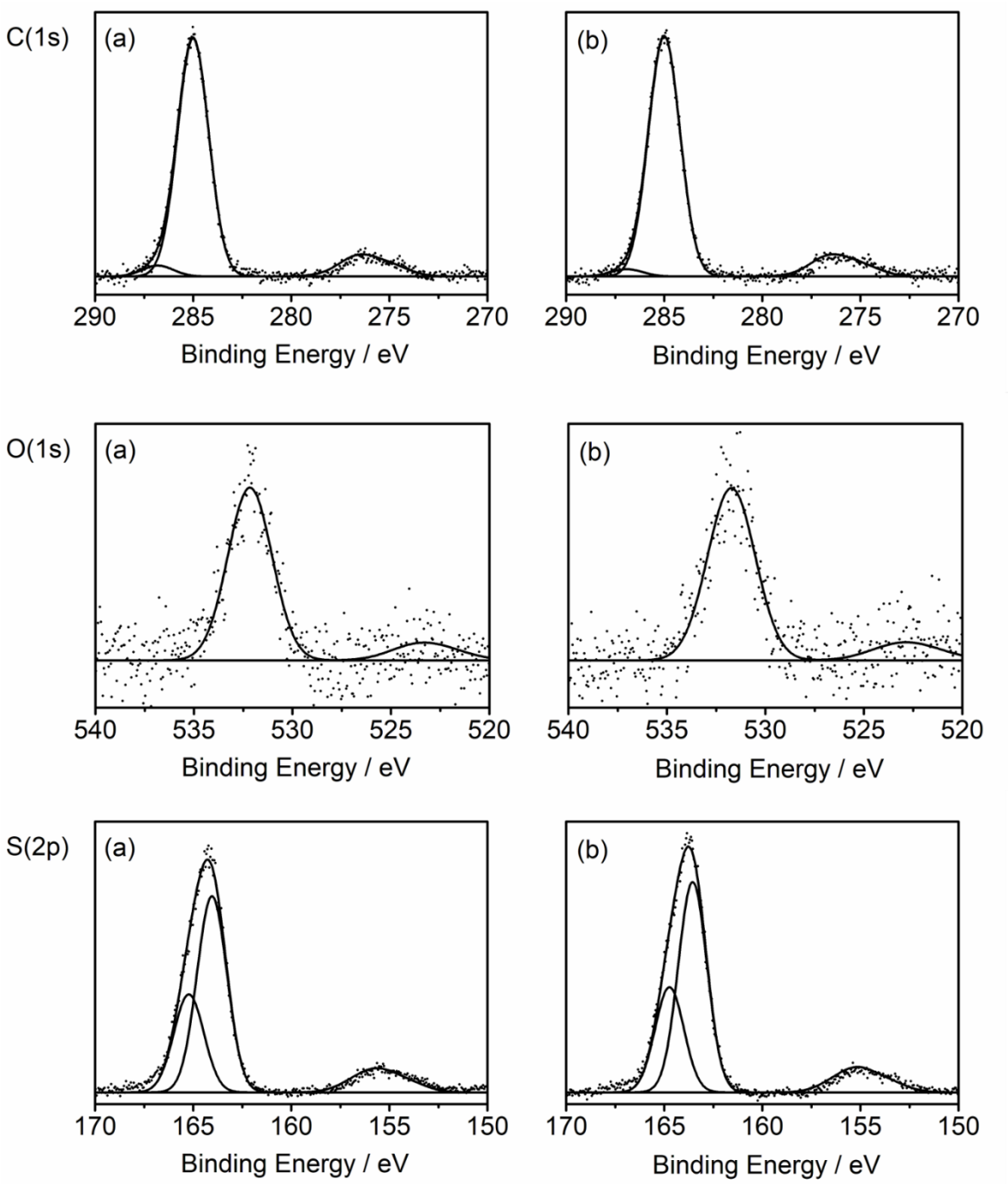

Figure 3-3: High resolution XPS spectra of continuous wave 2 W, 0.2 mbar plasma deposited layers: (a) 1-propanethiol; and (b) allyl mercaptan. The sulphur spectra are fitted to S($2p_{3/2}$) and S($2p_{1/2}$) components (separation 1.18 eV, and 2:1 relative peak area ratio). The background has been subtracted from these spectra for clarity.

Table 3-3: Elemental XPS compositions for 1-propanethiol and allyl mercaptan plasma polymer layers (continuous wave 2 W, 0.2 mbar).

Sample	C(1s)		S(2p)			O(1s)	
	%	Main Peak / eV	%	$S(2p_{3/2})$ Peak / eV	$S(2p_{1/2})$ Peak / eV	%	Peak Max. / eV
1-Propanethiol Theoretical	75	-	25	-	-	0	-
1-Propanethiol Plasma Polymer	65 ± 1	285.0	32 ± 2	164.0	165.2	3 ± 2	532.2
Allyl Mercaptan Theoretical	75	-	25	-	-	0	-
Allyl Mercaptan Plasma Polymer	62 ± 1	285.0	35 ± 3	163.6	164.8	3 ± 2	531.7

The infrared spectrum of allyl mercaptan precursor displayed a strong allyl CH_2 stretch absorbance (3080 cm^{-1}),[36] which disappeared upon plasma deposition, Figure 3-4. As expected, this feature was absent for both 1-propanethiol monomer and its corresponding plasma polymer. Both 1-propanethiol and allyl mercaptan precursors showed a weak S-H stretch (2555 cm^{-1}),[36,37] which was also observed for plasma deposited allyl mercaptan; however, it was absent for plasma deposited 1-propanethiol.

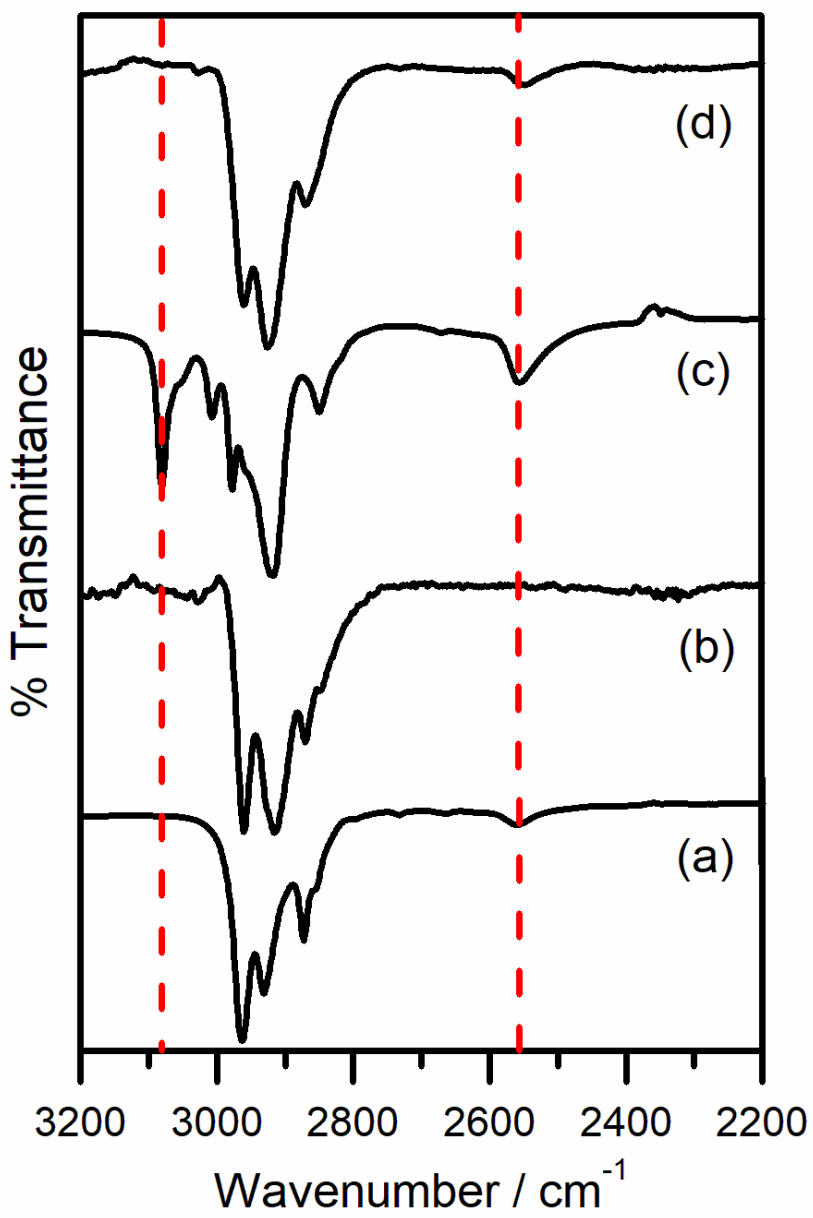

Figure 3-4: FTIR spectra of: (a) liquid 1-propanethiol; (b) continuous wave 2 W plasma, 0.2 mbar deposited 1-propanethiol; (c) liquid allyl mercaptan; and (d) continuous wave 2 W, 0.2 mbar plasma deposited allyl mercaptan. Dashed lines indicate allyl CH_2 (3080 cm^{-1}) and thiol S-H (2555 cm^{-1}) stretches respectively.

EDX measurements were taken for elemental identification of the coatings. Through this method, the presence of carbon, sulphur and copper could be clearly identified. Two layers were seen on top of the copper of the circuit board (orange): a thin carbon layer (magenta, polyisoprene) and a sulphur containing top layer (green, allyl mercaptan), circled. The lack of sulphur found in the polyisoprene layer suggests the presence of two separate layers.

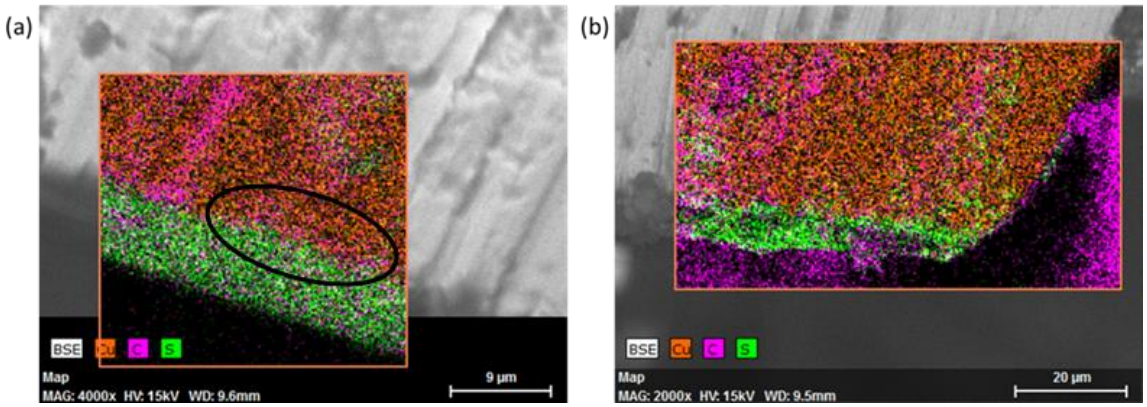

Figure 3-5: EDX images of the cross-section of the stripboard, showing the presence of carbon, sulphur and copper on: (a) the front edge of the copper track, where the layer distinction of the polyisoprene base layer and the ally mercaptan plasma polymer can be seen; and (b) the right edge of the copper track.

Several orders of magnitude improvement in wet electrical barrier performance has been found following allyl mercaptan plasma polymer deposition onto a polybutadiene base layer (> 10^5 Ω nm^{-1}), Figure 3-1. Furthermore, despite the similar chemical structures of allyl mercaptan and 1-propanethiol precursor molecules, their corresponding plasma deposited films display markedly different wet electrical barrier performances. This may be attributed to the allyl mercaptan carbon-carbon double bond playing a key role, Scheme 3.1. Two complementary sets of thiol-ene click chemistry crosslinking reactions are envisaged:[20,38,39] firstly there is the plasma deposited layer thiol groups reacting with carbon-carbon alkene bonds present within the underlying polymer base layer (e.g. polybutadiene); and secondly the allyl mercaptan thiol groups can crosslink and self-polymerise with adjacent monomer carbon-carbon double bonds during plasmachemical deposition, Scheme 3-1.[21,40] In both cases, the prerequisite thiyl radicals required for thiol-ene click chemistry are generated in-situ by the electrical discharge excited species (photons, electrons, etc.) rather than conventional thermal or photochemical initiation.[41,42] Such sulphur crosslinking improves hardness, strength, and durability of bulk polymers.[43–45] Overall, this gives rise to an allyl mercaptan plasma deposited sulphur crosslinked top layer which is also sulphur crosslinked to the polybutadiene base layer, leading to a tightly bonded interfacial region for optimal wet electrical barrier performance (synergistic effect). The assertation that the coatings were tightly bonded was supported by finding

that the coating could not be visibly scratched or removed from the substrate, even using solvents such as acetone and IPA, or scrubbing with a bottle brush and scouring pad.

In contrast, thiol-ene click chemistry occurs for 1-propanethiol through its thiol group crosslinking to the polymer base layer alkene bonds, whilst the molecule lacks the polymerisable allyl mercaptan carbon-carbon double bond needed to form a highly crosslinked top layer, hence explaining its relatively poor wet electrical barrier performance, Figure 3-1 and Scheme 3.1. Another contributing factor might be the much lower shrinkage stress for allyl sulphide versus propyl sulphide thiol-ene crosslinking.[46]

3.4.2. Polymer Base Layer

The specific role of the polymer base layer was investigated next by measuring the wet electrical barrier performance of allyl mercaptan plasma layers deposited onto polybutadiene, polyisoprene, and polystyrene, Figure 3-6. All of these polymers contain unsaturated carbon-carbon bonds, however only the former two contain alkene bonds necessary for thiol-ene reactions with plasma generated reactive sulphur species. Despite the polystyrene base layer exhibiting the highest wet electrical barrier in the absence of a plasma polymer overlayer, no significant improvement was observed following allyl mercaptan plasma polymer deposition. Whereas, in the case of polybutadiene, the electrical barrier showed a marked enhancement with increasing plasma polymer thickness. Polyisoprene was found to be the best performing polymer base layer when plasma coated with an allyl mercaptan top layer, with the wet electrical barrier rising sharply beyond 100 nm plasma polymer layer thicknesses to reach an absence of current flow above 300 nm. The role of base layer thickness was further investigated for polyisoprene whilst maintaining a fixed layer thickness of plasma deposited allyl mercaptan, Figure 3-7. This indicated a significant improvement in wet electrical barrier beyond 500 nm polyisoprene thickness, to reach high electrical barrier performance at approximately 900 nm.

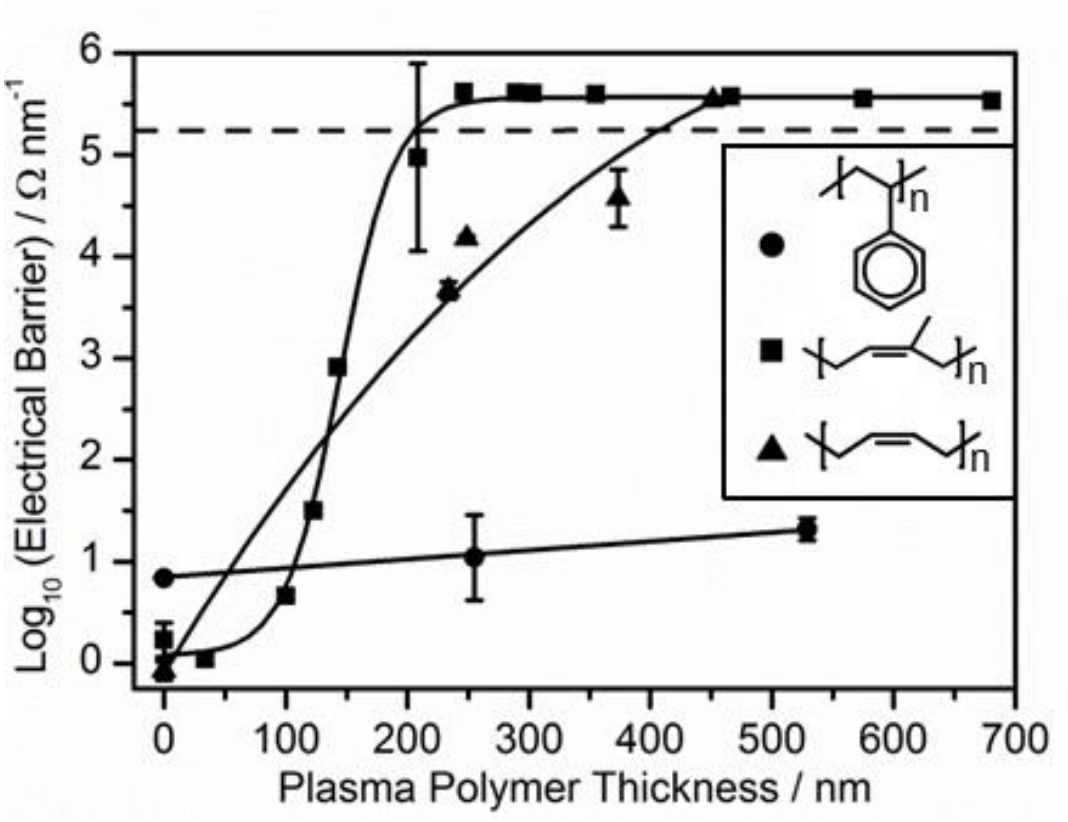

Figure 3-6: Wet electrical barrier after 13 min immersion in water under an applied electric field of 10 V mm^{-1}, for variable thickness plasma deposited allyl mercaptan (continuous wave 2 W, 0.2 mbar) onto a range of fixed thickness spin coated polymer base layers: polybutadiene (▲ thickness 1870 ± 40 nm); polyisoprene (■ thickness 1680 ± 40 nm); and polystyrene (● thickness 2040 ± 200 nm). Samples above the dashed line reached the instrument detection limit of 8 x 10^8 Ω. Lines have been included as a guide to the eye.

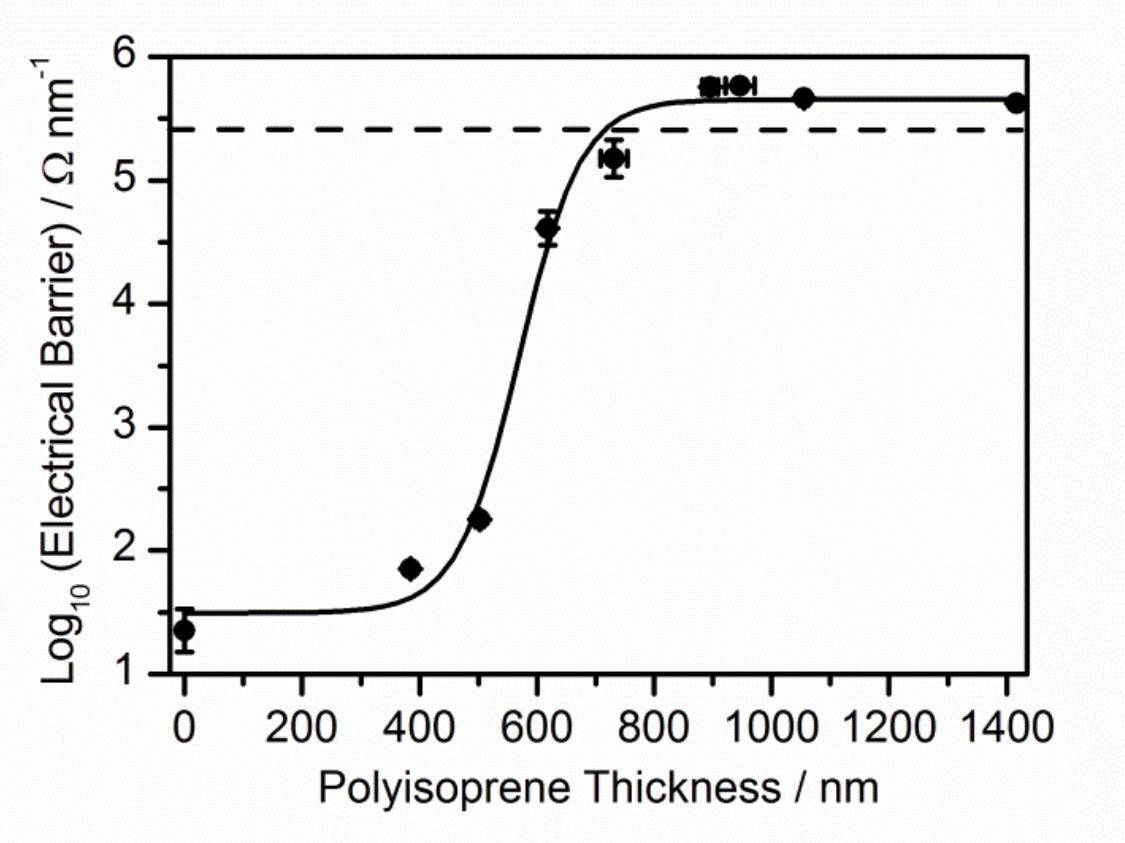

Figure 3-7: Wet electrical barrier after 13 min immersion in water under an applied electric field of 10 V mm^{-1}, for fixed thickness allyl mercaptan plasma polymer coatings (continuous wave 2 W, 0.2 mbar, 613 ± 71 nm) deposited onto varying thickness polyisoprene base layers. Samples above the dashed line reached the instrument detection limit of 8 x 10^8 Ω.

For the polymer base layers investigated, comparison of the obtained wet electrical barrier values with standard bulk polymer resistivity values shows that despite polystyrene possessing a high bulk resistivity value, (> 1 x 10^{16} Ω cm),[47] its measured wet electrical barrier value is poor, as was also observed for polyisoprene and polybutadiene, Figure 3-6. This is most likely due to the relatively high water vapour transmission rates (the mass of water moving through a specified coating area, over a predetermined length of time, normalised to the coating thickness) of polystyrene (1.60–3.37 g mm m^{-2} day^{-1}),[48] polybutadiene (17.7 g mm m^{-2} day^{-1}),[49] and vulcanised (crosslinked) polyisoprene (2.4 g mm m^{-2} day^{-1}).[50] Therefore, it can be assumed that conventional bulk electrical resistivity values measured in the absence of water cannot be taken as an indication of how well a polymer coating will perform as a wet electrical barrier.

Polybutadiene[51,52] and polyisoprene[53,54] have both been reported to undergo conventional thiol-ene click chemistry. Given that thiol-ene click reactions are reported to proceed much faster with electron rich double bonds compared to electron deficient double bonds,[20,21,55] one possible explanation for the disparity in wet electrical barrier performance between allyl mercaptan plasma polymer coated polybutadiene versus polyisoprene could be that polyisoprene should display a higher reactivity due to the electron donating methyl substituent adjacent to its carbon-carbon double bond.[56,57] The more gradual slope observed for polybutadiene compared to polyisoprene with increasing allyl mercaptan plasma polymer thickness suggests that there is a lower level of interfacial plasmachemical click thiol-ene crosslinking occurring, and therefore thicker films are necessary to achieve sufficient physical barrier for high wet electrical resistance, Figure 3-1 and Figure 3-6. The comparatively poor performance for polystyrene can be attributed to there being a total absence of alkene groups required for thiol-ene click chemistry within the polymer repeat unit.[58,59]

3.4.3. Wet Electrical Barrier Breakdown

The wet electrical barrier performance of the optimised thickness allyl mercaptan plasma polymer and polyisoprene layers was then investigated in relation to the magnitude of the applied electric field strength. This showed that the multilayer barrier was stable and resilient up to an applied electric field of 20 V mm^{-1}, beyond which there was some indication of deterioration, Figure 3-8. Even then, the drop in performance was not severe, with a final wet electrical barrier of 2 x 10^4 Ω nm^{-1} being measured at an applied field of 27.5 V mm^{-1}. Compared to modern smartphones, with cell voltages ranging from 3.70–3.85 V,[60,61] the much higher voltages (up to 20 V) utilised in the present study during wet electrical barrier measurements demonstrate an excellent level of performance.

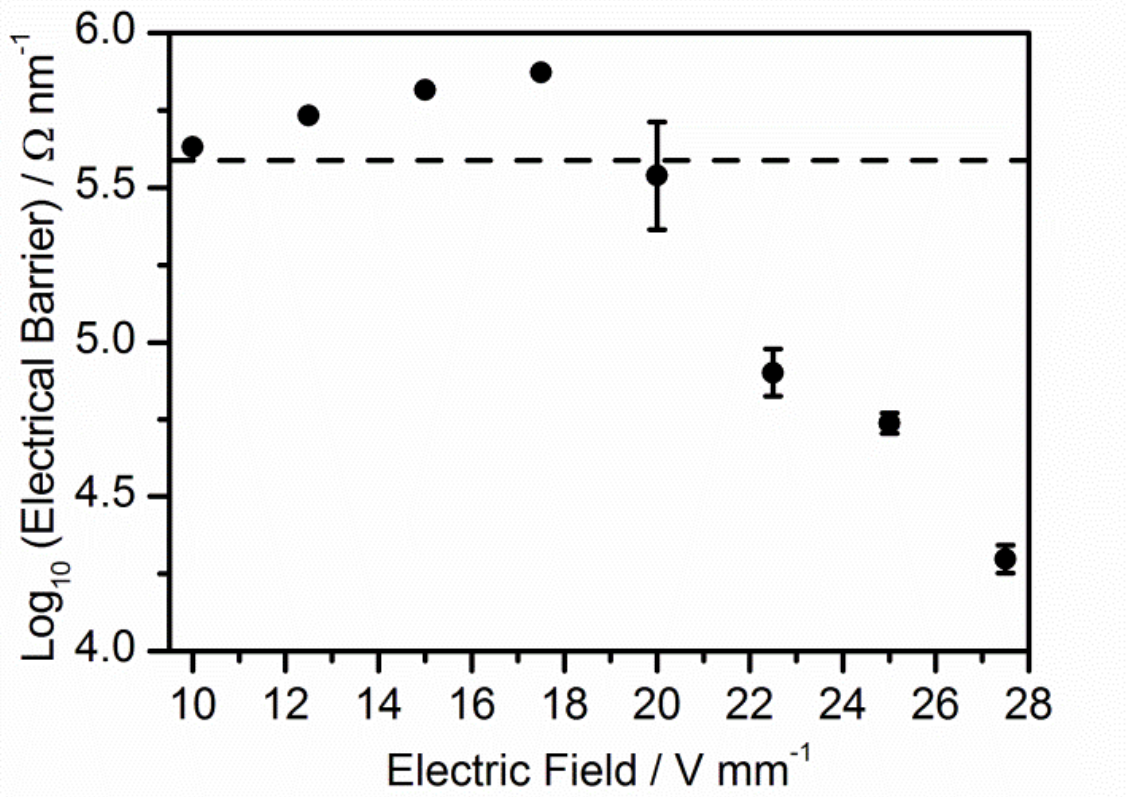

Figure 3-8: Wet electrical barrier after 13 min immersion in water as a function of applied electric field, for fixed thickness allyl mercaptan plasma polymer (continuous wave 2 W, 0.2 mbar, 507 ± 14 nm) and polyisoprene base layer (1350 ± 40 nm). Samples above the dashed line reached the instrument detection limit.

3.4.4. Scalability

The described low temperature two step fabrication method for achieving high wet electrical barrier coatings is easily scalable and suitable for high throughput electronic device assembly lines. In the case of non-planar circuit boards (e.g. wearable devices) the polyisoprene base layer can be applied by either spray or dip coating prior to conformal plasma deposition of allyl mercaptan. Future scope for the utilisation of plasmachemical click thiol-ene chemistry could include mixing of allyl thiol or multiple thiol group molecules into alkene bond containing monomer feeds for plasma deposition leading to even greater levels of crosslinking and a corresponding increase in the durability of the coating. Alkyne functionalised base layers and alkyne thiols are also potential candidates for plasmachemical thiol-ene click reactions.[62,63] Other variants include pulsed, downstream, and atmospheric

plasmas for generation of the prerequisite thiyl radicals. Additional improvements in wet electrical barrier performance are envisaged by depositing a hydrophobic layer on top of the aforementioned multilayer structure in order to incorporate enhanced liquid repellency.[64–66] Further work arising from this two-fold barrier coating mechanism would be to increase the number of layers of allyl mercaptan and polyisoprene. This would create a “sandwich-like” multilayered structure, with the benefits of the allyl mercaptan/polyisoprene interactions. This would require continued research to fully evaluate.

3.5. Conclusions

Thiol containing precursors have been found to undergo plasmachemical click thiol-ene reactions with surface alkene bonds. Structure-behaviour relationships have shown that plasmachemical deposition of allyl mercaptan onto a polyisoprene base layer provides a very high level of wet electrical barrier performance. This stems from the allyl mercaptan thiol group undergoing two-fold click thiol-ene reactions with both carbon-carbon alkene bonds contained within adjacent precursor molecules and the underlying polymer base layer, to form an overall tightly bonded multilayer for wet electrical barrier. In contrast, the structurally related 1-propanethiol precursor is significantly inferior due to its lack of any carbon-carbon alkene bonds required for click thiol–ene crosslinking within the plasma deposited layer.

3.6. References

1 Chen, T.-N.; Wuu, D.-S.; Wu, C.-C.; Horng, R.-H.; Wei, H.-F.; Jiang, L.-Y.; Lee, H.-U.; Chang, Y.-Y. Deposition and Characterization of Ultra-High Barrier Coatings for Flexible Electronic Applications. *Vacuum* **2010**, *84*, 1444–1447.

2 Hamouda, H. Cathodic Protection. In *Handbook of Environmental Degradation of Materials*; Kutz, M., Ed.; William Andrew Inc.: Norwich, 2005; pp 368–369.

3 Kao, K. C. Electrical Conduction and Breakdown in Insulating Polymers. In *Properties and Applications of Dielectric Materials*, Proceedings of the 6th International Conference, Xi'an, China, June 21–26, 2000; IEEE Dielectrics and Electrical Insulation Society: New York, 2000, 1–17.

4 Goosey, M. T. Permeability Effects in Electrical and Electronic Component Coatings. In *Polymer Permeability;* Comyn, J., Ed.; Elsevier Applied Science Publishers: Essex, 1985; pp 331.

5 Lachish, U.; Steinberger, I. T. Electrical Current Measurements on Polystyrene Films. *J. Phys. D.: Appl. Phys.* **1974**, *7*, 58–68.

6 Charlson, E. J.; Charlson, E. M.; Sharma, A. K.; Yasuda, H. K. Electrical Properties of Glow Discharge Polymers, Parylenes and Composite Films. *J. Appl. Polym. Sci.: Appl. Polym. Symp*. **1984**, *38*, 137–148.

7 Battisti, A.; Hirayama, K.; Okuno, A. Unique Polybutadiene Resin: Characteristics After Hardening and Application to IC. In *Electronic Components and Technology Conference,* Proceedings of the 40th Conference, Las Vegas, USA, May 20–23, 1990; IEEE Components Packaging and Manufacturing Technology Society: New York, 1990, 620–624.

8 Weng, C.-J.; Chen, Y.-L.; Jhuo, Y. S.; Yi-Li, L.; Yeh, J. M. Advanced Antistatic/Anticorrosion Coatings Prepared from Polystyrene Composites Incorporating Dodecylbenzene Sulphonic Acid-Doped SiO2 @Polyaniline Core-Shell Microspheres. *Polym. Int*. **2013**, *62*, 774–782.

9 Bubenzer, A.; Dischler, B.; Brandt, G.; Koidl, P. RF-Plasma Deposited Amorphous Hydrogenated Hard Carbon Thin Films: Preparation, Properties and Applications. *J. Appl. Phys.* **1983**, *54*, 4590–4595.

10 Biederman, H.; Slavínská, D. Plasma Polymer Films and Their Future Prospects. *Surf. Coat. Technol.* **2000**, *125*, 371–376.

11 Lee, J. K.; Cathey, D. A.; Tjaden, K. Method for Forming High Resistance Resistors for Limiting Cathode Current in Field Emission Displays. *Patent* WO1997004482, February 6, 1997.

12 Yasuda, H. *Plasma Polymerization.* Academic Press Inc.; Orlando: 1985, pp 395–396.

13 Pathak, S. S.; Khanna, A. S.; Sinha, T. J. M. HMMM Cured Corrosion Resistance Waterborne Ormosil Coating for Aluminum Alloy. *Prog. Org. Coat*. **2007**, *60*, 211–218.

14 Zandi-Zand, R.; Ershad-Langroudi, A.; Rahimi, A. Silica Based Organic-Inorganic Hybrid Nanocomposite Coatings for Corrosion Protection. *Prog. Org. Coat.* **2005**, *57*, 286–291.

15 Batey, J.; Boland, J. J.; Parsons, G. N. Pulsed Gas Plasma-Enhanced Chemical Vapour Deposition of Silicon. *Patent* US5242530, February 7, 1993.

16 Yoshida, S.; Okawara, C.; Ozeki, K. Process for Producing Multi-Layered Gas Barrier Film. *Patent* EP2397574, December 21, 2011.

17 Graff, G. L.; Williford, R. E.; Burrows, P. E. Mechanisms of Vapour Permeation Through Multilayer Barrier Films: Lag Time Versus Equilibrium Permeation. *J. Appl. Phys.* **2004**, *96*, 1840–1849.

18 Graff, G. L.; Gross, M. E.; Affinito, J. D.; Shi, M.-K.; Hall, M. G.; Mast, E. S. Environmental Barrier for Organic Light Emitting Device and Method of Making. *Patent WO*2000036665, June 22, 2000.

19 Yamanouchi, S.; Kondo, M.; Inoue, Y. Cross Linked Polyethylene-Insulated Cable. *Patent* EP0111393, June 20, 1984.

20 Hoyle, C. E.; Bowman, C. N. Thiol-ene Click Chemistry*. Angew. Chem. Int. Ed*. **2010**, *49*, 1540–1573.

21 Jacobine, A. F. Thiol-ene Photopolymers. In *Radiation Curing in Polymer Science and Technology*. Fouassier, J. P.; Rabek, J. F. Eds.; Elsevier Science: Essex; 1993, Vol. 3; pp 247–248.

22 Oswald, A. A.; Griesbaum, K. Radical Additions of Thiols to Diolefins and Acetylenes. In *The Chemistry of Organic Sulphur Compounds*. Kharasch, N.; Meyers, C. Y. Eds.; Pergamon Press: Oxford; 1966, Vol. 2; p 238–239.

23 Diebold, A. C.; Chism, W. W. Characterisation and Metrology of Medium Dielectric Constant Gate Dielectric Films. In *High Dielectric Constant Materials: VSLI MOSFET Applications*; Huff, H. R.; Gilmer, D. C., Eds. Springer-Verlag, Berlin Heidelberg; 2005, p 486.

24 Lovering, D. NKD-6000 Technical Manual; Aquila Instruments: Cambridge, U.K., 1999.

25 Moulder, J. F.; Stickle, W. F.; Sobol, P. E.; Bomben, K. D. *Handbook of X-ray Photoelectron Spectroscopy*; Chastain, J., Ed.; Perkin-Elmer Corporation: Eden Prairie, 1992; pp 11–28.

26 Beamson, G.; Briggs, D. *High Resolution XPS of Organic Polymers – The Scienta ESCA300 Database*, John Wiley & Sons: Chichester, 1992; pp 258–259.

27 Friedman, R. M.; Hudis, J.; Perlman, M. L. Chemical Effects on Linewidths Observed in Photoelectron Spectroscopy. *Phys. Rev. Lett*. **1972**, *29*, 692–695.

28 Taylor, S. R. Assessing the Moisture Barrier Properties of Polymeric Coatings Using Electrical and Electrochemical Methods. *IEEE Trans. Electr. Insul*. **1989**, *24*, 787–806.

29 Sangaj, N. S.; Malshe, V. C. Permeability of Polymers in Protective Organic Coatings – a Review. *Prog. Org. Coat.* **2004**, *50*, 28–39.

30 Coulson, S. Novel Products. *Patent* WO 2007/083122, July 26, 2007.

31 Donev, S.; Brack, N.; Paris, N. J.; Pigram, P. J.; Singh, N. K.; Usher, B. F. Surface Reactions of 1-Propanethiol on GaAs(100). *Langmuir* **2005**, *21*, 1866–1874.

32 Jiang, H.; Grant, J. T.; Enlow, J.; Su, W.; Bunning, T. J. Surface Oxygen in Plasma Polymerized Films. *J. Mater. Chem.* **2009**, *19*, 2234–2239.

33 Castner, D. G.; Hinds, K.; Grainger, D. W. X-ray Photoelectron Spectroscopy Sulphur 2p Study of Organic Thiol and Disulphide Binding Interactions with Gold Surfaces. *Langmuir* **1996**, *12*, 5083–5086.

34 Roh, J. H.; Lee, J. H.; Kim, N. I.; Kang, H. M.; Yoon, T. -H.; Song, K. H. DSC Analysis of Epoxy Molding Compound with Plasma Polymer-Coated Silica Fillers. *J. Appl. Polym. Sci.* **2003**, *90*, 2508–2516.

35 Nuzzo, R. G.; Zegarski, B. R.; Dubois, L. H. Fundamental Studies of the Chemisorption of Organosulphur Compounds on Au(111). Implications for Molecular Self-Assembly on Gold Surfaces. *J. Am. Chem. Soc.* **1987**, *109*, 733–740.

36 Lin-Vien, D.; Colthup, N. B.; Fateley, W. G.; Grasselli, J. G. *The Handbook of Infrared and Raman Characteristic Frequencies of Organic Molecules*, Academic Press Inc.: San Diego, 1991.

37 Schofield, W. C. E.; McGettrick, J.; Bradley, T. J.; Badyal, J. P. S.; Przyborski, S. Rewritable DNA Microarrays. *J. Am. Chem. Soc*. **2006**, *128*, 2280–2285.

38 Kade, M. J.; Burke, D. J.; Hawker, C. J. The Power of Thiol-Ene Chemistry. *J. Polym. Sci., Part A: Polym. Chem.* **2010**, *48*, 743-750.

39 Ladet, S.; Gravanga, P. Functionalized Adhesive Medical Gel. *Patent* WO2010095048, August 26, 2010.

40 Oswald, A. A.; Griesbaum, K. Radical Additions of Thiols to Diolefins and Acetylenes. In *The Chemistry of Organic Sulphur Compounds*. Kharasch, N.; Meyers, C. Y. Eds.; Pergamon Press: Oxford; 1966, Vol. 2; p 243.

41 Cole, M. A.; Jankousky, K. C.; Bowman, C. N. Redox Initiation of Bulk Thiol-Ene Polymerizations. *Polym. Chem*. **2013**, *4*, 1167–1175.

42 Nguyen, K. D. Q.; Megone, W. V.; Kong, D.; Gautrot, J. Thiol-Ene Cross-Linking and Functionalisation of Polydimethylsiloxane for Biomedical Applications *Front. Bioeng. Biotechnol*. Conference, 10th World Biomaterials Congress, Montreal, Canada, May 17–22, 2016.

43 Stringley, N. H. Highly Resilient Polybutadiene Ball. *Patent* US3241834, March 22, 1966.

44 Kato, H.; Nakatsubo, F.; Abe, K.; Yano, H. Crosslinking via Sulphur Vulcanization of Natural Rubber and Cellulose Nanofibers Incorporating Unsaturated Fatty Acids. *RSC Adv.* **2015**, *5*, 29814– 29819.

45 Hiraoka, H.; Kitaoh, K.; Maruoka, K.; Yamada, M. One-Piece Solid Golf Ball. *Patent* US4974852, December 4, 1990.

46 Kloxin, C. J.; Scott, T. F.; Bowman, C. N. Stress Relaxation via Addition-Fragmentation Chain Transfer in a Thiol-Ene Photopolymerization. *Macromolecules* **2009**, *42*, 2551–2556.

47 Matonis, V. A. Contemporary Thermoplastic Materials. In *Polymer Handbook,* 2nd ed.; Brandrup, J.; Immergut, E. H. Eds.; Wiley: New York, 1975; p VIII-6.

48 *Handbook of Modern Packaging Industries*, 2nd ed.; Asia Pacific Business Press Inc.: New Delhi, 2010; p 725–726.

49 Massey, L. K. *Permeability Properties of Plastics and Elastomers: A Guide to Packaging and Barrier materials*, 2nd ed.; Plastics Design Library, Norwich, 2003; p 456.

50 McKeen, L. W. *Permeability Properties of Plastics and Elastomers*, 3rd ed.; Elsevier Inc.: Waltham, 2012; p14.

51 Brummelhuis, N. T.; Diehl, C.; Schlaad, H. Thiol-Ene Modification of 1,2-Polybutadiene Using UV Light or Sunlight. *Macromolecules* **2008**, *41*, 9946–9947.

52 Justynska, J.; Hordyjewicz, Z.; Schlaad, H. Toward a Toolbox of Functional Block Copolymers via Free-Radical Addition of Mercaptans. *Polymer* **2005**, *46*, 12057–12064.

53 Wang, G.; Fan, X.; Huang, J. Investigation of Thiol-Ene Addition Reaction on Poly(isoprene) under UV Irradiation: Synthesis of Graft Copolymers with “V”-Shaped Side Chains. *J. Polym. Sci., Part A: Polym. Chem.* **2010**, *48*, 3797–3806.

54 Kienberger, J.; Noormofidi, N.; Mühlbacher, I.; Klarholz, I.; Harms, C.; Slugovc, C. Antimicrobial Equipment of Poly(isoprene) Applying Thiol-Ene Chemistry. *J. Polym. Sci., Part A: Polym. Chem.* **2012**, *50*, 2236–2243.

55 Hoyle, C. E.; Lee, T. Y.; Roper, T. Thiol-enes: Chemistry of the Past with Promise for the Future. *J. Polym. Sci., Part A: Polym. Chem.* **2004**, *42*, 5301–5338.

56 Clayden, J.; Greeves, N.; Warren, S.; Wothers, P. *Organic Chemistry*; Oxford University Press: Oxford, 2001; p 10561–564.

57 Roy, S.; Gupta, B. R.; De, S. K. Epoxidised Rubbers. In *Elastomer Technology Handbook*; Cheremisinoff, N. P., Ed.; CRC Press Inc.: Boca Raton, 1993; p 640.

58 Lowe, A. B. Thiol-Ene “Click” Reactions and Recent Applications in Polymer and Materials Synthesis. *Polym. Chem*. **2010**, *1*, 17–36.

59 Decker, C.; Nguyen Thi Viet, T. Photocrosslinking of Functionalized Rubbers IX. Thiol-ene Polymerization of Styrene-Butadiene-Block-Copolymers. *Polymer*, **2000**, *41*, 3905–3912.

60 Apple, Inc. iPhone 6 Technical Specifications. https://www.apple.com/iphone-6/specs/ (accessed May 17, 2016).

61 Samsung Electronics Ltd. Galaxy Note Edge Standard Battery Technical Specifications. http://www.samsung.com/us/mobile/cell-phones-accessories/EB-BN915BBUSTA (accessed May 17, 2016).

62 Nandivada, H.; Chen, H.-Y.; Bondarenko, L.; Lahann, J. Reactive Polymer Coatings that “Click”. *Angew. Chem. Int. Ed*. **2006**, *45*, 3360–3363.

63 Lowe, A. B.; Hoyle, C. E.; Bowman, C. N. Thiol-Yne Click Chemistry: A Powerful and Versatile Methodology for Materials Synthesis. *J. Mater. Chem.* **2010**, *20*, 4745–4750.

64 Coulson, S. R.; Woodward, I. S.; Badyal, J. P. S.; Brewer, S. A.; Willis, C. Ultra Low Surface Energy Plasma Polymer Films. *Chem. Mater*. **2000**, *12*, 2031–2038.

65 *Ward, L. J.; Goodwin, A. J.; Merlin, P. J.; Badyal, J. P. S. Solventless Coupling of Perfluoroalkylchlorosilanes to Atmospheric Plasma Activated Polymer Surfaces* Polymer ***2005****,* 46*, 3986–3991.*

66 Sorenson, M.; Stevens, B.; Rae, A.; Chason, M. Electronic Devices with Internal Moisture-Resistant Coatings. *Patent* US20150146396, May 25, 2015.

Chapter 4 : Bioinspired Superhydrophobic Electrical Barrier Coating

4.1. Abstract

A highly superhydrophobic coating is formed herein, able to maintain an air layer when immersed in water due to the exceedingly high contact angle and very low contact angle hysteresis. This coating is prepared by the plasma fluorination of an unsaturated polymer layer, in this case polyisoprene treated with CF_4. The extremely superhydrophobic effect is achieved by a two-fold process; the plasma treatment simultaneously fluorinates and roughens the polymer surface. When combined with a thin, plasma deposited base layer this coating can be applied as an effective wet electrical barrier system for electronics. Pulsing air into a tetramethylsilane plasma was used to deposit a base layer giving an improved wet electrical barrier coating performance compared to using other plasma deposited base layers, even at higher applied voltages. The improvement can be attributed to the lower contact angle of these layers allowing better wetting of the polymer top layer, as well as roughening of the surface to give a greater interfacial area between the layers.

4.2. Introduction

Exposure to water can result in the failure of electronic devices,[1,2] so barrier coatings which protect these devices from water damage can be very useful. Polymer coatings possessing high electrical insulation and low water permeation have been employed as barrier coatings.[3–12] Halogen-containing polymers such as poly(vinylidene fluoride), poly(chlorotrifluoroethylene), poly(vinyl chloride), poly(vinylidene chloride), poly(vinylidene fluoride), polychloroprene and poly(tetrafluoroethylene) have also been used as barrier coatings, due to their high electrical resistivities, with volume resistivities ranging from 2.0×10^{14}–1.0×10^{19} Ω cm.[13–21]

Expanding upon this, employing surface superhydrophobicity can provide protection from water permeation or ingress through the formation of a trapped air

layer between a liquid repellent roughened surface and the surrounding water.[22–31] Such air layers have been generated in the past using hydrophobic fumed silicon dioxide,[22] polytetrafluoroethylene (PTFE) and high-density polyethylene (HDPE) films,[24,26] hydrophobic functionalisation of silica,[25,28,32–35] methyltriethoxysilane meshes,[36] and fluoroalkylsilane and steel coated with electrodeposited zinc and then a silicone rubber layer.[28] Fluoroalkylsilane functionalised roughened TiO_2,[37] aerosol spray deposited silica nanoparticles,[32] $Fe(CH_3(CH_2)_{14}COO)_3$ particles on roughened steel,[27] and silica nanoparticles roughened and chemically modified dispersed in nanophase particles,[38] and finally functionalised with 1H,1H,2H,2H-perfuorodecyl triethoxysilane, have utilised the air layer effect for wet electrical barrier applications, giving electrical resistivity values up to 10^6 Ω cm^{-2} and water contact angles ranging between 150–160°. A specific bioinspired approach for wet electrical barrier coatings based upon the hierarchically structured surfaces of the *Xanthosoma Sagittifolium* plant species has been reported using electroactive epoxy resin or polyimide,[39,40] epoxy acrylate,[41] or poly(methyl methacrylate)/inorganic composites,[42,43] on leaf replica surfaces, giving trapped pockets of air between the surface and the water. These coatings gave corrosion resistance values ranging from 9.5×10^3–3.0×10^5 Ω cm^2 with a contact angle range of approximately 150–160°.[39–43] For many of the aforementioned approaches, preparation of the electrical barrier coatings can have extended process times,[38–43] require high temperatures,[37,39,40] involve acid and alkali etching steps to roughen the surface or be limited to specific substrate materials.[27,37]

Combining this degree of superhydrophobicity with a plasma deposited base layer would exploit the benefits of both the multilayering and water-repellent barrier coating types, Section 1.3. The sequential pulsing of a reactive species within a plasma reaction can be used to build up layers of a coating on a substrate, Scheme 4-1. For example, the deposition of nano-sized silicon patterns for thin film transistors can be achieved by pulsing silane gas into a carrier gas.[44–46] The selectivity afforded by this method is a highly desirable quality in the fabrication of microelectronics and thin films, but as the process is relatively complex and sensitive, it is not widely used in industry.[46]

There are several process advantages of using a standard electrical pulsed plasma deposition rather than a conventional continuous wave deposition, such as lower deposition temperatures, a greater degree of control over the plasma

dissociation, greater control of the fragmentation of the precursor to allow control of the layer structure, and greater cross-linking capabilities.[47] In the case of gas pulsing into a continually stimulated plasma there is no continuous flow of precursor gas, so a much smaller volume of precursor is consumed overall, leading to a cheaper deposition process.[48] Due to the selectivity, the highly specified reaction conditions and the easily manipulated deposition times, the thickness of a coating can be heavily controlled in these processes to obtain films of specific thicknesses, such as monolayers, and films less than 1 nm thick.[49,50] The methods of depositing layers can be modified to suit the desired purpose of the film, for example, tailoring the plasma deposition by adjusting the pressure or temperature of the deposition. When coating electronics high temperatures cannot be used, so methods which take the temperature down from 600°C are preferable, making pulsed gas processes desirable.[44,45,51]

The pulse can be manipulated to have a sufficient delay, such that undesired reactions between the reactive species of the pulses in the gas flow are minimized.[52] To avoid these undesired reactions entirely without pulsing the gas flow, it would be necessary to purge the reaction chamber of all reactants before re-introducing the desired precursor to generate the required reactive species.[52] The process of pulsing the gas flow through a plasma reaction separates the reactions associated with the excitation, deposition, surface modification or etching which occur during a standard plasma reaction.[46,53] The residence time, τ, can be found for the pulsed in gas or precursor molecules within the reaction chamber, Appendix 2.[54]

Multi-layered films can be used as extremely effective barrier layers, for the protection of electronics and perishable items,[55,56] and have been reported to achieve water transmission rates of less than 10^{-5} g m^{-2} day^{-1}.[52] Using this method, a wet electrical barrier coating could be prepared, forming a multi-layered, defect free coating.

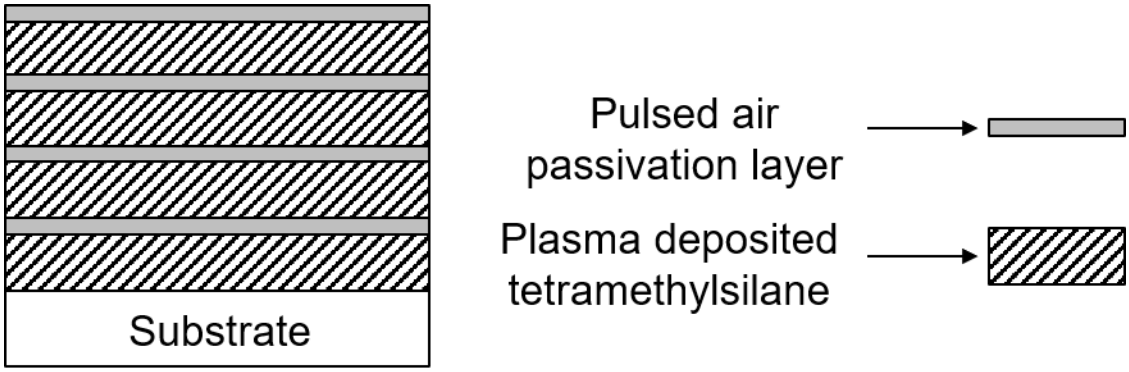

Scheme 4-1: Schematic representation of the air pulsed into the tetramethylsilane plasma, to facilitate the build-up of several layers.

Silicon based pulsed gas plasma deposited coatings are commonly used, for example in liquid crystal displays and transistor fabrication.[47] Pulsed gas plasmas can also be used to deposit solvent and gas impermeable barrier layers for use in storage containers, encapsulants and pouches by doping a pulsed silicon dioxide and boron nitride plasma with metal ions.[57] Often complementary gases are used, such as silane and hydrogen,[45,47,58] and the type of coating obtained can be tailored by altering the duty cycle, e.g. microcrystalline silicon can be obtained by lengthening the duty cycle,[59] or pulsing the hydrogen into a silane plasma, reversing the cycle.[51] Glassy SiO_2 can be deposited on a polymer base layer by pulsing tetraethoxysilane into an oxygen plasma, or other organosilicon films can be obtained by pulsing hexamethyldisiloxane into an argon plasma.[60,61] Similarly, atomic layer epitaxy can be performed this way, pulsing the vapour into a carrier gas to give alternately repeating separate surface reactions, resulting in a "sandwich-like" structure,[62] or pulsing a gas into a monomer plasma.[63] Metal oxide thin films can also be prepared using this method,[44,62,64] as well as random copolymers, e.g. polyimide/polyamide deposition.[65] Tungsten nitride deposition has been used for selective circuit board fabrication, by diborane pulsed gas injection into the chamber, followed by the injection of tungsten hexafluoride and ammonia.[66] Alternatively, a gas pulse can be used to break up liquid droplets to form liquid thin films.[67,68] The duty cycles are often long in these processes to allow the reactive species to be removed fully before the following pulse. The on time of the pulse can range from µs–s, whilst typically the off time is in the s range.[45,47,58,63]

A straightforward three-step approach is described herein comprising plasmachemical deposition of a base layer, such as allyl mercaptan or the gas pulsing of air into a tetramethylsilane plasma to form a substrate-independent, strong, adhesive nanocoating. This was followed by the application of a polyisoprene top layer, and finally plasmachemical combined surface fluorination and roughening to impart superhydrophobicity, Scheme 4-1. This yields an air layer during water immersion to result in a high wet electrical barrier performance.

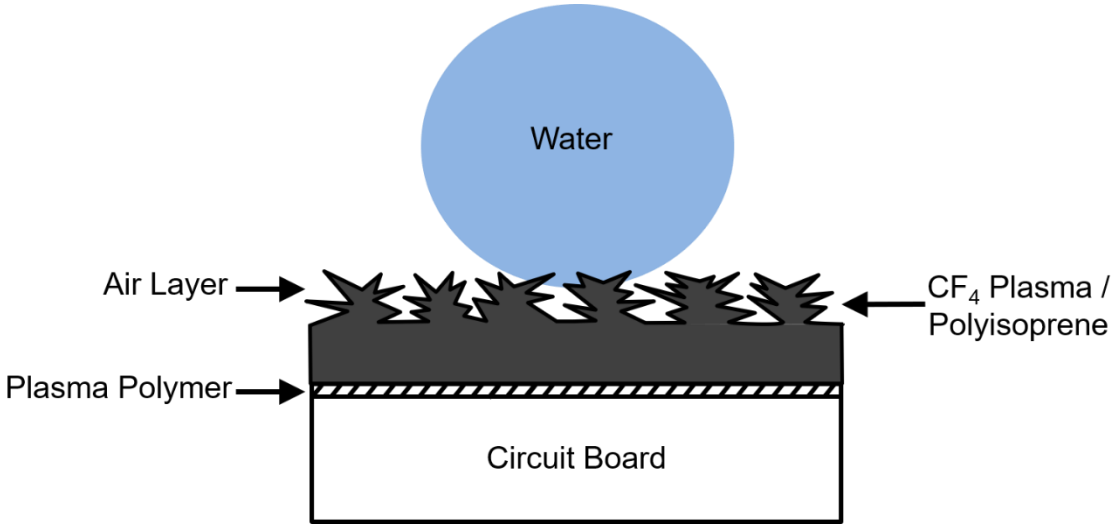

Scheme 4-2: Bioinspired wet barrier coating.

4.3. Experimental

4.3.1. Polymer Spin Coating

Spin coating was performed as per Section 2.4. For spin coating layers of varying thicknesses, 5–15% w/v polyisoprene solutions were prepared by dissolving the appropriate weights of polyisoprene (Mw ~40,000, Sigma-Aldrich Co.) in toluene (99.99 wt%, Fisher Scientific Ltd.) to make up to 20 mL total volume. The solution was agitated for two days to ensure the polyisoprene had completely dissolved. Each substrate was fixed onto a glass plate using double sided adhesive tape (product code 1445293, Henkel Ltd.), which in turn was attached to the chuck of a spincoater (model

No PRS14E, Cammax Precima Ltd.). The polymer solutions were spin coated at 2000–5000 rpm onto the prepared micro-circuit boards.

For spray coating, a 5% w/v polyisoprene solution was prepared by dissolving 5 g polyisoprene in tetrahydrofuran (>99.5 wt%, Fisher Scientific Ltd.) to make up to 100 mL total volume. The solution was agitated for two days to ensure the polyisoprene had completely dissolved. The substrate was spray coated using a manual spray gun (model RG-3L, Anest Iwata, Inc.), at a distance of 10 cm for 35 s.

4.3.2. Plasma Modification

Plasma depositions and modifications were carried out as per Section 2.5. The precursors used for plasma deposition were allyl mercaptan (2-propene-1-thiol, +80 wt% purity, Tokyo Chemical Industry Ltd.), glycidyl methacrylate (GMA, +97 wt% purity, Sigma-Aldrich Co.) and tetramethylsilane (TMS, +99.9 wt% purity, Sigma-Aldrich Co.). The precursors were degassed prior to use by 5 freeze-pump-thaw cycles. CF_4 gas (99.7% purity, Air Products and Chemicals, Inc.) was used for plasma surface modification. The substrate was placed into the centre of the reactor, followed by evacuation to system base pressure. Air pulsing into the plasma chamber was controlled by a gas pulse driver (Iota One, General Valve Corporation Ltd.) with the pulse monitored by an external oscilloscope.

4.3.3. Film Thickness

Film thickness measurements were carried out on coated silicon wafer pieces (1 cm^2, 5–20 Ω cm resistivity, Silicon Valley Microelectronics Inc.) using a spectrophotometer (model nkd-6000, Aquila Instruments Ltd.). The obtained transmittance–reflectance curves (350–1000 nm wavelength range, using a parallel (P) polarised light source at a 30° incident angle) were fitted to a Cauchy model for dielectric materials,[69] using a modified Levenberg–Marquardt method (version 2.2 software modified upgrade, Pro-Optix, Aquila Instruments Ltd.).[70] The thickness values quoted herein were measured in this way, and prior to taking these coatings towards scale up and industrialisation

the thicknesses should be confirmed using other methods, such as microscopy or SEM.

4.3.4. Optical Emission Spectroscopy

Optical emission spectroscopy (OES) was performed using an Ocean Optics SD1000 spectrometer, with the spectra gathered by 50 µm and 100 µm core fibre optic cables. The spectra were obtained over 250–800 nm and were analysed using the Ocean Optics software. A dark spectrum was taken prior to ignition of the plasma and subsequent data acquisition.

4.3.5. Contact Angle and Captive Bubble

Microlitre sessile drop contact angle analysis was carried out with a video capture system (VCA2500XE, AST Products Inc.) using 1.0 µL dispensation of ultra-high purity water (BS 3978 grade 1), hexadecane (99 wt% purity, Sigma-Aldrich Co.), tetradecane (+99 wt%, Sigma-Aldrich Co.), dodecane (99 wt% purity, Sigma-Aldrich Co.), decane (+99 wt% purity, Sigma-Aldrich Co.), octane (+99 wt% purity, Sigma-Aldrich Co.), heptane (99 wt% purity, Sigma-Aldrich Co.). After a droplet was placed onto the surface, a snapshot was taken. The resulting static image of the droplet was analysed (VCA-2500 Dynamic software) to calculate the right- and left-hand side contact angles. Advancing and receding contact angles were measured by respectively increasing and decreasing the droplet size until the contact line was observed to move.[71] A captive bubble attachment (VCA captive bubble accessory, AST Products Inc.) was used to detect the presence of an air layer between the plasma fluorinated surface and surrounding high purity water.

4.3.6. X-Ray Photoelectron Spectroscopy

X-ray photoelectron spectroscopy (XPS) analysis of the plasma deposited allyl mercaptan and 1-propanethiol samples was carried out using a VG ESCALAB II electron spectrometer equipped with a non-monochromated Mg Kα X-ray source (1253.6 eV) and a concentric hemispherical analyser. Photoemitted electrons were collected at a take-off angle of 20° from the substrate normal, with electron detection in the constant analyser energy mode (CAE, pass energy = 20 eV). The instrument sensitivity (multiplication) factors used were experimentally determined using a polysulphone standard (0.005 in film, Westlake Plastics Company Inc.) to be C(1s):F(1s):O(1s) equals 1.00:0.25:0.35. All binding energies were referenced to the C(1s) hydrocarbon peak at 285.0 eV.[72] A background was subtracted from each core level spectrum and then fitted using fixed full width half maximum (FWHM) Gaussian peaks.[72–74]

4.3.7. Infrared Spectroscopy

Fourier transform infrared (FTIR) spectroscopic analysis of the plasma polymers deposited onto silicon wafer was carried out using a FTIR Spectrometer (Spectrum One, PerkinElmer Inc.), equipped with a liquid nitrogen cooled MCT detector operating across the 450–4000 cm^{-1} range. Reflection–absorption infrared spectroscopy (RAIRS) measurements were performed using a variable angle accessory (Specac Ltd.) with the mirrors aligned at an angle of 66° to the sample normal. The spectra were averaged over 285 scans at a resolution of 4 cm^{-1}.

4.3.8. Atomic Force Microscopy

AFM images were acquired to obtain topographical information regarding the polymer and functionalised polymer surfaces (Digital Instruments Nanoscope III scanning probe microscope, Bruker Ltd.). Damage to the tip and sample surface was minimized by employing Tapping Mode AFM. Root-mean-square (RMS) roughness values were calculated over 50 µm × 50 µm scan areas.

4.3.9. Scanning Electron Microscopy

Samples were mounted onto carbon disks supported by aluminium stubs, then coated with a thin gold layer (5–10 nm, Polaron SEM Coating Unit, Quorum Technologies, Ltd.). Surface structure images were acquired on a scanning electron microscope (model Vega 3LMU, Tescan Orsay Holdings a.s.). operating in secondary electron detection mode at an accelerating voltage of 8 kV and a beam intensity of 8–12 kV. The images were then processed using Image-Pro Premier software (Media Cybernetics, Inc.).

4.4. Results

4.4.1. Wet Electrical Barrier

4.4.1.1. Polyisoprene Thickness

The role of thickness of the polyisoprene layer was investigated by maintaining a fixed plasma deposited allyl mercaptan base layer thickness, Figure 4-1. This indicated a significant improvement in electrical barrier beyond approximately 3 µm polyisoprene thickness, to achieve high electrical barrier performance at 4 µm. Crosslinking after plasma fluorination of the polyisoprene films by annealing at 150 °C for 60 min under vacuum (0.08 bar) in order to enhance hardness[84] showed no deterioration in performance of the wet electrical barrier coatings.

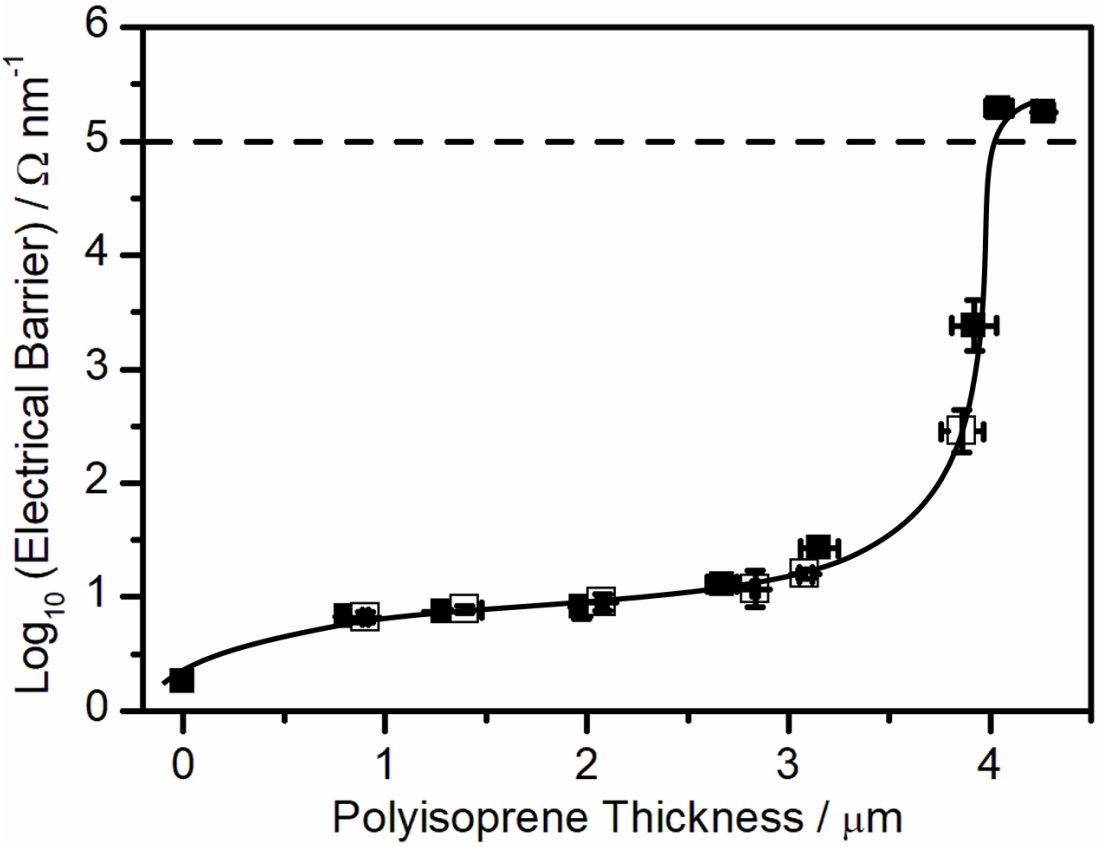

Figure 4-1: Final wet electrical barrier whilst immersed in water for 13 min under an applied electric field of 10 V mm^{-1}, for variable thickness crosslinked (□) and non-crosslinked (■) plasma fluorinated (30 W, 0.2 mbar, 5 min) polyisoprene spin coated onto a fixed thickness plasma polymer allyl mercaptan base layer (2 W, 0.2 mbar, 1 min, 138 ± 20 nm). Samples above the dashed line reached the instrument detection limit of 8 x 10^8 Ω.

4.4.1.2. Plasma Deposited Base Layer Thickness

Plasma fluorinated polyisoprene was measured under an applied electric field with and without a plasma deposited base layer, Figure 4-2. The wet electrical barrier performance of plasma fluorinated polyisoprene increased significantly with the application of a thin layer of allyl mercaptan plasma deposited onto the micro-circuit board prior to polyisoprene spin coating, with no current flow observed beyond a plasma polymer thickness of 90 nm. An increase in wet electrical barrier performance was also observed with the plasma deposition of a glycidyl methacrylate layer, although current flow was observed until a thickness of 185 nm.

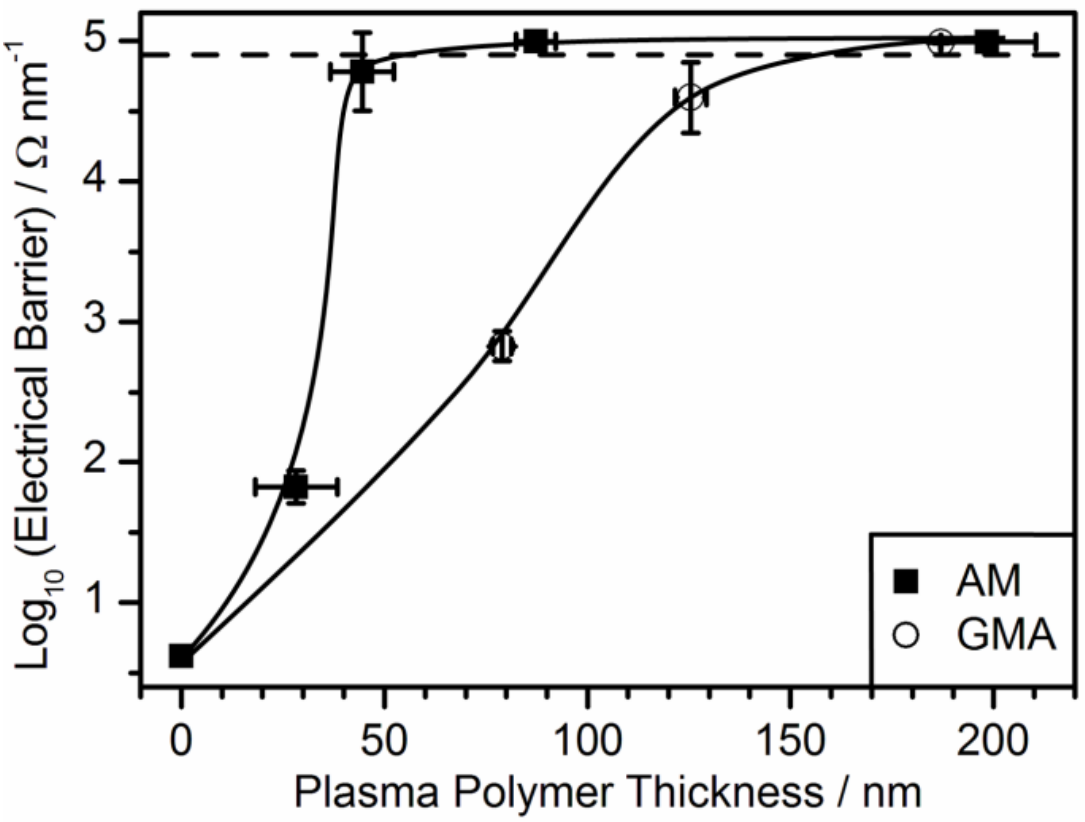

Figure 4-2: Final wet electrical barrier whilst immersed in water for 13 min under an applied electric field of 10 V mm^{-1}, for plasma fluorinated (30 W, 0.2 mbar, 5 min) polyisoprene (thickness 7930 ± 150 nm) spin coated onto variable thickness allyl mercaptan (■, 2 W, 0.2 mbar) and glycidyl methacrylate (○, 5 W, 0.2 mbar) plasma polymer base layers. Samples above the dashed line reached the instrument detection limit of 8 x 10^8 Ω. Lines have been included as a guide to the eye.

4.4.1.3. Tetramethysilane/Air Gas Pulsing Base Layer Deposition

The possibility of using air pulsed into a tetramethylsilane plasma to form a plasma deposited base layer comprised of several thin layers was investigated. Thickness measurements were taken for various duty cycles of the gas pulsing valve, Figure 4-3. The gas pulse times used were 100 µs on/10 ms off, 100 µs on/20 ms off, 50 µs on/500 ms off, and 50 µs on/5 s off. There was a clear relationship between the length of time the valve was open to air and the resultant thickness of the plasma deposited layer. The less time the valve was open, i.e. less air was allowed into the plasma chamber, the higher the thickness was of the deposited layer. This suggests that the air allowed into the chamber caused a decrease in the deposition rate of the tetramethylsilane, as

was expected. It should also be considered that there could be etching processes occurring as the air was introduced into the chamber. This was supported by the formation of a powdery deposit throughout the chamber.

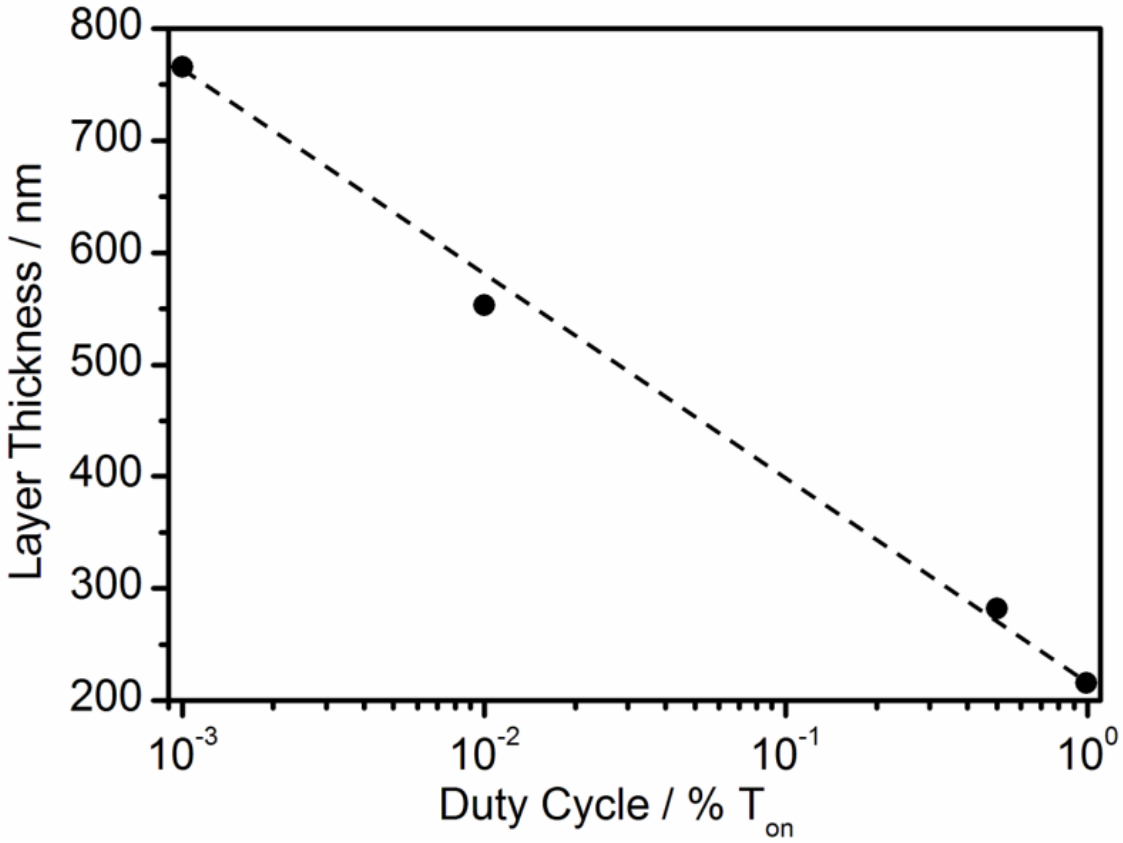

Figure 4-3: Relationship between the thickness of the tetramethylsilane/air layer and the duty cycle of the gas pulsing valve, with the gas pulse times of 100 µs on/10 ms off, 100 µs on/20 ms off, 50 µs on/500 ms off, and 50 µs on/5 s off, at 10 W and 0.2 mbar.

Electrical measurements were taken of the plasma deposited layers across the range of duty cycles, Figure 4-4. Very little information could be gleaned from these results: the low thickness obtained resulted in the coating failing almost immediately upon application of the voltage during immersion. Corrosion occurred across the board, resulting in the formation of oxygen bubbles on the electrode, which caused the current to drop, then increase as the bubbles were released, causing fluctuations throughout the measurement. This gave extremely mixed results, and a significant variation between the samples in each run.

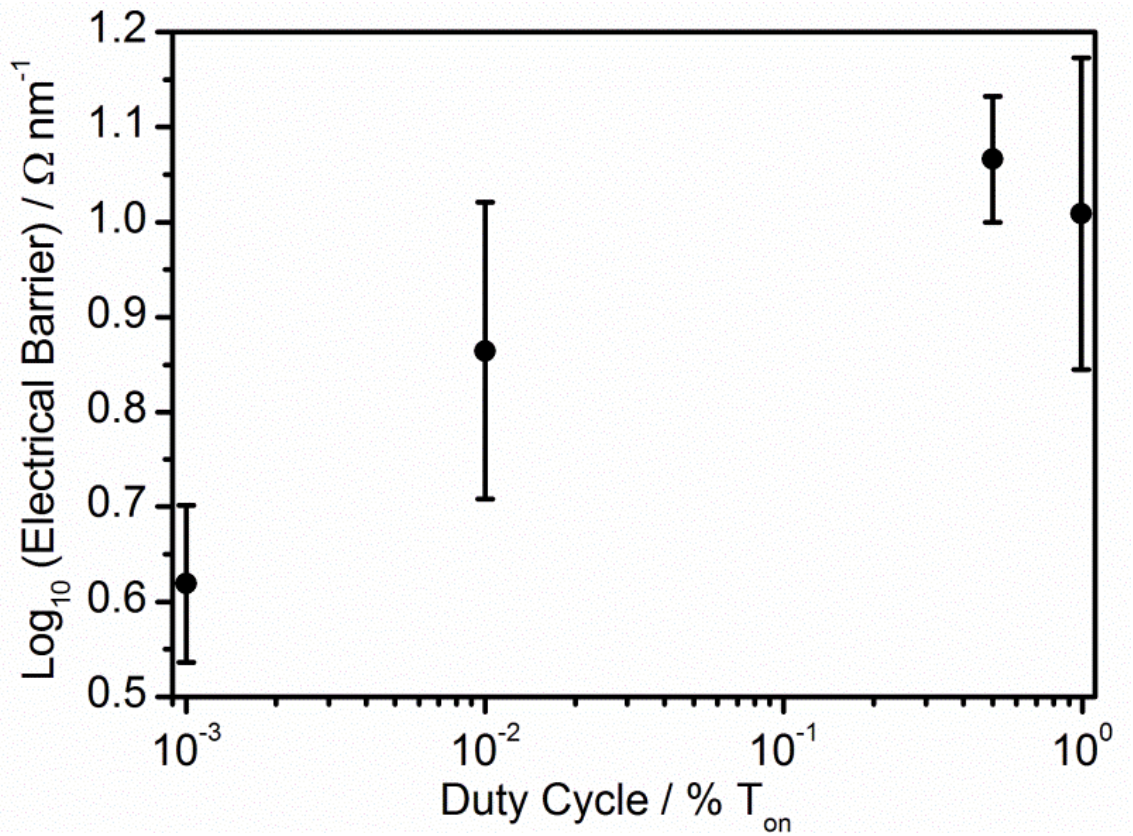

Figure 4-4: Wet electrical barrier response in relation to the duty cycle of the gas pulsing valve, measured at 8 V for 13 min and the gas pulse times of 100 µs on/10 ms off, 100 µs on/20 ms off, 50 µs on/500 ms off, and 50 µs on/5 s off at 10 W and 0.2 mbar.

Initially, the tetramethylsilane plasma was ignited, then after 30 s had elapsed the pulse valve was switched on with an open time of 100 µs and a close time of 5 s. OES was used to identify and track the pulse of air within the tetramethylsilane plasma, looking for any changes in the chemical composition of the plasma, Figure 4-5.

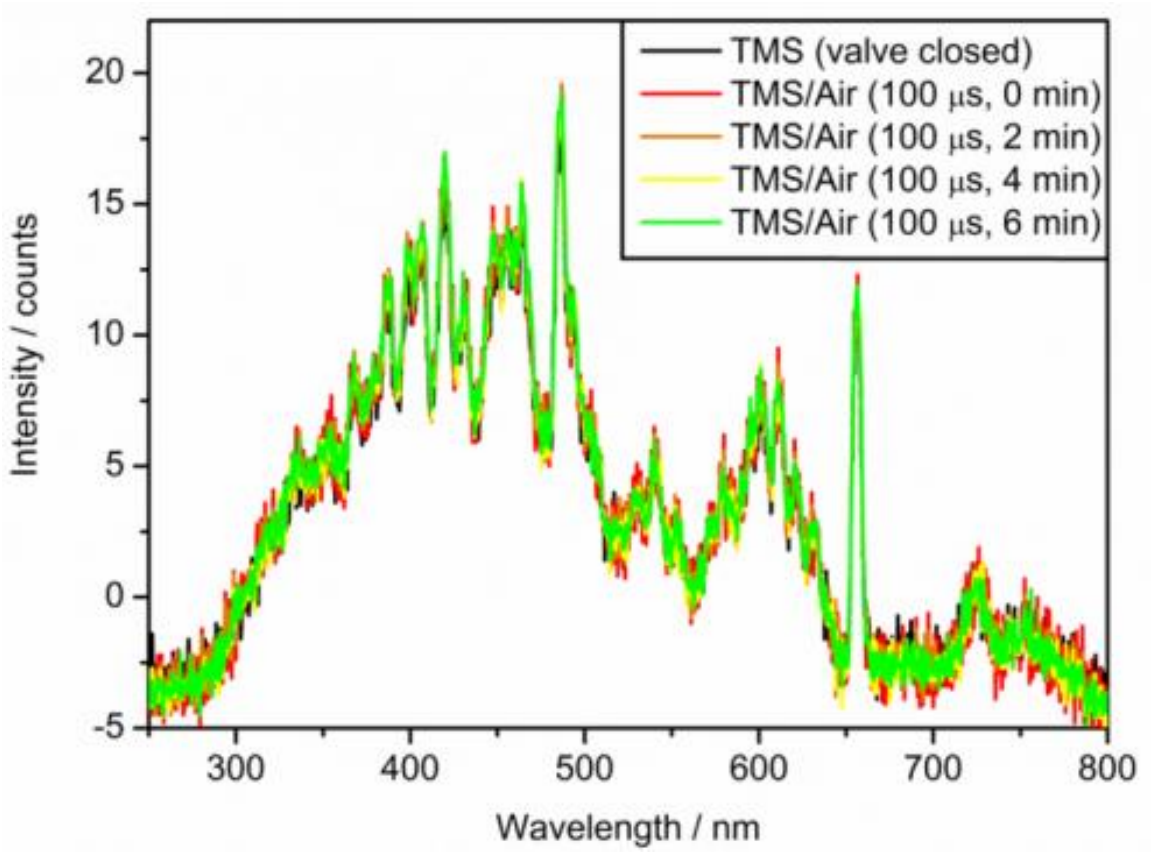

Figure 4-5: OES spectra of TMS plasma (20 W, 0.2 mbar, black line), TMS/air plasma with the valve triggered (20 W, 0.2 mbar, 100 µs on, 5 s off, red line), TMS/air plasma with the valve triggered after 2 min (20 W, 0.2 mbar, 100 µs on, 5 s off, orange line), TMS/air plasma with the valve triggered after 4 min (20 W, 0.2 mbar, 100 µs on, 5 s off, yellow line), and a TMS/air plasma with the valve triggered after 6 min (20 W, 0.2 mbar, 100 µs on, 5 s off, green line).

There was no change to the spectra over the duration of the plasma with the valve opened for 100 µs and closed for 5 s. The length of time the valve was open for was doubled to 200 µs and subsequent spectra were taken, before the valve was closed and a further spectrum was taken of the resulting plasma, Figure 4-6. Nitrogen peaks began to emerge on opening the valve for 200 µs, coming to an equilibrium in approximately 2 min. On switching off the pulse valve driver and closing the valve, these peaks disappeared within 30 s.

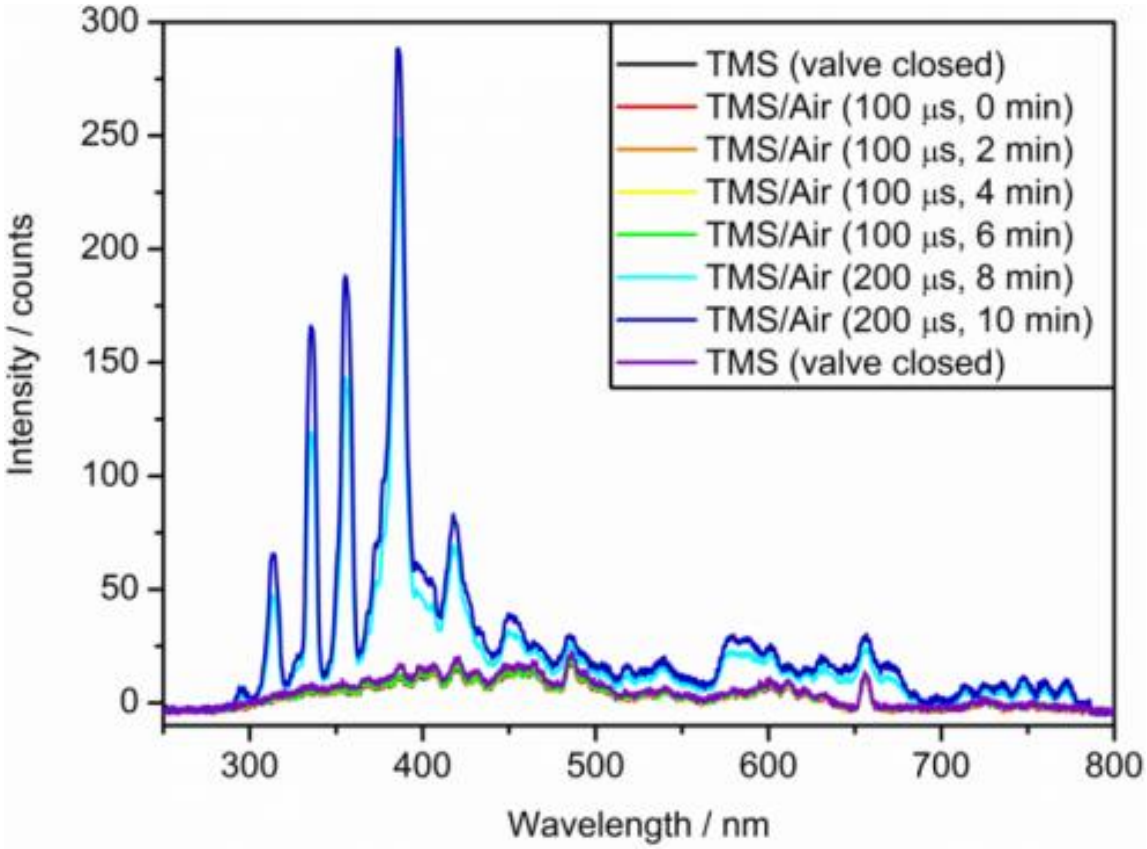

Figure 4-6: OES spectra of TMS plasma (20 W, 0.2 mbar, black line), TMS/air plasma with the valve triggered (20 W, 0.2 mbar, 100 µs on, 5 s off, red line), TMS/air plasma with the valve triggered after 2 min (20 W, 0.2 mbar, 100 µs on, 5 s off, orange line), TMS/air plasma with the valve triggered after 4 min (20 W, 0.2 mbar, 100 µs on, 5 s off, yellow line), TMS/air plasma with the valve triggered after 6 min (20 W, 0.2 mbar, 100 µs on, 5 s off, green line), TMS/air plasma with the valve triggered after 8 min (20 W, 0.2 mbar, 200 µs on, 5 s off, light blue line), TMS/air plasma with the valve triggered after 10 min (20 W, 0.2 mbar, 200 µs on, 5 s off, dark blue line), and a TMS/air plasma with the valve closed after <11 min (20 W, 0.2 mbar, purple line).

When compared to an air plasma at the same power the nitrogen peaks were comparitively weak, Figure 4-7, showing that there was significantly less air in the plasma during this process.

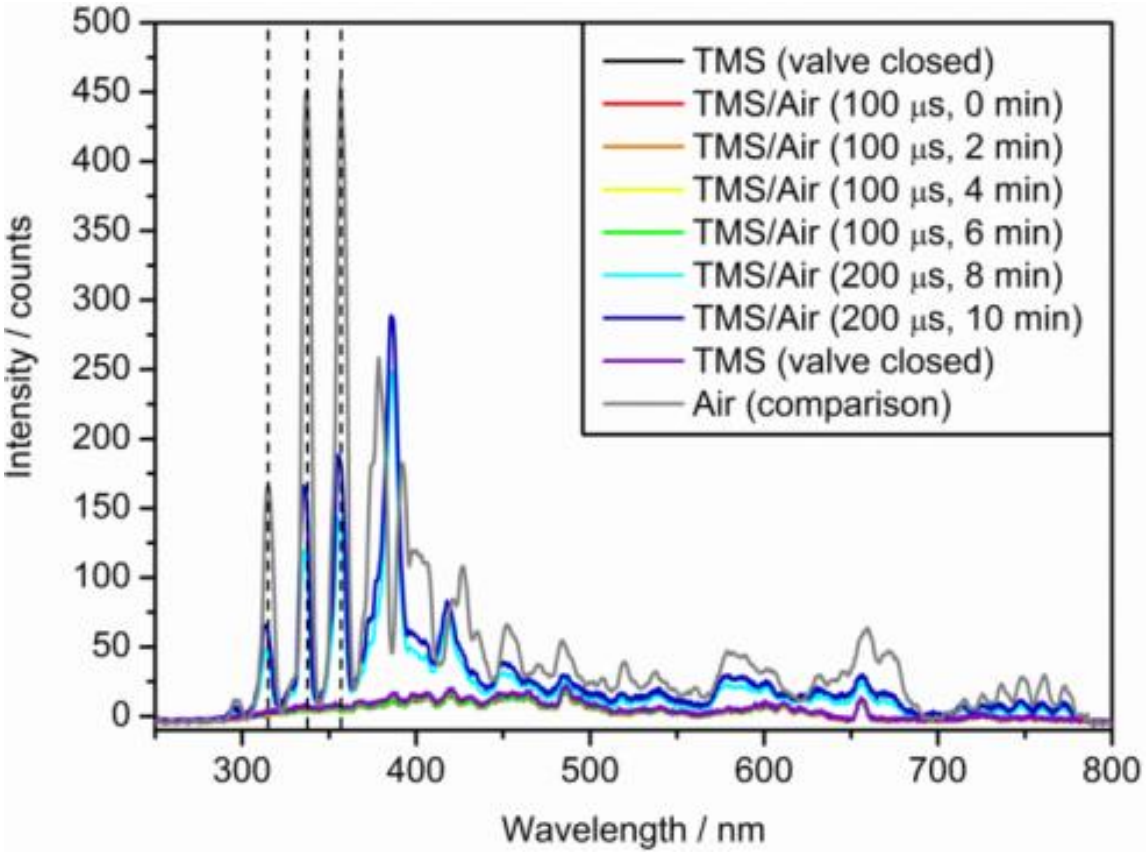

Figure 4-7: OES spectra of TMS plasma (20 W, 0.2 mbar, black line), TMS/air plasma with the valve triggered (20 W, 0.2 mbar, 100 µs on, 5 s off, red line), TMS/air plasma with the valve triggered after 2 min (20 W, 0.2 mbar, 100 µs on, 5 s off, orange line), TMS/air plasma with the valve triggered after 4 min (20 W, 0.2 mbar, 100 µs on, 5 s off, yellow line), TMS/air plasma with the valve triggered after 6 min (20 W, 0.2 mbar, 100 µs on, 5 s off, green line), TMS/air plasma with the valve triggered after 8 min (20 W, 0.2 mbar, 200 µs on, 5 s off, light blue line), TMS/air plasma with the valve triggered after 10 min (20 W, 0.2 mbar, 200 µs on, 5 s off, dark blue line), TMS/air plasma with the valve closed after <11 min (20 W, 0.2 mbar, purple line) and a solely air plasma for comparison (20 W, 0.2 mbar, grey line). Dashed lines indicated nitrogen peaks.

The pulse of air into the tetramethylsilane plasma could be clearly observed with the naked eye, as the colour change of the plasma was obvious when the nitrogen and oxygen were introduced. It was also clear that the nitrogen and oxygen had been somewhat removed from the plasma before the next pulse was introduced, Figure 4-8 (video included in data CD). It is likely that there would still be some air remaining in the chamber after the valve had closed, resulting in the coating containing some nitrogen and oxygen species, the concentration of which would affect the barrier

performance. The only way to fully avoid this would be to pump the chamber down to base pressure between each deposition.

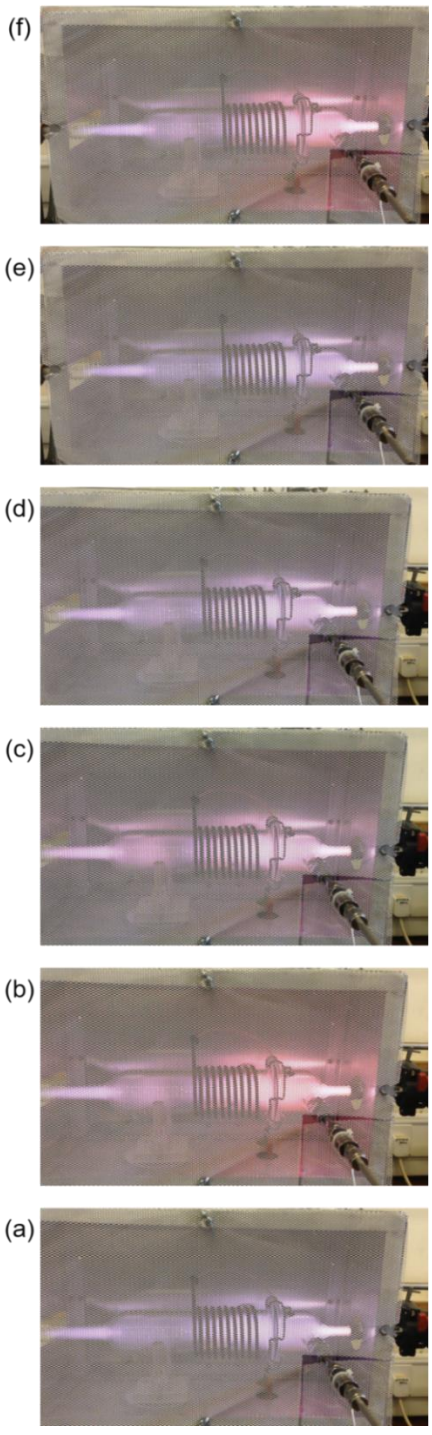

Figure 4-8: Snapshots of the air pulsing into the tetramethylsilane plasma (10 W, 0.2 mbar): (a) tetramethylsilane plasma, 1.95 s; (b) tetramethylsilane plasma with the first air pulse, 1.98 s; (c) tetramethylsilane plasma, 2.98 s; (d) tetramethylsilane plasma, 4.98 s; (e) tetramethylsilane plasma, 6.45 s; and (f) tetramethylsilane plasma with the first air pulse, 6.49 s.

ATR IR spectroscopy was taken of the powder which was found on the inside of the reactor after the plasma deposition, Figure 4-9. Peaks corresponding to C–H_2 and C–H_3 stretches were seen at 2960 cm^{-1} and 2890 cm^{-1} respectively.[75] Si–H stretches were seen at 2165 cm^{-1}, as well as a strong Si–CH_3 bending peak at 1252 cm^{-1}, a Si–CH_2 wagging peak at 1030 cm^{-1}, and Si–O_2 stretches at 760 cm^{-1}.[75–77] This supported the formation of an amorphous SiC:H based film.

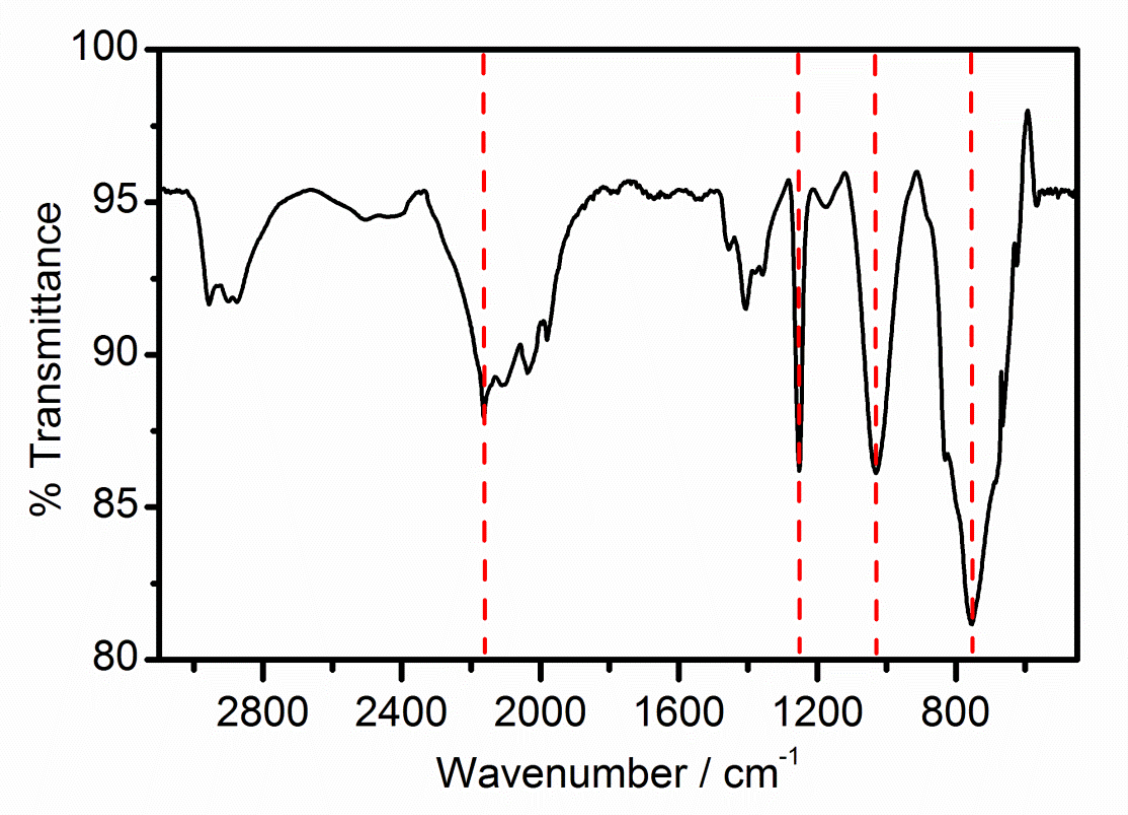

Figure 4-9: Infrared spectrum of the powder deposited by the TMS plasma (10 W, 0.2 mbar) with air continuously pulsed in at a valve open time of 200 µs and a close time of 5 s.

Although this coating system proved to be a poor wet electrical barrier on its own, air pulsed into a tetramethylsilane plasma can be used as a base layer for further coating and functionalisation, in a multilayer composite coating. At a comparable total coating thickness to plasma fluorinated polyisoprene with an allyl mercaptan base layer, plasma fluorinated polyisoprene on an air/tetramethylsilane plasma deposited base layer had a much-improved wet electrical barrier performance, exceeding the current detection limit, Figure 4-10. To obtain this result with an allyl mercaptan base layer the coating must exceed a total thickness of 4 µm, suggesting that a base layer deposited by a tetramethylsilane/air plasma improved the wet electrical barrier

performance. Comparing the tetramethylsilane/air–plasma fluorinated polyisoprene composite with a similar polyisoprene thickness to an allyl mercaptan–plasma fluorinated polyisoprene composite, the wet electrical barrier performance was significantly better, suggesting that the barrier improvement can be attributed to the base layer and not the plasma fluorinated polyisoprene.

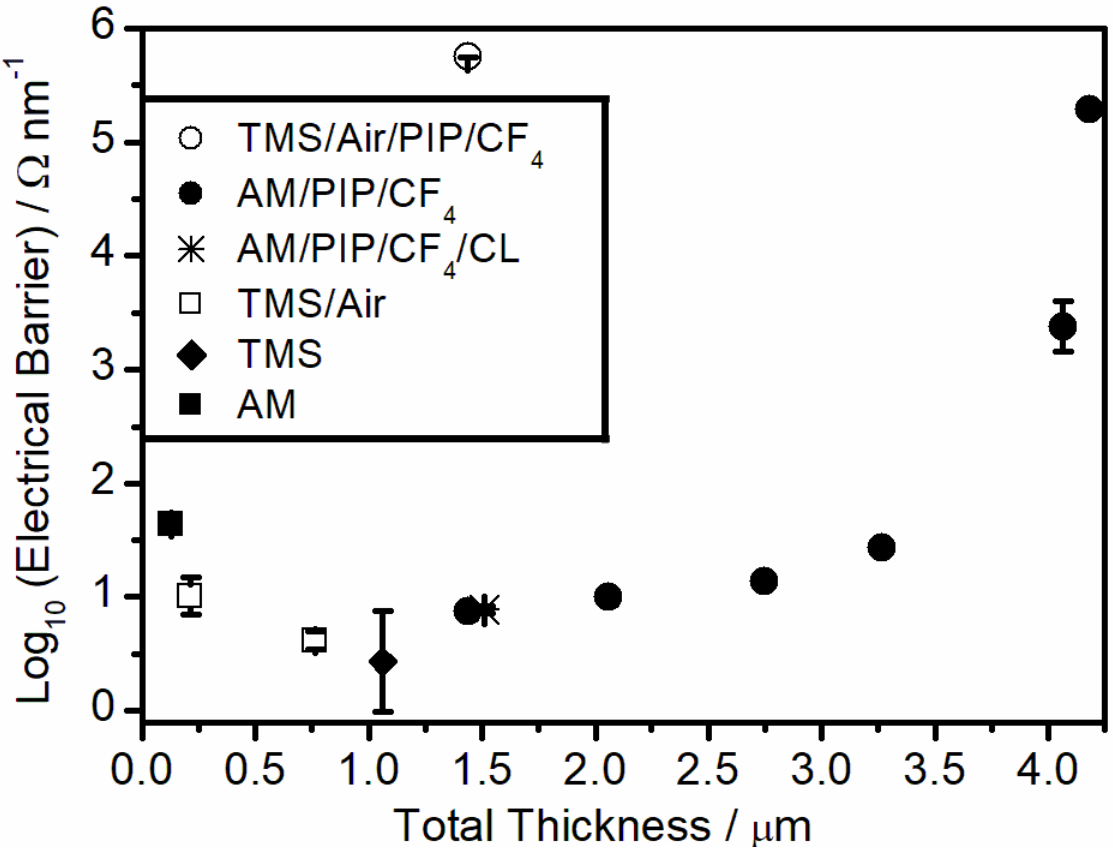

Figure 4-10: Final wet electrical barrier whilst immersed in water for 13 min under an applied electric field of 10 V mm^{-1} of: plasma fluorinated polyisoprene with a tetramethylsilane/air plasma deposited base layer (○, 10 W, 0.2 mbar, 50 μs on, 5 s off, 30 min); plasma fluorinated polyisoprene with an allyl mercaptan plasma polymer base layer (●, 2 W, 0.2 mbar, 10 min); crosslinked plasma fluorinated polyisoprene with an allyl mercaptan plasma polymer base layer (✳, 2 W, 0.2 mbar, 10 min); tetramethylsilane/air plasma deposited layer (□, 3 W, 0.2 mbar, 10–30 min, 50 μs on, 5 s off); tetramethylsilane plasma deposited layer (◆, 3 W, 0.2 mbar, 60 min); and an allyl mercaptan plasma polymer layer (■, 2 W, 0.2 mbar, 10 min). All plasma fluorinations were performed at 30 W, 0.2 mbar, for 5 min.

The improvement in the wet electrical barrier performance dependent solely on the chemistry of the base layer could be caused by the pulsed air roughening the surface of the tetramethylsilane layer, allowing for a greater surface area of contact

between the two layers, and thus more interaction between the two layers. Alternatively, the improved barrier performance could be due to the silane–ene click reactions utilising residual silane radicals on the surface to form strong interfacial links. Silane–ene reactions have been reported to form coatings with lower shrinkage stress and greater impact resistance than the corresponding thiol–ene coatings.[78] The lower contact angle of the tetramethylsilane/air layer would also allow better wetting of the spin coated polyisoprene onto the base layer, which would result in a more uniform coating, less likely to have defects. The contact angles of the base layers were compared, Table 4-1, and a significant drop in static water contact angle was found for a coating deposited by tetramethylsilane plasma with pulsed air, compared to a straightforward plasma deposited tetramethylsilane layer and allyl mercaptan. This is most likely due to the inclusion of oxygen in the plasma deposited layer.

Table 4-1: Sessile water drop contact angle measurements of the plasma deposited tetramethylsilane (5 W, 0.2 mbar), tetramethylsilane with pulsed air (10 W, 0.2 mbar, 200 µs open, 5 s closed) and allyl mercaptan (2 W, 0.2 mbar).

Coating	Deposition Method	Water Contact Angle / °
Tetramethylsilane	Continuous wave plasma	104 ± 1
Tetramethylsilane / air	Continuous wave plasma with pulsed air	74 ± 2
Allyl mercaptan	Continuous wave plasma	83 ± 1

When compared to the current best coating (plasmachemical double click thiol–ene, Chapter 3), the plasma deposited tetramethylsilane/air coating with a plasma fluorinated polyisoprene top layer showed an improvement in coating durability. It did not show any breakdown of the coating beyond the application of an electric field of 30 V mm^{-1}, whereas the polyisoprene coating with an ally mercaptan base layer, began to break down under an applied electric field of 20 V mm^{-1}, Figure 4-11. This suggests that there is an increase in wet electrical barrier performance beyond what could be seen during the standard electrical tests.

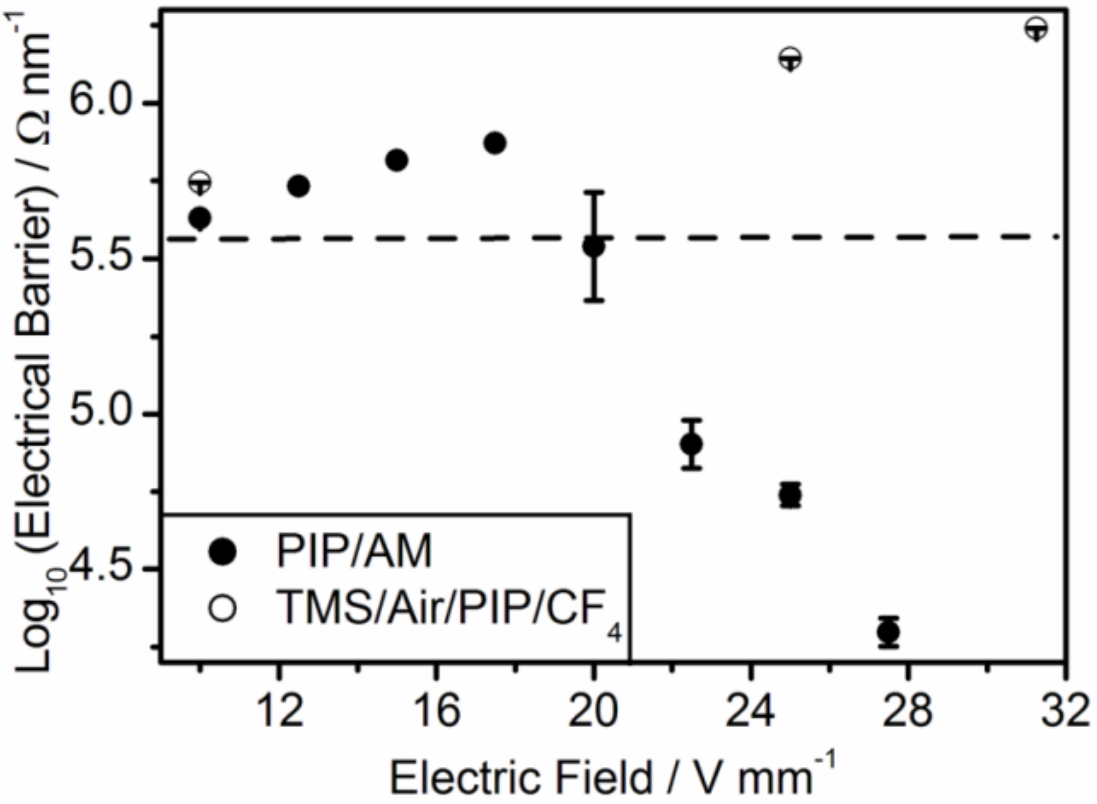

Figure 4-11: Wet electrical barrier after 13 min immersion in water as a function of applied electric field, for fixed thickness allyl mercaptan plasma polymer (continuous wave 2 W, 0.2 mbar, 507 ± 14 nm) and a polyisoprene base layer (1350 ± 40 nm), denoted by ●, and fixed thickness pulsed TMS/air plasma deposited layer (continuous wave 10 W, 0.2 mbar, 918 ± 1 nm) and a plasma fluorinated polyisoprene top layer (30 W, 5 min, 0.2 mbar, 519 ± 40 nm), denoted by ○. Samples above the dashed line reached the instrument detection limit.

4.4.2. Contact Angle and Captive Bubble

Sessile drop water contact angle values exceeded 170° for electrical discharge power level settings of 10–50 W, whilst the hexadecane contact angle reached a peak of 133° ± 2° at a 30 W plasma power, Figure 4-12. The lowest hexadecane contact angle observed was 113° ± 3°, for a plasma power of 10 W. Plasma fluorinated polyisoprene with an allyl mercaptan base layer was measured as a control sample, and showed no difference in contact angle, Figure 4-15.

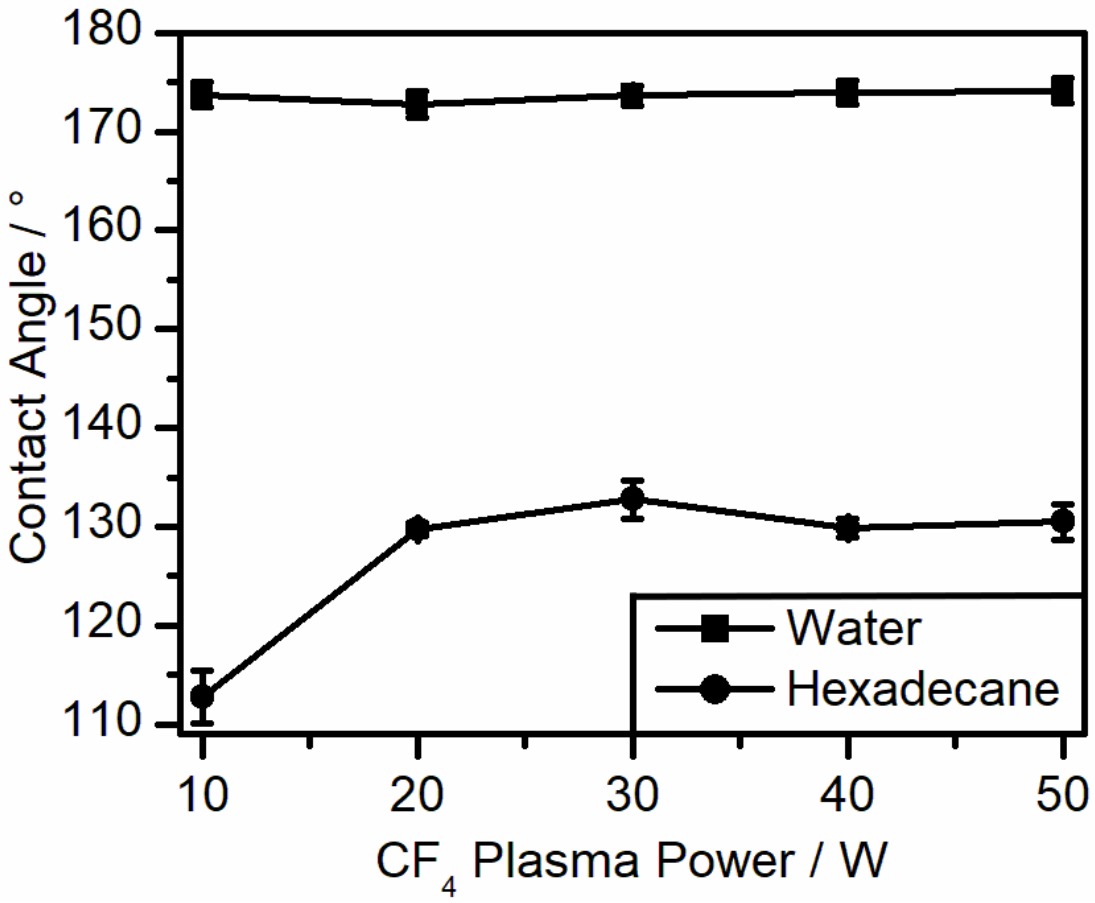

Figure 4-12: Contact angle values on CF_4 plasma fluorinated polyisoprene surfaces (thickness 1360 ± 20 nm) as a function of plasma power and fixed treatment time of 5 min and pressure of 0.2 mbar for ultra-high purity water (■) and hexadecane (●).

Contact angle hysteresis measurements were also taken for ultra-high purity water and hexadecane on the plasma fluorinated polyisoprene surfaces, Figure 4-13. There was little change in the water contact angle hysteresis, regardless of plasma power, but a decrease in hexadecane contact angle hysteresis was seen on increasing plasma power. This was thought to be due to increased etching of the polyisoprene surface at higher powers, and a subsequent increase in the surface roughness.[79] This is also supported by the lower hexadecane contact angle found for the10 W process, Figure 4-12. Texturing and roughening of surfaces typically increases the hydrophobicity or oleophobicity of an already hydrophobic or oleophobic coating.[80,81] A plasma fluorinated but not textured polybutadiene surface has been reported to have a water contact angle of 110°, whereas plasma fluorination combined with roughening of the polybutadiene can take the water contact angle up to 170°, and hexadecane contact angles up to 118°.[79,82] The fluorinated but not roughened polybutadiene

surface had a water contact angle hysteresis of 37° which was reduced to 4° upon roughening.[82] This supports the assertation that the reduction in hexadecane contact angle, Figure 4.12, was due to the decrease in roughness on decreasing the plasma power, and concurrently the reduction in hexadecane contact angle hysteresis, Figure 4-13, was due to the increase in roughness on increasing the plasma power.

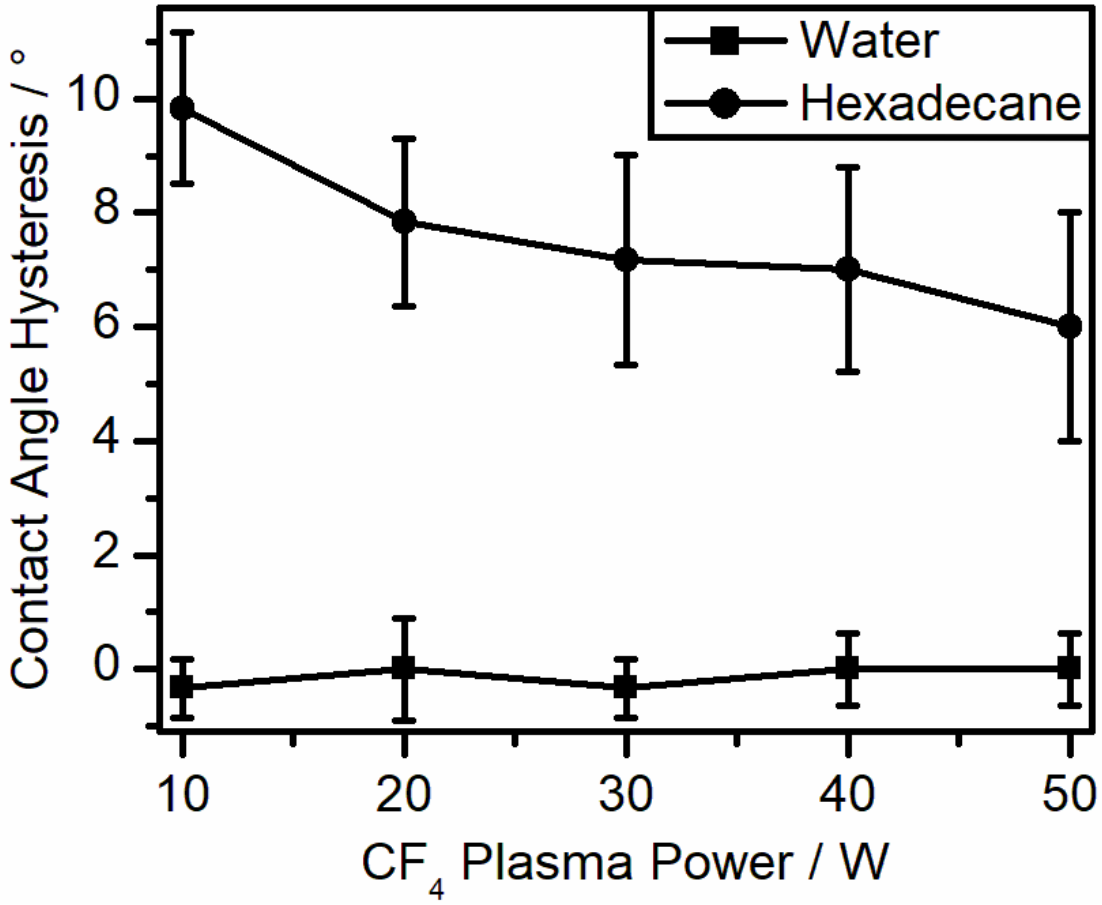

Figure 4-13: Contact angle hysteresis values on CF_4 plasma fluorinated polyisoprene surfaces (thickness 1360 ± 20 nm) as a function of plasma power and fixed treatment time of 5 min and pressure of 0.2 mbar for high purity water (■) and hexadecane (●).

Water contact angle measurements were taken for crosslinked plasma fluorinated polyisoprene in comparison to non-crosslinked plasma fluorinated polyisoprene, Figure 4-14. It was found that at lower thicknesses there was a drop in the contact angle after the crosslinking process (150 °C for 60 min), which was not maintained for the higher thickness samples. For non-crosslinked plasma fluorinated polyisoprene there was no such loss in hydrophobicity, and the contact angle remained high regardless of the thickness of the polymer layer.

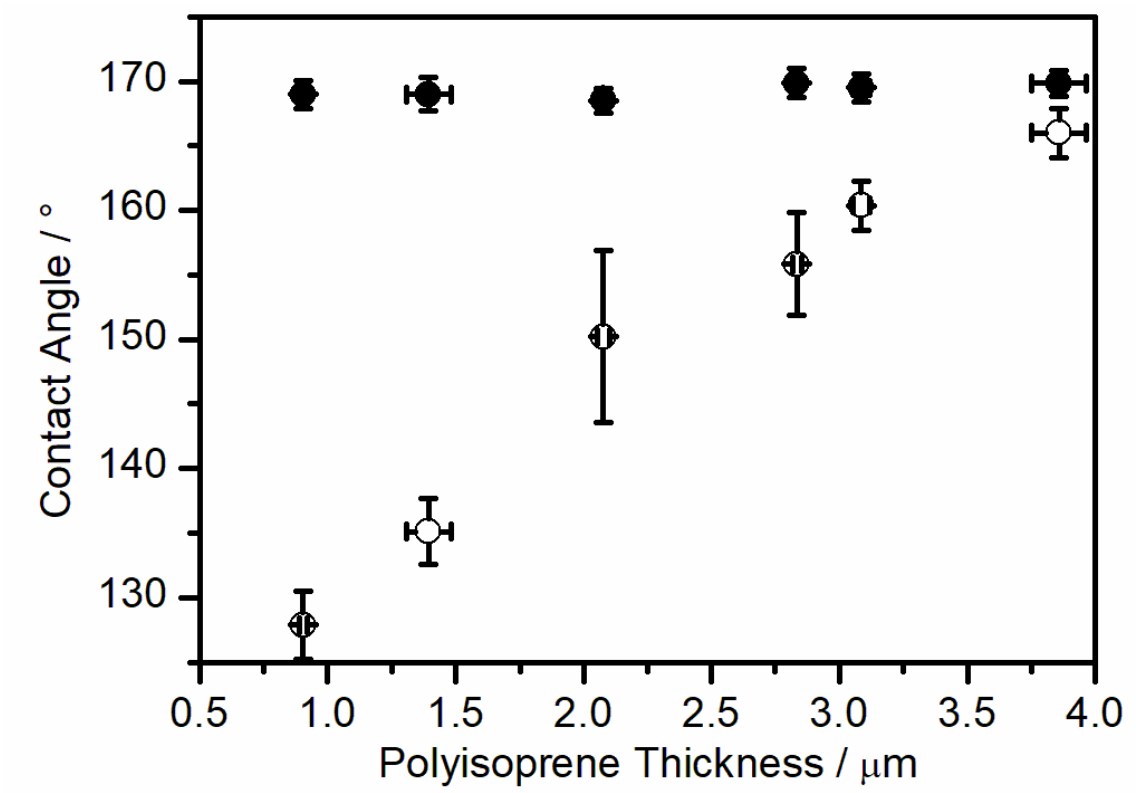

Figure 4-14: Sessile water contact angles of non-crosslinked (●) and crosslinked (○) plasma fluorinated (30 W, 0.2 mbar, 5 min) polyisoprene layers of varying thicknesses.

A range of different oils (carbon chain length 7–16) were tested by contact angle analysis, Figure 4-15, Table 4-2. The oil with the highest surface tension (the longest alkyl chain length), hexadecane, had the highest contact angle. The contact angles moved from oleophobic to oleophilic with the decrease in the surface energy of the oil. Although there was no change seen based on the water contact angle results, the oil contact angles showed a marked decrease across the chamber, with the highest contact angle being found closest to the gas inlet, and the lowest at the furthest point from the gas inlet. This corresponds to the changes in plasma density throughout the chamber. The region of highest plasma density occurs directly under the coils, and the lowest occurs downstream towards the pump. This effect has been previously reported with the same level of fluorination occurring in both the glow and downstream regions, but with a significant decrease in roughening in the downstream region compared to the glow.[82] This suggests that the whilst the fluorination and roughening of the polyisoprene was sufficient to maintain the water contact angle regardless of the position in the chamber, the decrease in roughness for the samples further away from the gas inlet resulted in a decrease in the oil contact angles.

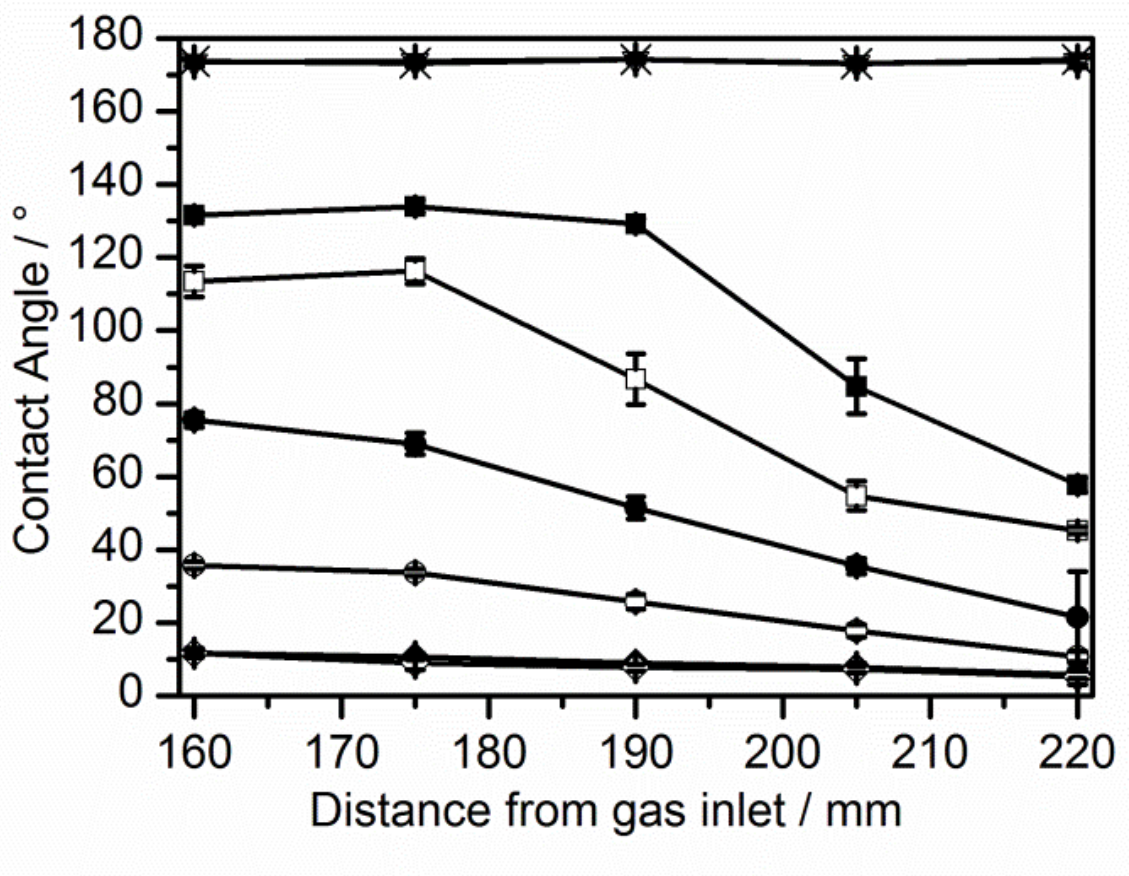

Figure 4-15: Sessile drop (1 µL) contact angle of water (▽), hexadecane (■), tetradecane (□), dodecane (●), decane (○), octane (◆) and heptane (◇) on a CF_4 plasma fluorinated (30 W, 5 min, 0.2 mbar) polyisoprene surface (thickness 1360 ± 20 nm). As a control, water contact angles were also taken on CF_4 plasma fluorinated (30 W, 5 min, 0.2 mbar) polyisoprene surface (thickness 1360 ± 20 nm) with a plasma polymer allyl mercaptan base layer (∗, 2 W, 0.2 mbar, 5 min, 198 ± 7 nm).

Table 4-2: Liquid contact angle values on a CF_4 plasma fluorinated (30 W, 5 min, 0.2 mbar) polyisoprene surface (thickness 1360 ± 20 nm).

Probe Liquid	Liquid Surface Energy[83] / mN m^{-1} (at 20 °C)	Contact Angle / °
Water	72.9	174 ± 1
Hexadecane	27.5	134 ± 2
Tetradecane	26.6	116 ± 4
Dodecane	25.4	69 ± 3
Decane	23.8	34 ± 1
Octane	21.6	11 ± 1
Propan-2-ol	21.3	38 ± 1

In order to look at the air contact angle of the plasma fluorinated polyisoprene surface, captive bubble measurements were taken, Figure 4-16. These showed the formation of an air layer when the air bubble came into contact with the surface, which is in agreement with the water contact angle results found previously, Figure 4-12.

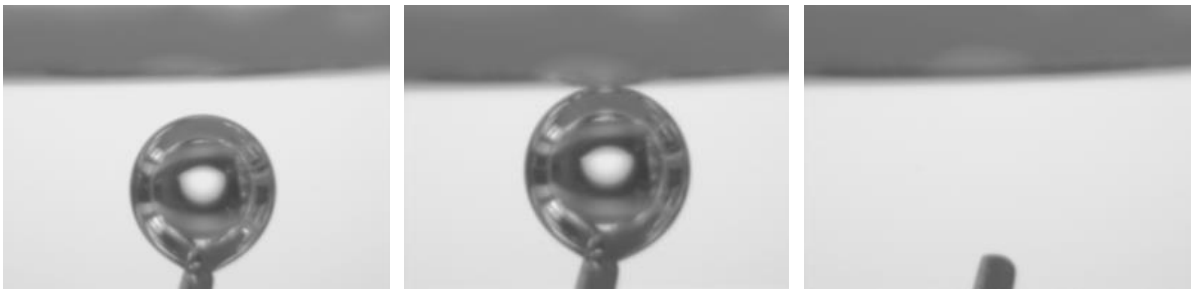

(a) (b) (c)

Figure 4-16: Photographs taken of captive air bubble in water approaching the surface of CF_4 plasma fluorinated (30 W, 5 min, 0.2 mbar) polyisoprene layer (thickness 1360 ± 20 nm): (a) the air bubble and the plasma fluorinated polyisoprene surface; (b) initial contact of the air bubble with the plasma fluorinated polyisoprene surface; and (c) the subsequent formation of a very thin air layer.

This air layer could be clearly seen when the samples were immersed in water and tilted, giving the air layer a “mirror-like” effect, Figure 4-17. Such superhydrophobic layers could be utilised to allow glass to float on water, Figure 4-18 (video included in data CD).

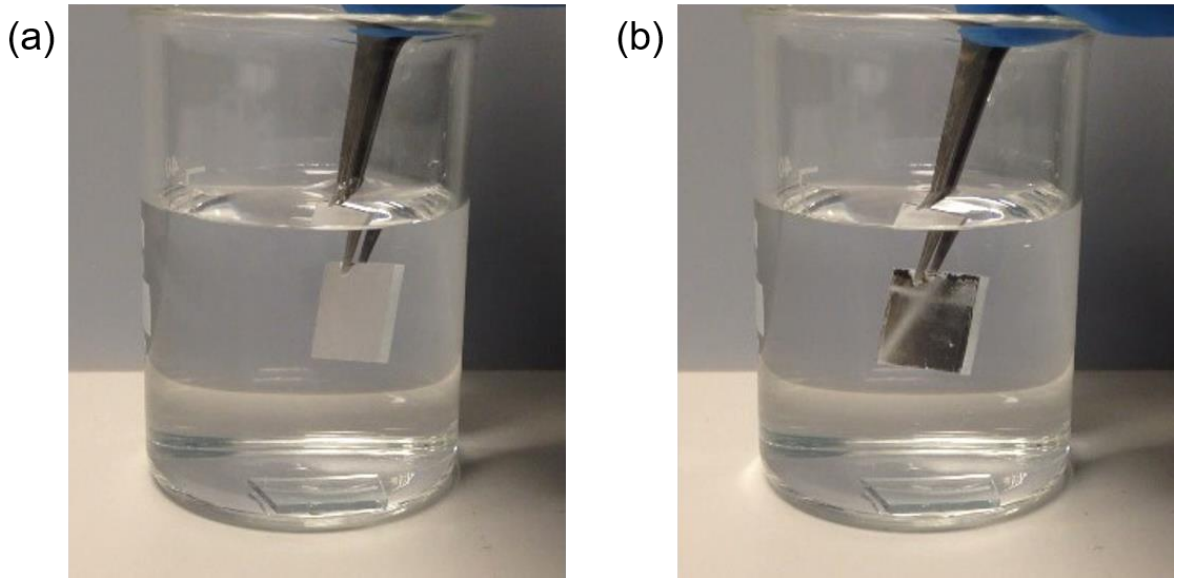

Figure 4-17: Plasma fluorinated (30 W, 0.2 mbar, 5 min) polyisoprene on glass: (a) immersed in water; and (b) tilted to show the “mirror-like” effect of the trapped air layer.

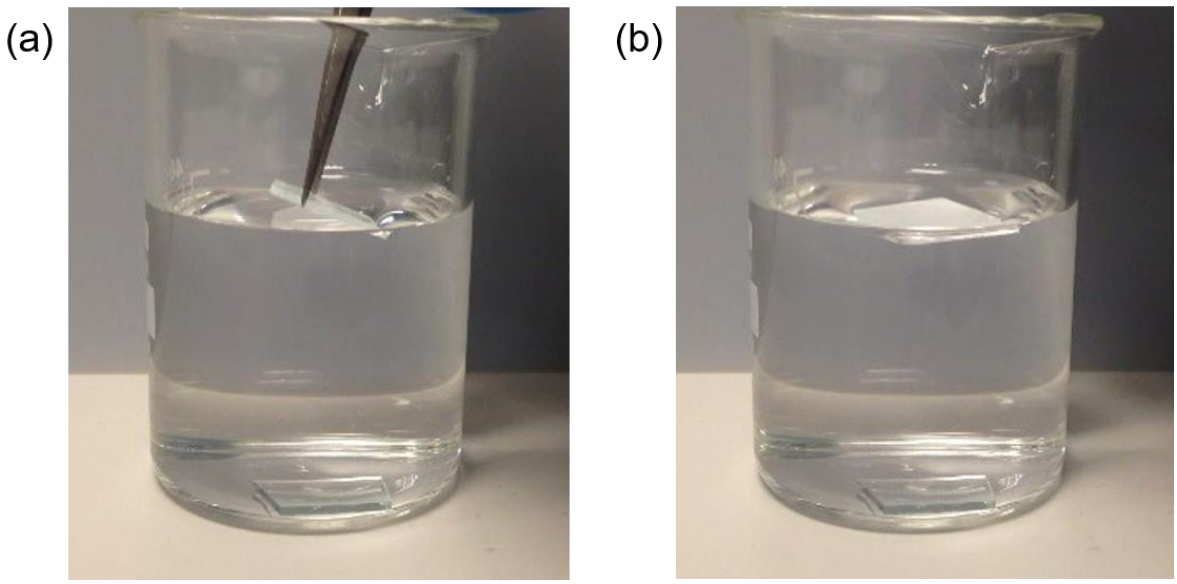

Figure 4-18: Plasma fluorinated (30 W, 0.2 mbar, 5 min) polyisoprene on glass: (a) dipping the edge below the surface of the water, with the water unable to move over the highly superhydrophobic surface; and (b) left to float on the surface of the water.

4.4.3. X-Ray Photoelectron Spectroscopy

High resolution XPS spectra were taken of the plasma fluorinated polyisoprene layer, Table 4-3 and Figure 4-19, showing the presence of carbon (41.9%), fluorine (54.7%), and a small amount of oxygen (3.3%). The C(1s) XPS spectrum of the plasma fluorinated polyisoprene spin coated layer was fitted to six Gaussian Mg $K\alpha_{1,2}$ components in conjunction with their corresponding Mg $K\alpha_3$ and Mg $K\alpha_4$ satellite peaks shifted towards lower binding energies by ~8.4 and ~10.2 eV respectively. The C(1s) Mg $K\alpha_{1,2}$ components were found to be: C_xH_y at 285.0, –<u>C</u>–CF_n at 286.4 eV, –<u>C</u>F– at 287.4 eV, –<u>C</u>F–CF_n at 289.2 eV, –<u>C</u>F_2– at 291.2 eV, and –<u>C</u>F_3 at 293.4 eV.[84,85] The single F(1s) Mg $K\alpha_{1,2}$ peak measured at 680.6 eV corresponds to covalently bonded fluorine atoms.

Table 4-3: XPS compositions for the plasma fluorinated (30 W, 0.2 mbar, 5 min) polyisoprene spin coated layer. Polyisoprene deposition, plasma fluorination and XPS analysis were performed by I.S.C.M.

System	Atomic Composition / %			C(1s) Component / %					
	C	F	O	<u>C</u>$_x$H$_y$	–<u>C</u>– CF_n	–<u>C</u>F–	–<u>C</u>F– CF_n	–<u>C</u>F_2–	–<u>C</u>F_3
Theoretical Polyisoprene	100			100	-	-	-	-	-
Plasma fluorinated polyisoprene spin coated layer	41.9	54.7	3.3	23.4	5.1	6.8	20.8	33.9	9.9

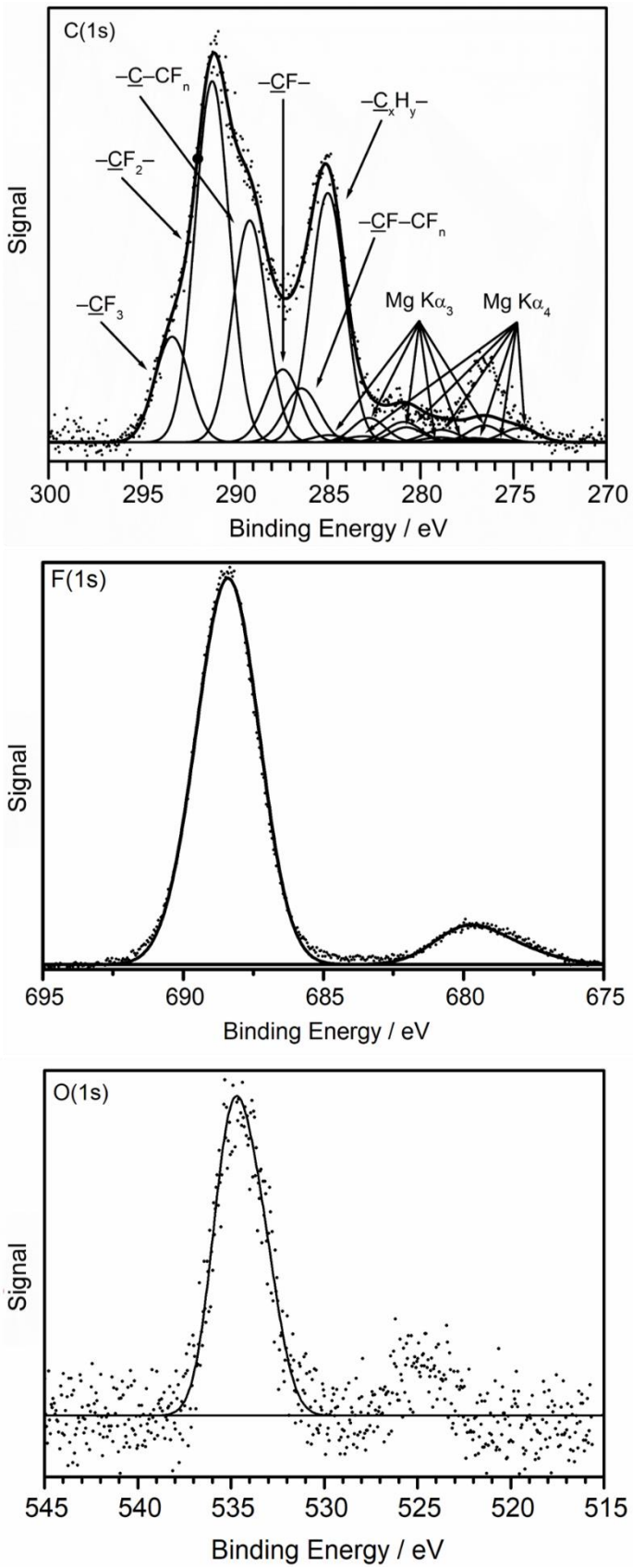

Figure 4-19: High resolution XPS spectra of a CF_4 plasma (30 W, 0.2 mbar, 5 min) fluorinated polyisoprene layer. Polyisoprene deposition, plasma fluorination and XPS analysis were performed by I.S.C.M.

4.4.4. Infrared Spectroscopy

Little difference was observed in the FTIR spectra of polyisoprene and oven dried polyisoprene, Figure 4-20, with both spectra showing an allyl C–H stretch (3040 cm^{-1}), indicative of unsaturation. This was not present in the spectrum of plasma fluorinated polyisoprene, however a strong C–F stretch can be observed at 1243 cm^{-1}, which was not present in the polyisoprene or oven dried polyisoprene spectra. This demonstrated that fluorination of the polymer had occurred.[86]

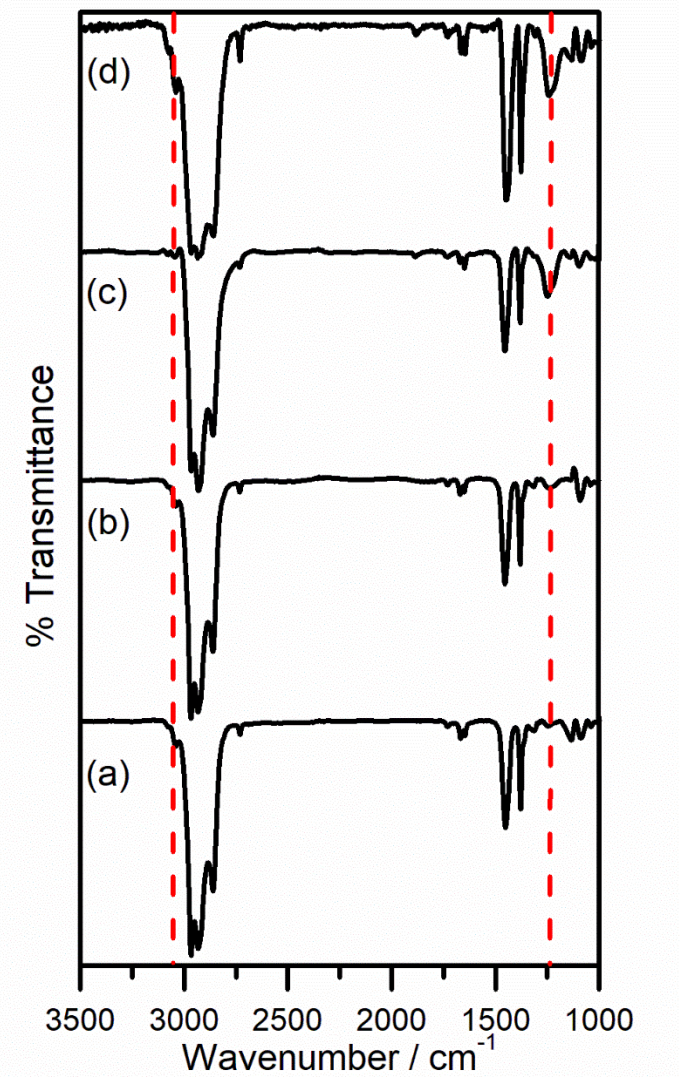

Figure 4-20: Infrared spectra of spin coated polyisoprene (thickness 1360 ± 20 nm): (a) as prepared; (b) after drying at 60 °C for 1 h; (c) after drying at 60 °C for 1 h followed by CF_4 plasma fluorination (30 W, 0.2 mbar, 5 min); and (d) after drying at 60 °C for 1 h followed by CF_4 plasma fluorination (30 W, 0.2 mbar, 5 min), on a plasma deposited allyl mercaptan base layer (thickness 198 ± 7 nm). Dashed lines indicate allyl C–H (3040 cm^{-1}) and C–F (1243 cm^{-1}) stretches respectively.

4.4.5. Surface Topography

By using AFM to study the topography of the treated and untreated polyisoprene layers it was established that the surface roughness increased significantly between untreated (rms = 34 ± 11 nm) and plasma fluorinated (rms = 847 ± 24 nm) polyisoprene, Figure 4-21. When examining the coatings by SEM it was clear that the plasma fluorination had caused significant roughening of the polyisoprene surface, Figure 4-22. It is unclear whether the surface is hierarchical or fractal in nature, and further investigation would be required to fully qualify the surface structure. This surface roughening gives rise to the high water contact angle and the low contact angle hysteresis, making it an extremely water repellent coating, Figure 4-12.

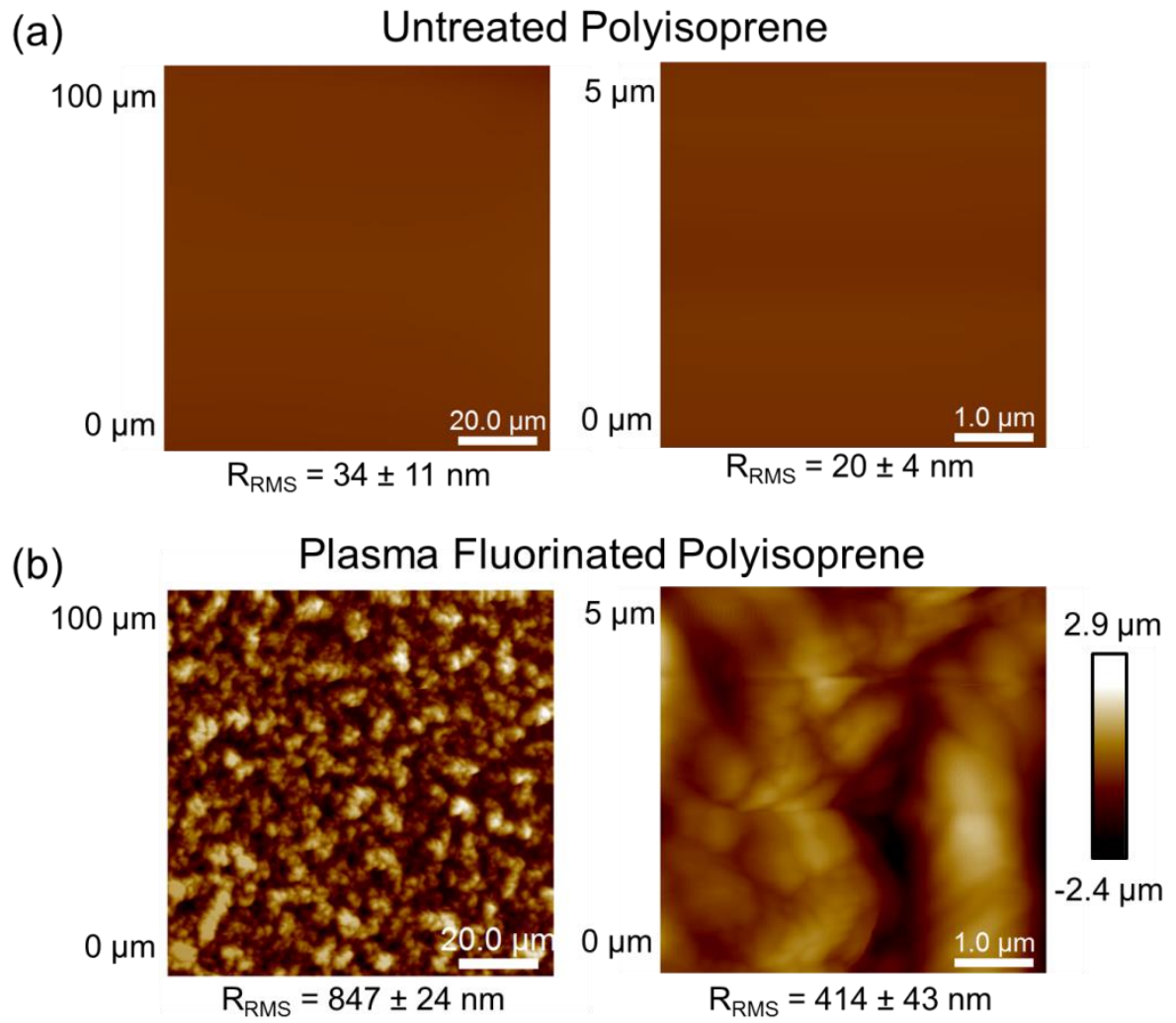

Figure 4-21: Atomic force microscopy height images of (a) polyisoprene and (b) CF_4 plasma fluorinated polyisoprene surface (30 W, 5 min, 0.2 mbar) at 20 µm and 1 µm length scales.

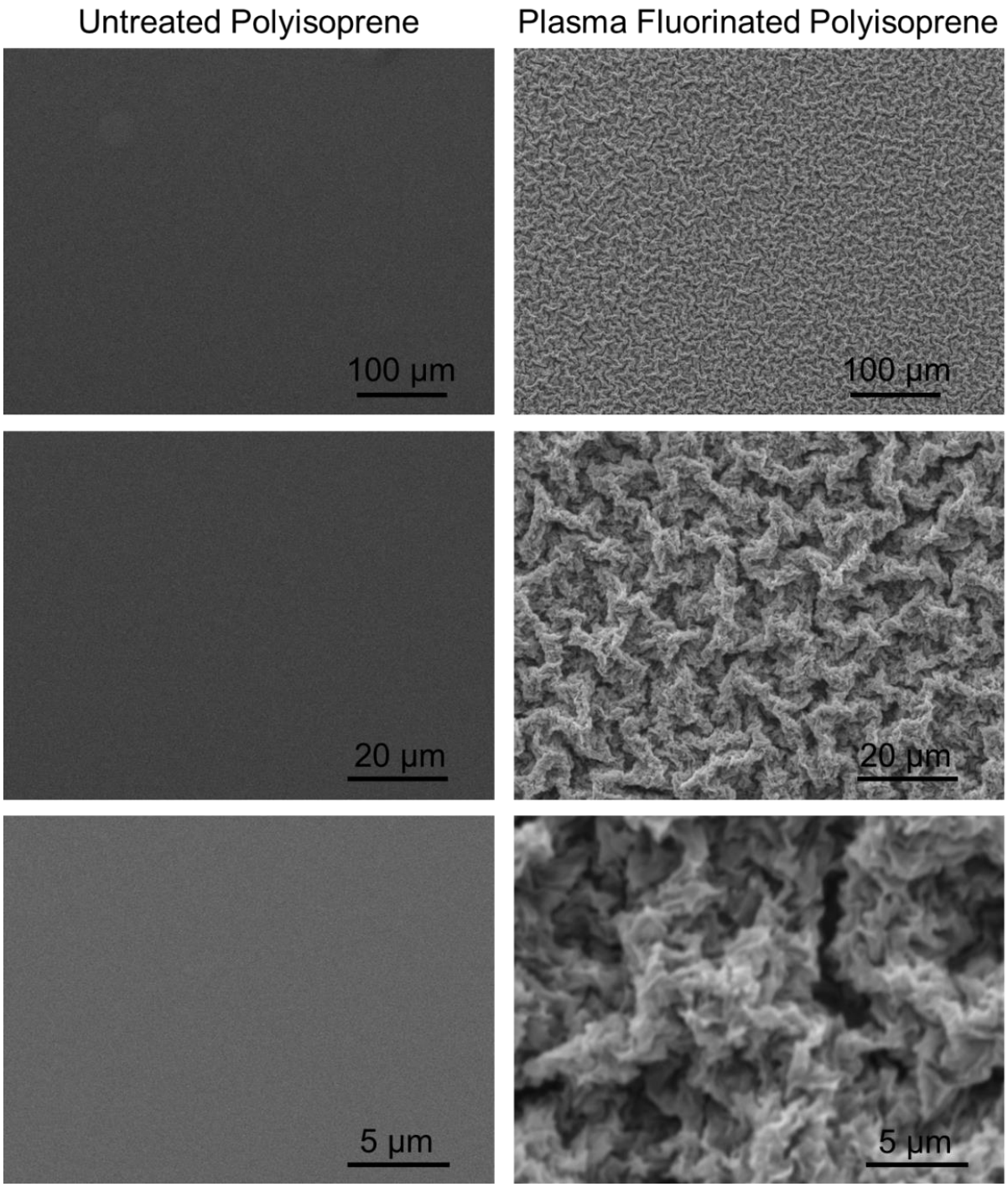

Figure 4-22: SEM micrographs of untreated polyisoprene and plasma fluorinated polyisoprene (30 W, 5 min, 0.2 mbar) at 100 µm, 20 µm and 5 µm length scales.

4.5. Discussion

The wet electrical barrier performance of plasma fluorinated polyisoprene was found to be better for plasma deposited tetramethylsilane/air base layers compared to allyl

mercaptan or glycidyl methacrylate base layers, Figure 4-2 and Figure 4-10. Differences in the surface wetting and penetration of the nanocoating base layers during the spin coating of the polyisoprene layer may play a role in how well the subsequent coating system functioned, Table 4-1. The difference in barrier performance between the allyl mercaptan and glycidyl methacrylate layers can be attributed to interactions between the trapped radicals of the thiol groups in the base layer and the double bonds of the polyisoprene layer, creating a strong linkage between the two layers.[87] For the allyl mercaptan base layer at least 4 µm thickness of polyisoprene was necessary in order to achieve a high wet electrical barrier performance, Figure 4-1.

Pulsing air into the tetramethylsilane plasma formed a plasma deposited coating which contained a significant amount of Si-O bonds, Figure 4-9. The full potential of these coatings should be exploited by optimisation of the gas pulsing conditions, such as varying the thickness of the tetramethylsilane prior to passivation with air, increasing the number of tetramethylsilane/air composite layers, and deposition of this coating onto a previously deposited base layer. A greater understanding of these coatings would be beneficial, and future work should include further investigation into the deposition and gas pulsing parameters and the subsequent coatings formed. Other methods of validating the different deposition parameters would be to look at the adhesion of the coating to the substrate, its abrasion resistance, and its thermal stability. Further information about the layer system could be attained by examining the coating by XPS, AFM and SEM to look at the chemical composition and surface morphology. Each layer in the composite coating should be examined in this way, which would give rise to a greater understanding of the mechanisms of the barrier coating. Alternatively, further investigation could reveal a lack of distinct layers, instead showing one continuous layer, with varying oxygen/nitrogen concentrations throughout, i.e. regions of higher oxygen/nitrogen concentration (when the air was pulsed into the chamber) separated by areas of lower oxygen/nitrogen concentration (when the pulse valve was closed).

Very high water contact angle values (>170°) in combination with very low contact angle hysteresis of the plasma fluorinated polyisoprene compared favourably against previous plasma fluorinated polymer surfaces, Figure 4-12.[81,88–96] This circumvents the need for a separate step incorporating surface texturing prior to

plasma treatment.[82] The plasma treatment of the polyisoprene surface gave rise to significant surface roughening, Figure 4-21 and Figure 4-22. This was caused by the etching processes during the plasma fluorination of the polyisoprene surface. Plasma surface etching involves the interaction of radicals, atoms and ions with the polymer surface.[97] First, the reactive species are formed in the plasma, and these are then adsorbed on the polymer surface. The surface reactions then occur, and the etch byproducts are generated. These then desorb, and the process continues with more of the reactive species from the plasma.[98] For example, the CF_x ($1 \leq x \leq 3$) radicals produced in the CF_4 plasma can react with the surface of the polymer, removing hydrogen. The volatile species produced in these reactions are then removed from the chamber. CF_4 plasma etching slows over the duration of the reaction, as the C-H bonds are replaced with stronger C-F bonds.[98]

Multiple surface length scales are beneficial to achieving superhydrophobicity by roughening and structuring of the surface.[99–101] Previous work has shown comparable superhydrophobicity using surface structuring followed by plasma fluorination[94] or extended processes[102] to give micro- (up to 30 μm) and nano-roughness. Similar length scales of structuring have been seen in the natural world,[103–108] and in biomimetic surfaces.[96,102,109–114] The oleophobicity of the surface, Table 4-2, showed a relatively high contact angle for hexadecane compared to other oleophobic surfaces.[82,114–117] The oleophobic nature of the coating is maintained with tetradecane, but is lost for oils of lower chain lengths. Other ways to vary properties such as surface wetting and hardness would be to incorporate filler materials such as nanoparticles, clays and graphene, etc.

4.6. Conclusions

A highly superhydrophobic coating was prepared by the plasma deposition of a base layer, followed by the subsequent coating with an unsaturated polymer. This polymer top layer was then plasma fluorinated, leading to a roughened surface structure able to achieve contact angles up to >170° with a negligible contact angle hysteresis. This coating system was applicable as a wet electrical barrier coating, able to protect a circuit board from corrosion when immersed in tap water under an applied voltage.

The degree of protection from electrical breakdown could be tailored by changing the chemistry of the plasma deposited base layer. The coating formed by plasma deposited tetramethylsilane with sequentially pulsed air proved to be a superior base layer for the plasma fluorinated polyisoprene layer than other plasma deposited layers. Additionally, this coating proved to be more effective as a wet electrical barrier coating than the previous best coating, allyl mercaptan plasma deposited onto polyisoprene, Chapter 3, as it provided complete electrical protection at an even lower total coating thickness.

The wet electrical barrier coating described herein should be considered for scaling up to industrial production. The base layer can be deposited on 3D circuit boards uniformly and conformally, the polymer layer can be spray or dip coated on the larger scale, rather than spin coated, so as not to negatively affect throughput. The final plasma process of dual fluorination and roughening of the polymer surface is both quick, and conformal; all regions of a circuit board comprising 3D structures would receive the same degree of functionalisation, and thus the high degree of water repellency.

Additionally, it can be observed that the degree of oleophobicity can be determined by adjusting the position of the substrate relative to the power density of the CF_4 plasma, whilst the hydrophobicity was unchanged. This property could be manipulated to give tailorable surfaces, achieving a high water contact angle with an oil contact angle which could be selected as the application required. The reduction in oleophobicity in relation to oils with shorter chain lengths would allow this coating to be applied in other areas than corrosion protection, such as in oil-water separation, and the high water contact angle and very low hysteresis would allow this coating to be used in fog harvesting applications. For applications such as these, it is the surface properties which are most critical, rather than barrier coating strength. This means that the initial step of plasma depositing a base layer would be unnecessary, further shortening the process duration.

It could also be useful to apply the gas pulsing method to other coatings. For example, the sequential pulsing of allyl mercaptan into a vinyl, acrylate or methacrylate containing precursor plasma, Chapter 5. Ideally, if the plasma power was kept low throughout the reaction, not all of the unsaturated bonds in the precursor would be

consumed. The pulsing of a monomer like allyl mercaptan into such a plasma would facilitate the formation of a strong, highly crosslinked layer within the deposited coating, and taking this up to a multi-layered system would theoretically give a much-improved barrier coating.

4.7. References

1 Evitts, R. W. Cathodic Protection. In *Handbook of Environmental Degradation of Materials*; Kutz, M., Ed.; William Andrew Inc.: Norwich, 2005; pp 368–369.

2 Insure My Smartphone. Gadget Insurance: Smartphone Insurance Survey. http://www.insuremysmartphone.co.uk/news/smartphone-insurance-survey (accessed September 13, 2016).

3 Kao, K. C. Electrical conduction and breakdown in insulating polymers. In *Properties and Applications of Dielectric Materials*, Proceedings of the 6th International Conference, Xi'an, China, June 21–26, 2000; IEEE Dielectrics and Electrical Insulation Society: New York, 2000, 1–17.

4 Goosey, M. T. Permeability Effects in Electrical and Electronic Component Coatings. In *Polymer Permeability;* Comyn, J., Ed.; Elsevier Applied Science Publishers: Essex, 1985; pp 331.

5 Lachish, U.; Steinberger, I. T. Electrical Current Measurements on Polystyrene Films. *J. Phys. D.: Appl. Phys.* **1974**, *7*, 58–68.

6 Charlson, E. J.; Charlson, E. M.; Sharma, A. K.; Yasuda, H. K. Electrical Properties of Glow Discharge Polymers, Parylenes and Composite Films. *J. Appl. Polym. Sci.: Appl. Polym. Symp*. **1984**, *38*, 137–148.

7 Battisti, A.; Hirayama, K.; Okuno, A. Unique Polybutadiene Resin: Characteristics After Hardening and Application to IC. In *Electronic Components and Technology Conference,* Proceedings of the 40th Conference, Las Vegas, USA, May 20–23, 1990; IEEE Components Packaging and Manufacturing Technology Society: New York, 1990, 620–624.

8 Weng, C.-J.; Chen, Y.-L.; Jhuo, Y. S.; Yi-Li, L.; Yeh, J. M. Advanced Antistatic/Anticorrosion Coatings Prepared from Polystyrene Composites Incorporating Dodecylbenzene Sulphonic Acid-Doped SiO_2 @Polyaniline Core-Shell Microspheres. *Polym. Int*. **2013**, *62*, 774–782.

9 Bubenzer, A.; Dischler, B.; Brandt, G.; Koidl, P. Rf-Plasma Deposited Amorphous Hydrogenated Hard Carbon Thin Films: Preparation, Properties and Applications. *J. Appl. Phys.* **1983**, *54*, 4590-4595.

10 Biederman, H.; Slavínská, D. Plasma Polymer Films and Their Future Prospects. *Surf. Coat. Technol.* **2000**, *125*, 371–376.

11 Lee, J. K.; Cathey, D. A.; Tjaden, K. Method for Forming High Resistance Resistors for Limiting Cathode Current in Field Emission Displays. *Patent* WO1997004482, February 6, 1997.

12 Yasuda, H. *Plasma Polymerization.* Academic Press Inc.; Orlando: 1985, pp 395–396.

13 Matonis, V. A. Contemporary Thermoplastic Materials. In *Polymer Handbook,* 2nd edition; Brandrup, J.; Immergut, E. H. Eds.; Wiley: New York, 1975; p VIII-6.

14 Polymer Database (PoLyInfo), National Institute for Materials Science. http://polymer.nims.go.jp/index_en.html (Accessed 09/06/14).

15 Matonis, V. A. Contemporary Thermoplastic Material – Property Chart. In *Polymer Handbook, Second Edition*; Brandrub, J.; Immergut, E. H. Ed.; Wiley: New York, 1975, p III-229.

16 Bergman, B. R. Barrier Layer for Inflatable Articles. *Patent* US20130186540, July 25, 2013.

17 Mark, V.; Hedges, C. V. Polycarbonate Compositions Having Improved Barrier Properties. *Patent* US4195157, March 25, 1980.

18 D'Angelo, P. F. Treating Hydrocarbon Polymer with Fluorine and Bromine Source. *Patent* US4142032, February 27, 1979.

19 Singh, B. High Barrier Solutions for Plastic Containers Using Fluorination Process. *The Economic Times Polymers*, 2008, *19-24* (Accessed 01/07/14).

20 Irwin, C. Blow Moulding. In *The Wiley Encyclopedia of Packaging Technology*. Yam, K. T., Ed.; John Wiley and Sons. 2009.

21 Borcia, G.; Brown, N. M. D. Hydrophobic Coatings on Selected Polymers in an Atmospheric Pressure Dielectric Barrier Discharge. *J. Phys. D.: Appl. Phys.* **2007**, *40*, 1927-1936.

22 Reick, F. G. Substrate Coated with Superhydrophobic Layers. *Patent* US3931428A, January 6, 1976.

23 Cassie, A. D. B.; Baxter, S. Wettability of Porous Surfaces. *T. Faraday Soc.* **1944**, *40*, 546–551.

24 Tokunaga, J. M. E.; Kumada, M. M. E. S.; Sugiyama, Y. M. E. S.; Watanabe, N.; Chong, Y.-B. Z. O.; Matsubara, N. M. E. S. Method of Forming Air Film on Submerged Surface of Submerged Part-Carrying Structure, and Film Structure on Submerged Surface. *Patent* WO1994007740A1, April 14, 1994.

25 Hsieh, T.-C.; Wu, F.-L.; Chen, W.-Y. Superhydrophobicity and Superoleophobicity from Hierarchical Silica Sphere Stacking Layers. *Mater. Chem. Phys*. **2010**, *121*, 14–21.

26 Lee, Y.; Park, S.-H.; Kim, K.-B.; Lee, J.-K. Fabrication of Hierarchical Structures on a Polymer Surface to Mimic Natural Superhydrophobic Surfaces. *Adv. Mater.* **2007**, *19*, 2330–2335.

27 Fan, Y.; He, Y.; Luo, P.; Chen, X.; Liu, B. A Facile Electrodeposition Process to Fabricate Corrosion-Resistant Superhydrophobic Surface on Carbon Steel. *Appl. Surf. Sci.* **2016**, *368*, 435–442.

28 Brassard, J. D.; Sarkar, D. K.; Perron, J.; Audibert-Hayet, A.; Melot, D. Nano-Micro Structured Superhydrophobic Zinc Coating on Steel for Prevention of Corrosion and Ice Adhesion. *J. Colloid Interface Sci.* **2014**, *297*, 109–115.

29 Wagner, P.; Fürster, R.; Barthlott, W.; Neinhuis, C. Quantitative Assessment to the Structural Basis of Water Repellency in Natural and Technical Surfaces. *J. Exp. Bot*. **2003**, *54*, 1295–1313.

30 Barthlott, W.; Neinhuis, C. Purity of the Sacred Lotus, or Escape from Contamination in Biological Surfaces. *Planta* **1997**, *202*, 1–8.

31 Wang, M.-F.; Raghunathan, N.; Ziaie, B. A Nonlithographic Top-Down Electrochemical Approach for Creating Hierarchical (Micro-Nano) Superhydrophobic Silicon Surfaces. *Langmuir* **2007**, *23*, 2300–2303.

32 Vakarelski, I. U.; Patankar, N. A.; Marston, J. O.; Chan, D. Y. C.; Thoroddsen, S. T. Stabilization of Leidenfrost Vapour Layer by Textured Superhydrophobic Surfaces. *Nature* **2012**, *489*, 274–277.

33 McCulloch, C. R.; Gill, R. C. Submersible Object Having Drag Reduction and Method. *Patent* US3973510A, August 10, 1976.

34 Tulis, A. J. Flowability Techniques in the Processing of Powdered Explosives, Propellants, and Pyrotechnics. *J. Hazard Mater.* **1980**, *4*, 3–10.

35 Tully, P. R. Water-Repellent Coating Compositions and Method for their Preparation. *Patent* US4102703A, July 25, 1978.

36 Shirtcliffe, N. J.; McHale, G.; Newton, M. I.; Perry, C. C.; Pyatt, F. P. Plastron Properties of a Superhydrophobic Surface. *Appl. Phys. Lett*. **2006**, *89*, 104106.

37 Lin, Y.; Shen, Y.; Liu, A.; Zhu, Y.; Liu, S.; Jiang, H. Bio-Inspiredly Fabricating the Hierarchical 3D Porous Structure Superhydrophobic Surfaces for Corrosion Protection. *Mater. Des.* **2016**, *103*, 300–307.

38 Ding, C. D.; Liu, Y.; Wang, M. D.; Wang, T.; Fu, J. J. Self-Healing Superhydrophobic Coating Based on Mechanised Silica Nanoparticles for Reliable Protection of Magnesium Alloys. *J. Mater. Chem. A* **2016**, *4*, 8041–8052.

39 Weng, C.-J.; Chang, C.-H.; Peng, C.-W.; Chen, S.-W.; Yeh, J.-M.; Hsu, C.-L.; Wei, Y. Advanced Anticorrosive Coatings Prepared from the Mimicked Xanthosoma Sagittifolium-Leaf-Like Electroactive Epoxy with Synergistic Effects

of Superhydrophobicity and Redox Catalytic Capability. *Chem. Mater.* **2011**, *23*, 2075–2083.

40 Chang, K.-C.; Lu, H.-I.; Peng, C.-W.; Lai, M.-C.; Hsu, S.-C.; Hsu, M.-H.; Tsai, Y.-K.; Chang, C.-H.; Hung, W.-I.; Wei, Y.; Yeh, J.-M. Nanocasting Technique to Prepare Lotus-Leaf-Like Superhydrophobic Electroactive Polyimide as Advanced Anticorrosive Coatings. *ACS Appl. Mater. Interfaces* **2013**, *5*, 1460–1467.

41 Peng, C.-W.; Chang, K.-C.; Weng, C.-J.; Lai, M.-C.; Hsu, C.-H.; Hsu, S.-C.; Li, S.-Y.; Wei, Y.; Yeh, J.-M. UV-Curable Nanocasting Technique to Prepare Bio-Mimetic Super-Hydrophobic Non-Fluorinated Polymeric Surfaces for Advanced Anticorrosive Coatings. *Polym. Chem.* **2013**, *4,* 926–932.

42 Chang, K.-C.; Chuang, T. L.; Ji, W. F.; Chang, C. H.; Peng, Y. Y.; Shih, H.; Hsu, C. L.; Yeh, J. M.; Tang, W. C.; Su, Y. C. UV-Curable Nanocasting Technique to Prepare Bioinspired Superhydrophobic Organic-Inorganic Composite Anticorrosion Coatings. *Express Polym. Lett*. **2015**, *9*, 143–153.

43 Yeh, J.-M.; Chang, K.-C.; Hsu, C.-H.; Ji, W.-F.; Hsu, M.-H.; Lu, H.-I.; Lai, M.-C.; Liu, P.-J.; Chuang, T.-L.; Wei, L.; Liu, W.-R.; Hsiao, Y.-R. Anticorrosive Layer Having a Biomimetic Leaf Surface Nano-Microstructure and Application Thereof. *Patent* US20160032111A1, February 4, 2016.

44 Batey, J.; Boland, J.; Parsons, G. N. Pulsed Gas Plasma-Enhanced Chemical Vapour Deposition of Silicon. *Patent* EP0526779, February 10, **1993**.

45 Parsons, G. N. Selective Deposition of Silicon by Plasma-Enhanced Chemical Vapour Deposition Using Pulsed Silane Flow. *Appl. Phys. Lett.* **1991**, *50*, 2456-2458.

46 Chowdhury, A. I.; Read, W. W.; Rubloff, G. W.; Teddler, L. L.; Parsons, G. N. Real-time Process Sensing and Metrology in Amorphous and Selective Area Silicon Plasma Enhanced Chemical Vapour Deposition Using *In-Situ* Mass Spectrometry. *J. Vac. Sci. Technol. B.* **1997**, *15*, 127-132.

47 Hienecke, R. A.; Ojha, S. M.; Llewellyn, I. P. Pulsed Plasma Apparatus and Process. *Patent* US4935661, June 19, **1990**.]

48 Wilmott, P. R.; Huber, J. R. Pulsed Laser Vaporization and Deposition. *Rev. Mod. Phys.* **2000**, *72*, 315-328.

49 Nishiguchi, K.; Hara, S.; Amano, T.; Hatatani, S.; Oda, S. Preparation of Nanocrystalline Silicon Quantum Dots by Pulsed Plasma Processes with High Deposition Rates. *Mater. Res. Soc. Symp. Proc.* **2011**, *571*, 1–6.

50 Ifuku, T.; Otbe, M.; Ita, A.; Oda, S. Fabrication of Nanocrystalline Silicon with a Small Spread of Particle Size by Pulsed Gas Plasma. *Jpn. J. Appl. Phys.* **1997**, *36*, 4031–4034

51 Graff, G. L.; Williford, R. E.; Burrows, P. E. Mechanisms of Vapour Permeation Through Multilayer Barrier Films: Lag Time Versus Equilibrium Permeation. *J. Appl. Phys.* **2004**, *96*, 1840–1849.

52 Raaijmakers, I. Apparatus and Method for Growth of a Thin Film. *Patent* US6511539, January 28, **2003**.

53 Teunissen, J.; Sun, A.; Ebert, U., A Time Scale for Electrical Screening in Pulsed Gas Discharges. *J. Phys. D.: Appl. Phys.* **2014,** *47* (36), 65203-65203.

54 Chapman, B. Glow Discharge Processes: Sputtering and Plasma Etching. John Wiley and Sons, Chichester, 1980.

55 Yoshida, S.; Okawara, C.; Ozeki, K. Process for Producing Multi-Layered Gas Barrier Film. *Patent* EP2397574, December 21, **2011**.

56 Beeson, C. L.; Cole, R. T.; Deak, G. I.; Leidolf, H. H. Jr. Alternating Layers of Polyvinylidene Chloride and Polyvinyl Alcohol. *Patent* US5225288, July 6, **1993**.

57 Kuehnle, M.; Hagenlocher, A.; Schuegraf, K.; Stratz, H. Gas Impermeable, Chemically Inert Container Structure for Food and Volatile Substances and the Method and Apparatus for Producing Same. *Patent* US20020041942A1, April 11, 2002.

58 Parsons, G. N. Selective Deposition of Silicon by Plasma-Enhanced Chemical Vapour Deposition Using Pulsed Silane Flow. *Appl. Phys. Lett.* **1991**, *50*, 2456–2458.

59 Sheng, S.; Chae, Y. K. Pulsed Plasma Deposition for Forming Microcrystalline Silicon Layer for Solar Applications. *Patent* US20100258169A1, October 14, 2010.

60 Daniel, A.; Le Pen, C.; Archambeau, C.; Reniers, F. Use of a PECVD-PVD Process for the Deposition of Copper Containing Organosilicon Thin Films on Steel. *Appl. Surf. Sci.* **2009**, *265*, 82–85.

61 Despax, B.; Raynaud, P. Deposition of “Polysiloxane” Thin Films Containing Silver Particles by an RF Asymmetrical Discharge. *Plasma Process Polym.* **2007**, *4*, 127–134.

62 Suntola, T. S.; Pakkala, A. J.; Lindfors, S. G. Apparatus for Performing Growth of Compound Thin Films. *Patent* US4389973A, June 28, 1983.

63 Badyal, J. P. S.; Hutton, S. J. Applying a Fluoropolymer Film to a Body. *Patent* WO1999032235A1, July 1, 1999.

64 Howson, R. P.; Danson, N.; Safi, I. High Rate Reactive Sputtering Using Gas Pulsing: A Technique for the Creation of Films onto Large, Flat Surfaces. *Thin Solid Films* **1999**, *351*, 32–36.

65 Miyamae, T.; Tsukagoshi, K.; Matsuoka, O.; Yamamoto, S.; Nozoye, H. Preparation of Polyimide-Polyamide Random Copolymer Thin Film by Sequential Vapour Deposition Polymerization. *Jpn. J. Appl. Phys*. **2002**, *41*, 746–748.

66 Hwang, Y.-H.; Cho, W.-J.; Kim, Y., Investigation of Tungsten Nitride Deposition Using Tungsten Hexafluoride Precursor for Via and Plug Metallization. *Jpn. J. Appl. Phys.* **2013,** *52*, 10MCO7-1–10MCO7-4.

67 Haaland, P. D. Hybrid Pulsed Valve for Thin Film Coating and Method. *Patent* US5403617A, April 4, 1995.

68 Goeckner, M.; Ogawa, D.; Saraf, I.; Overzet, L. J. Progress Report: Direct Injection of Liquids into Low Pressure Plasmas. *J. Phys.: Conf. Ser*. **2009**, *162*, 1–9.

69 Diebold, A. C.; Chism, W. W. Characterisation and Metrology of Medium Dielectric Constant Gate Dielectric Films. In *High Dielectric Constant Materials: VSLI MOSFET Applications*; Huff, H. R.; Gilmer, D. C., Eds. Springer-Verlag, Berlin Heidelberg 2005, p 486.

70 Lovering, D. NKD-6000 Technical Manual; Aquila Instruments: Cambridge, U.K., 1999.

71 Johnson, R. E. Jr.; Dettre, R. H. In *Wettability*; Berg J. C., Ed.; Marcel Dekker, Inc.: New York, 1993; Chapter 1, pp 1–75.

72 Beamson, G.; Briggs, D. *High Resolution XPS of Organic Polymers – The Scienta ESCA300 Database*, John Wiley & Sons: Chichester, 1992; pp 258–259.

73 Moulder, J. F.; Stickle, W. F.; Sobol, P. E.; Bomben, K. D. *Handbook of X-ray Photoelectron Spectroscopy*; Chastain, J., Ed.; Perkin-Elmer Corporation: Eden Prairie, 1992; pp 11–28.

74 Friedman, R. M.; Hudis, J.; Perlman, M. L. Chemical Effects on Linewidths Observed in Photoelectron Spectroscopy. *Phys. Rev. Lett*. **1972**, *29*, 692-695.

75 Lin-Vien, D.; Colthup, N. B.; Fateley, W. G.; Grasselli, J. G. The Handbook of Infrared and Raman Characteristic Frequencies of Organic Molecules, Academic Press, Inc.: San Diego, 1991.

76 Kaneko, T.; Nemoto, D.; Horiguchi, A.; Miyakawa, N. FTIR Analysis of a a-SiC:H Films Grown by Plasma Enhanced CVD. *J. Cryst. Growth* **2005**, *275*, 1097–1101.

77 Sancho-Parramon, J.; Bosch, S.; Canillas, A. Optical Characterization of ns-SiN:H in the Infrared by Spectroscopic Ellipsometry. *Appl. Surf. Sci.* **2006**, *253,* 65–69.

78 Steindl, J.; Koch, T.; Moszner, N.; Gorsche, C. Silane – Acrylate Chemistry for Regulating Network Formation in Radical Photopolymerization. *Macromolecules* **2017**, *50*, 7448–7457.

79 Cassie, A. D. B.; Baxter, S. Wettability of Porous Surfaces. *T. Faraday Soc.* **1944**, *40*, 546–551.

80 Extrand, C. W. Model for Contact Angles and Hysteresis on Rough and Ultraphobic Surfaces. *Langmuir* **2002**, *18*, 7991–7999.

81 Woodward, I.; Schofield, W. C. E.; Roucoules, V.; Badyal, J. P. S. Super-Hydrophobic Surfaces Produced by Plasma Fluorination of Polybutadiene Films. *Langmuir* **2003,** *19,* 3432–3438.

82 Brown, P. S.; Talbot, E. L.; Wood, T. J.; Bain, C. D.; Badyal, J. P. S. Superhydrophobic Hierarchical Honeycomb Surfaces. *Langmuir* **2012**, *28*, 13712–13719.

83 Jasper, J. J. Surface Tension of Pure Liquid Compounds. *J. Phys. Chem. Ref. Data* **1972**, *1*, 841–1009.

84 Moulder, J. F.; Stickle, W. F.; Sobol, P. E.; Bomben, K. D. *Handbook of X-ray Photoelectron Spectroscopy*; Chastain, J., Ed.; Perkin-Elmer Corporation: Eden Prairie, 1992.

85 Beamson, G.; Briggs, D. *High Resolution XPS of Organic Polymers – The Scienta ESCA300 Database*, John Wiley & Sons: Chichester, 1992.

86 Lin-Vien, D.; Colthup, N. B.; Fateley, W. G.; Grasselli, J. G. The Handbook of Infrared and Raman Characteristic Frequencies of Organic Molecules, Academic Press, Inc.: San Diego, 1991.

87 Yasuda, H. *Plasma Polymerization.* Academic Press Inc.; Orlando: 1985, pp 86–88.

88 Olde Riekerink, M. B.; Terlingen, J. G. A.; Engbers, G. H. M.; Feijen, J. Selective Etching of Semicrystalline Polymers: CF_4 Gas Plasma Treatment of Poly(ethylene). *Langmuir* **1999**, *15*, 4847–4856.

89 Butter, R. S.; Waterman, D. R.; Lettington, A. H.; Ramos, R. T.; Fordham, E. J. Production and Wetting Properties of Fluorinated Diamond-Like Carbon Coatings. *Thin Solid Films* **1997**, *311*, 107–113.

90 Vesel, A.; Hydrophobization of Polymer Polystyrene in Fluorine Plasma. *Mater. Technol.* **2011**, *45*, 217–220.

91 Kim, Y.; Lee, Y.; Han, S.; Kim, K.–J. Improvement of Hydrophobic Properties of Polymer Surfaces by Plasma Source Ion Implantation. *Surf. Coat. Technol*. **2006**, *200*, 4763–4769.

92 Dowling, D. P.; Miller, I. S.; Ardhaoui, M.; Gallagher, W. M. Effect of Surface Wettability and Topography on the Adhesion of Osteosarcoma Cells on Plasma Modified Polystyrene. *J. Biomater. Appl*. **2010**, *1*, 1–21.

93 Sigurdsson, S.; Shishoo, R. Surface Properties of Polymers Treated with Tetrafluoromethane Plasma. *J. Appl. Poly. Sci.* **1997**, *66*, 1591–1601.

94 Garrod, R. P.; Harris, L. G.; Schofield, W. C. E.; McGettrick, J.; Ward, L. J.; Teare, D. O. H.; Badyal, J. P. S. Mimicking a Stenocara Beetle's Back for Microcondensation Using Plasmachemical Patterned Superhydrophobic-Superhydrophilic Surfaces. *Langmuir* **2007**, *23*, 689–693.

95 Wen, C.-H.; Chuang, M.-J.; Hsiue, G.-H. Plasma Fluorination of Polymers in Glow Discharge Plasma with a Continuous Process. *Thin Solid Films* **2006**, *503*, 103–109.

96 Di Mundo, R.; De Benedictis, V.; Palumbo, F.; d'Agostino, R. Fluorocarbon Plasmas for Nanotexturing of Polymers: A Route to Water-Repellent Antireflective Surfaces. *Appl. Surf. Sci.* **2009**, *255*, 5461–5465.

97 Winters, H. F.; Coburn, J. W.; Chuang, T. J. Surface Processes in Plasma-Assisted Etching Environments. *J. Vac. Sci. Technol. B* **1983**, *469*.

98 Nojiri, K. Mechanisms of Dry Etching. In *Dry Etching Technology for Semiconductors*. Springer International Publishing, **2015**.

99 Li, W.; Amirfazli, A. A Thermodynamic Approach for Determining the Contact Angle Hysteresis for Superhydrophobic Surfaces. *J. Colloid Interface Sci.* **2005**, *292*, 195–201.

100 Li, W.; Amirfazli, A. Microtextured Superhydrophobic Surfaces: A Thermodynamic Study. *Adv. Colloid Interface Sci*. **2007**, *132*, 51–68.

101 Li, W.; Amirfazli, A. Hierarchical Structures for Natural Superhydrophobic Surfaces. *Soft Matter* **2008**, *4*, 462–466.

102 Brown, P. S.; Berson, A.; Talbot, E. L.; Wood, T. J.; Schofield, W. C. E.; Bain, C. D.; Badyal, J. P. S. Impact of Picoliter Droplets on Superhydrophobic Surfaces with Ultralow Spreading Ratios. *Langmuir* **2011**, *27*, 13897–13903.

103 Otten, A.; Herminghaus, S. How Plants Keep Dry: A Physicists Point of View. *Langmuir* **2004**, *20*, 2405–2408.

104 Neinhuis, C.; Barthlott, W. Characterization and Distribution of Water-Repellent, Self-Cleaning Plant Surfaces. *Ann. Bot*. **1997**, *79*, 667–677.

105 Herminhaus, S. Roughness-Induced Non-Wetting. *Europhys. Lett.* **2000**, *52*, 165–170.

106 Wagner, P.; Fürstner, R.; Barthlott, W.; Neinhius, C. Quantitative Assessment to the Structural Basis of Water Repellency in Natural and Technical Surfaces. *J. Exp. Bot.* **2003**, *54*, 1295–1303.

107 Koch, K.; Barthlott, W. Superhydrophobic and Superhydrophilic Plant Surfaces: An Inspiration for Biomimetic Materials. *Phil. Trans. R. Soc. A* **2009**, *367*, 1487–1509.

108 Cheng, Y. T.; Rodak, D. E.; Wong, C. A.; Hayden, C. A. Effects of Micro- and Nano-Structures on the Self-Cleaning Behaviour of Lotus Leaves. *Nanotechnology* **2006**, *17*, 1359–1362.

109 Lee, Y.; Park, S.-H.; Kim, K.-B.; Lee, J.-K. Fabrication of Hierarchical Structures on a Polymer Surface to Mimic Natural Superhydrophobic Surfaces. *Adv. Mater.* **2007**, *19*, 2330–2335.

110 Fürstner, R.; Barthlott, W.; Neinhius, C.; Walzel, P. Wetting and Self-Cleaning Properties of Artificial Superhydrophobic Surfaces. *Langmuir* **2005**, *21*, 956–961.

111 Xiu, Y.; Zhu, L.; Hess, D. W.; Wong, C. P. Biomimetic Creation of Hierarchical Surface Structures by Combining Colloidal Self-Assembly and Au Sputter Deposition. *Langmuir* **2006**, *22*, 9676–9681.

112 Bico, J.; Marzolin, C.; Quéré, D. Pearl Drops. *Europhys. Lett*. **1999**, *147*, 220–226.

113 Nosonovsky, M.; Bhushan, B. Hierarchical Roughness Optimization for Biomimetic Superhydrophobic Surfaces. *Ultramicroscopy* **2007**, *107*, 969–979.

114 Koch, K.; Bhushan, B.; Jung, Y. C.; Barthlott, W. Fabrication of Artificial Lotus Leaves and Significance of Hierarchical Structure for Superhydrophobicity and Low Adhesion. *Soft Matter* **2009**, *5*, 1386–1393.

115 Choi, H.–J.; Choo, S.; Shin, J.–H.; Kim, K.–I.; Lee, H. Fabrication of Superhydrophobic and Oleophobic Surfaces with Overhang Structure by Reverse Nanoimprint Lithography. *J. Phys. Chem. C* **2013**, *117*, 24354–24359.

116 Lakshmi, R. V.; Bharathidasan, T.; Bera, P.; Basu, B. J. Fabrication of Superhydrophobic and Oleophobic Sol-Gel Nanocomposite Coating. *Surf. Coat. Technol.* **2012**, *206*, 3888–3894.

117 Gao, S.-H.; Gao, L.-H.; Zhou, K.-S. Super-Hydrophobicity and Oleophobicity of Silicon Rubber Modified by CF_4 Radio Frequency Plasma. *Appl. Surf. Sci.* **2011**, *257*, 4945–4950.

Chapter 5 : Plasmachemical Thiol–Acrylate Electrical Barrier

5.1. Abstract

Using the principles of thiol–ene and thiol–acrylate reactions, coatings were formed from the dual-feed plasma deposition of an acrylate and an unsaturated thiol-containing precursor. These coatings proved to be effective wet electrical barrier coatings when deposited onto an unsaturated polymer base layer. This coating system showed similar electrical barrier results to the deposition of solely an unsaturated thiol-containing precursor on an unsaturated polymer base layer using the standard electrical measurement method. However, the dual-feed thiol–acrylate plasma deposited coatings showed a much-improved response at higher applied voltages, suggesting the formation of a strong, crosslinked top layer.

5.2. Introduction

As they are a more specific subset of the traditional thiol–ene reactions which were referred to previously, see Chapter 1 and Chapter 3, thiol-acrylate photopolymerisations can be used to form strong, highly-crosslinked polymer networks.[1–10] This utilises the favourable reactions between thiyl radicals (typically generated by photoinitiation) and the double bonds of the acrylate functional groups, Scheme 5-1.[2–6] The step growth radical initiation of thiol–acrylate photopolymerisations can progress in a very similar way to the thiol–ene reaction. However, acrylates homopolymerise easily via chain-growth polymerisation as well as being able to abstract hydrogen from neighbouring thiol species. The thiyl radical, generated by photoinitiation, propagates the reaction through the acrylate monomer carbon-carbon double bond. With the radical then residing on the chain, chain transfer reactions can occur, abstracting the hydrogen from a nearby thiol, leaving an intact polymer chain and a newly regenerated thiyl radical. Alternatively, the radical situated on the chain can react with the carbon-carbon double bond of another acrylate monomer, leading to chain branching and the creation of crosslinks between monomers or polymer chains.[2,6]

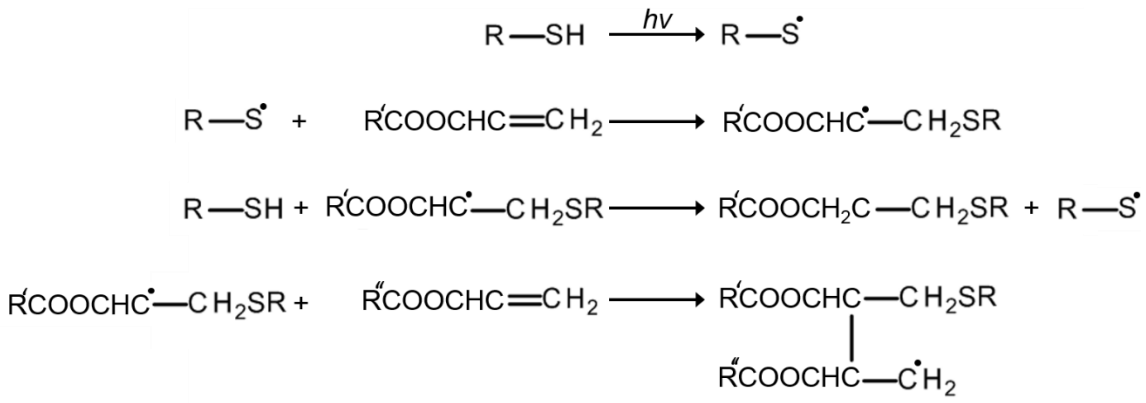

Scheme 5-1: Thiol–acrylate reaction mechanism.[1,2,6]

These reactions can occur very quickly and require only a low light intensity, allowing the very rapid formation of a crosslinked network under very mild conditions.[1,4] Following the step growth mechanism, the networks obtained tend to have a more uniform density and low shrinkage stress compared to polymers formed from a chain growth mechanism.[4] The reaction can also be facilitated by the use of a base or a nucleophile, also known as the thiol–Michael addition.[11,12] This can be accelerated by the selection of an activated vinyl group, such as a vinyl group conjugated to a carbonyl group, to make the required nucleophilic attack more favourable.[4,13]

The thiol assisted opening of the acrylate double bonds can be applied to methacrylate and dimethacrylate systems, as they also contain the required carbon-carbon double bonds.[14–16] The necessary unsaturation can similarly be found in carbon-carbon triple bond systems, resulting in thiol–yne reactions.[12,17,18]

Due to the extent of crosslinking, these rapid and efficient reactions have often been used in the formation of hydrogels,[7,16,19,20] and have been used as oxygen barriers for food packaging.[21] As such, a strongly crosslinked, dense thiol–acrylate polymerised layer could be highly beneficial as a barrier coating to protect electronics from water damage.[22] In principle, a combination of crosslinking and multilayering should lead to further improvement in electrical barrier performance.[23] However, existing fabrication processes involve multiple steps, taking an extended length of time, as well as requiring elevated temperatures. The rapidity and mild conditions required for thiol–acrylate crosslinking reactions gives an advantage over previously existing methods of electrical barrier fabrication. In

this chapter, the attributes of combining interfacial crosslinking with multilayering is accomplished through the utilisation of plasmachemical thiol–acrylate reactions leading to high wet electrical barrier performance.

5.3. Experimental

5.3.1. Polymer Spin Coating

Polymer spin coating was performed as per Section 2.4. A 5% w/v polybutadiene solution was prepared by dissolving 2.5 g polybutadiene (PBD, Mw ~200,000, Sigma-Aldrich Co.) in toluene (99.99 wt%, Fisher Scientific Ltd.) in a 50 mL volumetric flask. The solution was agitated for 3 days (sample shaker Vibrax-VXR Model No. VX 2, IKA-Werke GmbH) to ensure the polybutadiene had completely dissolved. The polybutadiene solution was spin coated at 3000 rpm onto the prepared micro-circuit boards.

A 10% w/v polyisoprene solution was prepared by dissolving 2 g polyisoprene (PIP, Mw ~40,000, Sigma-Aldrich Co.) in toluene to make up to 20 mL total volume. The solution was agitated for 2 days to ensure the polyisoprene had completely dissolved. The polyisoprene solution was spin coated at 3000 rpm onto the prepared micro-circuit boards.

A 10% w/v polystyrene solution was prepared by dissolving 1 g polystyrene (PS, Mw ~280,000, Sigma-Aldrich Co.) in toluene in a 10 mL volumetric flask. The solution was agitated for 2 days on the sample shaker to ensure the polystyrene was completely dissolved. 3 drops (~240 µL) of the polystyrene solution were spin coated onto the prepared micro-circuit boards at 2000 rpm.

For spray coating, a 5% w/v polyisoprene solution was prepared by dissolving 5 g polyisoprene in tetrahydrofuran (>99.5 wt%, Fisher Scientific Ltd.) to make up to 100 mL total volume. The solution was agitated for two days to ensure the polyisoprene had completely dissolved. The substrate was spray coated using a manual spray gun (model RG-3L, Anest Iwata, Inc.), at a distance of 10 cm for 35 s.

5.3.2. Plasma Modification

Plasma depositions were carried out as per Section 2.5. The precursors used for plasma deposition were allyl mercaptan (2-propene-1-thiol, AM, +80 wt% purity, Tokyo Chemical Industry Ltd.), ethylene glycol dimethacrylate (EGDM, 98 wt% purity, Sigma-Aldrich Co.), 1-propanethiol (+99 wt% purity, Sigma-Aldrich Co.) tetramethylsilane (TMS, +99.9 wt% purity, Alfa Aesar Co. Ltd.), glycidyl methacrylate (GMA, +97 wt% purity, Sigma-Aldrich Co.), 1H,1H,2H,2H-perfluorooctyl acrylate (PFAC-6, +95 wt% purity, Fluorochem Ltd.), and tripropylene glycol diacrylate (TGDA, +90 wt% purity Tokyo Chemical Industry Ltd.). The precursors were degassed prior to use by 5 freeze-pump-thaw cycles. H_2S gas (+99.5% purity, Sigma-Aldrich Co.) was used for plasma surface modification. The substrate was placed into the centre of the reactor, followed by evacuation to system base pressure.

5.3.3. Film Thickness

Film thickness measurements were carried out on coated silicon wafer pieces (1 cm^2, 5–20 Ω cm resistivity, Silicon Valley Microelectronics Inc.) using a spectrophotometer (model nkd-6000, Aquila Instruments Ltd.). The obtained transmittance–reflectance curves (350–1000 nm wavelength range, using a parallel (P) polarised light source at a 30° incident angle) were fitted to a Cauchy model for dielectric materials,[24] using a modified Levenberg–Marquardt method (version 2.2 software modified upgrade, Pro-Optix, Aquila Instruments Ltd.).[25] The thickness values quoted herein were measured in this way, and prior to taking these coatings towards scale up and industrialisation the thicknesses should be confirmed using other methods, such as microscopy or SEM.

5.3.4. Contact Angle

Microlitre sessile drop contact angle analysis was carried out with a video capture system (VCA2500XE, AST Products Inc.) using 1.0 µL dispensation of ultra-high purity water (BS 3978 grade 1), hexadecane (99%, Sigma Aldrich Ltd.), tetradecane (+99%, Sigma Aldrich Ltd.), dodecane (99%, Sigma Aldrich Ltd.), decane (+99%, Sigma Aldrich Ltd.), octane (+99%, Sigma Aldrich Ltd.), heptane (99%, Sigma Aldrich Ltd.). After a droplet was placed onto the surface, a snapshot was taken. The resulting static image of the droplet was analysed (VCA-2500 Dynamic software) to calculate the right- and left-hand side contact angles. Advancing and receding contact angles were measured by respectively increasing and decreasing the droplet size until the contact line was observed to move.[26] A captive bubble attachment (VCA captive bubble accessory, AST Products Inc.) was used to detect the presence of an air layer between the plasma fluorinated surface and surrounding high purity water.

5.3.5. Infrared Spectroscopy

Fourier transform infrared (FTIR) spectroscopic analysis of the plasma polymers deposited onto silicon wafer was carried out using a FTIR Spectrometer (Spectrum One, PerkinElmer Inc.), equipped with a liquid nitrogen cooled MCT detector operating across the 450–4000 cm^{-1} range. Reflection–absorption infrared spectroscopy (RAIRS) measurements were performed using a variable angle accessory (Specac Ltd.) with the mirrors aligned at an angle of 66° to the sample normal. The spectra were averaged over 285 scans at a resolution of 4 cm^{-1}.

5.4. Results and Discussion

5.4.1. Dual Feed Plasma Layer Deposition

Water contact angle measurements were taken of single feed plasma deposited allyl mercaptan and ethylene glycol dimethacrylate layers, as well as the dual

monomer feed plasma deposited layers to determine whether one plasma polymer was depositing preferentially, Table 5-1. Although there was a small decrease in the contact angle of the composite layer compared to the solely allyl mercaptan layer, no significant difference was seen, so assessment of the coatings via contact angle was not possible. It also suggested that the allyl mercaptan deposited preferentially over the ethylene glycol dimethacrylate, leading to a single component layer, rather than a composite.

Table 5-1: Water contact angles of the plasma deposited (2 W, 0.2 mbar, 10 min) allyl mercaptan, ethylene glycol dimethacrylate (2 W, 0.1 mbar, 20 min), and composite allyl mercaptan/ethylene glycol dimethacrylate layers (2 W, 0.15 mbar, 10 min).

Coating	**Deposition Method**	**Water Contact Angle / °**
Allyl mercaptan	Continuous wave plasma	83 ± 1
Ethylene glycol dimethacrylate	Continuous wave plasma	61 ± 2
Allyl mercaptan and ethylene glycol dimethacrylate	Dual feed continuous wave plasma	80 ± 1

However, infrared spectroscopy demonstrated that preferential deposition of the allyl mercaptan was not the case. The spectra obtained showed the presence of carbonyl stretches (1732 cm^{-1}) in the dual feed plasma deposited allyl mercaptan and ethylene glycol dimethacrylate layer, as well as the solely ethylene glycol dimethacrylate plasma deposited layer, but these were not present in the allyl mercaptan spectrum, Figure 5-1. Likewise, the C-O-C stretches (1170 cm^{-1}) were present in the allyl mercaptan and composite layers. The allyl mercaptan and the composite layers showed sulphoxide stretches (1050 cm^{-1}) and thiocarbonyl stretches (1236 cm^{-1}).[27–30] This demonstrates that the dual feed plasma deposition process allowed the deposition of composite layers, rather than the preferential deposition of one plasma polymer in preference to the other.

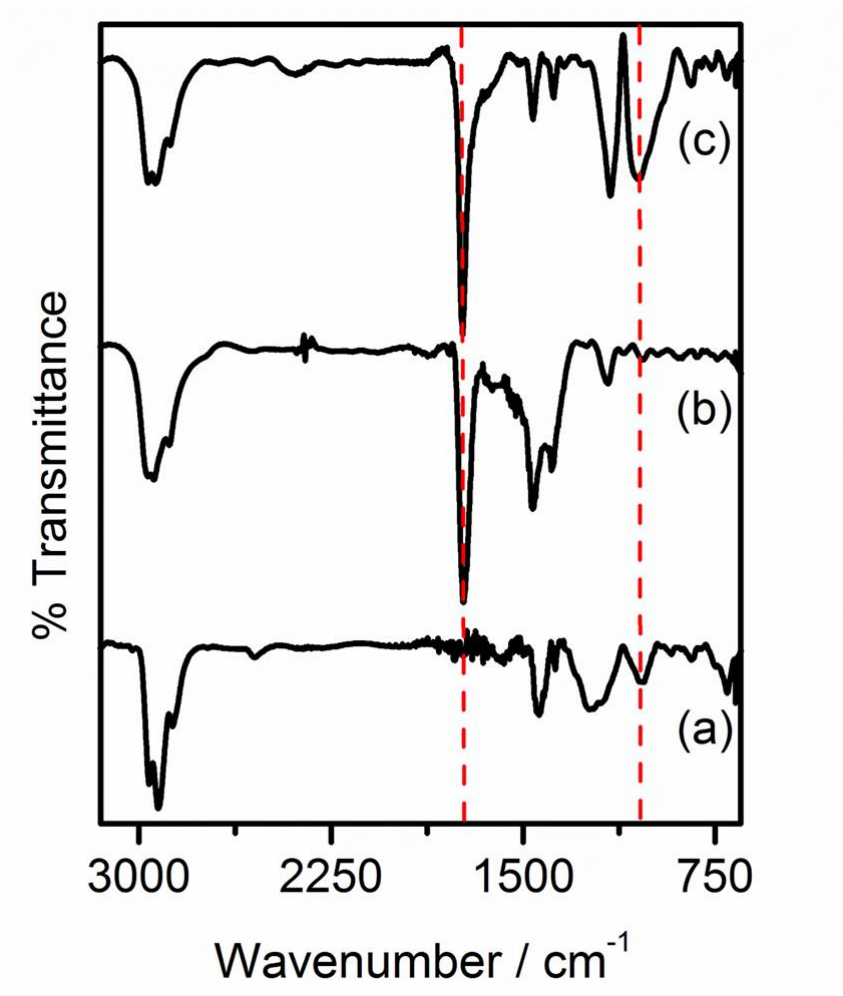

Figure 5-1: FTIR of: (a) plasma deposited allyl mercaptan (continuous wave 2 W, 0.2 mbar, 10 min); (b) plasma deposited ethylene glycol dimethacrylate (continuous wave 2 W, 0.1 mbar, 20 min); and (c) dual feed plasma deposited allyl mercaptan and ethylene glycol dimethacrylate (continuous wave 2 W, 0.15 mbar, 10 min). Dashed lines indicate C=O (1732 cm^{-1}) and thiol S=O (1050 cm^{-1}) stretches respectively.

5.4.2. Wet Electrical Barrier

The structure behaviour relationship shown in Chapter 3, Figure 3-1, demonstrated the validity of the concept of applying a plasmachemical crosslinked top layer on a polymer base layer. The thinnest plasma deposited layers displaying high electrical barrier were obtained when using an allyl mercaptan precursor; whilst in contrast, structurally related 1-propanethiol was found to be poor at a comparable plasma layer thickness.

Using the results found from these plasma depositions and electrical barrier measurements, it was postulated that further crosslinking could be obtained from the thiol–ene top layer by the addition of an acrylate, to facilitate thiol–acrylate crosslinking. This was accomplished by introducing the methacrylate containing precursor, ethylene glycol dimethacrylate, and the allyl mercaptan to the plasma chamber concurrently, for plasmachemical deposition onto a polyisoprene base layer, Figure 5-2. The wet electrical barrier results showed that there was little difference in the water barrier performance of the allyl mercaptan plasma deposited layer and the allyl mercaptan/ethylene glycol dimethacrylate plasma deposited composite layer, with both achieving a high barrier performance at around 800 nm on a sub-micron polyisoprene base layer. The plasma coatings were also deposited onto a polystyrene base layer. Both polyisoprene and polystyrene contain unsaturated carbon-carbon bonds, however only the polyisoprene layers contain the alkene bonds required for thiol–ene reactions with the plasma generated reactive sulphur species (e.g. thiyl radicals). This is demonstrated by the very poor wet electrical barrier performance of both the allyl mercaptan and the allyl mercaptan/ethylene glycol dimethacrylate composite layers on the polystyrene base layer even at high thicknesses. It is thus shown that part of what makes the wet electrical barrier so successful on polyisoprene is the availability of the double bonds for crosslinking with the thiyl radicals.

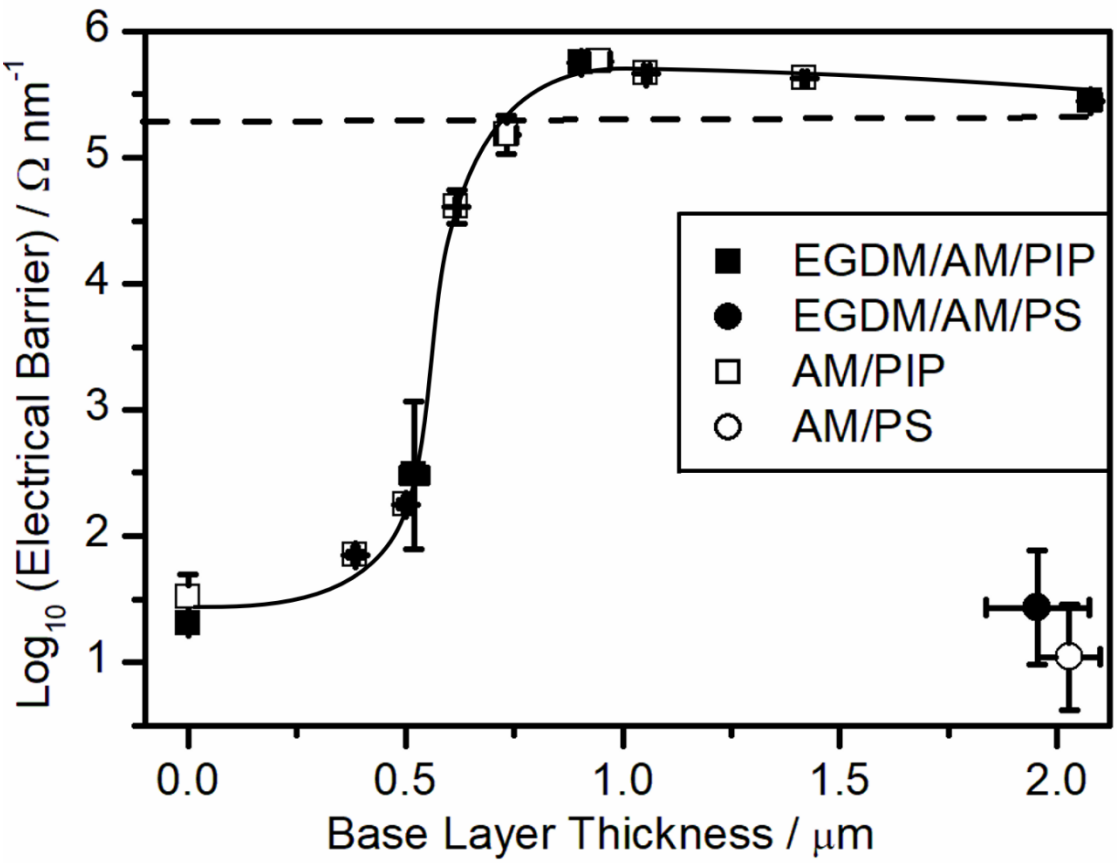

Figure 5-2: Wet electrical barrier performance of plasma deposited allyl mercaptan (continuous wave, 2 W, 0.2 mbar, 10 min) and dual feed plasma deposited ethylene glycol dimethacrylate/allyl mercaptan (continuous wave, 2 W, 0.15 mbar, 10 min) on polyisoprene (PIP) and polystyrene (PS) base layers, measured at 8 V for 13 min. Samples above the dashed line reached the instrument detection limit of 8 x 10^8 Ω. Lines have been included as a guide to the eye.

It was proposed that the reactions of the thiyl radicals with the carbon-carbon double bonds of the acrylates could possibly create a crosslinked network which would be sufficient as a barrier coating on its own, Figure 5-3. Allyl mercaptan and either ethylene glycol dimethacrylate or tripropylene glycol diacrylate were fed concurrently into the plasma chamber, in order to deposit composite layers. Additionally, alternate layers of allyl mercaptan and ethylene glycol dimethacrylate were deposited. However, these coatings proved to be poor wet electrical barriers in comparison to an allyl mercaptan layer on polyisoprene, suggesting that the unsaturated bonds in the polyisoprene were more available for crosslinking than the acrylate or methacrylate precursors. However, continued research into this

could benefit from further optimisation of the plasma deposition parameters, to fully exploit the thiol–acrylate reactions.

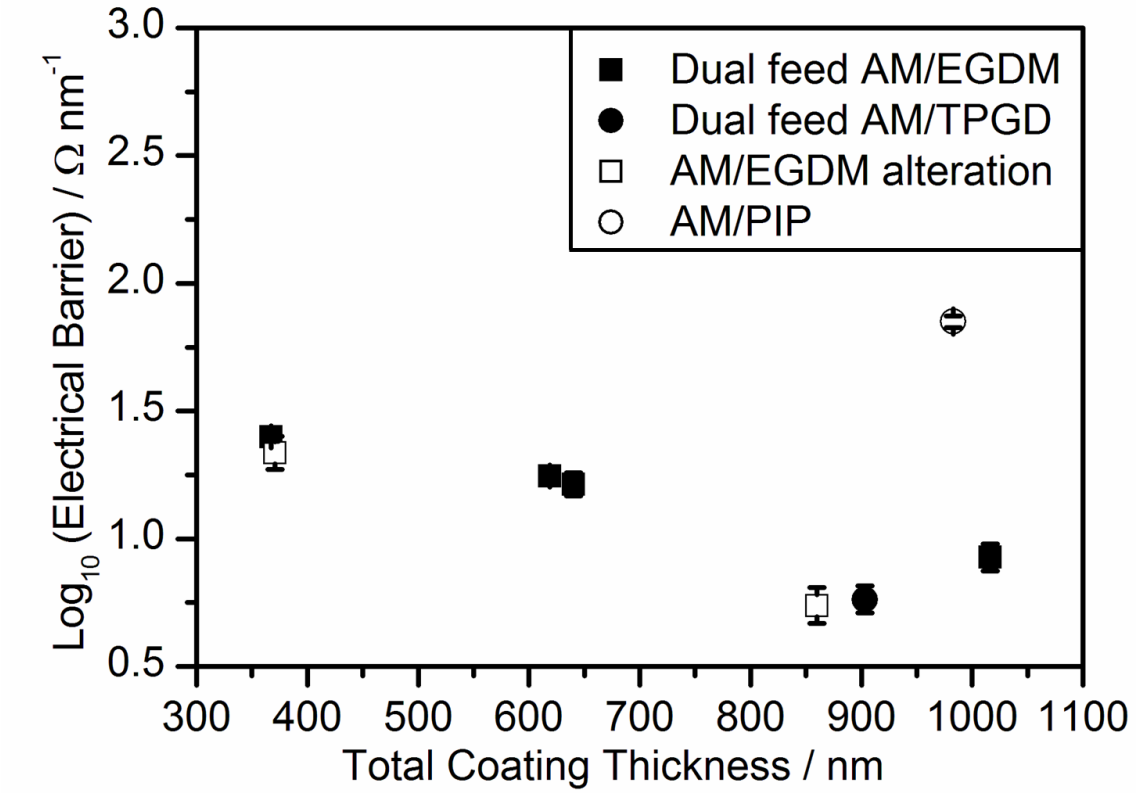

Figure 5-3: Wet electrical barrier performance of dual feed plasma deposited allyl mercaptan/ethylene glycol dimethacrylate (continuous wave, 2 W, 0.15 mbar, 10 min), dual feel plasma deposited allyl methacrylate/tripropylene glycol diacrylate (continuous wave, 2 W, 0.2 mbar, 20 min), alternating layers of allyl mercaptan and ethylene glycol dimethacrylate (continuous wave, 2 W, 0.2 and 0.1 mbar, 20 min), compared to plasma deposited allyl mercaptan (continuous wave, 2 W, 0.2 mbar, 10 min) on a polyisoprene base layer, measured at 8 V for 13 min.

The polyisoprene coating with an allyl mercaptan base layer, Chapter 3, began to break down under an applied electric field of 20 V mm^{-1}, Figure 3-8, however, the dual feed plasma deposited allyl mercaptan and ethylene glycol dimethacrylate composite on a polyisoprene base layer did not show any breakdown of the coating beyond the application of an electric field of 30 V mm^{-1}, Figure 5-4. This demonstrated that there was an increase in wet electrical barrier performance for the dual feed allyl mercaptan and ethylene glycol dimethacrylate compared to solely allyl mercaptan, even if it was not immediately apparent when measured under the standard conditions.

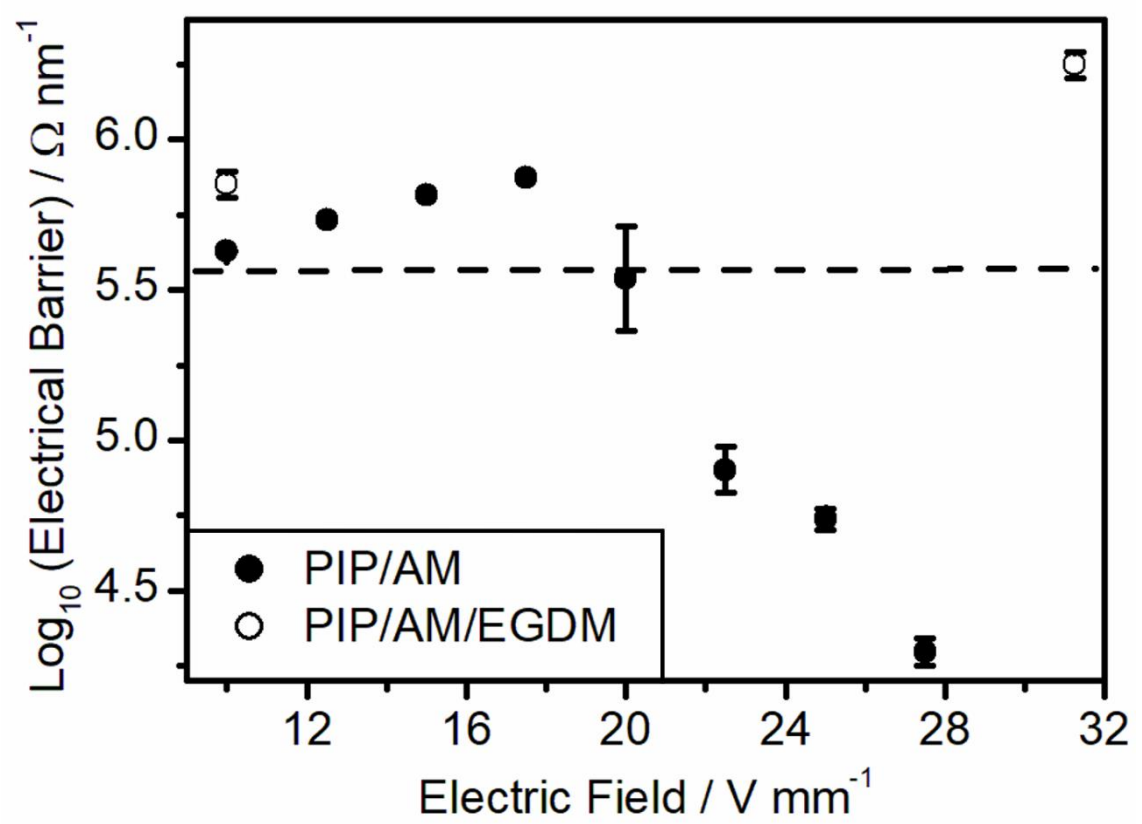

Figure 5-4: Wet electrical barrier after 13 min immersion in water as a function of applied electric field, for fixed thickness allyl mercaptan plasma polymer (continuous wave, 2 W, 0.2 mbar, 507 ± 14 nm) and a polyisoprene base layer (thickness 1350 ± 40 nm), denoted by ●, and fixed thickness dual feed allyl mercaptan/ethylene glycol dimethacrylate deposited layer (continuous wave, 12 W, 0.2 mbar, 512 ± 178 nm) and polyisoprene base layer (thickness 904 ± 15 nm), denoted by ○. Samples above the dashed line reached the instrument detection limit.

5.5. Conclusions and Further Work

The dual deposition of allyl mercaptan and acrylates was used to form a composite layer, Table 5-1 and Figure 5-1, in order to try to improve the wet electrical barrier performance over what was found using only allyl mercaptan plasma deposited on a polyisoprene base layer. However, it was seen that there was no improvement in the wet electrical barrier performance using the dual deposition of allyl mercaptan and ethylene glycol dimethacrylate, with the results showing an almost exactly matching trend of increase in barrier performance along with an increase in the layer thickness, Figure 5-2. Without the polyisoprene base layer, dual

deposition of allyl mercaptan and ethylene glycol dimethacrylate or tripropylene glycol diacrylate showed no promise as wet electrical barrier coatings, Figure 5-3, and a poor performance was found using alternating layers of allyl mercaptan and ethylene glycol dimethacrylate. With these results taken into consideration, it would appear that there was little reason to pursue dual feed depositions of allyl mercaptan and ethylene glycol dimethacrylate.

However, under further investigation, differences in the coating performances could be established. Measuring the coatings under an applied electric field of 31.25 V mm^{-1} highlighted the improvements found using the dual feed deposition of allyl mercaptan and ethylene glycol dimethacrylate over the sole deposition allyl mercaptan, Figure 5-4. With further examination the coatings could be subjected to harsher testing, such as time to failure analysis, wherein the coated circuit boards are immersed in water under an applied voltage for the length of time needed to see coating breakdown. As the composite allyl mercaptan and ethylene glycol dimethacrylate coatings on polyisoprene showed a similar improvement in wet electrical barrier performance with increasing thickness compared to the solely allyl mercaptan on polyisoprene coatings during the standard immersion measurement, the wet electrical barrier performance of the coatings could be measured when immersed in salt water or other liquids a phone may come into contact with, such as coffee or dishwater.

Aside from wet electrical barrier performance there may be other benefits imparted by the reactions of the allyl mercaptan with the acrylate groups. Depositing the acrylate groups along with the allyl mercaptan on top of the polyisoprene base layer, whilst not obviously improving the barrier performance at during the standard 8 V immersion test, could show other types improvements. Micro- or nano-indentation could be used to determine the hardness of the crosslinked network, and the different coatings could be abraded or scratched to determine the cohesion of the internal structure and the adhesion of the coating to the circuit board. Using these proposed methods in further investigations of the coatings it could be possible to determine whether there was any significant improvement in the inclusion of acrylates in dual plasma depositions. The initial research conducted here provides a base for further investigations.

5.6. References

1 Rydholm, A. E.; Bowman, C. E.; Anseth, K. S. Degradable Thiol-Acrylate Photopolymers: Polymerization and Degradation Behaviour of an In Situ Forming Biomaterial. *Biomaterials* **2005**, *26*, 4495–4506.

2 Cramer, N. B.; Bowman, C. N. Kinetics of Thiol-Ene and Thiol-Acrylate Photopolymerizations with Real-Time Fourier Transform Infrared. *J. Polym. Sci., Part A: Polym. Chem.* **2001**, *39*, 3311–3319.

3 Senyurt, A. F.; Wei, H.; Hoyle, C. E.; Piland, S. G.; Gould, T. E. Ternary Thiol-Ene/Acrylate Photopolymers: Effect of Acrylate Structure on Mechanical Properties. *Macromolecules* **2007**, *40*, 4901–4909.

4 Chatani, S.; Nair, D. P.; Bowman, C. N. Relative Reactivity and Selectivity of Vinyl Sulphones and Acrylates Towards the Thiol-Michael Addition Reaction and Polymerization. *Polym. Chem.* **2013**, *4*, 1048–1055.

5 Lowe, A. B. Thiol-Ene “Click” Reactions and Recent Applications in Polymer and Materials Synthesis. *Polym. Chem*. **2010**, *1*, 17–36.

6 Kade, M. J.; Burke, D. J.; Hawker, C. J. The Power of Thiol-Ene Chemistry. *J. Polym. Sci., Part A: Polym. Chem.* **2010**, *48*, 743-750.

7 Shih, H.; Fraser, A. K.; Lin, C.-C. Interfacial Thiol-Ene Photoclick Reactions for Forming Multilayer Hydrogels. *ACS Appl. Mater. Interfaces* **2013**, *5*, 1673–1680.

8 Jacobine, A. F. Thiol-ene photopolymers. In *Radiation Curing in Polymer Science and Technology*. J. P. Fouassier, Rabek, J. F. Eds.; Elsevier Science: Essex; 1993, Vol. 3; p 247–248.

9 Khire, V. S.; Lee, T. Y.; Bowman, C. N. Surface Modification Using Thiol-Acrylate Conjugate Addition Reactions. *Macromolecules* **2007**, *46*, 5669–5677.

10 Tehfe, M.-A.; Mondal, S.; Nechab, M.; Dumur, F.; Bertrand, M. P.; Graff, B.; Gigmes, D.; Fouassier, J.-P.; Lalevée, J. New Thiols for Photoinitiator Free Thiol-Acrylate Polymerization. *Macromol. Chem. Phys.* **2013**, *214*, 1302–1308.

11 Chan, J. W.; Hoyle, C. E.; Lowe, A. B. Sequential Phosphine-Catalyzed, Nucleophilic Thiol-Ene/Radical-Mediated Thiol-Yne Reactions and the Facile Orthogonal Synthesis of Polyfunctional Materials. *J. Am. Chem. Soc.* **2009**, *131*, 5751–5753.

12 Li, G.-Z.; Randev, R. K.; Soeriyadi, A. H.; Rees, G.; Boyer, C.; Tong, Z.; Davis, T. P.; Becer, C. R.; Haddleton, D. M. Investigation into Thiol-(Meth)Acrylate Michael Addition Reactions using Amine and Phosphine Catalysts. *Polym. Chem.* **2010**, *1*, 1196–1204.

13 Mather, B. D.; Viswanathan, K.; Miller, K. M.; Long, T. E. Michael Addition Reactions in Macromolecular Design for Emerging Technologies. *Prog. Polym. Sci.* **2006**, *31*, 487–531.

14 Lecamp, L.; Houllier, F.; Youssef, B.; Bunel, C. Photoinitiated Cross-linking of a Thiol-Methacrylate System. *Polymer* **2001**, *42*, 2727–2736.

15 Lu, H.; Carioscia, J. A.; Stansbury J. W.; Bowman, C. N. Investigations of Step-Growth Thiol-Ene Polymerizations for Novel Dental Restoratives. *Dent. Mater. J.* **2005**, *21*, 1129–1136.

16 Higham, A. K.; Garber, L. A.; Latshaw II, D. C.; Hall, C. K.; Pojman, J. A.; Khan, S. A. Gelation and Cross-Linking in Multifunctional Thiol and Multifunctional Acrylate Involving an in Situ Comonomer Catalyst. *Macromolecules* **2014**, *47*, 821–829.

17 Ye, S.; Cramer, N. B.; Smith, I. R.; Voigt, K. R.; Bowman, C. N. Reaction Kinetics and Reduced Shrinkage Stress of Thiol-Yne Methacrylate and Thiol-Yne Acrylate Ternary Systems. *Macromolecules* **2011**, *44*, 9084–9090.

18 Fairbanks, B. D.; Scott, T. F.; Kloxin, C. J.; Anseth, K. S.; Bowan, C. N. Thiol-Yne Photopolymerizations: Novel Mechanism, Kinetics, and Step-Growth

Formation of Highly Cross-Linked Networks. *Macromolecules* **2009**, *42*, 211–217.

19 Pritchard, C. D.; O'Shea, T. M.; Siegwart, D. J.; Calo, E.; Anderson, D. G.; Reynolds, F. M.; Thomas, J. A.; Slotkin, J. R.; Woodard, E. J.; Langer, R. An Injectable Thiol-Acrylate Poly(Ethylene Glycol) Hydrogel for Sustained Release of Methylprednisolone Sodium Succinate. *Biomaterials* **2011**, *32*, 587–597.

20 Salinas, C. N.; Anseth, K. S. Mixed Mode Thiol-Acrylate Photopolymerizations for the Synthesis of PEG-Peptide Hydrogels. *Macromolecules* **2008**, *41*, 6019–6026.

21 Kwisnek, L.; Nazarenko, S.; Hoyle, C. E. Oxygen Transport Properties of Thiol-Ene Networks. *Macromolecules* **2009**, *42*, 7031–7041.

22 Hamouda, H. Cathodic Protection. In *Handbook of Environmental Degradation of Materials*; Kutz, M., Ed.; William Andrew Inc.: Norwich, 2005; pp 368–369.

23 Yamanouchi, S.; Kondo, M.; Inoue, Y. Cross Linked Polyethylene-Insulated Cable. *Patent* EP0111393, June 20, 1984.

24 Diebold, A. C.; Chism, W. W. Characterisation and Metrology of Medium Dielectric Constant Gate Dielectric Films. In *High Dielectric Constant Materials: VSLI MOSFET Applications*; Huff, H. R.; Gilmer, D. C., Eds. Springer-Verlag, Berlin Heidelberg 2005, p 486.

25 Lovering, D. NKD-6000 Technical Manual; Aquila Instruments: Cambridge, U.K., 1999.

26 Johnson, R. E. Jr.; Dettre, R. H. In *Wettability*; Berg J. C., Ed.; Marcel Dekker, Inc.: New York, 1993; Chapter 1, pp 1–75.

27 Lin-Vien, D.; Colthup, N. B.; Fateley, W. G.; Grasselli, J. G. The Handbook of Infrared and Raman Characteristic Frequencies of Organic Molecules, Academic Press, Inc.: San Diego, 1991.

28 Rao, C. N. R.; Venkataraghavan, R.; Kasturi, T. R. Contribution to the Infrared Spectra of Organosulphur Compounds. *Can. J. Chem.* **1964**, *42*, 36–42.

29 Schofield, W. C. E.; McGettrick, J.; Bradley, T. J.; Badyal, J. P. S.; Przyborski, S. Rewritable DNA Microarrays. *J. Am. Chem. Soc.* **2006**, *128*, 2280–2285.

30 Tarducci, C.; Schofield, W. C. E.; Badyal, J. P. S.; Brewer, S. A.; Willis, C. Synthesis of Cross-Linked Ethylene Glycol Dimethacrylate and Cyclic Methacrylic Anhydride Polymer Structures by Pulsed Plasma Deposition. *Macromolecules* **2002**, *35*, 8724–8727.

Chapter 6 : Conclusions

The results presented in this thesis demonstrate various methods for depositing barrier coatings, suitable for the protection of electronic items from corrosion and electrical breakdown during immersion in water. These coatings have the potential to be taken for industrial applications and used for the protection of personal electronics, such as smartphones and wearable devices, which are often subject to damage by accidental water contact. Water contact with a circuit board can cause corrosion and irreversible damage, leaving the device unusable. As more people worldwide are using smartphones and other small personal electronic devices, the loss of these devices to accidental water damage is increasing. The financial and environmental cost of repairing and replacing personal devices is high, to both the consumer and the seller, and the more that can be done to reduce these costs, the better.

It was demonstrated that depositing a thin layer of an unsaturated polymer, such as polybutadiene or polyisoprene, prior to plasma deposition or functionalisation can be a quick and straight forward way to obtain a highly effective barrier coating. In the first case, Chapter 3, an unsaturated polymer base layer was plasma coated with an unsaturated thiol containing compound, allyl mercaptan. This combination of coatings proved to be an outstanding wet electrical barrier, due to the nature of the materials and the plasma induced interactions. The sulphur radicals produced in the allyl mercaptan plasma reacted with the double bonds in the polymer base layer in a “vulcanisation-like” reaction, whilst the double bonds from the allyl mercaptan plasma formed a strong crosslinked network on top of the polyisoprene layer. This resulted in a durable coating which was strong enough to withstand prolonged immersion in water under an applied electric field of 10 V mm^{-1}, far higher than the nominal cell voltage used in most smartphones today. It should be taken into account that the field strength on the circuit board of a smartphone may be higher than the field strength that was used herein as a representative test. As these coatings can withstand even higher voltages it suggests that they would be sufficient, but this can only be confirmed by further testing on immersed smartphone circuitry.

In the second case, Chapter 4, surface functionalisation of the unsaturated polymer layer resulted in an highly superhydrophobic coating, showing a very high water contact angle in conjunction with a very low water contact angle hysteresis. This coating was prepared by plasma fluorination of a polyisoprene layer, where the plasma activated carbon-fluorine species could react with the unsaturated sites on the polymer layer during the plasma process, to give a fluorinated surface. The plasma fluorination of the unsaturated layer resulted in a highly roughened surface. This coating also showed a significant degree of oleophobicity, and when applied to a glass substrate allowed it to be floated on water. This short, low power plasma functionalisation process was able to maintain a layer of air between the surface and any surrounding water when immersed due to the extreme hydrophobicity. The deposition of a plasma polymer base layer such as allyl mercaptan or tetramethylsilane with pulsed air prior to the unsaturated polymer layer allowed the coating to be used as a wet electrical barrier coating, protecting the substrate from corrosion when subjected to an applied electric field of 10 V mm^{-1}.

Based on the results found in Chapter 3, it was postulated that the inclusion of an acrylate or methacrylate containing precursor would aid in the crosslinking of the top layer of the coating system, Chapter 5. Thiol–acrylate and thiol–ene reactions proceed in similar ways, so the mechanism proposed for the plasmachemical double click thiol–ene should be preserved. The plasma deposition of the allyl mercaptan and ethylene glycol dimethacrylate was performed simultaneously, with both precursors depositing non-preferentially. In terms of wet electrical barrier performance, the coatings performed similarly, increasing in barrier performance with thickness at the same rate. Further research into these barrier systems could provide some differentiation between the properties of the coatings. The hardness, adhesion, cohesion and thermal stability of the coatings should be investigated to determine how these coatings would perform in a real-world scenario.

These coating systems, when applied to a circuit board, showed a more than sufficient wet electrical barrier performance, protecting the electrodes from corrosion by preventing them from coming into contact with water. The standard 13 min tap water immersion used to obtain the wet electrical barrier performance of the coatings was carried out at 8 V, which exceeded the nominal cell voltage of

a typical smartphone (~4 V). As stated previously, in order to fully assess the functionality of these coatings on a smartphone or other electronic item, it would have to be applied to the circuit board in question and subjected to immersion testing.

More information about the structure and precise mechanisms of these coatings should be attained with further research into this area. Layer-by-layer analysis of the coatings should be taken throughout the deposition processes, including AFM and SEM to attain information on the surface topography. As the thickness of these coatings is of critical importance when considering the quality of the electrical barrier, a secondary method of thickness measurement should be utilised to confirm the results and ensure they are accurate. Additionally, EIS, dielectric strength and surface resistivity measurements should be taken of the electrical barrier coatings described in this thesis to allow direct comparison with other work in the field. The work carried out herein was not done in this way due to alignment with the P2i's methods of barrier testing. The immersion method used was analogous, but not identical to the recommended method, and validation of this method was carried out on externally coated samples.

Further immersion testing of the coatings would be valuable, as it is not only with tap water that personal electronics come into contact. To evaluate the level of protection in other circumstances, the coatings could be pushed to their limits; immersion in salt water or any electrolyte containing solution would put more strain on the coating than immersion in tap water and accelerate the breakdown of the coating. This provides scope for further enhancements and improvements to these coatings. Future work in this area should take this into consideration, and the wet electrical barrier performance should be evaluated under a variety of conditions: immersion in the types of liquids which a personal device may come into contact with on a regular basis, such as tea, coffee, milk, alcoholic drinks, sea water and soapy water. Wearable devices should also be tested with regards to their resistance to soap and sweat. Furthermore, other tests should be employed to evaluate the quality of the barrier coatings. Nano and micro-indentation should be used to assess the hardness of the coating, and handling, tape peel and abrasion testing can be used to measure the adhesion of the coating to the substrate. Ideally a coating would be strong, able to withstand the conditions and potential hazards

of an assembly line, but have a low enough breakthrough force to allow connection of the various electronic components through the coating where necessary. It would also be beneficial to treat electronic items such as smartphones with these coatings, then after reassembly they should be subjected to repeated IPx7 (immersion in 1 m water for 30 min) and IPx8 (immersion in 2 m water for 30 min) tests until failure of the device. This would provide a realistic demonstration of the capabilities of the coatings.

Scalability from the small lab to the industrial scale should always be considered when designing a wet electrical barrier coating; the high throughput required in smartphone manufacturing and assembly lines means the applied coating should have minimal process steps and not require harsh conditions or reactants. The plasma treatments used in the formation of these barrier coatings are short, low powered, and use only a small volume of precursor, which is ideal for scaling the process up to the industrial level. Longer processes requiring higher powers and greater precursor volumes decrease the number of units which can be processed per hour in a factory, as well as increasing the treatment costs. The polymer base layers used herein can be applied on a large scale by spray or dip coating, allowing for the uniform coating of the 3D structures on circuit boards. Alternatively, the unsaturated layers could also be plasma deposited, with careful selection of the parameters to maintain the required double bonds. The subsequent plasma treatments (whether functionalisation, deposition, or a combination of the two) of this base layer are conformal in nature, allowing every surface of the polymer layer to be treated, meaning that every surface of the circuit board would receive the same level of wet electrical barrier protection.

Chapter 7 : Appendices

7.1. Appendix 1

7.1.1. Validation

7.1.1.1. Circuit Board Validation

The micro-stripboards used to obtain the resistance of the applied barrier coatings when immersed in liquid were shown to respond to an applied voltage with a proportional increase in current, Figure 7-1. An increase in current was seen immediately on applying 0.5 V to the stripboard. The current remained stable until the voltage was increased to 1 V and increased in a step like pattern until 6 V was reached. Beyond this point the steps became less defined, as more severe corrosion was occurring, forming bubbles on the surface of the coating which would temporarily lower the current response by preventing further corrosion at that point.

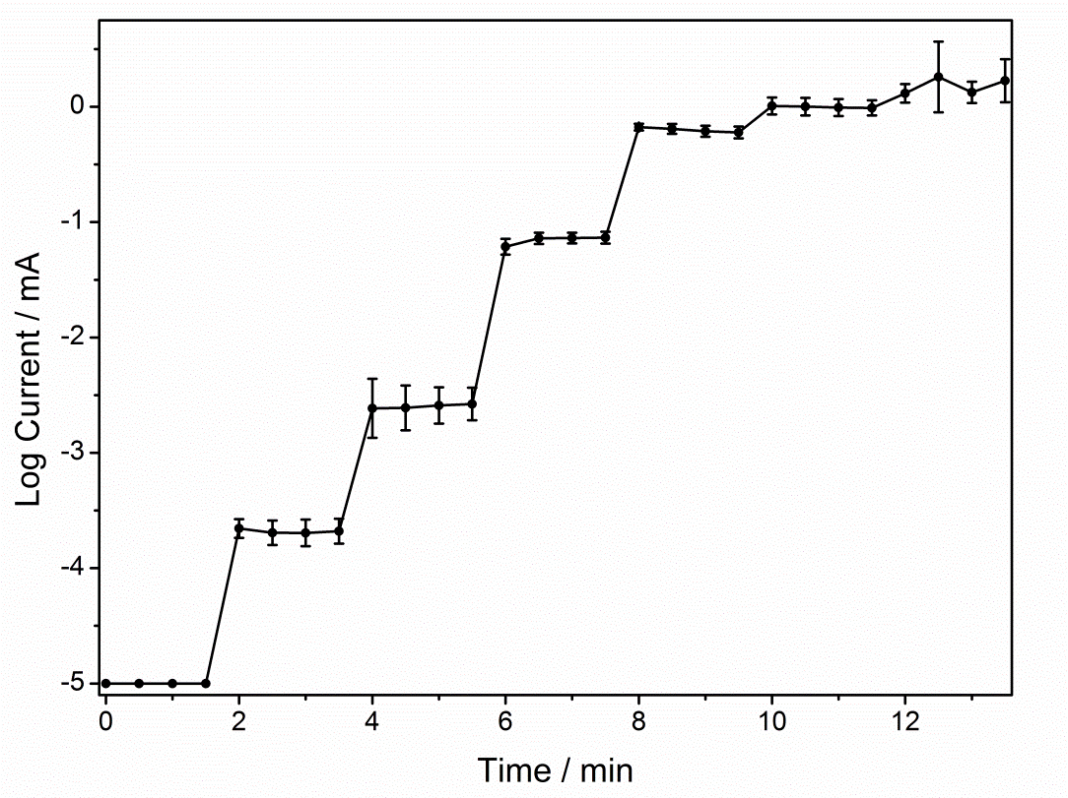

Figure 7-1: Current change in response to gradual voltage increase across micro-stripboards, starting at 0 V, increasing to 0.5 V, and subsequently doubling the voltage every 2 min to reach 8 V after 12 min.

7.1.1.2. Polymer Layer Validation

There was a clear correlation between the average final current measurements of the samples with the thickness of a polybutadiene base layer. Below 1000 nm coating thickness, the resistance was very low, but by 1800 nm there was no current increase over 13 min at 8 V, Figure 7-2. This showed that the measurement system employed gave a current response corresponding to the properties of the coating in question.

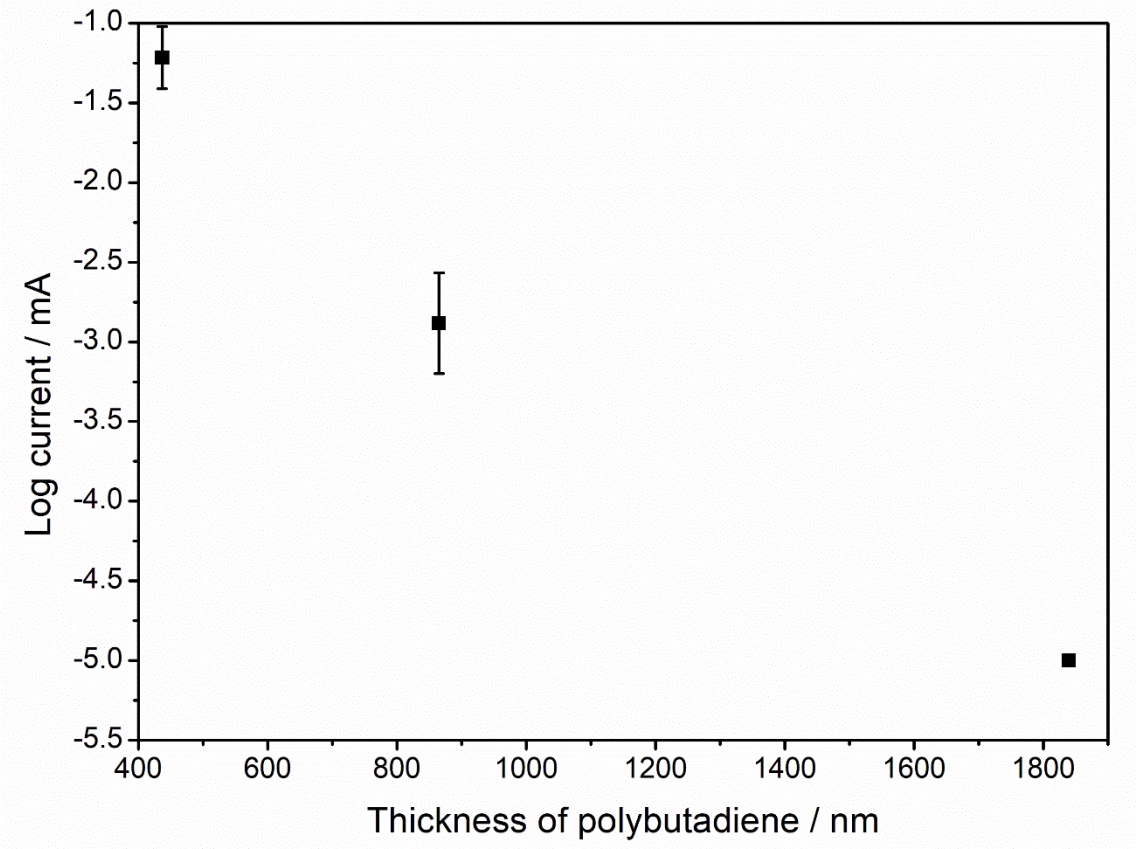

Figure 7-2: Current measurements of plasma fluorinated crosslinked polybutadiene layers of varying thicknesses, coated with plasma deposited GMA (5 W, 0.2 mbar, 820–2000 nm) measured at 8 V, for 13 min.

7.1.1.3. Optimisation of Spin Coating Procedure

The thickness of spin coated base layers can be determined in part by the concentration of the polymer solution, with higher concentrations resulting in thicker layers, Figure 7-3.

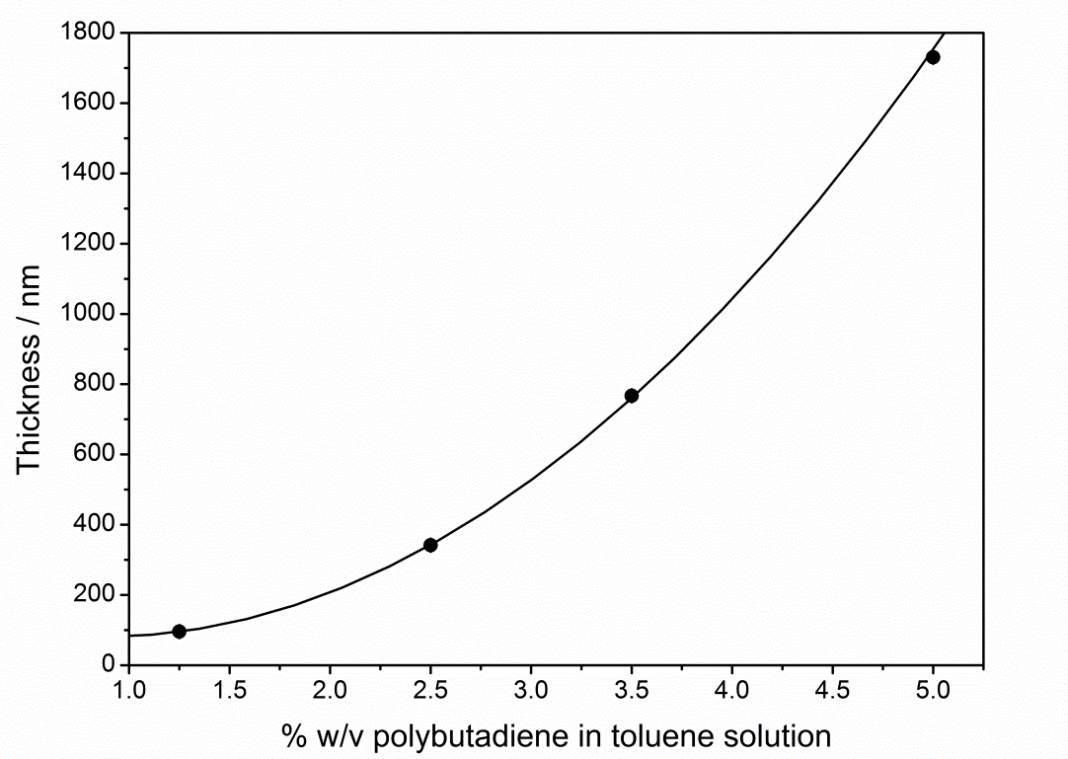

Figure 7-3: Thickness of polybutadiene base layers spin coated from 1.25% w/v, 2.50% w/v, 3.50% w/v, and 5.00% w/v polybutadiene in toluene solution.

It was found that equivalent layer thicknesses could not be attained when using different solution concentrations, Figure 7-4. A 2.5% w/v solution could not give a layer of similar thickness to a 5.0% w/v solution, despite the number of drops deposited. Additionally, it was noted that increasing the number of drops deposited decreased the total layer thickness. This was thought to be because the most recently deposited drop would “wash” the already deposited polymer off the surface during the spin coating procedure.

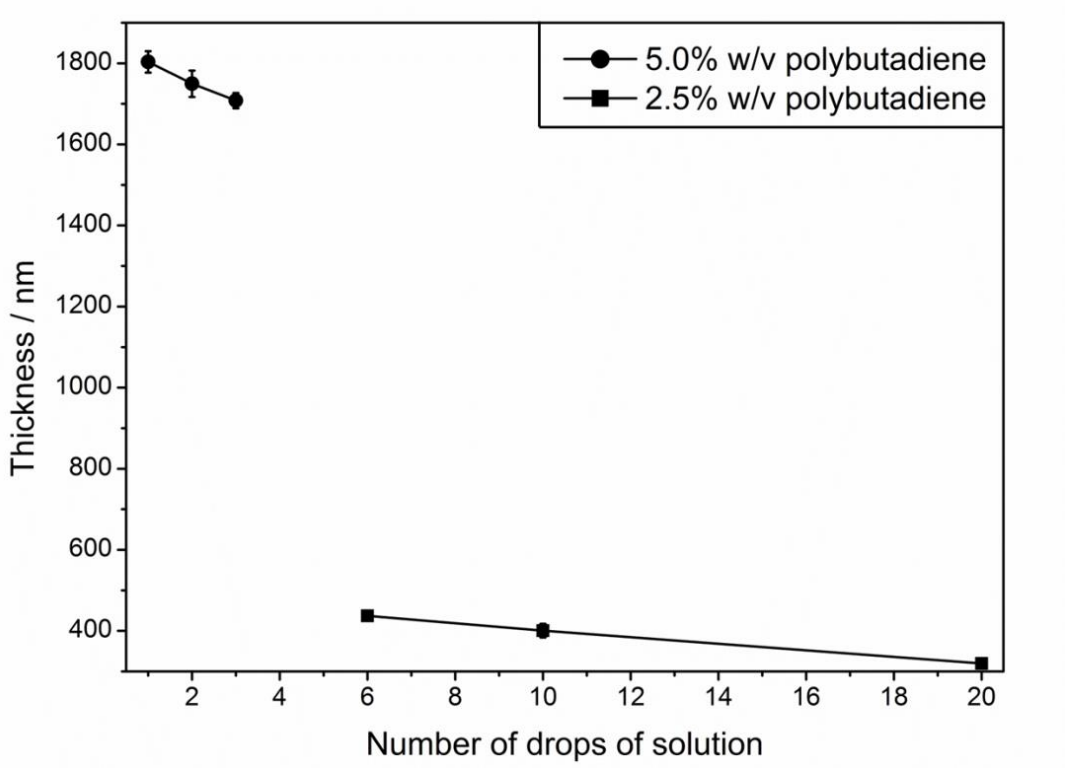

Figure 7-4: Thickness of the polybutadiene base layer in relation to the concentration of the solution (2.5% w/v and 5.0% w/v polybutadiene in toluene) and the number of drops deposited.

7.2. Appendix 2

7.2.1. Residence Time Calculation

The molar leakage rate, Qm, must be calculated from the plasma chamber variables, Equation 7-1,

$$\boldsymbol{Qm} = \frac{\left[\left(\Delta \boldsymbol{P}/_{\Delta \boldsymbol{t}}\right) - \left(\Delta \boldsymbol{P_0}/_{\Delta \boldsymbol{t_0}}\right)\right]\boldsymbol{V}}{(\boldsymbol{RT})} \qquad \textbf{Equation 7-1}$$

where Δt is the time required for the pressure to rise over the pressure range, ΔP, with the chamber isolated from the pump with monomer flow, Δt_0 is the time required for the pressure to rise over the pressure range, ΔP_0, when the chamber is isolated from the pump without monomer flow, V is the volume of the chamber,

R is the gas constant, and T is the temperature. The throughput, Q, can be calculated using the obtained molecular flow rate, Equation 7-2,[1]

$$\boldsymbol{Qm} = \frac{\boldsymbol{Q}}{\boldsymbol{RT}} \qquad \textbf{Equation 7-2}$$

The residence time can be then calculated from Equation 7-3,

$$\boldsymbol{\tau} = \frac{\boldsymbol{PV}}{\boldsymbol{Q}} \qquad \textbf{Equation 7-3}$$

where Q is the throughput, which is the rate of change with time of the product of the pressure of a gas and the volume in which it is contained (Pa m^3 s^{-1}), P is the pressure (Pa) and V is the volume of the chamber (m^3).

Example:

The measured parameters were as follows:

Initial Pressure:	0.2 mbar
Final Pressure:	0.4 mbar
Duration:	30 s
Volume of Reactor:	470 cm^3
Temperature:	25 °C

Following unit conversions, the following parameters were inputted into the leakage rate equation, Equation 7-1:

Initial Pressure:	20 Pa
Final Pressure:	40 Pa
Duration:	30 s
Volume of Reactor:	4.7 x10^{-4} m^3
Temperature:	298 K

Change in leak rate pressure:	10 Pa
Leak rate duration:	7200 s

$$\boldsymbol{Qm} = \frac{\left[\left(\boldsymbol{\Delta P}/\boldsymbol{\Delta t}\right) - \left(\boldsymbol{\Delta P_0}/\boldsymbol{\Delta t_0}\right)\right]\boldsymbol{V}}{(\boldsymbol{RT})}$$

$$Qm = \frac{[(40-20/1440)-(20-10/7200)]0.00047}{(8.3144621)(298)}$$

$$Qm = \frac{[(0.666667)-(0.001389)]0.00047}{(8.3144621)(298)}$$

$$Qm = \frac{3.127 \times 10^{-4}}{(2477.71)}$$

$$Qm = 1.26 \times 10^{-7} \text{ mol s}^{-1}$$

The obtained leak rate was used to calculate the throughput, Q, Equation 7-2:

$$Qm = \frac{Q}{RT}$$

$$Q = Qm \times RT$$

$$Q = 1.26 \times 10^{-7} \times 2477.71$$

$$Q = 3.12 \times 10^{-4} \text{ Pa m}^3 \text{ s}^{-1}$$

The calculated throughput was then used to calculate the gas residence time, τ, Equation 7-3:

$$\tau = \frac{PV}{Q}$$

$$\tau = \frac{20 \times 0.00047}{3.12 \times 10^{-4}}$$

$$\tau = 30 \text{ s}$$

7.3. Appendix 3

7.3.1. General Wet Electrical Barrier Improvements

7.3.1.1. Polybutadiene Improvements

An unmodified, solely polybutadiene layer was a poor wet electrical barrier coating, but some significant improvements could be made, Figure 7-5 and Figure 7-6, using only simple methods. Crosslinking by heating the coatings to 150 °C improved the barrier performance slightly, as well as smoothing out the current response to give fewer fluctuations. This was due to the reorganisation of the polymer chains above their T_g, reducing the number of defects and pin holes during the reorganisation. A further improvement could be found by fluorinating the surface of the polybutadiene with a CF_4 plasma. However, through a combination of these treatments, first fluorination then crosslinking, the current was lowered even further, to give a much better wet electrical barrier performance. The combination of these processes had a more significant effect on the barrier performance than the two separate processes.

This is thought to be due to the plasma fluorination incorporating the large fluorine atoms on the surface, blocking the pores in the polymer network as well as imparting a degree of water repellency to the surface. The crosslinking then caused any remaining unsaturated bonds in the polymer structure to form a strong polymer network, as well as allowing rearrangement of the polymer chains, reducing the size of any remaining pores present in the film. This rearrangement also allowed complete reorientation of the surface $–CF_3$, $–CF_2$ and –CF groups to the surface, making it more water repellent. Neither the crosslinking nor the fluorination of the polybutadiene layer had any bearing on the thickness of the coating, showing that the wet electrical barrier performance can be improved without necessarily making the coating thicker.

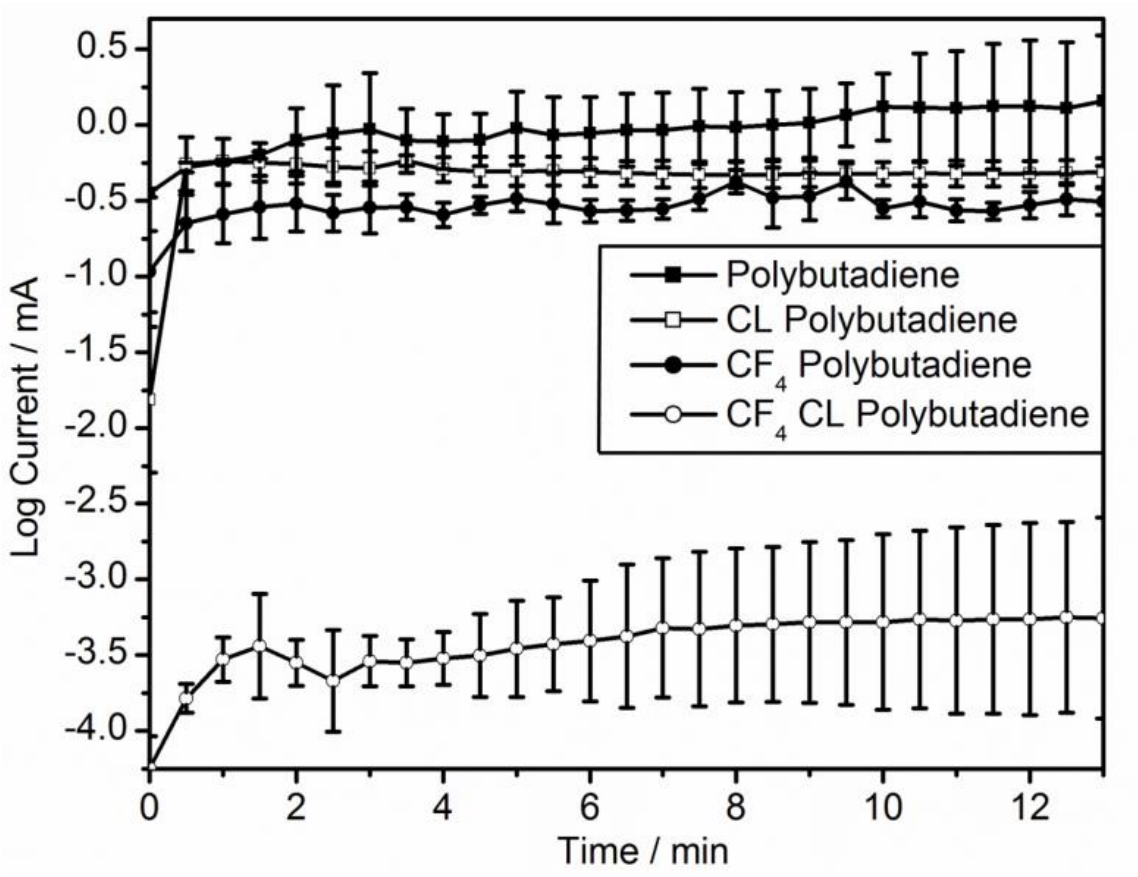

Figure 7-5: Current response for polybutadiene, crosslinked polybutadiene, plasma fluorinated (30 W, 0.2 mbar, 5 min) polybutadiene and crosslinked plasma fluorinated polybutadiene, with an average thickness of 1880 ± 30 nm, measured at 4 V for 13 min.

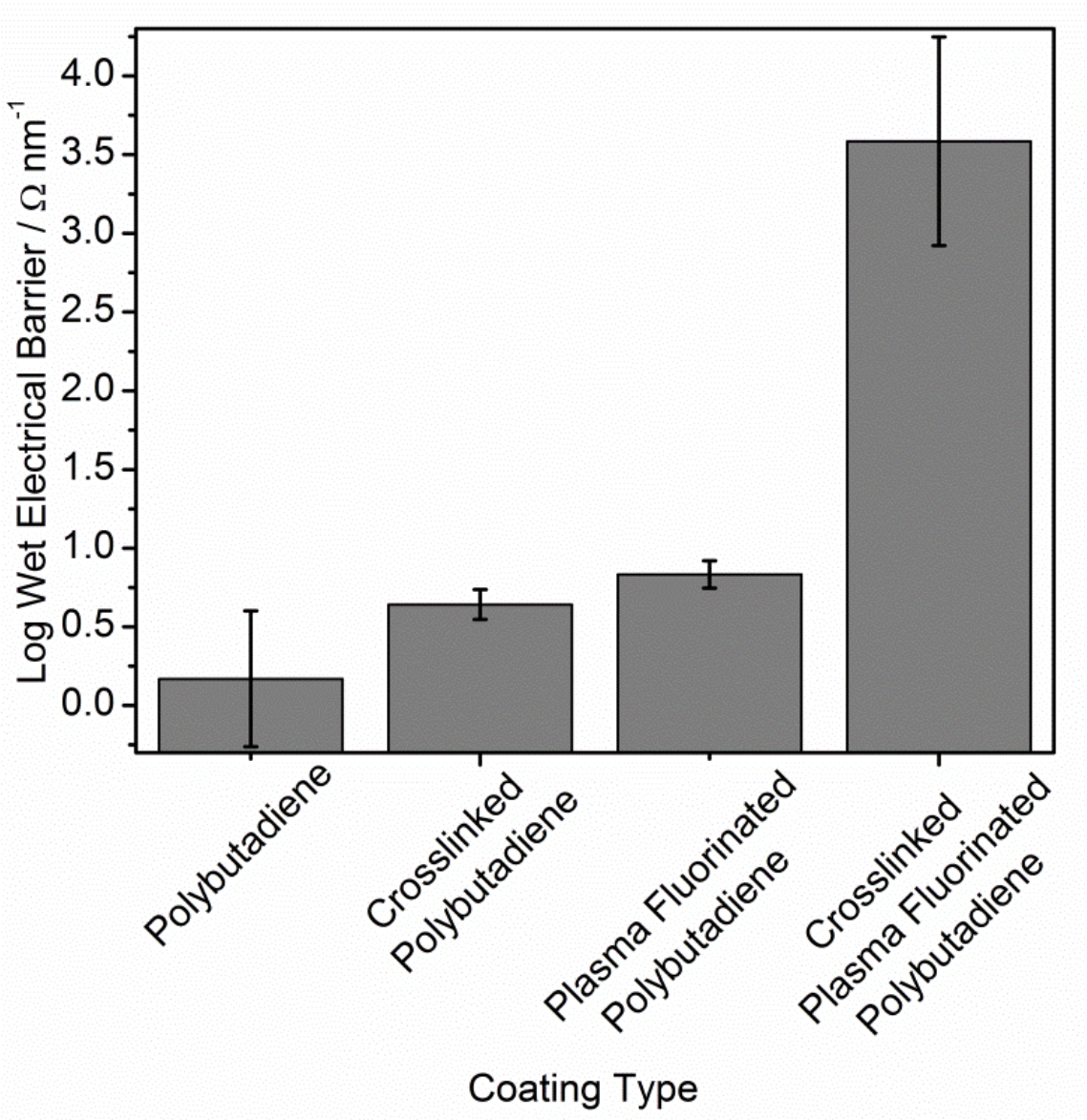

Figure 7-6: Log wet electrical barrier response for polybutadiene, crosslinked polybutadiene, plasma fluorinated (30 W, 0.2 mbar, 5 min) polybutadiene and crosslinked plasma fluorinated polybutadiene, with an average thickness of 1880 ± 30 nm, measured at 4 V for 13 min.

Although the wet electrical barrier measurements for modified polybutadiene did not reach the resistance necessary for barrier function (4 x10^8 Ω), these results showed that a significant increase in barrier performance could be attained by crosslinking and plasma fluorination.

7.3.1.2. Gas Plasma Treatment of Polymer Layers

It was investigated whether the wet electrical barrier performance of a polymer layer could be improved simply by exposure to a gas plasma, or exposure to a gas plasma followed by exposure to monomer vapour, Figure 7-7. It was postulated that the exposure of the polymer layer to an inert gas plasma, such as argon, could possibly stimulate crosslinking of the polymer to improve the wet electrical barrier properties. Based on the results seen for exposing a polymer substrate to an allyl mercaptan plasma, Chapter 3, it was postulated that exposing the layer to a hydrogen sulphide plasma could trigger vulcanisation of the unsaturated carbon-carbon double bonds, to give a better wet electrical barrier performance. However, the electrical results showed no significant barrier improvement for either polybutadiene or polyisoprene base layers.

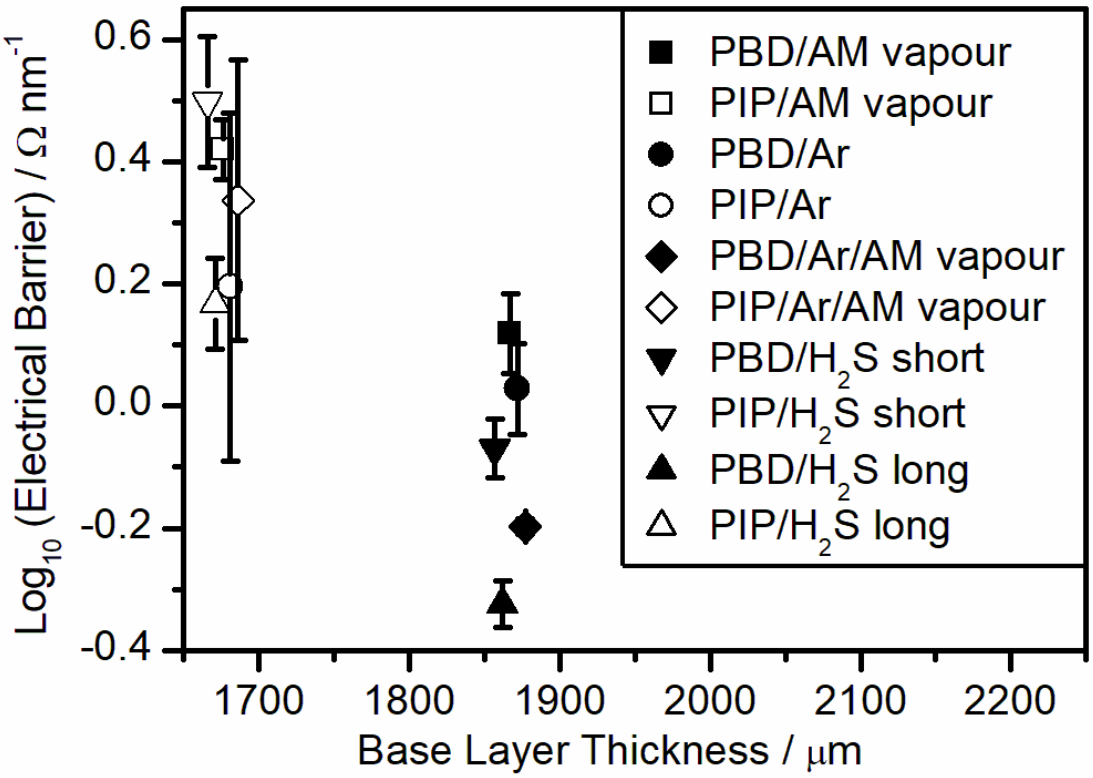

Figure 7-7: Wet electrical barrier performance of polybutadiene (PBD, 1870 nm ± 40 nm) and polyisoprene (PIP, 1680 nm ± 40 nm) layers treated by various means: exposed to allyl mercaptan vapour (0 W, 0.2 mbar, 20 min), exposed to an argon plasma (40 W, 0.2 mbar, 5 min), exposed to an argon plasma (40 W, 0.2 mbar, 5 min) followed by allyl

mercaptan vapour (0 W, 0.2 mbar, 20 min), and exposed to a H_2S plasma (2 W, 0.2 mbar, 1 and 10 min), measured at 8 V for 13 min.

A slight difference was found between the polybutadiene and polyisoprene results, Figure 7-8, which can be explained by the conjugation present in the polyisoprene. The electron donation allows for the unsaturated bonds to be broken more easily, leading to a greater degree of crosslinking. The diminished effect of extending the plasma process time of the H_2S plasma can be explained by the etching processes being dominant for this type of plasma surface modification.

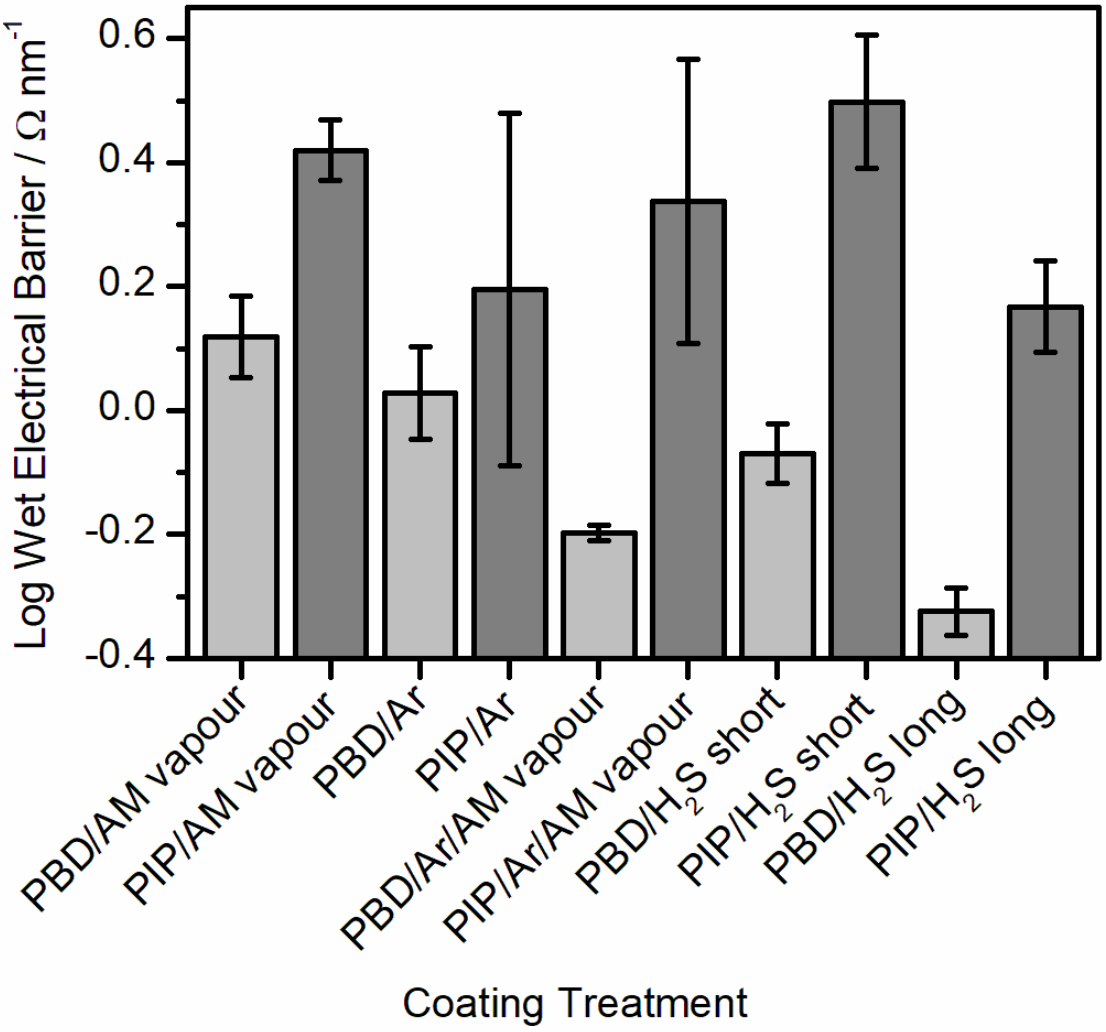

Figure 7-8: Wet electrical barrier performance of polybutadiene (PBD, 1870 nm ± 40 nm) and polyisoprene (PIP, 1680 nm ± 40 nm) layers treated by various means: exposed to allyl mercaptan vapour (0 W, 0.2 mbar, 20 min), exposed to an argon plasma (40 W, 0.2 mbar, 5 min), exposed to an argon plasma (40 W, 0.2 mbar, 5 min) followed by allyl

mercaptan vapour (0 W, 0.2 mbar, 20 min), and exposed to a H_2S plasma (2 W, 0.2 mbar, 1 and 10 min), measured at 8 V for 13 min.

Water contact angles of polybutadiene, polyisoprene and PTFE layers treated by an argon plasma, followed by exposure allyl mercaptan and the structurally similar 1-propanethiol vapour, Table 7-1. Treating the unsaturated polymers with only an argon plasma lowered the contact angle to make the layers hydrophilic. Further treatment by exposing the layers to allyl mercaptan or 1-propanethiol vapour changed the contact angle again: exposure to allyl mercaptan vapour further decreased the contact angle, whereas exposure to 1-propanethiol vapour decreased the contact angle for polybutadiene but gave a slight increase to the polyisoprene. Argon plasma treatment of PTFE followed by exposure to allyl mercaptan and 1-propanethiol gave a minor decrease in the contact angle, but it was not nearly as significant as with the unsaturated polymer layers.

Table 7-1: Contact angles (1 µL ultra-high purity water) of spin coated polybutadiene, spin coated polyisoprene, plasma deposited 1-propanethiol (2 W, 0.2 mbar), plasma deposited allyl mercaptan (2 W, 0.2 mbar), argon plasma treated (40 W, 0.2 mbar, 5 min) polybutadiene, argon plasma treated (40 W, 0.2 mbar, 5 min) polyisoprene, argon plasma treated (40 W, 0.2 mbar, 5 min) polybutadiene after exposure to allyl mercaptan, and argon plasma treated (40 W, 0.2 mbar, 5 min) polyisoprene after exposure to allyl mercaptan.

Polymer Surface	**Contact Angle / °**
Polybutadiene	105 ± 1
Argon plasma treated polybutadiene	31 ± 2
Polyisoprene	98 ± 1
Argon plasma treated polyisoprene	35 ± 2
Plasma deposited allyl mercaptan	83 ± 1
Argon plasma treated polybutadiene/allyl mercaptan vapour	14 ± 2
Argon plasma treated polyisoprene/allyl mercaptan vapour	16 ± 3
Argon plasma treated PTFE/allyl mercaptan vapour	106 ± 1
Argon plasma treated PTFE/allyl mercaptan vapour, rinsed in cyclohexane–IPA	96 ± 5
Plasma deposited 1-propanethiol	85 ± 1
Argon plasma treated polybutadiene/1-propanethiol vapour	22 ± 1
Argon plasma treated polyisoprene/1-propanethiol vapour	41 ± 1
Argon plasma treated PTFE/1-propanethiol vapour	106 ± 5
Argon plasma treated PTFE/1-propanethiol vapour, rinsed in cyclohexane–IPA	97 ± 5

1 Ehrlich, C. D.; Basford, J. A. Recommended Practices for the Calibration and use of Leaks. *J. Vac. Sci. Technol. A* **1992**, *10*, 1–17.